The Physical Basis of Morphogenesis:
Shaping and Patterning of Tissues via Cell-Cell Forces

by

Hayden Nunley

A dissertation submitted in partial fulfillment
of the requirements for the degree of
Doctor of Philosophy
(Biophysics)
in the University of Michigan
2020

Doctoral Committee:

Professor David K. Lubensky, Chair
Professor Pamela A. Raymond
Assistant Professor Kevin Wood
Assistant Professor Qiong Yang

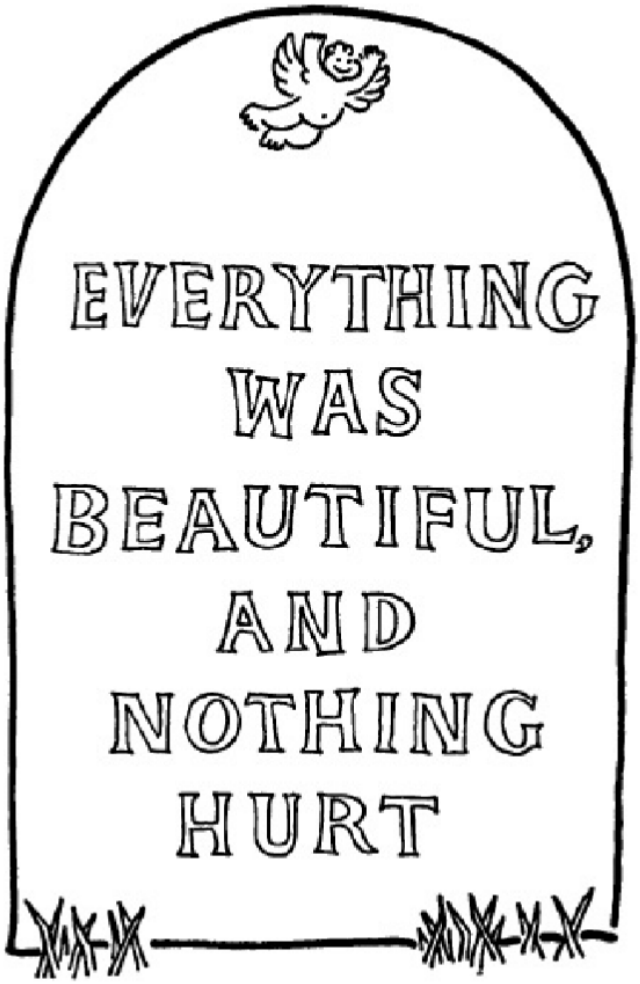
EVERYTHING
WAS
BEAUTIFUL,
AND
NOTHING
HURT

Hayden Nunley

nunley@umich.edu

ORCID iD: 0000-0002-4634-9422

Acknowledgements

This work would not have been possible without excellent collaborators from whom I have learned so much. A collaboration that I treasure immensely is with Pamela Raymond and her lab. Pamela always shares her vast biological knowledge with me, gives me great feedback and advice, and is deeply kind to me. Mikiko is one of the most talented experimentalists I have encountered and provided me with exquisite data to motivate my modeling. I will never forget when Mikiko and Kamirah showed me their experimental process for photoconversion of proteins in the retina. I got to see a juvenile zebrafish, watch its heart beat under the microscope, and then see its crystalline array of UV cones change colors before my eyes.

I, later, joined a collaboration with a lab at the Institut Curie. Though I entered this collaboration with Yohanns Bellaïche and Jesús López-Gay about four years after its start, the collaboration has profoundly influenced my scientific development. I spent many late afternoons skyping with Jesús in Paris. We discussed personal lives, joked around, and bounced scientific ideas off of each other. The amount of experimental data he generated and his incredible work ethic in digesting the data have always impressed me. Yohanns encouraged us to think freely, gave quick and useful comments, and pushed us when necessary. I am indebted to both Yohanns and Jesús, and I look forward to fruitful interactions with them in the future.

The collaboration that forms the basis of the last project of this thesis started in late 2017. This collaboration with Jianping Fu's lab at the University of Michigan deeply challenged me. I spent a few months in the dark: the model that I first built was inconsistent with key parts of their published experimental work. To them I probably seemed useless and confused as a collaborator at the beginning, but they gave me space and time to probe what was wrong with our model. Once I discovered the feature our model was missing (*i.e.,* mechanically distinct cells at the colony boundary), our new model made a prediction that conflicted with their intuitions; nonetheless, they tested the prediction and found it to be true! Of my three thesis projects, this collaboration produced results with the greatest potential scientific impact. I hope that this research forms the basis of a prolonged collaboration between the Lubensky and Fu labs.

I would like to acknowledge both Qiong Yang and Kevin Wood. Qiong has been an excellent committee member, always supportive and asking interesting questions. Kevin Wood let me rotate in his lab, helped me with NSF GRFP preparation, and wrote recommendation letters for me. As a matter of fact, he was the professor who called me to notify me that I had been accepted into the Biophysics Program. Although I ended up joining David's lab rather than Kevin's, he has continued to support me and encourage me throughout graduate school.

The biggest acknowledgment for this thesis needs to go to my P. I. David Lubensky. He has been an excellent match for me as a P. I. He has always pushed me to think bigger and harder. He has extremely high scientific standards, which can be frustrating to Ph.D. students. I liken the experience in his lab to the formation of a diamond under pressure. The experience can be unpleasant, but the unpleasant parts make you a much better scientist. He makes it immensely clear that he cares about his students' personal well-being. I did cry a couple of times in his office, and he encouraged me to be less of a perfectionist and to understand that a couple of failures are not the end of the world. As I move forward into scientific adventures away from Michigan, I look forward to staying in touch with him.

I would like to thank the members of the Lubensky lab. I first met some members, including Meryl Spencer and Alex Golden and Jeremy Hadidjojo, during my time as an R.E.U. student in 2014. Meryl and Jeremy provided early mentorship to me and taught me a lot of coding. When I later joined the lab as a graduate student, I enjoyed spending late afternoons with Meryl as we worked out various scientific/coding problems on the chalkboard. Though he was farther away from me (in the office across the hallway), I loved getting to know Ojan as a person and as a scientist. I also would like to thank two undergraduates with whom I have worked: Jakob Sheridan and Declan Norton. From his freshman year to his senior year, Jakob has developed into a competent scientist, and I hope that I had some meaningful impact on that development. Declan was an excellent R.E.U. student in our lab who made significant contributions in such a short time; he recently received an NSF GRFP based on a proposal he developed while in our lab.

Outside of the lab, my friends from Biophysics kept me sane and uplifted me. Consuming cocktails and nachos, Katie Gentry and I spent countless Friday nights together at Jolly Pumpkin. She is my forever brunch buddy with whom I can vent and laugh. Jeff Folz makes me laugh like no other person does. I have loved adventuring with him, from Detroit to Sleeping Bear. Kelsey Hallinen was a great roommate to me. Whether we were watching Revenge or playing card games

or ranting about our day at work, she always made my life more enjoyable. I would also like to thank Koji Takahashi; I cannot and do not want to imagine the past four years without you.

My family back in Oklahoma has supported me immensely throughout my Ph. D. My mom has listened to me gripe in my lows and celebrated with me in my highs. I know that she has hated my being so far from home, but that never kept her from being there for me. My dad never attended college and has always been proud of me for pursuing a Ph.D. I am grateful for his support and care. My sister is a great friend, protector, and supporter. She has stood up for me, cheered for me, and cared for me. I have spent many late nights on the phone with her. I consider myself privileged to have such a great family.

Table of Contents

List of Tables

Table

List of Figures

Figure

(pseudo-colored magenta) form an anisotropic triangular sublattice that interpenetrates with an anisotropic triangular sublattice of Blue cones (pseudo-colored blue). We connect (white lines) a subset of nearest neighbors in the Blue cone sublattice. **E)** Blue (pseudo-colored blue) and Red (pseudo-colored red) cones in flat-mount retinal preparation from panel B. Red cones neighbor Blue cones in each column. The Red cones form an anisotropic honeycomb sublattice. We connect (white lines) a subset of nearest neighbors in the Red cone sublattice; note the different nearest neighbor patterns in the Blue cone triangular sublattice (panel D) and the Red cone honeycomb sublattice (panel E). The Green cones form a honeycomb sublattice (not shown here).....11

2.2 **A Y-Junction, a topological defect in the cone mosaic, is an insertion of a row and a column. A)** Schematic of simple row insertion in cone mosaic. As new cone photoreceptors are incorporated to right of the defect, a series of improper cone contacts (black box) within columns form. If colors were reversed in one of the new columns, so that a Red cone contacts a Green cone, there would instead be improper Red-UV and Blue-Green contacts. White dashed lines: rows associated with defect. **B)** Schematic of a Y-Junction, a topological defect in the zebrafish cone mosaic. A Y-Junction only disrupts the cone mosaic near the core rather than along an entire line of contacts. White (black) dashed lines: rows (columns) associated with the defect. **C)** A Y-Junction in a flat-mount retinal preparation from an adult, double transgenic (Tg[*sws1:GFP*; *sws2:mCherry*]) line in which UV and Blue cones express distinct fluorescent reporters (pseudo-colored magenta and blue, respectively) under control of UV and Blue opsin promoters, respectively. Antibody staining labels Red and Green cones (both pseudo-colored green). **D)** Each UV cone from panel C is connected (white bonds) to its nearest UV cone neighbors. To the left and right of the defect, rows are counted. Seven-sided (five-sided) star: seven-coordinated (five-coordinated) UV cone. **E)** A circuit of triangulation bonds around defect from panels C-D. Red

photoconvert a patch of UV cones (purple box) near the margin, where new UV cone photoreceptors are incorporated by mitotic addition. After two, three or four days of retinal growth, we image the photo-converted region. **B)** Example of patch of UV cones immediately after photo-conversion and two days later. In this line (Tg[*sws1:nEOS*]), UV cones express a nuclear-localized, photoconvertible fluorescent protein under control of UV cone opsin promoter. The non-photoconverted fluorescent protein is pseudo-colored yellow, and the photoconverted fluorescent protein is pseudo-colored magenta. Retinal margin is to the right of each image. Approximately eight columns of UV cones have been added in two days since photoconversion. **C)** Glide motion involves subtle motion of individual UV cones near Y-junction core. Magenta circles are UV cones with photoconverted fluorescent signal, and yellow circles are surrounding UV cones with non-photoconverted fluorescent signal. Every cone is connected to nearest neighbors. The five-sided and seven-sided star indicate five-coordinated and seven-coordinated UV cones, respectively. Dashed black line is the "inserted" row. The two triangulations on the right describe positions of UV cones (from the left triangulation) after glide in the direction denoted by gray arrow. Note that the assignment of five- and seven-coordinated UV cones has shifted. by one row.....18

2.5 **By estimating timescale of Y-Junction motion, we conclude that Y- Junctions line up into grain boundaries during initial mosaic formation rather than by subsequent Y-Junction motion. A)** Expected motion of individual UV cones in case of glide motion by one row in either direction. Left triangulation is of UV cones near the defect core; a UV cone sits on each site of triangulation. Two triangulations on the right are positions of UV cones (from left triangulation) after glide in the direction denoted by the gray arrow. The UV cones (originally sitting on sites of black triangulation) shift to sites of gray triangulation. Note that the originally five- and seven-coordinated UV cones in black triangulation become six-coordinated. **B)** Example of Y-Junction

where proteins distributions and quantifications are reported at 26 hAPF, unless otherwise stated. Inset in A shows the cell resolution capacity of multi-position confocal microscopy. **B)** Medial-lateral (m-l) tissue elongation (mean ± SEM, blue) and inferred junctional mechanical stress anisotropy (mean ± SEM, red; positive values indicate tensile stress is higher along the m l axis) in the region boxed in A. N: number of animals at each timepoint. **C)** E-Cad:3xmKate2 and MyoII:3xGFP distributions within the region boxed in A at 18 hAPF (left) and 26 hAPF (right). Arrowheads: aSFs. **D)** Number of aSFs per cell (blue, mean ± SEM) and tissue stress anisotropy estimated by laser ablation (red, mean ± SEM) between 14 and 28 hAPF. n and N: minimum numbers of cells and ablations used at each time-point, respectively. **E)** Rose plot of the orientation of aSFs at 26 hAPF. n: aSF number. **F)** E-Cad:3xmKate2 and MyoII:3xGFP distributions before ablation (left) as well as at 1.3s (middle) and 9.2s (right) after aSF ablation. Dashed box: ablated region. Time at ablation is set to 0. Arrowheads: positions of the AJs prior to and after aSF ablation. **G, G')** E-Cad:3xmKate2 and MyoII:3xGFP distributions at level of the AJ (G) and along the cell apical-basal (a-b) axis (G'). Arrowheads in G indicate position of a-b section shown in G'. Conversely, the arrowheads in G' indicate the a-b position of the section shown in G. **H-J)** Distributions of Zyx:ChFP and MyoII:3xGFP (H), Ena:GFP and MyoII:3xmKate2 (I) and Actn:GFP and MyoII:3xmKate2 (J) at 26 hAPF. Arrowheads indicate some aSFs. **K, K')** E-Cad:3xmKate2 and MyoII:3xGFP distributions in the posterior central region in the *mirr-G4>LifeAct:GFP* (control, K) and *mirr-G4>zip^{DN}:YFP* (K') animals. *mirr*-G4 specifically drives expression in the lateral tissue domain. See also Fig. B.1M-M'. Arrowheads: aSFs. **L)** Graph of the m-l tissue recoil velocity upon a-p ablation (mean ± SEM,) in control *mirr-G4>LifeAct:GFP* versus *mirr-G4>zip^{DN}:YFP* tissues. N: number of ablations; p-value<10^{-3}. **M)** Graph of the number of aSFs per cell (mean ± SEM) in control *mirr-G4>LifeAct:GFP* versus *mirr-G4>zip^{DN}:YFP*

measurement schematic. Upon AJ or aSF laser ablation, the $l0$ and lt distances (corresponding to distances at t=0 and t=1.3s) were used to calculate AJ or aSF recoil velocity, respectively. **G)** Graph of recoil velocity (µm/s, orange, mean ± SEM,) of ablated AJ without prior aSF ablation and 30s after aSF ablation was performed; (*n*: number of ablations; *p*-value<0.05); graph of recoil velocity (µm/s, blue, mean ± SEM) upon aSF ablation without prior junction ablation and 30s after prior ablation of a neighbouring AJ (*n*: number of ablations; *p*-value<10^{-5}). Only aSFs and AJs oriented between 72° and 118° relative to the a-p axis were used. See Fig. B.2E for junction and aSF velocity recoil after ablation as a function of their orientation relative to a-p axis. n: number of ablations. **H**) Graph of junction recoil velocity (µm/s, mean ± SEM) upon AJ ablation in w^{RNAi} control and $actn^{RNAi}$ cells at 18 hAPF (ns) and at 26 hAPF (*p*-value<10^{-4}). n: number of ablations. **I)** Schematic of the vertex model of a regular cell packing with aSFs under uniaxial stress (see Appendix B and Fig. B.3A-C). **J)** Cell elongation and tension distribution (γ, color scale) in vertex model without (top) or with (bottom) aSFs at fixed cell size and cell orientation and at fixed uniaxial tissue stress. Grey cells illustrate differential cell elongation, whereas colored cells illustrate the magnitude of tension at AJ and individual aSFs in high stress anisotropy case (at fixed tension per aSF). **K)** Number of aSFs per cell (at fixed tension per aSF) required for cells to remain regular under uniaxial stress as a function of cell apical area. See Fig. B.3I,J for vertex model parameter values. **L**) Graph of aSF number per cell (mean ± SEM) as a function of apical cell size in w^{RNAi} control and $actn^{RNAi}$ cells at 26 hAPF. n: number of cells. *p*-value< 10^{-5}. **M**) Graph of changes in cell elongation (percentage, mean ± SEM) without ablation, upon mock aSF ablation (i.e. ablation next to an aSF), and upon ablation of increasing number of aSFs in cells. *p*-value<10^{-4}. Cell elongation variations were determined for an interval of 9.2s in absence of ablation or between t=0s (time of ablation) and t=9.2s after ablation. n: number of cells without

ablation, with mock ablations or with ablations on aSFs. **N)** Graphs of cell apical area (left, mean ± SEM) and aSF number per cell (right, mean ± SEM) 1h before and 1h after telophase in w^{RNAi} control cells (p-values<10^{-5} for area and p-values<10^{-5} for aSF number) and $auroraB^{RNAi}$ ($aurB^{RNAi}$) cells, ns for area and number of aSFs). n: number of cells. **O)** Graphs of cell apical area (horizontal axis, mean ± SEM) versus aSF number per cell (vertical axis, mean ± SEM) in control w^{RNAi}, $survivin^{RNAi}$ (svn^{RNAi}), $aurB^{RNAi}$, *tribbles overpression* ($trbl^{up}$) and $cdc2^{RNAi}$ cells. Number of cells w^{RNAi} (n: 2903), svn^{RNAi} (n: 872), $aurB^{RNAi}$ (n: 402) $trbl^{UP}$ (n: 356) and $cdc2^{RNAi}$ (n: 227). **P**) Graph of difference in cell elongation (mean ± SEM) upon ablation of all aSFs in a given cell as a function of apical area. Differences were measured 9.2s after ablation. n: number of cells. p-value<0.05 (25-35µm^2) and p-value<10^{-3} (+35µm^2) for differences with the first bin. **Q**) Graph of difference in m-l cell elongation between $actn^{RNAi}$ cells and w^{RNAi} control cells (mean ± SEM) as a function of apical cell size at 18, 20, 22, 24 and 26 hAPF. n: minimum number of cells used at each hAPF and condition. p-value<10^{-4}. Scale bars: 5µm (A). Statistical tests: Kruskal-Wallis tests (B, C, E, G, H and N), Kruskal-Wallis tests with Conover post hoc (M and P), Ancova tests (L and P) and mixed-ANOVA (D). ns: not significant. Statistically significant differences (p-value<0.05) are indicated by one asterisk. In the case of multiple pairwise comparisons, only maximum p-values (of the set of asterisked comparisons) are reported.....49

3.3 **Hippo component clustering and aSF formation.** Unless otherwise stated, protein distributions and quantifications are reported for region boxed in Fig. 3.1A at 26 hAPF. **A-B)** Distributions of Jub:GFP (A), Wts:GFP (B) and MyoII:3xmKate2 (A,B) at 26 hAPF. Arrowheads: aSF tips. **C)** Graph of the ratios of Jub:GFP and Wts:GFP in clusters versus along AJ ($ratio^{in/out}$ of cluster, mean ± SEM) at 18 hAPF (low stress) and 26hAPF (high stress). n: number of cells; p-values<10^{-5} for comparison between 18 hAPF and 26 hAPF for both Jub:GFP and Wts:GFP. See

Fig. B.4B-B''' for cluster identification and quantifications. **D-D')** Distributions of Jub:mKate2 and Wts:GFP at 18 hAPF (low stress, D) and at 26 hAPF (high stress, D'). Arrowheads: Jub:mKate2 and Wts:GFP co-clusters. **E**) Graph of colocalization (Pearson Correlation Coefficient, mean ± SEM) between Jub:mKate2 and Jub:GFP or between Jub:mKate2 and Wts:GFP at 18 hAPF (low stress) and 26 hAPF (high stress). Pearson coefficients were normalized by the mean of the Pearson coefficient between Jub:GFP and Jub:mKate2 at 18 hAPF. n: number of cells; Jub:mKate2 and Jub:GFP colocalization: ns; Jub:mKate2 and Wts:GFP colocalization: *p*-value<10^{-5}. **F-F')** Distributions of Jub:mKate2 (green, F and fire, F') and MyoII:3xGFP (F) during aSF formation. t=0 corresponds to aSF nucleation. Arrowheads: yellow aSF (F) and light green Jub:mKate2 cluster (F'). **G-G')** Distribution of Jub:GFP before and after (t=90s) ablation of the aSF labelled by MyoII:3xmKate2 (G). Time was set to 0 just before ablation (ablation at t~0.01s). Arrowheads: cluster prior to and after ablation. Graph of Jub:GFP cluster intensities (mean ± SEM) in mock ablated aSF (control) and upon aSF ablation (G'). n: number of ablations; *p*-value<10^{-3} after timepoint 30s. **H-H')** Wts:CitFP (H) before and after (t=210s) ablation of aSF labelled by MyoII:3xmKate2. Time was set to 0 just before ablation (ablation at t~0.01s). Arrowheads: cluster prior to and after ablation. Graph of Wts:CitFP cluster intensities (mean ± SEM) in mock ablated aSF (control) and upon aSF ablation (H'). n: number of ablations, *p*-value<10^{-2} after timepoint 120s. **I-J**) Distributions of Jub:GFP (I) and Wts:CitFP (J) in $actn^{RNAi}$ cells (marked by the expression of Caax:tBFP, not shown) outlined by orange dotted line and surrounding control cells. **K**) Graphs of the Jub:GFP and Wts:CitFP ratio$^{in/out}$ of clusters (mean ± SEM) in w^{RNAi} control and $actn^{RNAi}$ cells at 26 hAPF. n: number of cells; *p*-values<10^{-5} for Jub:GFP and Wts:CiFP. **L**) Graph of normalized colocalization (Pearson Correlation Coefficient) of Jub:mKate2 and Wts:GFP (mean ± SEM) in w^{RNAi} control and in $actn^{RNAi}$ cells at 26h APF. n: number of cells; *p*-value<10^{-4}.

M) Graph of *ban-nls:GFP* intensity (mean ± SEM) in w^{RNAi} control and $actn^{RNAi}$ cells at 18 hAPF and 26 hAPF. Average intensities were normalized by mean intensities of w^{RNAi} cells at 18hAPF. N: number of animals; 18 hAPF: ns; 26 hAPF: p-value<10^{-3}. **N)** Graph of the fraction of cells that divide (mean ± SEM) between 18 and 26 hAPF and between 26 hAPF and 34 hAPF in *pnr-G4>*w^{dsRNA} (control) versus *pnr-G4>*$actn^{dsRNA}$ tissues; prior to 26 hAPF: ns; after 26 hAPF: p-value<0.05. N: number of animals. Scale bars: 2µm (A, D, F, G and H), 5µm (I-J) Statistical tests: Kruskal-Wallis test (C, E and K-M), Kruskal-Wallis tests with Conover post hoc (G', H') and One-tailed Wilcoxon signed rank test (N). ns: not significant. Statistically significant differences (p-value<0.05) are indicated by one asterisk. In the case of multiple pairwise comparisons, only the maximum p-values (of the set of asterisked comparisons) are reported. 52

3.4 **Hippo signalling and scaling of aSF number with cell size.** Unless otherwise stated, protein distributions and quantifications are reported for region boxed in Fig. 3.1A at 26 hAPF. **A)** Graph of intensity of *ban-nls:GFP* and *Ubi-nls:GFP* (mean ± SEM) as a function of apical cell area. n: cell numbers. p-value<10^{-5}. **B)** Graph of *ban-nls:GFP* intensity (mean ± SEM) as a function of the Jub:mKate2 ratio$^{in/out}$ of cluster. n: number of cells. **C)** Graph of Wts:CitFP and Jub:GFP ratio$^{in/out}$ of cluster (mean ± SEM) as a function of apical cell area. n: number of cells. **D, E)** Graphs of Jub:GFP (D) and Wts:CitFP (E) ratio$^{in/out}$ of cluster (mean ± SEM) as a function of apical cell size in w^{RNAi} control and $actn^{RNAi}$ cells. n: number of cells; p-value<10^{-4}. **F)** Graph of the fraction of cells that divide between 22 hAPF and 34 hAPF as a function of apical cell size (mean ± SEM) in *pnr-G4>*w^{dsRNA} (control) versus *pnr-G4>*$actn^{dsRNA}$ tissues. N: number of animals (regions used of each animal contained on average 380 cells for w^{RNAi} and 243 cells for $actn^{RNAi}$, see M&M); p-value<0.05. **F)** Graph of the fraction of cells that divide between 22 hAPF and 34 hAPF as a function of apical cell size (mean ± SEM) in *pnr-G4>*w^{dsRNA} (control) versus *pnr-G4>*$actn^{dsRNA}$

tissues. N: number of animals (regions used of each animal contained on average 380 cells for w^{RNAi} and 243 cells for $actn^{RNAi}$, see M&M); p-value<0.05. **G)** Distribution of E-Cad:3xmKate2 and MyoII:3xGFP at aSF nucleation (t=0 min), as the aSF peels from the cortex (t=2 min to 14 min), reaching TCJs (t=22 min), at TCJs (t=34 min) and after breakage (t=42 min). Red arrowhead: nucleating TCJ; yellow arrowheads: aSF tips; blue arrowheads: breaking TCJs. Blue "x" marks absence of the aSF. **H)** Schematic of aSF nucleating at a TCJ (red arrowhead) and peeling from the cortex until aSF tips reach breaking TCJs (blue arrowhead). Orange arrows indicate the TCJ bisector, that makes an angle θ with the a-p axis ($\theta \approx 5°$ for nucleating TCJ at right; $\theta \approx 80°$ for breaking TCJ at bottom). **I)** Graph of proportion of aSF nucleation (red) and breakage (blue) events at TCJs. Each bar includes absolute number of aSFs observed in that group. n: total number of aSFs. **J)** Cumulative distribution of TCJ bisector orientations for TCJs where aSFs are observed to nucleate (red) and break (blue). See Appendix B.2 for our criterion for aSF breakage at a TCJ. n: number of nucleation and breakage events. **K-M)** Graphs of average aSF number per cell (K), aSF nucleation rate (L) and aSF lifetime (M) measured between 25 and 27 hAPF as a function of cell apical area. Dashed lines: best-fit linear regressions; n: number of cells. **N)** Graph of experimental (grey) and model-predicted (green) aSF number per cell (mean ± SEM) as a function of cell apical area. Our model explains approximately 75 percent of variance of aSF number with cell apical area. n: number of cells; see Fig. B.6, Fig. B.7 and Appendix B. **O)** Schematic based on a Jub:GFP confocal image illustrating positions of control cells (white) as well as the border (brown) and bulk (blue) $trbl^{UP}$ clone cells marked by Caax:tBFP accumulation. **P)** Graph of nucleating TCJs per cell (mean ± SEM) in $trbl^{UP}$ border and $trbl^{UP}$ bulk cells. n: number of cells; p-value<10^{-5}. **Q)** Graph of aSF number per cell (mean ± SEM) in $trbl^{UP}$ border and $trbl^{UP}$ bulk cells. n: number of cells; p-value<10^{-2} controlling for cell apical area differences (see Fig. B.9B,C

and Appendix B.3). **R)** Graph of predicted aSF lifetime (mean ± SEM) in $trbl^{UP}$ border and $trbl^{UP}$ cells. n: number of cells. **S)** Graph of predicted aSF number per cell (mean ± SEM) in $trbl^{UP}$ border and $trbl^{UP}$ cells. n: number of cells; p-value<10^{-2} controlling for cell apical area differences (see Fig. B.9F,G and Appendix B.3). **T)** Schematic of elongated (top) and ortho-elongated (bottom) cells having same number of nucleating TCJs and same apical area; aSFs must travel farther between nucleating and breaking TCJs in the ortho-elongated case. **U)** Graph of aSF number per cell (mean ± SEM) in elongated and ortho-elongated cells. n: number of cells; p-value<10^{-5}. **V)** Graph of number of nucleating TCJs per cell (mean ± SEM) in elongated and ortho-elongated cells. n: number of cells. **W)** Graph of cell apical area (mean ± SEM) in elongated and ortho-elongated cells. n: number of cells. **X)** Graph of predicted aSF lifetime (mean ± SEM) in elongated and ortho-elongated cells. n: number of cells; p-value<10^{-5}. **Y)** Graph of predicted aSF number per cell (mean ± SEM) in elongated and ortho-elongated cells. n: number of cells; p-value<10^{-5}. Scale bars: 2μm (G). Statistical tests: Kruskal-Wallis tests (P-S and U-Y), Ancova tests for difference in regression slopes (A,C-F) and Mixed-ANOVA (F). r: Pearson correlation coefficients. ns: not significant. Statistically significant differences (p-value<0.05): one asterisk.....55

4.1 ***In vitro*** **model of neural induction. A)** Schematic of neural induction in vivo. Astrip of cells in the embryonic ectoderm differentiates into neural plate (NP, red). Cells on either side form the neural plate border (NPB, cyan). **B)** Schematic of neural induction in vitro. Human pluripotent stem (hPS) cells bind to circular regions of elastic substrate (tan). Seven days after neural induction initiation, we stain for NP (red) and NPB (cyan). Schematics are Voronoi tessellations of nuclear positions before and after neural induction initiation. **C)** Representative immunofluorescence images of colony at day 9. DAPI counterstains nuclei. PAX3 and PAX6 staining label nuclei of NPB cells and NP cells, respectively. Scale bar, 20 μm. **D)** Schematic of cell-cell communication

B.1 **Tissue mechanical stress and aSF organization.** Unless otherwise stated, protein distributions and quantifications are reported for the region boxed in Fig. 3.1A at 26 hAPF. **A-A')** Picture of the *Drosophila melanogaster* pupa (A) and close-up picture of the adult dorsal thorax (notum, A'). Orange region in A delineates the pupal dorsal thorax (notum). Dashed box: Posterior and central region where aSFs form and corresponding region in the adult. Red line: midline. **B)** Graph of the tissue recoil velocity (mean ± SEM) along the a-p axis (red) and m-l axis (blue) between 14 hAPF and 28 hAPF. Blue asterisks: calculated for the comparison of the recoiled velocities measured at 18 hAPF and at a later timepoint for a-p ablation, p-values<0.05 from 22 hAFP. Red asterisks: calculated for the comparison of the recoiled velocity measured along the a-p and m-l tissue axes, p-values<10^{-5} from 22 hAFP. n: minimum number of ablations at each timepoint and orientation. **C,C')** E-Cad:3xmKate2, nls:mRFP and MyoII:3xGFP distributions at the level of the AJ (C**)** and along the cell a-b axis (C'**)**. Yellow arrowheads in C indicate the position of a-b section shown in C'. Conversely, the yellow arrowheads in C' indicate the a-b position of the section shown in C. **D-D'')** Dlg:YFP and MyoII:3xmKate2 distributions at the level of the AJ (D), of the septate junction (D') and along the a-b axis (D''). Yellow arrowheads in D indicate the position of a-b section shown in D''. Yellow and blue arrowheads in D'' indicate the a-b position of the section shown in D and D', respectively. **E-L)** Localization of LifeAct:GFP and MyoII:3xmKate2 (E), Vinc:GFP and MyoII:3xmKate2 (F), Kst:YFP and MyoII:3xmKate2 (G), Zasp52:GFP and MyoII:3xmKate2 (H), Pax:YFP and MyoII:3xmKate2 (I), Cher:YFP and MyoII:3xmKate2 (J), Rhea:GFP and MyoII:3xmKate2 (K) and Mys:GFP and MyoII:3xmKate2 (L). **M-M')** MyoII:3xGFP and E-Cad:3xmKate2 in control *mirr-G4>LifeAct:GFP* (M) and in

function of cell apical area. n: number of cells. **G-H)** Graph of number of aSFs per cell as a function of cell apical area (F) or volume (H). n: number of cells. **I)** Graph of cell elongation (mean ± SEM) as a function of cell apical area in w^{RNAi} and $actn^{RNAi}$ cells at 26 hAPF. n: number of cells; *p*-value<10^{-5}. Scale bars: 5µm (B). Statistical tests: Kruskal-Wallis tests (C, D and E'') and Ancova tests for difference in regression slopes (I). r: Pearson correlation coefficient. ns: not significant. Statistically significant differences (*p*-value<0.05) are indicated by one asterisk. 137

B.3 **Theoretical modelling of cell elongation as a function of tissue stress anisotropy and aSF number.** *To gain a physical understanding of the contributions of aSFs to epithelial cells under anisotropic mechanical stress, we consider regular hexagonal epithelia under uniaxial tensile stress (by convention, along the vertical axis). The regular hexagonal epithelia are organized into one of two orientations, called the cable-forming (CFO) and non-cable-forming (NCFO) orientations, relative to the uniaxial stress (A-C). Tensile forces on cell-cell junctions and on aSFs allow these epithelial cells to resist elongation (D-H). Given that no cell has an infinite pool of MyoII, there is a finite bound on the stress anisotropy that the cells can resist ($\sigma_{max} > \sigma_D \equiv \sigma_{yy} - \sigma_{yy} > 0$). We ask whether cells resist elongation more or less effectively by redistributing junctional MyoII to aSFs (D-H). The vertex model with aSFs predicts that for cells to remain regular hexagons under uniaxial stress, the number of aSFs, or the total aSF tension, per cell must scale linearly with the square root of the cell apical area (I). Larger cells must compensate for the greater distance between edges (orthogonal to the uniaxial stress) by increasing the aSF number, or total aSF tension, per cell.* **A)** Schematic of hexagonal epithelium in the cable-forming orientation (CFO) with aSFs (green). Epithelial geometry is characterized by two edge lengths ($l1$ and $l2$) and one angle (θ). Edges of length $l1$ have tension $\gamma 1$; edges of length $l2$ have tension $\gamma 2$. Total aSF tension per cell is γf. **B)** Schematic of hexagonal epithelium in the non-cable-forming

orientation (NCFO) with aSFs (green). Epithelial geometry is characterized by two edge lengths ($l3$ and $l4$) and one angle (ϕ). Edges of length $l3$ have tension $\gamma 3$; edges of length $l4$ have tension $\gamma 4$. Total aSF tension per cell is γf. **C)** Schematic of stress anisotropy calculation in epithelium from (B). Using linear cuts of the epithelium along axes parallel (magenta dashed line) or perpendicular (blue dashed line) to the aSFs, we sum projections (perpendicular to the cut) of tensile forces from edges and aSFs to calculate a tensile force per length (*i.e.*, 2D stress) along the cut. **D-E)** Schematics of cell shapes and edge tensions for fixed stress anisotropy ($\sigma D \sigma max$ indicated in each panel) in the CFO (top) and NCFO (bottom). Edge and aSF widths correspond to magnitudes of tension. Cells with more aSFs (vertical lines in each cell) have a larger total aSF tension γf. As the number of aSFs increases, cell elongation in the direction of imposed tension decreases. Blue dashed lines form regular hexagons (see Appendix B Eqs. 11, 12). **F)** Graph of cell elongation normalized by the elongation $Sreg, hex$ of a regular hexagon ($S/Sreg, hex$) as a function of stress anisotropy (σ_D/σ_{max}). We compare cells in the CFO without aSFs to cells in the NCFO with total aSF tension (γf). **G-H)** Plot of normalized cell elongation ($S/Sreg, hex$) as a function of total aSF tension (γf) and stress anisotropy (σ_D/σ_{max}) for cells in the CFO and NCFO. Tension is scaled such that $\gamma f = 1$ corresponds to the edge tension in the case of isotropic stress without aSFs. Note that large total aSF tensions (upper left-hand quadrant of plot) generate cells which are elongated orthogonal to the uniaxial stress. The elongation measure S does not distinguish between elongation along the uniaxial stress and elongation orthogonal to the uniaxial stress. **I)** Plot of aSF number per cell (at fixed tension per aSF) as a function of the square root of cell apical area in the vertex model. For this plot, $\sigma_D = 2/3\sigma_{max}$ and the tension per aSF is equal to one third of the edge tension in the case of isotropic stress without aSFs. **J)** Graph of the cell apical area as a function of the square root of the cell apical area between 10 and 40μm, illustrating

to measure the mean intensity in each cluster (Ic) and the area occupied by each cluster (Ac); (ii) The mean intensity along the AJ, (Iaj): the AJ cell contour was selected using Fiji segmented line tool (blue, B''') and used to measure (Iaj) and the total area of the cell junction (Aaj); (iii) The mean fluorescent background intensity (Ib) was measured by selecting the apical medial region of the cells (red, B'''). **C)** Graph of the number of Jub:GFP and Wts:GFP clusters per cell (mean ± SEM) at 18 hAPF (low stress) and 26hAPF (high stress). n: number of cells; p-values<10^{-4} for the difference between 18 hAPF and 26 hAPF for both Jub:GFP and Wts:GFP. **D-D')** Distributions of Cry2Olig:ChFP and Wts:GFP at the time of blue light illumination at t=0s (D) and at t=950s upon blue light illumination every 50 s (D'). **E-E')** Distributions of Cry2Olig:ChFP:Jub and Wts:GFP at the time of blue light illumination at t=0s (E) and at t=950s upon blue light illumination every 50 s (E'). **F)** Graph of the intensity of the *DIAP1-nls:GFP* Yorkie reporter (mean ± SEM) in tissues expressing Cry2Olig:ChFP or Cry2Olig:ChFP:Jub in dark (ns) or light (p-value<0.01) conditions. Fluorescence intensities were measured at 0h (beginning of the experiment) and 4h. The fluorescence intensities measured at 4h were divided by fluorescence intensities measured at 0h, and the resulting ratios were normalized by the mean of the ratios calculated for Cry2Olig:ChFP of each condition. Clustering was induced by two initial steps of high blue laser illumination (491nm, interval 5 min), and then was maintained at low laser power for GFP imaging, every 5 min. N: number of experiments. **G-G')** Distributions of Wts:CitFP (green, G and fire, G') and MyoII:3xGFP during aSF displacement. Yellow arrowheads: aSF (G); light green arrowheads: Wts:CitFP cluster (G'). **H-I)** Graph of cortical Jub:GFP (H) and Wts:GFP (I) normalized integrated intensity (mean ± SEM) in w^{RNAi} control and $actn^{RNAi}$ cells. Integrated intensities of the w^{RNAi} control or $actn^{RNAi}$ cells were normalized by the mean integrated intensity of surrounding cells not juxtaposed with the w^{RNAi} control and $actn^{RNAi}$ cells, respectively. **J**) Graphs of the number

of Jub:GFP and Wts:CitFP clusters (mean ± SEM) in w^{RNAi} control and $actn^{RNAi}$ cells at 26 hAPF. n: number of cells; p-values<10^{-3} for Jub:GFP and Wts:CiFP. **K)** Graph of *ban-nls:GFP* intensity (mean ± SEM) in control and $actn^{IG1}$ cells at 26 hAPF. Average intensities were normalized by mean intensities of control cells. N: number of animals; p-value<10^{-2}. **L)** Graph of cell division rate between 16 and 40 hAPF (mean ± SEM) in *pnr-G4>*w^{dsRNA} (control) and *pnr-G4>*$actn^{dsRNA}$ tissues. At the central and posterior region of the tissue (box in Fig. 3.1A), cell proliferation occurs as two successive waves. The first wave occurs between 18 and 24 hAPF, while the second one occurs after 24 hAPF. This second wave of division corresponds to cells that have progressed through the cell cycle under higher mechanical stress. The reduction of Actn function leads to a specific decrease in the number of cell divisions during this second wave. Average number of cells used per animal in w^{RNAi} is 218 and in $actn^{RNAi}$ is 148. N: number of animals. p-value<10^{-2}. Scale bars: 2 µm (D, G). Statistical tests: Kruskal-Wallis tests (A, C, F and H-K) and mixed-ANOVA test (L). ns: not significant. Statistically significant differences (p-value<0.05) are indicated by one asterisk. 140

B.5 **Hippo/Yki scaling with cell apical area.** Unless otherwise stated, protein distributions and quantifications are reported for the region boxed in Fig. 3.1A at 26 hAPF. **A)** Graph of Wts:GFP $ratio^{in/out}$ of cluster (mean ± SEM) as a function of apical cell size at 18 hAPF and 26 hAPF. n: number of cells; p-value<10^{-4}. **B)** Graph of Wts:CitFP and Jub.GFP $ratio^{in/out}$ of cluster (mean ± SEM) as a function of apical cell size at 18 hAPF. n: number of cells; p-value<0.05. **C)** Graph of the number of Jub:GFP clusters (mean ± SEM) as a function of apical cell size in w^{RNAi} control and $actn^{RNAi}$ cells at 26 hAPF. n: number of cells; p-value<10^{-5}. **D)** Graph of apical cell area (mean ± SEM) versus *ban-nls:GFP* intensity (mean ± SEM) in w^{RNAi}, $actn^{RNAi}$, $aurB^{RNAi}$ and svn^{RNAi} cells. Number of cells (n) used to calculate cell apical area (and clustering of Jub:GFP, in Fig. B.5E) and

number of animals (N) *ban-nls:GFP* w^{RNAi} (n: 140 and N: 8), $actn^{RNAi}$ (n: 125 and N: 13), $aurB^{RNAi}$ (n: 45 and N: 9) and suv^{RNAi} (n: 140 and N: 10). Dotted line is the regression line for the w^{RNAi}, $aurB^{RNAi}$ and svn^{RNAi} data points. **E)** Graph of Jub:GFP ratio$^{in/out}$ of cluster (mean ± SEM) versus *ban-nls:GFP* intensity (mean ± SEM) in w^{RNAi}, $actn^{RNAi}$, $aurB^{RNAi}$ and svn^{RNAi} cells. Number of cells (n) used for Jub:GFP clustering (and cell apical area, in Fig. B.5D) and number of animals (N) *ban-nls:GFP* w^{RNAi} (n: 140 and N: 8), $actn^{RNAi}$ (n: 125 and N: 13), $aurB^{RNAi}$ (n: 45 and N: 9) and svn^{RNAi} (n: 140 and N: 10). Dotted line is the regression line for w^{RNAi}, $actn^{RNAi}$, $aurB^{RNAi}$ and svn^{RNAi} data points. Statistical tests: Ancova tests for difference in regression slopes (A-C). ns: not significant. Statistically significant differences (p-value<0.05) are indicated by one asterisk. ..142

B.6 **Quantitative characterization of aSF nucleation at TCJs.** *More than 95 percent of aSFs nucleate at a TCJ (n=624, Fig. 3.4I). For a given cell's shape, we would like to predict which TCJs are sites of aSF nucleation for that cell. When an aSF nucleates at a TCJ, we calculate both the TCJ's opening angle and the orientation of its bisector in that cell relative to the a-p axis (A); these are the angles for the pair of adjacent edges that meet at the TCJ (A). We compare the geometric properties of nucleating TCJs to the geometric properties of the set of all TCJs (B-C). The TCJ bisector orientation is strongly predictive of aSF nucleation; nucleating TCJs are TCJs with a bisector pointing mostly along the a-p axis (D-F). We check that the nucleation rate per cell is proportional to the number of nucleating TCJs (G). After verifying that the number of nucleating TCJs increases with cell apical area (H), we explore whether large cells have more aSFs because they have more nucleating TCJs. Using an aSF-nucleating TCJ criterion derived from the data, we find that a "nucleation-only" model (in which the nucleation rate per cell is proportional to the number of nucleating TCJs) generates a weak scaling of aSF number with cell apical area (I).* Unless otherwise stated, protein distributions and quantifications are reported for

the region boxed in Fig. 3.1A at 26 hAPF. **A)** Illustration of TCJ opening angle α and TCJ bisector orientation θ with respect to the a-p axis. **B)** Grey-coded plot of fraction of TCJs with opening angle (α) and bisector orientation (θ). n: pairs of adjacent edges (3 pairs of adjacent edges per individual TCJ). **C)** Grey-coded plot of fraction of aSF nucleation events as a function of opening (α) and bisector (θ) TCJ angles. n: number of nucleation events. **D)** Grey-coded plot of nucleation rate as a function of opening (α) and bisector (θ) TCJ angles. This relative nucleation rate is the ratio of the data in (C) to the data in (B). The white region with dashed lines corresponds to TCJs which are rarely observed (less than 0.01% in (B)). n: number of nucleation events. **E)** Empirical cumulative distribution of the aSF nucleation data as a function of bisector orientation θ (red curve). The aSF-nucleating TCJ cutoff (dashed magenta line) is based on the ninety-fifth percentile of aSF nucleation events. n: number of nucleation events. **F)** Graph of the nucleation rate as a function of TCJ bisector orientation θ. Within each bin of θ, we compute the ratio of the number of nucleation events to the fraction of the total number of adjacent edge pairs in that bin and normalize all bins by the largest ratio. The vertical (dashed magenta) line denotes the aSF nucleation cutoff in (D). n: number of nucleation events. **G)** Graph of aSF nucleation rate (h^{-1}) as a function of the average number of nucleating TCJs over 2h (25-27 hAPF). n: number of cells. **H)** Graph of number of TCJs per cell (grey, mean ± SEM) and number of aSF-nucleating TCJ per cell (red, mean ± SEM) as a function of cell apical area. n: number of cells. **I)** Graph of experimental (grey, mean ± SEM) and predicted (red, mean ± SEM) aSF number per cell as a function of cell apical area. The red line is the result of the "nucleation-only" model. n: number of cells. r: Pearson correlation coefficient. ns: not significant. Statistically significant differences (p-value<0.05) are indicated by using one asterisk. 142

B.7 **Quantitative characterization of aSF breakage at TCJs.** *To determine where aSFs break, we track aSF positions from midlife to breakage in E-Cad:3xmKate2 and MyoII:3xGFP time-lapse images. Since no aSF is perfectly aligned with the uniaxial stress, for each aSF we can define a leading tip and a lagging tip. The leading tip is the aSF tip that has moved farther from the nucleating TCJ along the a-p axis, and the lagging tip is the other aSF endpoint (A-B). To quantify the aSF position, we measure the distance along the a-p axis between the nucleating TCJ and the leading aSF tip (B). We, first, show that aSFs break near the cell centroid and that aSFs are closer to the cell centroid at breakage than at midlife (C-D). Furthermore, aSFs are more likely to break near TCJs than would be expected solely from a bias towards breaking near the cell centroid (E-I). We assign an aSF breakage event to a specific TCJ, if the distance between the leading aSF tip and the TCJ is less than the cortex thickness, estimated in (L). We determine the geometric characteristics of these aSF-breaking TCJs (M-N). After defining an aSF-breaking TCJ criterion (N), we develop a phenomenological model in which aSFs move at a constant speed (O) from aSF-nucleating TCJs to aSF-breaking TCJs. As validated by experimental data (P), our model assumes that aSF lifetime is proportional to how far each aSF moves from nucleation to breakage (Q).* Unless otherwise stated, protein distributions and quantifications are reported for the region boxed in Fig. 3.1A at 26 hAPF. **A)** Distribution of E-Cad:3xmKate2 and MyoII:3xGFP immediately before aSF breakage. In this example, both aSF tips are attached to TCJs at the time of aSF breakage. **B)** Schematic for calculation of aSF penetration distance (orange dashed line) and cell centroid position (red dashed line) along the a-p axis relative to the nucleating TCJ (red arrow). The aSF is green. aSF tips are indicated by yellow arrows. The cell centroid is indicated by a blue dot. **C)** Graph of aSF penetration distance as a function of the separation between the aSF's nucleating TCJ and the cell centroid position at aSF midlife. The dashed line is the line of best fit,

which indicates that the extent of aSF penetration at midlife depends on the distance between the nucleating TCJ and the cell centroid (p-value<10^{-5}). n: number of aSFs. **D)** Graph of aSF penetration distance as a function of the separation between the aSF's nucleating TCJ and the cell centroid position at aSF breakage. The dashed line is the line of best fit, indicating that the extent of aSF penetration at the time of breakage depends on the distance between the nucleating TCJ and the cell centroid (p-value<10^{-5}). aSFs penetrate farther by the time of breakage than at midlife (see Appendix B.2). n: number of aSFs. **E-F)** Two examples of aSFs at the time of breakage in two distinct cells. In both cases, the aSF breaks near the cell centroid and is aligned with two TCJs. The red dashed line is the a-p distance between the aSF-nucleating TCJ (red arrows) and the cell centroid (blue circles), which is plotted in (D, x-coordinate). The orange dashed line is the distance between the position of the aSF nucleation and the leading aSF tip, which is plotted in (D, y-coordinate). Although the cell in (E) and (F) are distinct, the distances between the nucleating TCJ and the cell centroid are the same for both examples. **G)** To illustrate our procedure for defining a distance $\delta aSF - TCJ\ swapped$ for each breakage event (see Appendix B), we swap the aSF from the cell in (E) into the cell in (F). $\delta aSF - TCJ\ swapped$ (yellow line) is the distance along the a-p axis from the breaking TCJ to the leading tip of the swapped aSF. **H)** Histogram of distance between the leading tip of each aSF and its nearest TCJ at the time of aSF midlife. n: number of aSFs. **I)** Histogram of distance between the leading tip of each swapped aSF and its nearest TCJ in the cell into which it has been swapped at aSF midlife. n: number of aSFs. **J)** Histogram of distance between the leading tip of each aSF and its nearest TCJ at the time of aSF breakage. n: number of aSFs. **K)** Histogram of distance between the leading tip of each swapped aSF and its nearest TCJ in the cell into which it has been swapped at the time of aSF breakage. n: number of aSFs. **L)** Graph of E-Cad:3xmKate2 and MyoII:3xGFP intensities (mean ± SEM) as a function of

the distance to a nucleating TCJ. E-Cad:3xmKate2 and MyoII:3xGFP intensity profiles were measured along a line of 5 pixels wide (0.13 µm per pixel), which passes through the nucleating TCJ (2 min before aSF nucleation) orthogonal to the nascent aSF. Positive distances correspond to pixels within the cell in which an aSF will nucleate; negative distances correspond to pixels on the other side of the TCJ. We selected pixels that are between -0.5 µm and 2.0 µm from the nucleating TCJ. We normalized both E-Cad:3xmKate2 and MyoII:3xGFP intensity profiles. Maximum intensity peaks were found for E-Cad:3xmKate2 (magenta arrow) and MyoII:3xGFP on the average intensity profiles. Junctional cortex thickness was estimated via a cross-correlation between average intensity profiles of E-Cad:3xmKate2 and MyoII:3xGFP (junctional cortex thickness estimation 0.52 µm). Alternately, individual MyoII:3xGFP and E-Cad:3xmKate2 intensity profiles of TCJs were used to estimated junctional cortex thickness by measuring, for each sample, the distance between MyoII:3xGFP maximum peak and E-Cad:3xmKate2 maximum peak and by also estimating junctional cortex thickness, using 66% (dotted blue line) of the maximum peak of MyoII:3xGFP as a limit to define cortex. Both measurements result in similar junctional cortex thickness values: 0.52 µm versus 0.51 ± 0.12 µm. n: number of TCJs. **M)** Grey-coded plot of the fraction of aSF breakage events as a function of the opening (α) and bisector angle (θ) of the breaking TCJ. n: number of aSFs. **N)** Empirical cumulative distribution of aSF breakage events as a function of TCJ bisector angle θ (blue curve). Dashed magenta line: θ cutoff for aSF-breaking TCJ. n: number of aSFs. **O)** Graph of average aSF velocity per cell ($\mu m.min^{-1}$) as a function of cell apical area. n: number of cells. **P)** Graph of average aSF lifetime (min) as a function of average aSF total distance travelled (µm) from the nucleating TCJ. n: number of cells. **Q)** Schematic for model of aSF lifetimes as a function of cell geometry. First, the aSF (green) nucleates a short distance (burgundy; shown in inset) from its nucleating TCJ (red arrow). The aSF

moves away from its nucleating TCJ until its tips (green arrows) reach breaking TCJs (blue arrows). The aSF breaks when its tips (green arrows) are within a short distance (orange; shown in inset) from breaking TCJs. (Note that $x0 < 0$ would correspond to aSF breakage *after* passing breaking TCJs.) The predicted aSF lifetime is proportional to the distance (along the a-p axis) that the aSF moves, on average, from its nucleation site to its breakage site(bracketed red dotted line). Statistical tests: *F*-test (C-D). 144

B.8 **Analyses of *trbl^{UP}* cell clones.** Unless otherwise stated, protein distributions and quantifications are reported for the region boxed in Fig. 3.1A at 26 hAPF. **A)** Graph of cell apical area (mean ± SEM) for *trbl^{UP}* border and bulk cells. n: number of cells; *p*-value<10^{-3}. **B)** Graph of the experimental number of aSFs (mean ± SEM) as a function of cell apical area in *trbl^{UP}* border and bulk cells. n: number of cells. **C)** Graph of the experimental number of aSFs (mean ± SEM) and cell apical area (mean ± SEM) in *trbl^{UP}* border and bulk cells. n: number of cells; *p*-value<10^{-2}. For each group, the dashed line represents the scaling of aSF number with cell area given by the analysis of covariance. The scaling of aSF number with cell area is 0.031 $aSF\mu m2$. **D)** Graph of number of TCJs per cell (mean ± SEM) for *trbl^{UP}* border and bulk cells. n: number of cells; *p*-value<10^{-5}. **E)** Graph of the number of TCJs per cell (mean ± SEM) as function of cell apical area in *trbl^{UP}* border and bulk cells. n: number of cells. **F)** Graph of the predicted number of aSFs (mean ± SEM.) as a function of cell area in *trbl^{UP}* border and bulk cells. n: number of cells. **G)** Graph of the predicted number of aSFs (mean ± SEM) and cell apical area (mean ± SEM) in *trbl^{UP}* border and bulk cells. n: number of cells; *p*-value<10^{-2}. For each cell group, the dashed line represents the scaling of aSF number with cell area given by the analysis of covariance. The scaling of aSF number with cell area is 0.030 $aSF\mu m2$. Statistical tests: Kruskal-Wallis tests (A,D) and Ancova

List of Appendices

Appendix

Abstract

Somehow, a fertilized egg develops into a multicellular organism with several organs that perform distinct functions. Much research regarding the development of multi-cellular organisms is chemical in nature: from networks of interacting intracellular bio-molecules to intercellular gradients of secreted chemicals. The role of mechanical forces, between neighboring cells or between cells and their environment, in development is often neglected. Here, based on models of mechanical forces during development, we study three processes: cone mosaic formation in zebrafish, apical stress fiber generation in *Drosophila*, and neural induction in stem cell colonies.

One of the most ordered vertebrate tissues, the zebrafish cone mosaic is a crystalline array of cells on the retina's hemispheric surface. The cone mosaic grows from the retina's rim; because of geometric constraints, defects form to maintain approximately constant cell spacing. These defects line up from the center to the periphery of the retina as it grows. A model based on chemical signaling in a fixed cell packing generates many excess defects; in contrast, a model based on repulsive interactions between cone cells reproduces the spatial distribution of defects observed in the retina. Unlike influential studies of the *Drosophila* R8 photoreceptor array, our findings suggest that cell motion governed by repulsive cell-cell interactions can play a key role in generating regular patterns in living systems.

Rather than repulsive intercellular interactions, in *Drosophila* we study how an entire tissue responds to morphogenetic forces from groups of neighboring cells. Apical stress fibers (aSFs) form to resist cell elongation. Importantly, the number of aSFs per cell scales with cell area to prevent elongation of large cells. To understand this scaling between mechanical response and cell area, we develop a model to predict the number of aSFs within any given cell based on its shape. Since aSFs nucleate and break at tricellular junctions (TCJs), the number of aSFs in each cell depends on the cell's number of TCJs and the spacing between those TCJs. Our findings highlight how, based on area, cells scale their mechanical responses to resist deformations.

Finally, we study how mechanical stresses can bias cell fate. Our experimental system is a stem-cell-based model of neural induction, the process by which certain cells in the outer

embryonic layer become neural. Two domains, the neural plate and the neural plate border (NPB), form. Motivated by experimental observations, we construct a mathematical model that couples cell fate and cell mechanical stress. In our model, cells at the colony boundary generate a fate pattern by transmitting forces to interior cells. Our mathematical model predicts that the NPB's width depends non-monotonically on the stiffness of the cells' substrate. With experimental validation of this prediction, we argue that cells can communicate with each other via mechanical forces, biasing each other's fates.

Mechanical forces guide the shaping and patterning of tissues, from juvenile zebrafish to *Drosophila* embryos to human stem cells. Repulsion between cells of fixed fate can generate a crystalline array of cells. By helping cells resist deformations due to external stresses, apical stress fibers can tune a tissue's final shape. Mechanical stresses, transmitted between cells, can produce fate patterns with a length scale that depends on the extracellular matrix's stiffness. Starting as early as gastrulation, when three embryonic layers form, mechanical forces between cells shape the embryo and its constituent tissues into proper form.

Chapter 1 Introduction

Development is the process by which a fertilized egg becomes a multicellular organism. From one cell form many organs, including eyes, skin, and a heart. Cells in these distinct organs, other than eggs and sperm, have the same genome; what makes cells in different organs distinct from one another is that they express different genes. Scientists over the past century have probed questions of how cell fate is specified and of how cells are positioned (in properly shaped organs) after differentiation. Several problems, often pertaining to the role of mechanical forces in development, remain poorly known. For example, how do cells control their own shapes in response to morphogenetic forces from neighboring tissues? When necessary for proper development, how do cells segregate themselves based on fate? How do cells spatially coordinate their force generation to fold tissues?

Many studies of development focus on how cells' external chemical environment can influence cellular behavior. Suppose, for example, that two or more domains of different cell fates need to form along an axis of an embryo. The mother could deposit a chemical on one side of the embryo [3, 4]. Then, each cell's local chemical concentration depends on its position in the embryo relative to the maternal source. Cells, then, change their own gene expression based on the concentration they sense [3].

The paradigmatic model for chemical-concentration-based fate specification is called the French Flag model: in the late 1960s, theoretical biologist Lewis Wolpert hypothesized that cells could estimate local chemical concentration and choose a fate by comparing their estimate to fixed thresholds [5, 6]. For example, if a cell's estimate of chemical concentration is greater than threshold 1, this cell becomes a cell of the blue fate. If a cell's estimate of chemical concentration is between threshold 1 and threshold 2, it becomes a cell of the white fate, and if a cell's chemical concentration is less than threshold 2, it becomes a cell of the red fate. Given some chemical concentration gradient along one embryonic axis, a French flag ("bleu, blanc, et rouge") could form in the embryo.

The French Flag model obviously oversimplifies embryonic development [7, 8], but subsequent experimental studies motivated by this model have provided deep insights into mechanisms for spatial patterning of cell fate [9, 10]. Relative to fate patterning by chemical gradients, the effects of mechanical forces on development, by tuning cells' gene expression and by physically moving cells, remain underexplored [11-13]. In the last ten to twenty years, scientists have begun to uncover the role of mechanical forces in development. This has created opportunities for physically minded scientists to model self-organization in biological systems, from individual cells *in vitro* to invertebrate embryos like *Drosophila* and vertebrate embryos like zebrafish. Here we grapple with various ways in which mechanical forces affect development: biasing fate choices (Chapter 4), positioning fate-specified cells (Chapter 2), and generating shape transformations (Chapters 3,4).

Regarding the biasing of cell fate choices, in Chapter 4 of this thesis, we construct and test a mathematical model of how mechanical stresses affect cell fate choices in a process called neural induction. Importantly, the extracellular matrix (to which cells bind) tunes intercellular force transmission and thereby affects fate patterning. Other researchers have experimentally probed how forces affect differentiation; here we briefly introduce what is known, from single cells to entire embryonic tissues, about the effects of mechanical forces on fate choices.

Once cells are fate-specified, mechanical interactions between cells can aid in the generation and refinement of spatial patterns. In this thesis, we explore the role of cell-cell mechanical interactions in fate-dependent positioning of cells in zebrafish retinae (Chapter 2). For appropriate context, we review a few other examples in which mechanical interactions between fate-specified cells space them out into a crystal or a more disordered mosaic. We also briefly discuss how fate-dependent cell-cell mechanical interactions can segregate cells into different layers or sharpen boundaries between different tissue domains.

Beyond generating tissue domains or cell lattices, intercellular mechanical forces can tune the morphology of an entire tissue. For example, in Chapter 3, we explore how cells in a tissue respond to extensile stresses generated by neighboring groups of cells; to resist elongation, cells generate stress fibers. We find that in the absence of stress fibers, the entire tissue becomes abnormally elongated along the uniaxial stress. In Chapter 4, we discuss how the coupling between cell fate and contractility has potential implications for the folding of an embryonic tube called the

neural tube. In anticipation of Chapter 3 and Chapter 4, we discuss below some illustrative examples of how spatiotemporally coordinated cell contraction generates shape changes.

Extracellular matrix stiffness affects differentiation of individual cells.

To quantify mechanical effects on cell fate specification, it is often useful to study individual stem cells in well-controlled chemical media. In this experimental setup, one can keep constant the chemical properties of the media and precisely change the mechanical properties of the cell's substrate. In such a setup, Discher et al. demonstrated that the elastic modulus of a stem cell's substrate can bias the cell to become a neuron, muscle cell, or bone [14]. Intriguingly, stiffer extracellular environments also produce stiffer and tenser cells, suggesting that the effect of environmental stiffness on individual cells could be amplified by stiffening of neighboring cells in a tissue context [14].

A later study by Chen et al. revealed that the effect of substrate mechanics on cell differentiation might be mediated by changes in cytoskeletal tension [15, 16]. Increased (decreased) cell contractility 1-3 days after initiation of differentiation is predictive of bone (fat) cell fate by the 7^{th} day, respectively. Furthermore, at fixed substrate stiffness, other studies have revealed that constraining individual cells to larger areas increases cell-substrate active forces, biasing cells' fates [17]. These studies make clear that extracellular matrix mechanics influences the differentiation of individual cells via effects on cell stiffness, contractility, and spread area. The degree of experimental control afforded by these *in vitro* systems is immense, but *in vivo* experimental studies are, in general, necessary to establish definitively the role of mechanical forces in fate specification and patterning.

Mechanical extension and compression generate fate patterns.

Elegant studies in embryos have extended knowledge of mechanical effects on cell fate in *Drosophila* and in zebrafish. Here it is more difficult to control precisely the stiffness of the cellular environment; instead, many studies involve mechanical compression or extension of cells. For example, Carl-Philipp Heisenberg et al. recently demonstrated in zebrafish oogenesis that growth of a cell, called the micropyle precursor, generates compression of neighboring cells, and that compression prohibits neighboring cells from differentiating into a micropyle precursor [18]. Interestingly, the micropyle precursor feeds back onto its differentiation by expressing more proteins for binding to its extracellular matrix. In *Drosophila*, Desprat et al. demonstrated that

morphogenetic forces from germ band extension cause compression of neighboring tissue and that compression affects differentiation of those cells [19]. In both cases, compression affects nuclear translocation of specific proteins, including β-catenin and TAZ, facilitating cell differentiation.

Unsurprisingly, like compression, mechanical extension affects gene expression and fate specification. In zebrafish, Brunet et al. demonstrated that as the enveloping layer of cells spreads to cover the yolk, mechanical strains due to cell spreading cause nuclear translocation of β-catenin, affecting differentiation of cells to mesodermal fate [20]. In *Drosophila*, they demonstrated that invagination similarly generates mechanical strains in cells and that those mechanical strains cause nuclear translocation of β-catenin, helping to maintain mesodermal fate [20]. Mechanical forces affect cell fate specification in early embryonic development in animals as distinct as fruit flies and fish.

Cell-cell repulsion via cellular appendages spaces out fate-specified cells.

Mechanical forces not only affect cell differentiation, but also play a key role in properly positioning cells after differentiation. Because cells of different types often have different proteins in their membranes, intercellular forces can depend on the fates of the interacting cells. A striking example is horizontal cells in mouse retinae [21]. During embryonic development and soon after birth, these horizontal cells move across several layers of the retina to attain their final positions. Once horizontal cells reach the outer layer of the retina, they interact with other horizontal cells via cellular appendages, called neurites. By homotypic repulsion, these cells set up a tiling of the outer retina. Wong et al. provided evidence of homotypic repulsion by ablating a few horizontal cells and observing other horizontal cells actively invade the ablated region with their own neurites [21]. A similar phenomenon occurs in *Drosophila*; certain classes of neurons form non-overlapping domains that tile the body wall. Here, by ablating neurons of certain classes, Grueber et al. observed that dendrites of neighboring neurons actively grow into the domain previously occupied by the ablated neuron [22].

Patterning of the mammalian inner ear also occurs via a cell-cell repulsion mechanism. By tracking cells in cochlear explants, Cohen et al. reported both shear motion of and local repulsion between outer hair cells. Motivated by these observations, they built a computational model of shear motion plus local repulsion plus type-dependent tensions on cell-cell junctions. This model is sufficient to reproduce patterning of hair cells observed in the inner ear [23]. These three examples, from fruit flies to mice, demonstrate that cell-cell contacts often mediate repulsive

interactions between cells of fixed fate. These repulsive interactions can generate crystalline arrays of cells or mosaics of cells with short-ranged order.

Fate-dependent adhesions make compartments and layers.

Mechanical forces between cells after differentiation can create more than regular cell mosaics. Intercellular forces can also segregate cells of different fates. Suppose, for example, that a tissue contains two compartments, spatial domains containing distinct populations of cells. Which mechanisms prevent mixing of two compartments and maintain a sharp boundary between the two? For the dorsoventral (D/V) compartmental boundary in *Drosophila*, Aliee et al. demonstrated that increased tension on cell-cell contacts at the D/V boundary aids in straightening the boundary between the two compartments [24].

Similarly, after dissociation the remarkable *Hydra,* composed of endodermal and ectodermal cells, sorts itself back into its original form with sharp boundaries between the two groups of cells [25, 26]. This regeneration is based on differential adhesion between the two cell types. A different mechanism of adhesion-based cell sorting acts in human prostate and mammary glands [27]. In these two cases, the cell type that lines the outside of the gland binds strongly to extracellular matrix (ECM) relative to the other cell type; this differential adhesion with the ECM, rather than between cells, drives separation of the cell types. Across several model systems, adhesive forces, between cells or between cells and the environment, depend on fate; this cell-fate dependence can aid in separating cells of different fates into discrete compartments or layers.

Spatiotemporal patterns of contractility generate complex shape changes.

The above discussion demonstrated that mechanical forces generate fate patterns of cells, either by biasing cell fate acquisition or by moving cells after fate acquisition. The resultant patterns have been rather simple, from crystalline arrays of cells to large domains of distinct cell fates. The shapes have been restricted either to spheres or to ellipsoids surrounded by an epithelial layer. Shapes that are significantly more complex can be generated via spatially and temporally patterned contractility during development.

A key example of complex embryonic shaping based on patterned contractility, which connects to earlier discussion of mechanical signals in Drosophila mesoderm differentiation, is ventral furrow formation. In this case, contractile force from a network of actomyosin structures, spanning ventral cells along the anterior-posterior axis, causes an invagination [28]. Not only is

contractility spatially structured in this case, but also stiffness is. These actomyosin structures, when aligned along the anterior-posterior axis, stiffen, and this ensures folding of the embryo along the proper axis [28]. Mechanical forces, in this case, generate an invagination on an ellipsoidal surface, leading to the formation of a multi-layered structure.

Mechanical forces can also allow for closure of folds and invaginations [29]. For example, a fold, centered on a group of neural cells, develops in the outer layer of vertebrate embryos early in development. This fold later closes to form a neural tube. In a basal chordate model system, Munro et al. elegantly showed that at the boundary between neural cells and epidermal cells, enrichment of actomyosin occurs progressively from posterior to anterior. The temporally sequenced actomyosin contractility "zippers" epidermal cells together and encloses the neural cells [29]. Spatiotemporal regulation of active contractility in cells sculpts the form of embryos by creating invaginations and enclosing them as necessary.

From cone crystallization to stress fiber generation to neural induction

This thesis contributes to the knowledge of the role of mechanics in morphogenesis: the role of type-dependent cell-cell repulsion in forming cell mosaics (Chapter 2, zebrafish cone crystallization), the role of mechanical forces coordinated across many cells in regulating tissue form (Chapter 3, *Drosophila* stress fiber generation), the role of mechanical stress in biasing fate (Chapter 4, stress-biased neural induction). These findings depend crucially on contributions of my experimental collaborators. The corresponding mathematical models are intentionally simple; they only contain details that are necessary to reproduce experimentally observed phenomena and to make biologically meaningful predictions. Since many key molecular players in these processes remain unknown, with incomplete knowledge, we rely on these simple models for quantitative characterization of these biological systems.

In his seminal paper "The Chemical Basis of Morphogenesis," Alan Turing said, "This model [of a growing embryo] will be a simplification and an idealization, and consequently a falsification" [30]. In a similar spirit, our models are meant to account for the main features of the developmental processes but fail to capture their remarkable complexity. In his paper, he gave attention to cases "where the mechanical aspect can be ignored and the chemical aspect is the most significant" [30]. This thesis does the opposite.

Chapter 2 Defect Patterns on the Curved Surface of Fish Retinae Suggest Mechanism of Cone Mosaic Formation

Acknowledgements: This manuscript results from a collaboration with Pamela Raymond's lab. Kamirah Martin and Mikiko Nagashima performed the majority of the experimental work, including flat-mounting of retinae, tracing of UV cone columns, and photoconversion of UV cones. Alcides Lorenzo Gonzalez generated the zebrafish line with photoconvertible nEOS. Sachihiro Suzuki in Rachel Wong's lab generated the *trβ2* mutant line. Declan Norton developed the simulations of lateral inhibition on a motionless cell packing. I developed codes and algorithms for analyzing defect distributions in flat-mounted retina and for tracking UV cone motion in live fish. I also developed the simulations of the phase-field crystal model and wrote the manuscript.

Abstract

The outer epithelial layer of zebrafish retinae contains a crystalline array of cone photoreceptors, called the cone mosaic. As this mosaic grows by mitotic addition of new photoreceptors at the rim of the hemispheric retina, topological defects, called "Y-Junctions", form to maintain approximately constant cell spacing. The generation of topological defects due to growth on a curved surface is a distinct feature of the cone mosaic not seen in other well-studied biological patterns like the R8 photoreceptor array in the *Drosophila* compound eye. Since defects can provide insight into cell-cell interactions responsible for pattern formation, we characterize the arrangement of cones in individual Y-Junction cores as well as the spatial distribution of Y-junctions across entire retinae. We find that for individual Y-junctions, the distribution of cones near the core corresponds closely to structures observed in physical crystals. In addition, Y-Junctions are organized into lines, called grain boundaries, from the retinal center to the periphery. In physical crystals, regardless of the initial distribution of defects, grain boundaries can form via the mobility of individual particles. By imaging in live fish, we demonstrate that grain boundaries in the cone mosaic instead appear during initial mosaic formation, without requiring defect motion.

Motivated by this observation, we show that a computational model of repulsive cell-cell interactions generates a mosaic with grain boundaries. In contrast to paradigmatic models of fate specification in mostly motionless cell packings, this study emphasizes the role of cell motion, guided by cell-cell interactions during morphological differentiation, in forming biological crystals. Such a route to the formation of regular patterns may be especially valuable in situations, like growth on a curved surface, where long-ranged, elastic, effective interactions between defects can help to group them into grain boundaries.

Author summary

From hair cells in the mammalian inner ear to the bristles on a fly's back, sensory cells often form precise arrays, ensuring that these cells are evenly spread out on the tissue's surface. Here we consider the zebrafish cone mosaic, a crystal of cone photoreceptors in the outer retinal layer. Because the cone mosaic grows from the rim of the curved retinal surface, new rows of cones (*i.e.*, defects) are inserted to maintain constant spacing between sensory cells. We study the spatial distribution of these defects to gain insight into how the cone pattern forms. By imaging retinae in live fish, we find that as differentiating cones are incorporated into the mosaic, defects form lines (grain boundaries) that separate mostly defect-free domains. Then, we show that a computational model based on repulsion between mobile cells during their incorporation into the mosaic generates similar grain boundaries. This study thus suggests that cell motion governed by repulsive cell-cell interactions can play an important role in establishing regular patterns in living systems.

Introduction

In epithelial sheets that sense an external stimulus, the sensory function often depends on the spatial ordering of the constituent cells. In several examples [23, 31-38], the pattern is sufficiently precise that if one knows the fate of just one cell, one can determine the identities of all the others. It remains a major challenge to understand how these extraordinarily regular cell arrays are created during development. Here we focus on one such system, the photoreceptor cell layer in the zebrafish retina, in which cone photoreceptors are organized by spectral subtype into a crystalline, two-dimensional lattice called the cone mosaic [39-41]; in particular, we use defects in this lattice as a window into possible mechanisms of mosaic formation. Although the precise evolutionary advantage and functional significance of the cone mosaic remains unknown, establishing an organized lattice in which each cone maintains some characteristic spacing from neighboring

cones of the same subtype is thought to optimize sensitivity to a broad range of wavelengths over the full spatial extent of the retina [42, 43].

Four spectral subtypes form the zebrafish cone mosaic: Red, Green, Blue, and Ultraviolet (UV) [44, 45]. The 'unit cell', or the smallest repeating unit necessary to build the entire lattice, is composed of one Blue cone, one UV cone, two Green cones, and two Red cones (Fig. 2.1A-B). Blue and UV cones form interpenetrating anisotropic triangular sublattices (Fig. 2.1D). Green and Red cones form interpenetrating anisotropic honeycomb sublattices (Fig. 2.1E). Along 'rows', Blue cones alternate with UV cones, and Red cones alternate with Green cones (Fig. 2.1A-B). Along 'columns', each Blue cone is flanked by two Red cones, and each UV cone is flanked by two Green cones (Fig. 2.1A-B). Rows radiate from the center of the retina to the periphery. Columns are approximately parallel to the rim of the retina (Fig. 2.1A-C).

The retinal hemisphere grows outward from the rim by mitotic addition of new photoreceptors (and other retinal cells) (Fig. 2.1C) [46-49]. Until approximately two to three weeks post-fertilization, the newly incorporated cones are not arranged in an ordered mosaic [50, 51]. Then, a disorder-to-order transition, in which newly incorporated cones begin to form regular lattice, occurs. The region of cones generated earlier than this transition, called the 'larval remnant', remains disordered [50, 51]. We call the rows that originate from the boundary of the larval remnant the 'original rows' (Fig. 2.1C).

As new cells are incorporated at the rim, the circumference of the retinal hemisphere enlarges, and the spacing between the original rows necessarily increases (Fig. 2.1C). To maintain approximately constant spacing between rows, new rows, that do not originate at the larval remnant, are inserted (Fig. 2.1C). The topological defects that generate new rows are called Y-Junctions [50, 52]. For a crystal on a spherical (closed) surface, defects are inevitable, as required by Euler's formula [53-56]. In contrast, defects in the hemispheric photoreceptor layer, a non-closed surface, result not from a fundamental topological constraint but from the biophysical requirement to maintain reasonable cell sizes and not to leave gaps between cells in the retinal epithelium.

The generation of topological defects to maintain approximately constant cell spacing during growth on a curved surface makes the cone mosaic distinct from other patterned tissues, such as sensory bristles [57] and R8 photoreceptors in *Drosophila* [31-33, 35-38]. Previous investigators have noted the existence of defects in the teleost cone mosaic [50, 52]. Because these topological

defects can provide insight into the biological mechanisms of pattern formation [58-60], in this paper we characterize the spatial distribution of each cone subtype in the Y-Junction core and compare Y-junction cores to defect cores in physical crystals. We show that a Y-Junction is a dislocation [61, 62], the insertion of a row and a column.

Additionally, we characterize the spatial distribution of Y-Junctions in the retinae. We demonstrate that the spatial distribution of Y-Junctions is as expected in a physical crystal near an energy minimum on a hemisphere [53, 63-68]. As in a physical crystal, the defects form lines, called grain boundaries, from the center of the retina to the periphery [53, 63-68]. In a physical crystal at finite temperature, defects are mobile; therefore, defects can coalesce into grain boundaries after formation of the crystal, regardless of the initial spatial distribution of defects [61, 62, 66, 68, 69]. We demonstrate that in the zebrafish retina, in contrast, grain boundaries appear during initial mosaic formation and do not require subsequent defect motion.

Having observed grain boundaries in fish retinae, we seek to take advantage of this finding to gain insight into the mechanisms of cone mosaic formation. We previously reported that cones of different subtypes are in approximately correct locations relative to each other within hours after they are generated by the terminal divisions of progenitor cells [70]. Though previous studies have documented interactions between cones in mature columns [51, 71], little is known about the mechanisms by which premature columns initially form; in particular, the genetic and signaling networks that lead to spectral fate specification remain almost completely unexplored. Evidence from embryonic retina suggests that the spectral subtype of each cone is determined at the time of a symmetric, terminal division of its precursor [72]. If this finding from embryonic retinae holds for juvenile and adult retinae, it implies that the two daughter cells of the same subtype must move away from each other after their birth in order to reach the correct positions in the cone mosaic. This would suggest that interactions between differentiating cones with an established subtype generate crystalline order as these cones are incorporated into the retina.

Inspired by this evidence from embryonic retinae as well as other examples of neural cell mosaics [21, 22, 73-75], we propose a computational model in which fate-committed cells repel each other in an anisotropic medium. This model generates grain boundaries during initial mosaic formation, consistent with our observations of fish retinae. We, then, contrast our model of motile, fate-committed cells with a second model in which cells are neither fate-committed nor motile. In this second model, inspired by the example of Notch-mediated lateral inhibition in neural fate

specification, static cells in a disordered packing signal to each other at short range to set up a fate pattern [31, 33, 35-38, 57]. Because the signaling range is approximately equal to the cell size, we find that in the absence of cell motion, this mechanism of cell-cell signaling generates many excess defects (consistent with a very recent, independent study [23]). We conclude that our model of motile, fate-committed cells is more consistent with observations of cone mosaic formation than a model of cell-cell signaling in a disordered packing.

The biological example of grain boundary formation during initial patterning in zebrafish retinae also poses interesting physical questions. A primary concern in the existing physics literature has been the existence of grain boundaries in the ground state of crystals on curved surfaces [53, 54, 56, 64, 76, 77]; although some aspects of the kinetics of crystal growth have also been considered [78, 79], the question of how the growth geometry affects the positioning of defects has received little attention [69, 80]. For example, in which growth geometries does crystallization produce defect distributions that are close to the ground state without defect motion? We show that for crystal growth in geometries comparable to the zebrafish retina, repulsive cell-cell (more generally, particle-particle) interactions produce just such low energy defect distributions during the initial growth process.

In the remainder of this paper, after characterizing the spatial distribution of each cone subtype in the Y-Junction core, we demonstrate the presence of grain boundaries in fish retinae. To quantify whether grain boundary formation occurs via defect motion, we track motion of individual defects in the retina in live fish. By comparing the timescales of defect motion and grain boundary growth, we conclude that grain boundaries form as cones are initially incorporated into the mosaic. We explain why cone mosaic formation is unlikely to occur via fate specification in a static, disordered cell packing, and we test a model of cell motion guided by cell-cell repulsion in an anisotropic medium. The latter model generates grain boundaries during initial mosaic formation, consistent with our observations of the retina.

Figure 2.1 **The cone mosaic is composed of four interpenetrating sublattices: two triangular sublattices and two honeycomb sublattices. A)** Schematic of cone photoreceptors (colored by subtype) in apical plane of zebrafish retina. The 'unit cell' (yellow parallelogram) contains one UV cone, one Blue cone, two Green cones, and two Red cones. White dashed line: 'row' axis. Black dashed line: 'column' axis. **B)** Cone mosaic from flat-mount retinal preparation of an adult, triple transgenic fish, Tg[*sws2:GFP*; *trβ2:tdTomato*; *gnat2:CFP*]. Blue cones express a fluorescent reporter (pseudo-colored blue) under control of *sws2* promoter, and Red cones express a fluorescent reporter (pseudo-colored red) under control of ***trβ2*** promoter. All cones express an additional reporter (pseudo-colored gray) under control of *gnat2* promoter. We distinguish between UV and Green cone subtypes based on morphology. **C)** Schematic of photoreceptor epithelium, lining the outer surface of the hemispheric retina. Central retina, which surrounds the hemispheric pole and forms during the larval period, is unpatterned. As the retina grows by mitotic addition of new photoreceptors (and other retinal cells) at the hemispheric rim (gray arrows), there is a disorder-to-order transition (black dashed line). After this transition, the cone mosaic grows by neurogenesis at the hemispheric rim throughout the fish's life. Because the hemispheric

circumference grows, rows of cells are inserted to maintain approximately constant cell spacing. **D)** UV and Blue cones in flat-mount retinal preparation from a double transgenic (Tg[*sws1:GFP*; *sws2:mCherry*]) line in which UV and Blue cones express distinct fluorescent reporters. UV cones (pseudo-colored magenta) form an anisotropic triangular sublattice that interpenetrates with an anisotropic triangular sublattice of Blue cones (pseudo-colored blue). We connect (white lines) a subset of nearest neighbors in the Blue cone sublattice. **E)** Blue (pseudo-colored blue) and Red (pseudo-colored red) cones in flat-mount retinal preparation from panel B. Red cones neighbor Blue cones in each column. The Red cones form an anisotropic honeycomb sublattice. We connect (white lines) a subset of nearest neighbors in the Red cone sublattice; note the different nearest neighbor patterns in the Blue cone triangular sublattice (panel D) and the Red cone honeycomb sublattice (panel E). The Green cones form a honeycomb sublattice (not shown here).

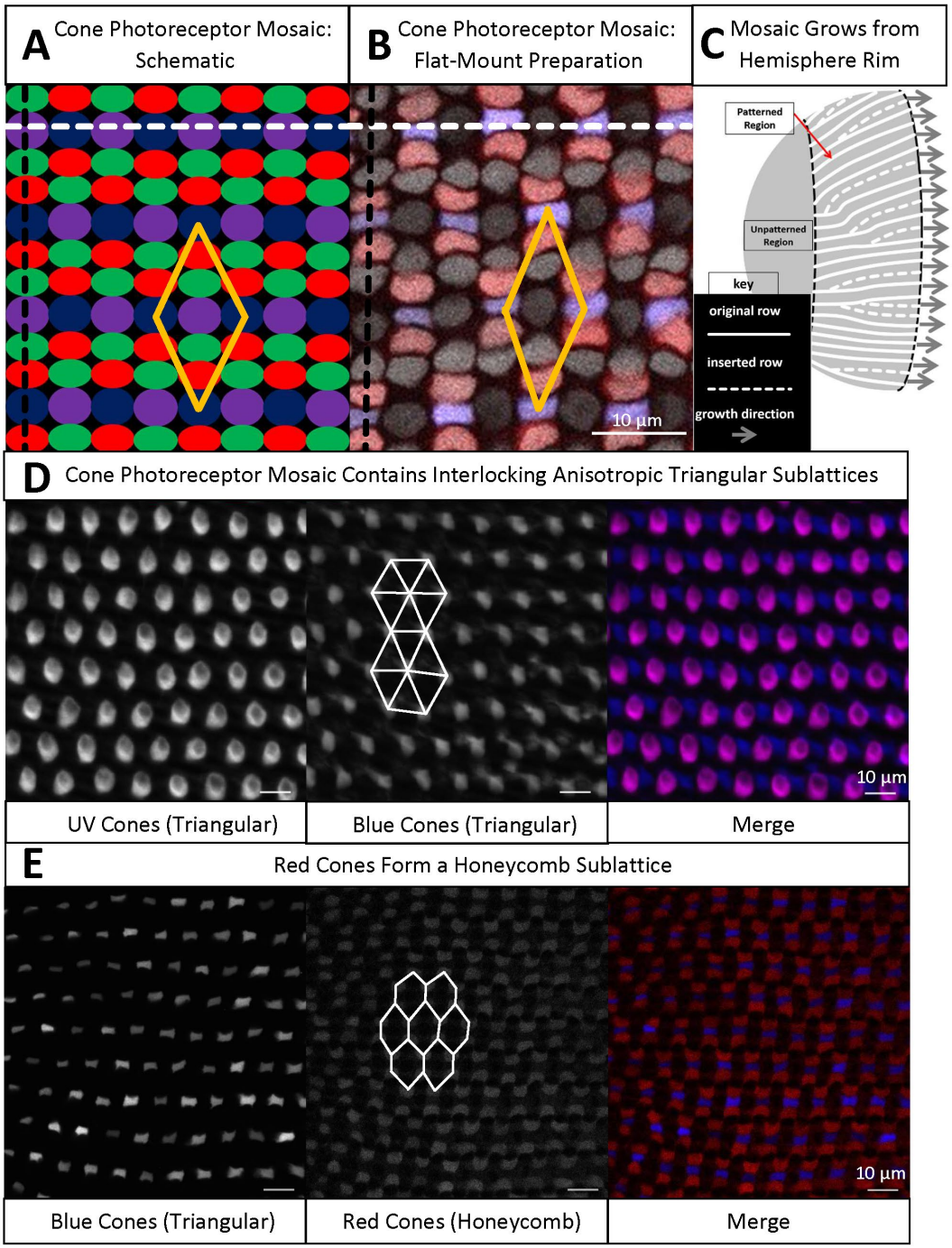

Figure 2.2 **A Y-Junction, a topological defect in the cone mosaic, is an insertion of a row and a column. A)** Schematic of simple row insertion in cone mosaic. As new cone photoreceptors are incorporated to right of the defect, a series of

improper cone contacts (black box) within columns form. If colors were reversed in one of the new columns, so that a Red cone contacts a Green cone, there would instead be improper Red-UV and Blue-Green contacts. White dashed lines: rows associated with defect. **B)** Schematic of a Y-Junction, a topological defect in the zebrafish cone mosaic. A Y-Junction only disrupts the cone mosaic near the core rather than along an entire line of contacts. White (black) dashed lines: rows (columns) associated with the defect. **C)** A Y-Junction in a flat-mount retinal preparation from an adult, double transgenic (Tg[*sws1:GFP*; *sws2:mCherry*]) line in which UV and Blue cones express distinct fluorescent reporters (pseudo-colored magenta and blue, respectively) under control of UV and Blue opsin promoters, respectively. Antibody staining labels Red and Green cones (both pseudo-colored green). **D)** Each UV cone from panel C is connected (white bonds) to its nearest UV cone neighbors. To the left and right of the defect, rows are counted. Seven-sided (five-sided) star: seven-coordinated (five-coordinated) UV cone. **E)** A circuit of triangulation bonds around defect from panels C-D. Red arrow is the Burgers vector, the additional bond necessary to close the circuit containing a dislocation. **F)** Y-Junction in the same flat-mount retinal preparation as in Fig. 2.1B. The round cells with dim fluorescence are UV cones. The Red cones are pseudo-colored red. The Blue cones are pseudo-colored blue. The remaining cones (bright gray fluorescence) are Green cones. We connect (solid white lines) nearest neighbors inthe Red cone sublattice and Blue cone sublattice.

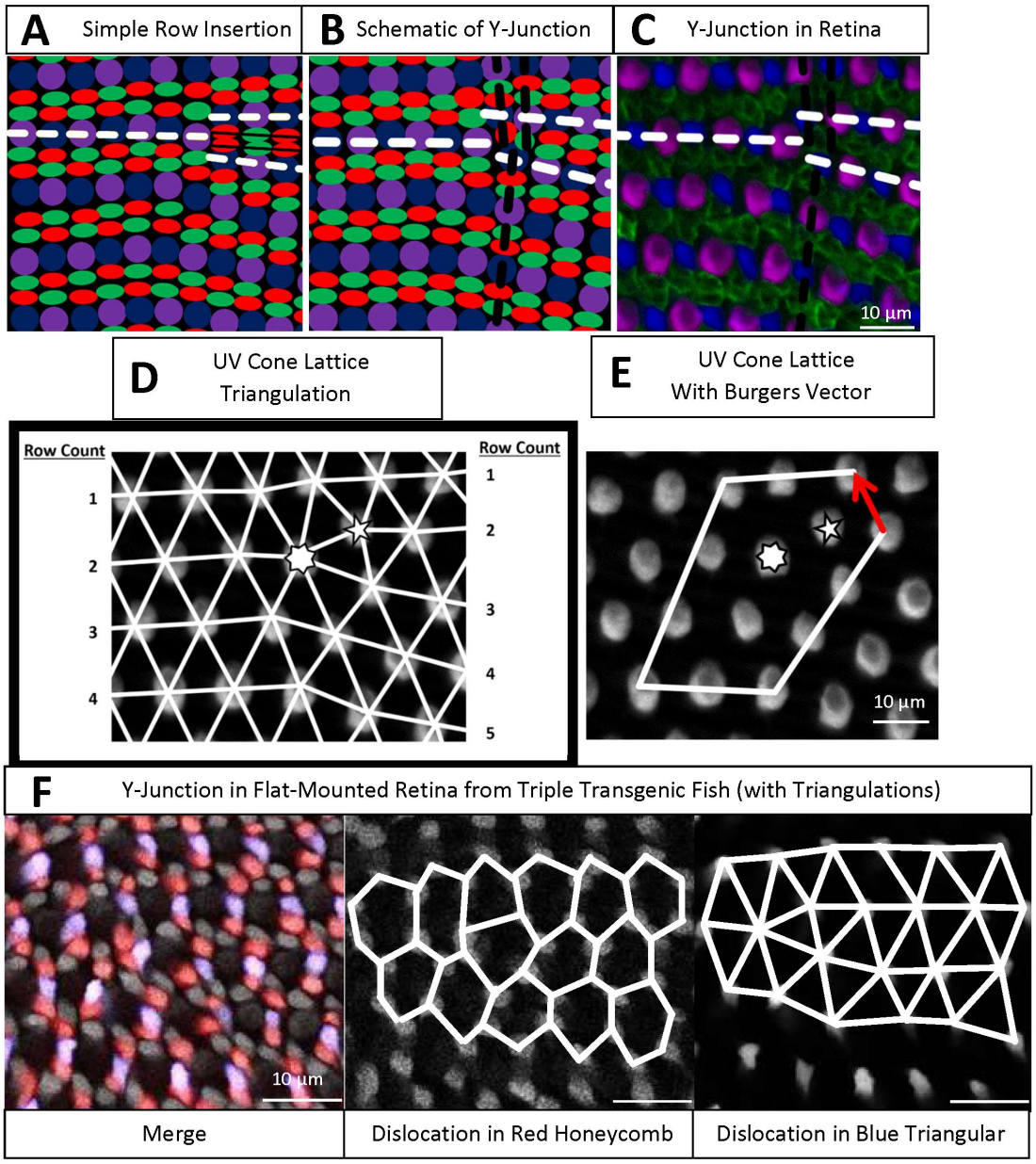

Results

A Y-Junction is the insertion of a row and a column

To maintain approximately constant cell spacing as the retina grows by mitotic addition of cone photoreceptors at the rim, rows must be inserted (Fig. 2.1C) [50, 52]. It is straightforward to demonstrate that a simple row insertion causes a disruption, that is not limited to a point defect but extends along an entire line, in the cone mosaic (Fig. 2.2A). To avoid this disruption along an entire line of the cone mosaic, it is necessary to consider more complex defects: the insertion of two rows (Fig. A.1) or the insertion of a row and a column, neither of which disrupts formation of the cone mosaic. In the zebrafish cone mosaic, the most common topological defect is the insertion of a row and a column, *i.e.*, a 'Y-Junction' (Fig. 2.2B-C). To understand why the insertion of a row and a column is expected to be the most prevalent defect, we employ a tool used in analyzing defects in physical crystals: the Burgers vector [61, 62].

A Y-Junction generates minimal lattice deformation, as quantified by Burgers vector

As discussed in the introduction, the unit cell of the cone mosaic is composed of one Blue cone, one UV cone, two Green cones, and two Red cones (Fig. 2.1A-B). One can generate an infinite cone mosaic on a flat plane given the unit cell and two lattice vectors, which define the Bravais lattice [81]. The Bravais lattice defines which defects one expects to observe in the cone mosaic lattice, though the distribution of particles in the defect core may vary [61, 62, 81]. For the sake of clarity, we analyze the defects in the cone mosaic from the perspective of a cone subtype that appears only once in the unit cell: UV cones.

To define the Burgers vector, we build a triangulation for the UV cones in which we connect nearest neighbors of the same cone subtype (Fig. 2.2D-E). Away from the core of the defect, every UV cone is surrounded by six nearest UV cone neighbors [61, 62, 81]. Near the defect core, as in physical crystals that are triangular, one UV cone is surrounded by seven nearest UV cone neighbors. Neighboring this seven-coordinated UV cone is a UV cone which has only five nearest UV cone neighbors. This pair of five- and seven-coordinated UV cones constitutes the core of the dislocation.

We, then, construct a circuit that surrounds the core of the defect. If there were no defect, the circuit would be a parallelogram (Fig. 2.2E). The bottom side of the circuit would contain as

many bonds as the top side of the circuit. The right side of the circuit would contain as many bonds as the left side of the circuit. If there is a dislocation inside of the circuit, to close the circuit, one must add a bond, called the Burgers vector [61, 62]. The magnitude of the Burgers vector quantifies the amount of lattice deformation associated with the dislocation [61, 62].

In physical crystals, where the elastic deformation associated with the dislocation is proportional to the magnitude of the Burgers vector squared, the defect that generates the least deformation is expected to be the most prevalent. Even though we have no reason *a priori* to treat this biological crystal as elastic, we expect this measure of deformation to be generally applicable. The mechanism that drives ordering in a non-physical crystal likely also resists large deformations due to defects in the lattice.

The Y-Junction in the cone mosaic lattice is the dislocation that introduces the smallest deformation. This can be seen by comparing the Burgers vector of a Y-Junction to the Burgers vector of a double row insertion. For a double row insertion, the length of the Burgers vector is equal to the spacing between UV cones along a column, which is approximately twelve and a quarter microns, as compared to the Burgers vector of a Y-Junction, with a length of approximately eight microns (for quantification of spacings between UV cones in same column and in same row, see Fig. A.2). For the sake of minimizing lattice deformations, we expect double row insertions to be less prevalent than Y-Junctions.

Distribution of Red and Green cones near the Y-Junction core

For Red and Green cones, that each appear twice in the unit cell, we connect nearest neighbors of the same subtype and analyze the spatial distribution in the Y-Junction core. Away from a Y-Junction core, the cells that form the lattice can be grouped into hexagons (Figs. 2.1E, 2.2F, A.3) [81-83], but this grouping breaks down near the defect core. The distribution of Red and Green cones in the Y-Junction core is variable but is often either a 'glide' dislocation or a 'shuffle' dislocation, which differ in the distributions of cones at the core.

A 'glide' dislocation has a heptagon and a pentagon in the core. For example, in Fig. A.3A-B, one heptagon of Red cones neighbors a pentagon of Red cones. A 'shuffle' dislocation has a single octagon in the core. For Red cones (Fig. A.3E), the octagon contains two UV cones, and for Green cones (Fig. A.3D, F), the octagon contains two Blue cones. Interestingly, both 'glide' and 'shuffle' dislocations are commonly observed in honeycomb crystals like graphene [82, 83].

Y-Junctions form lines, called grain boundaries, from center to periphery of retina

Having verified that individual Y-Junctions are the dislocations that generate minimal lattice deformation, we next study the spatial distribution of Y-Junctions on the retinal surface. On the retinal hemisphere, the row direction rotates by 2π about the pole of the hemisphere, similar to the convergence of longitudinal lines toward a pole on the globe (Fig. 2.1C). For physical crystals in this orientation, the ground state contains lines of dislocations, called grain boundaries, from the center (pole) of the hemisphere to the edge (equator) [53, 84]. In physical crystals, dislocations are mobile; therefore, in physical crystals, it is possible for defects to rearrange into grain boundaries after crystallization, regardless of the initial spatial distribution of defects [61, 62, 66, 68, 69, 84].

In a biological crystal, it is not obvious that the Y-Junctions will form a spatial pattern that is equivalent to the ground state of a physical crystal. If Y-Junctions do form grain boundaries, however, we may be able to leverage that information to understand the mechanism by which the biological crystal forms. By manually tracing rows of UV cones over approximately fifty percent of the retinal area in eight retinae (see Methods), we identified the locations of approximately one thousand seven hundred Y-Junctions.

In flat-mounted retinae, a large fraction of Y-Junctions form grain boundaries

Y-Junctions do, indeed, form grain boundaries that run from the center of the retina to the periphery (Figs. 2.3A-B, A.4). These grain boundaries reconcile domains of differing crystallographic orientations (Fig. 2.3C-D). The angle by which the local row direction rotates from one side of a grain boundary to the other side is determined by the linear density of Y-Junctions in the grain boundary and the length of the Burgers vector of an individual Y-Junction [61, 62, 84].

Although these grain boundaries are identifiable by eye, we developed an objective definition of grain boundaries, which can be applied to biological data and, later, to simulation results of potential models of cone mosaic formation. To count which defects are in grain boundaries, the measure tests whether a defect belongs to an approximately linear chain of at least four other defects, which are each other's nearest neighbors (see Methods). By applying this measure to the eight analyzed retinae, we found that approximately fifty percent of the identified Y-Junctions are in grain boundaries (Figs. 2.3E, A.4).

Figure 2.3 **Y-Junctions form lines, called grain boundaries, from the center of the retina to the periphery. A)** Flat-mounted retina in which UV cones express a transgenic reporter (pseudo-colored magenta) under control of the UV cone opsin promoter. White squares indicate onset of pattern. Dorsal side is left; ventral side is right. Temporal side is down; nasal side is up. White lines: rows of UV cones. Yellow dots: Y-Junctions. Red dots: reverse Y-Junctions, generating row deletions. **B)** Row tracing and identification of defects from retina in panel A. **C)** Grain boundary from retina in panel A. Gray arrows show grain boundary reconciling domains of different crystallographic orientation. **D)** Grain boundary presented in panel C with row tracing. **E)** From seven retinae, we show the percentage of retinal area analyzed and number of Y-Junctions identified and fraction of defects in grain boundaries (see Methods). **F)** Illustration of potential role of defect motion in generating final spatial distribution of defects. Black region is photoreceptor epithelium, and gray region is the margin where photoreceptor epithelium grows. Yellow circles denote Y-Junctions. If defect motion does occur, it could allow defects to line up into grain boundaries. If defect motion is too slow, the cone mosaic patterning mechanism must make grain boundaries during initial mosaic formation.

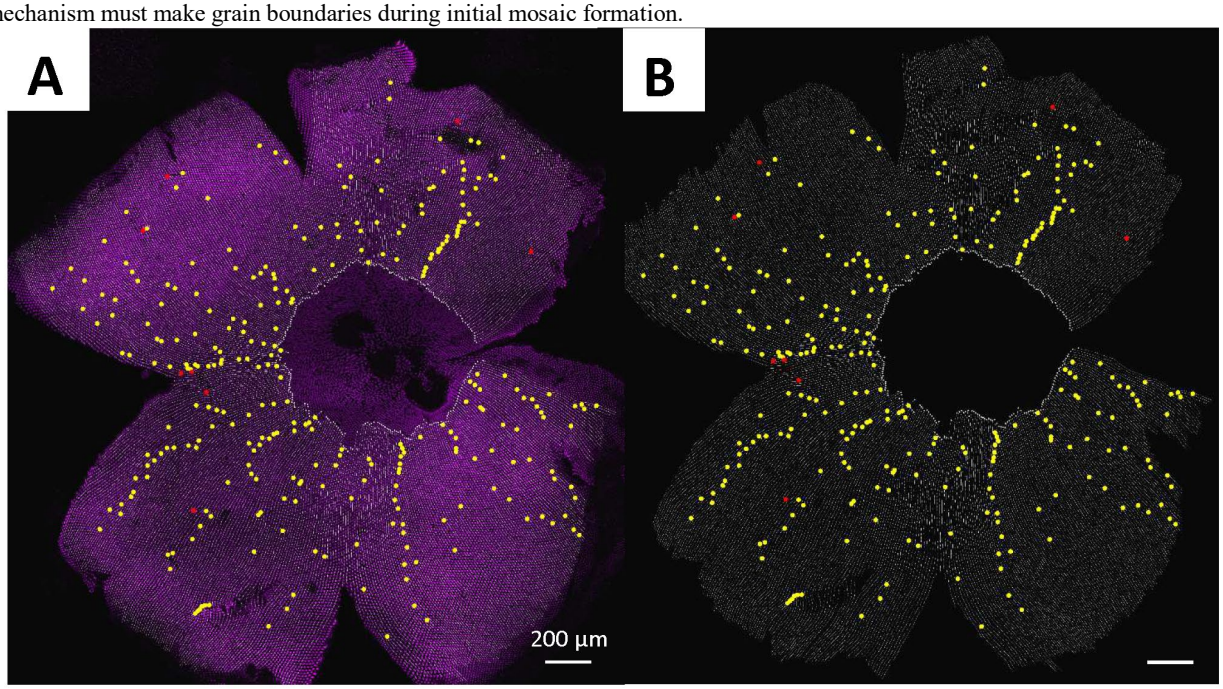

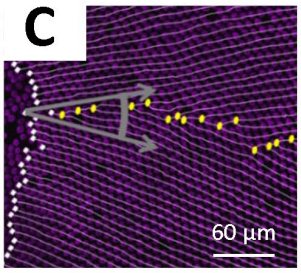

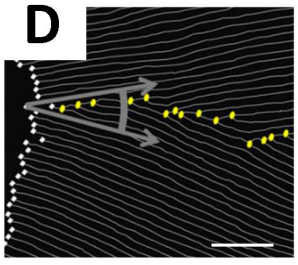

E Fraction of Defects in Grain Boundaries

Fish #	Retinal Area ($10^6\ \mu m^2$)	% Area Analyzed	Y-Junction Count	% of Y-Junctions in GB
1	2.4	47	155	54
2	2.1	46	166	42
3	3.9	57	221	48
4	3.8	70	275	48
5	5.3	66	249	55
6	4.2	61	184	36
7	5.4	51	182	42
8	5.4	63	285	51

F Coalescence into Grain Boundaries?

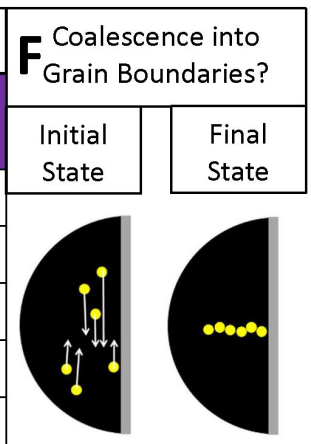

Figure 2.4 **By photoconverting UV cones near the retinal margin, we track Y-Junction motion. A)** Schematic of photoconverted UV cones in photoreceptor epithelium near the retinal margin. We photoconvert a patch of UV cones (purple box) near the margin, where new UV cone photoreceptors are incorporated by mitotic addition. After two, three or four days of retinal growth, we image the photo-converted region. **B)** Example of patch of UV cones immediately after photo-conversion and two days later. In this line (Tg[*sws1:nEOS*]), UV cones express a nuclear-localized, photoconvertible fluorescent protein under control of UV cone opsin promoter. The non-photoconverted fluorescent protein is pseudo-colored yellow, and the photoconverted fluorescent protein is pseudo-colored magenta. Retinal margin is to the right of each image. Approximately eight columns of UV cones have been added in two days since photoconversion. **C)** Glide motion involves subtle motion of individual UV cones near Y-junction core. Magenta circles are UV cones with photoconverted fluorescent signal, and yellow circles are surrounding UV cones with non-photoconverted fluorescent signal. Every cone is connected to nearest neighbors. The five-sided and seven-sided star indicate five-coordinated and seven-coordinated UV cones, respectively. Dashed black line is the "inserted" row. The two triangulations on the right describe positions of UV cones (from the left triangulation) after glide in the direction denoted by gray arrow. Note that the assignment of five- and seven-coordinated UV cones has shifted. by one row.

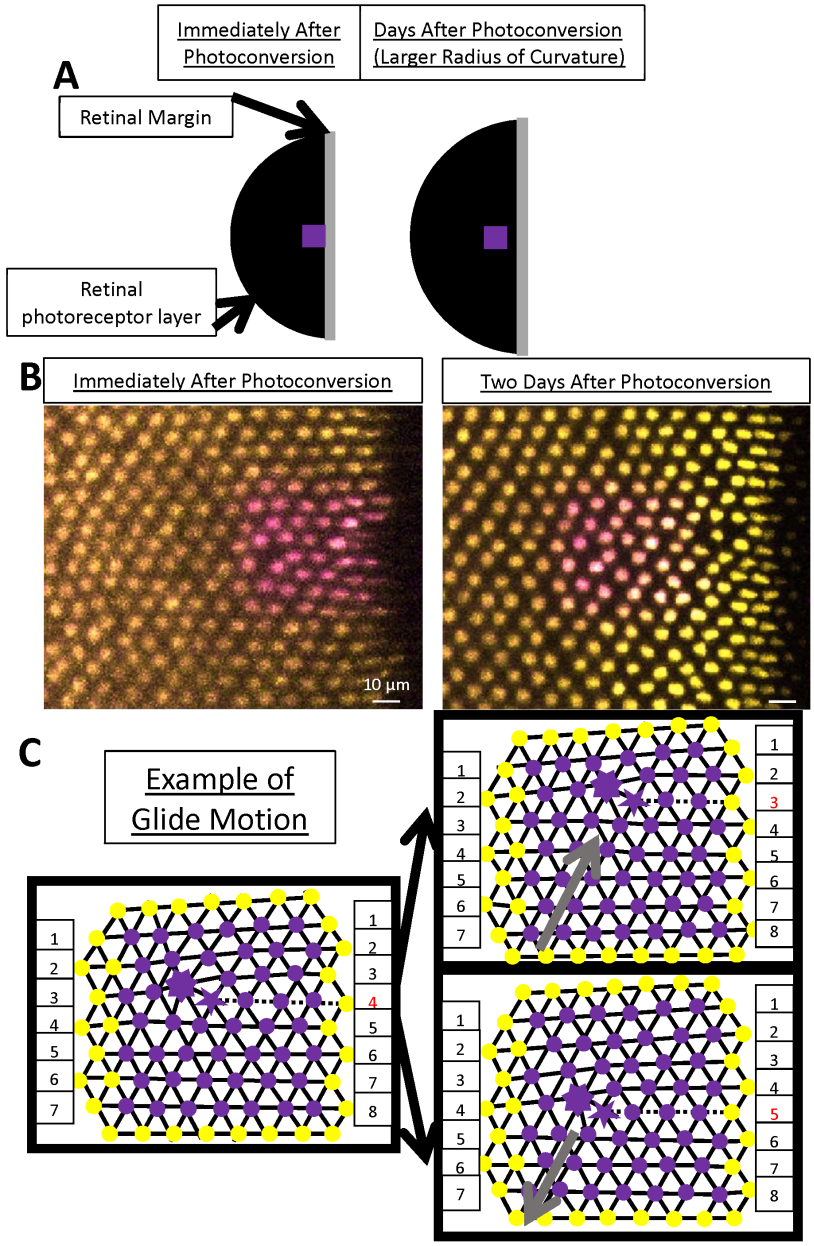

Defect motion is not responsible for grain boundary formation

To study whether defect motion is responsible for the existence of grain boundaries, we need to observe the dynamics of individual cones during cone mosaic formation in live fish rather than the fixed positions of cones in flat-mounted retinae. If defect motion is not responsible for the existence of grain boundaries, we will be able to test potential models of cone mosaic formation based on their ability to form grain boundaries.

To quantify the motion of individual UV cones during cone mosaic development, one must observe the same region of the retina in the same fish at two distinct time points as the fish remains alive. To make sure that one can locate the same set of UV cones at the two distinct time points, one must have some common point or common boundary as a reference for UV cone positions in the two images.

To locate the same set of UV cones at two different timepoints in live fish, we use transgenic zebrafish in which the UV cones express a nuclear-localized, photoconvertible fluorescent protein under the control of the UV cone opsin promoter (see Methods). We photoconvert and image a small patch at the retinal margin, near where newly generated UV cones are incorporated into the growing retina (Fig. 2.4A-B). At the time of imaging, the cone mosaic is composed of approximately eighty columns and is growing by approximately three columns of cones per day [70]. Two, three, or four days later, we image both photoconverted and non-photoconverted UV cones in the same retinal area (Fig. 2.4A-B).

Eliminating the possibility of defect motion perpendicular to the Burgers vector

To understand what types of motion we expect to observe, it is useful to revisit the concept of a Burgers vector. When a dislocation moves along the direction defined by the Burgers vector, this motion requires only subtle rearrangements of individual particles, here UV cones, near the core of the dislocation. This motion is called glide motion [61, 62]. To illustrate this motion in Fig. 2.4C, we denote the inserted row associated with the Y-Junction as well as the five- and seven-coordinated UV cones. When the dislocation glides by one row, as illustrated in Fig. 2.4C, the initial inserted row incorporates itself into a neighboring row, as a new inserted row is generated. The assignment of the five- and seven-coordinated UV cones shifts by one row in the direction of the glide motion. Glide by one row is the flipping of one bond in the UV cone triangulation near the Y-Junction core.

On the other hand, motion of dislocations perpendicular to the direction defined by the Burgers vector, called glide motion, requires the creation or annihilation of point defects, which are interstitials or vacancies in the crystal [61, 62]. A vacancy in the cone mosaic corresponds to the absence of six cones in the same site, which we never observe (Fig. A.5). Therefore, in monitoring the motion of individual UV cones, we test specifically for glide motion rather than climb motion [68].

Quantifying glide motion

Based on the positions of UV cones, we connect nearest neighbors in the lattice (triangulation method described in Methods). We identify the location of the Y-Junction core based on the location of the inserted row (Fig. 2.5A). To quantify glide motion, we search for bond flips (Figs. 2.4C, 2.5A) along the glide line (see Methods) near the Y-Junction core between the time of photoconversion and the time of subsequent imaging (two, three, or four days later).

We observe non-negligible motion near the core, but we never observe glide motion by more than one row per two days, where glide motion by one row is illustrated in Fig. 2.4C. We show two examples of Y-Junctions within photoconverted regions: an example in which there is no glide motion (Fig. 2.5B) and an example in which the Y-Junction glides by one row in two days (Fig. 2.5C). These experiments provide an upper bound on the rate of glide motion (*i.e.*, one row per two days). If we compare this constraint on the timescale of glide motion to the timescale of grain boundary formation, we can determine whether grain boundaries form via the coalescence of initially isolated dislocations that move together after initial crystallization.

Comparing the timescale of glide motion to the timescale of grain boundary formation

In many of our photoconversion experiments, we photoconvert patches of UV cones near at least one existing grain boundary (Figs. 2.5D, A.6). At the time of subsequent imaging of the UV cones near the photoconverted region (*i.e.*, two to four days later), approximately eight UV cone columns are newly incorporated into the cone mosaic. After identifying Y-Junctions in the newly incorporated columns of UV cones, we ask whether their locations are correlated with the positions of existing grain boundaries (*i.e.*, observed at the time of photoconversion). If we do observe a correlation between the positions of new Y-Junctions and existing lines of Y-Junctions, we ask whether that correlation could be explained by Y-Junction motion.

Out of the eighteen samples, twelve samples have grain boundaries near the retinal margin at the time of photoconversion. Since some samples have two grain boundaries, in total we observe fifteen grain boundaries in live fish (Figs. 2.5E, A.6; see Methods). Two to four days later, we identify the positions of newly incorporated Y-Junctions. To these samples, we apply the following null model: each new Y-Junction's initial position is uncorrelated with existing grain boundaries, but after formation, each new defect moves approximately one row closer to the closest grain boundary (see Methods). We find that newly incorporated defects are more aligned with existing grain boundaries than can be explained by this null model ($p < 0.0001$; see Methods). Because glide motion is slow relative to the grain boundary growth, we conclude that grain boundaries form at the time of cone mosaic formation, not by subsequent defect motion.

Figure 2.5 **By estimating timescale of Y-Junction motion, we conclude that Y- Junctions line up into grain boundaries during initial mosaic formation rather than by subsequent Y-Junction motion. A)** Expected motion of individual UV cones in case of glide motion by one row in either direction. Left triangulation is of UV cones near the defect core; a UV cone sits on each site of triangulation. Two triangulations on the right are positions of UV cones (from left triangulation) after glide in the direction denoted by the gray arrow. The UV cones (originally sitting on sites of black triangulation) shift to sites of gray triangulation. Note that the originally five- and seven-coordinated UV cones in black triangulation become six-coordinated. **B)** Example of Y-Junction in photoconverted region in which no bond flips in two days. The photo-converted fluorescent signal in UV cone nuclei is pseudo-colored magenta. For reference, same five cones are labeled in both images. White lines: triangulation of UV cones. **C)** Y-Junction in photoconverted region from Fig. 2.4B. One bond has flipped in the triangulation over two days, meaning that Y-Junction has glided in the direction of the gray arrow by a row. **D)** Observation of grain boundary growth during initial mosaic formation. Immediately after photoconversion, one observes seven Y-Junctions (yellow dots), six within a grain boundary and an isolated Y-Junction nearby. White dashed lines are rows of UV cones. Two days later, one observes two additional Y-Junctions in grain boundary. Based on constraint that a Y-Junction does not glide faster than one row in two days, Y-Junctions must have formed within the regions indicated by red arrows. Black arrow indicates columns of cones incorporated since photo-conversion. **E)** Growth of fifteen grain boundaries in live fish. For image immediately after photoconversion, we measure how much row direction rotates at the retinal margin (see Methods). For all fifteen cases in which the row direction rotates by more than ten degrees at the margin, we count defects in grain boundary at the time of photoconversion. We, then, count defects added to grain boundary by the time of later imaging. Though we photoconverted one region per fish, that region sometimes neighbors two grain boundaries, allowing us to measure growth of two grain boundaries in the same fish (*e.g.*, 4-1 and 4-2). Image in panel D is grain boundary 3.

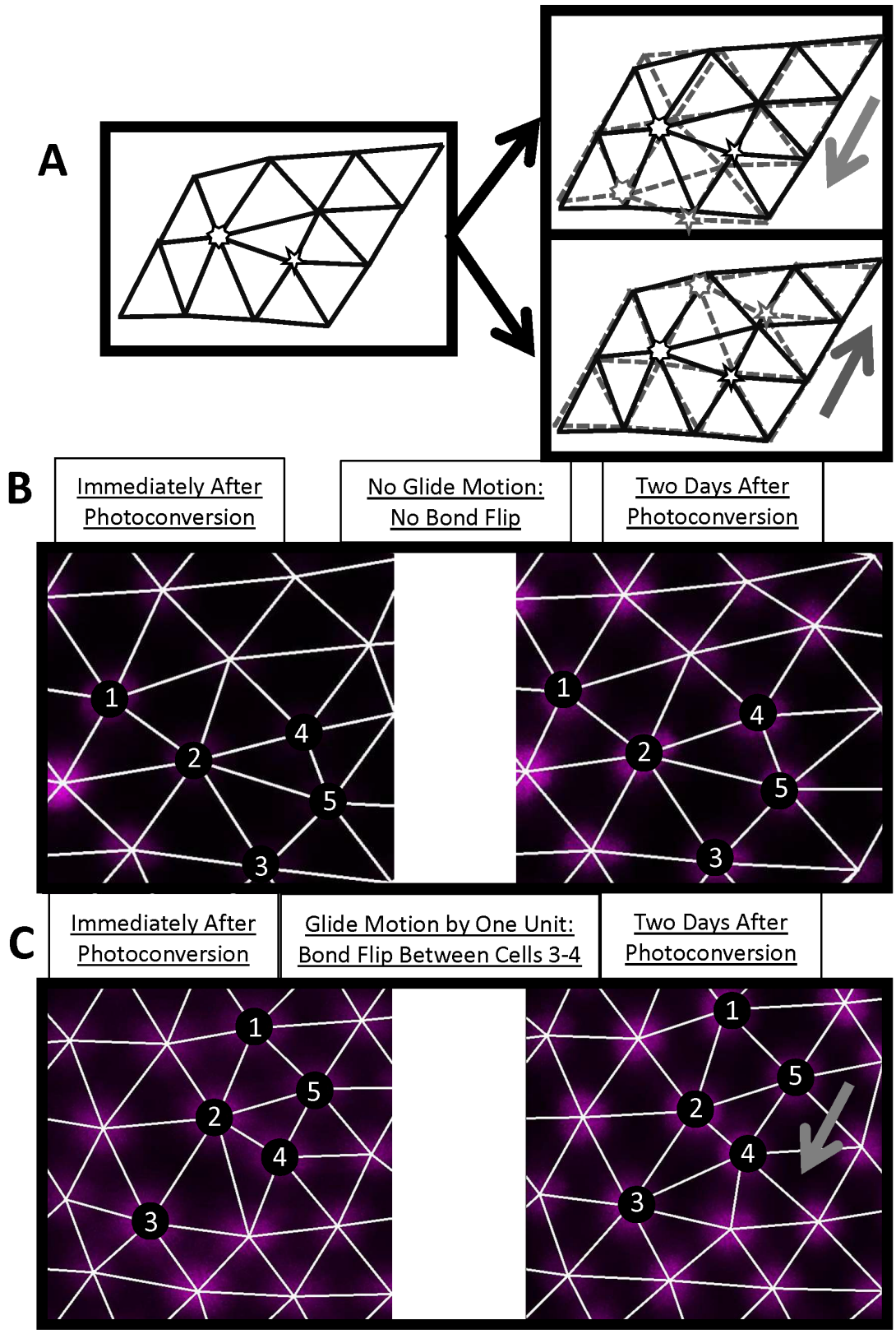
A
B
Immediately After Photoconversion
No Glide Motion: No Bond Flip
Two Days After Photoconversion
1
2
3
4
5
C
Immediately After Photoconversion
Glide Motion by One Unit: Bond Flip Between Cells 3-4
Two Days After Photoconversion

Figure 2.5 (Continued)

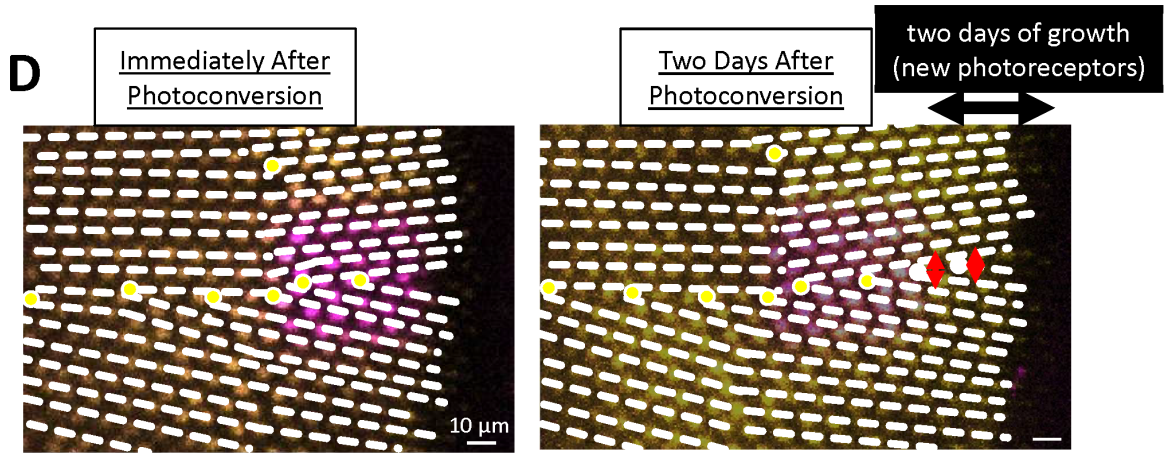

E

Grain Boundary	1	2	3	4-1	4-2	5	6	7	8	9	10	11-1	11-2	12-1	12-2
Δt (days)	2	2	2	2	2	2	2	2	2	2	3	4	4	4	4
DOMAIN ROTATION DAY 0 (°)	24	19	16	19	17	10	14	11	12	12	16	18	10	16	14
NUMBER DEFECTS DAY 0	4	8	6	4	9	4	8	5	5	6	3	4	3	2	2
NUMBER DEFECTS ADDED LATER	+5	+1	+2	+2	+2	+1	+2	+1	+0	+2	+2	+3	+2	+3	+0

Testing computational models of cone mosaic formation

Near the rim of the retinal hemisphere (Fig. 2.6A) is a region defined as the precolumn area, where newly generated but not fully differentiated cones are in approximately correct locations relative to each other based on cone subtype before the formation of mature columns [70]. Composed of differentiating post-mitotic cones, this precolumn area lies between two regions: a central region of mature columns and the rim, which contains proliferative cells. It remains unclear how proper positioning of cones by subtype in the precolumn area occurs, but importantly, this must occur within hours of the generation of post-mitotic cells by terminal divisions of neighboring proliferative cells [70].

In this section, we ask whether our observations of grain boundary creation can provide information about the mechanism for proper positioning of cones by subtype into immature

columns. In principle, one can imagine two extremal models for the creation of regular cell fate patterns in biological tissues. In the first model, cell fates are specified first, and motile cells with a clear identity then rearrange themselves into the final pattern; in the second model, cells instead first arrange themselves in space, then the correct fate pattern is imposed on this static cell packing by cell-cell signaling. Evidence from embryonic retinae suggests that post-mitotic cones are of fixed subtype and move relative to each other during integration into the retina [72].

This finding from embryonic retinae, together with other examples of cell-cell repulsion in neural cell mosaics [21, 22, 73-75], suggests that mosaic formation in zebrafish retina falls closer to the first model. To test whether such a picture is consistent with the observed behavior of grain boundaries, we construct a computational model in which fate-specified cones repel each other during differentiation. After finding that this cell-cell repulsion model does indeed generate grain boundaries during the initial process of differentiation, we demonstrate that the alternative model, in which cell fate patterns arise through lateral inhibition in a static and disordered packing, is not likely to be responsible for cone mosaic formation. Before turning to the descriptions of the two models, we first gather some additional experimental data, on which cone subtypes are essential to establishing a crystalline mosaic and on lattice anisotropy in the zebrafish mosaic, to help in model formulation.

Absence of Red cones does not disrupt cone mosaic formation, but the absence of UV cones does

As noted above, crystals are described by identifying the smallest repeating unit that can be used to build the crystal, the unit cell – consisting of one Blue, one UV, two Red, and two Green cones (Fig. 2.1A) for the zebrafish retina – and the way different unit cells are positioned relative to each other in space, the Bravais lattice – for the zebrafish retina, a slightly anisotropic triangular lattice [61, 62, 81]. It is well-established that the defect core structures can depend on all the features of the unit cell but that elastic interactions between two defects are determined only by the Bravais lattice and the defects' Burgers vectors [53, 54, 64, 81, 85]. Thus, we expect that most features of the spatial distribution of Y-junctions, which should depend primarily on defect-defect interactions [53, 54, 64, 67, 76, 77], can be recapitulated by a model in which each unit cell is replaced by a single cone photoreceptor. In order to provide biological justification for this simplification of the cone mosaic and to determine which cone subtype to focus on, we consider mutants in which certain cone subtypes are absent.

To evaluate the role of Red cones in establishing a crystalline mosaic, we generated a targeted mutation in a single gene that resulted in a loss of Red cones (Fig. 2.6B; see Methods). This gene, *trβ2*, is an early fate marker of Red cones and is expressed in proliferating progenitors and mature Red cones, but not other cone subtypes [70, 72]. All other cone subtypes are still present in the outer retinal layer (Fig. A.7A). Strikingly, in the *trβ2* mutant, we find that cone mosaic formation, including ordering of UV cones, is not disrupted by the absence of Red cones (Fig. 2.6D).

The robustness of cone mosaic formation to the absence of Red cones is in marked contrast with previous experiments with *tbx2b* mutants in which UV cones are largely absent [86]. In *tbx2b* mutants, it is difficult to discern long-ranged crystalline order in the cone positions (Fig. 2.6E). The spatial distribution of cones and absence of long-ranged order is similar in other zebrafish mutants in which cell-cell adhesion is perturbed [51, 71]. Given this evidence from both *trβ2* mutants and *tbx2b* mutants, we simplify the cone mosaic to a lattice of UV cones.

Measuring lattice anisotropy of the cone mosaic in live fish

Previous studies have established the importance of anisotropy of the mosaic lattice both in its formation and refinement [51, 70-72]. In modeling the cone mosaic lattice as a lattice of UV cones, we need to make sure that we produce a lattice with the same anisotropic spacing as the cone mosaic. For this reason, we first measure the lattice vectors of the UV cone sublattice in live fish. We use images of photoconverted regions, immediately after photoconversion, in which there are no Y-Junctions (Fig. A.2).

In an isotropic triangular lattice, the ratio of the distance between UV cones in the column direction to the distance between UV cones in the row direction would be equal to the square root of three. We find that this ratio is approximately six-fifths in our live images of the UV cone sublattice (Fig. A.2). This means that the spacing along the row direction is longer than would be expected in an isotropic triangular lattice. We use this degree of anisotropy as an input for modelling the cone mosaic formation.

Figure 2.6 **Cone mosaic formation is not disrupted in Red cone mutant but is disrupted in UV cone mutant. A)** Cross-section of wild-type retina in which immunostaining of Red cone opsin labels Red cones. White arrow is approximate location of precolumn area. **B)** Cross-section of *trβ2* mutant in which immunostaining of Red cone opsin labels Red cones. Note absence of differentiated Red cones. White arrow is approximate location of precolumn area. **C)** Apical plane of wild-type cone mosaic lattice in retinal flat-mounts in which anti-ZO-1 stains cell profiles. UV cones indicated in the inset. **D)** Apical plane of cone mosaic in retinal flat-mount from *trβ2* mutant, which lacks Red cones. Anti-ZO-1 stains cell profiles. UV cones (indicated in inset) identified based on large, rounded profiles. Note that the triangular lattice of UV cones is minimally disrupted in absence of Red cones. **E)** Apical plane of cones in retinal flat-mount from *tbx2b* mutant, which lacks UV cones. The cone mosaic is disrupted in this mutant.

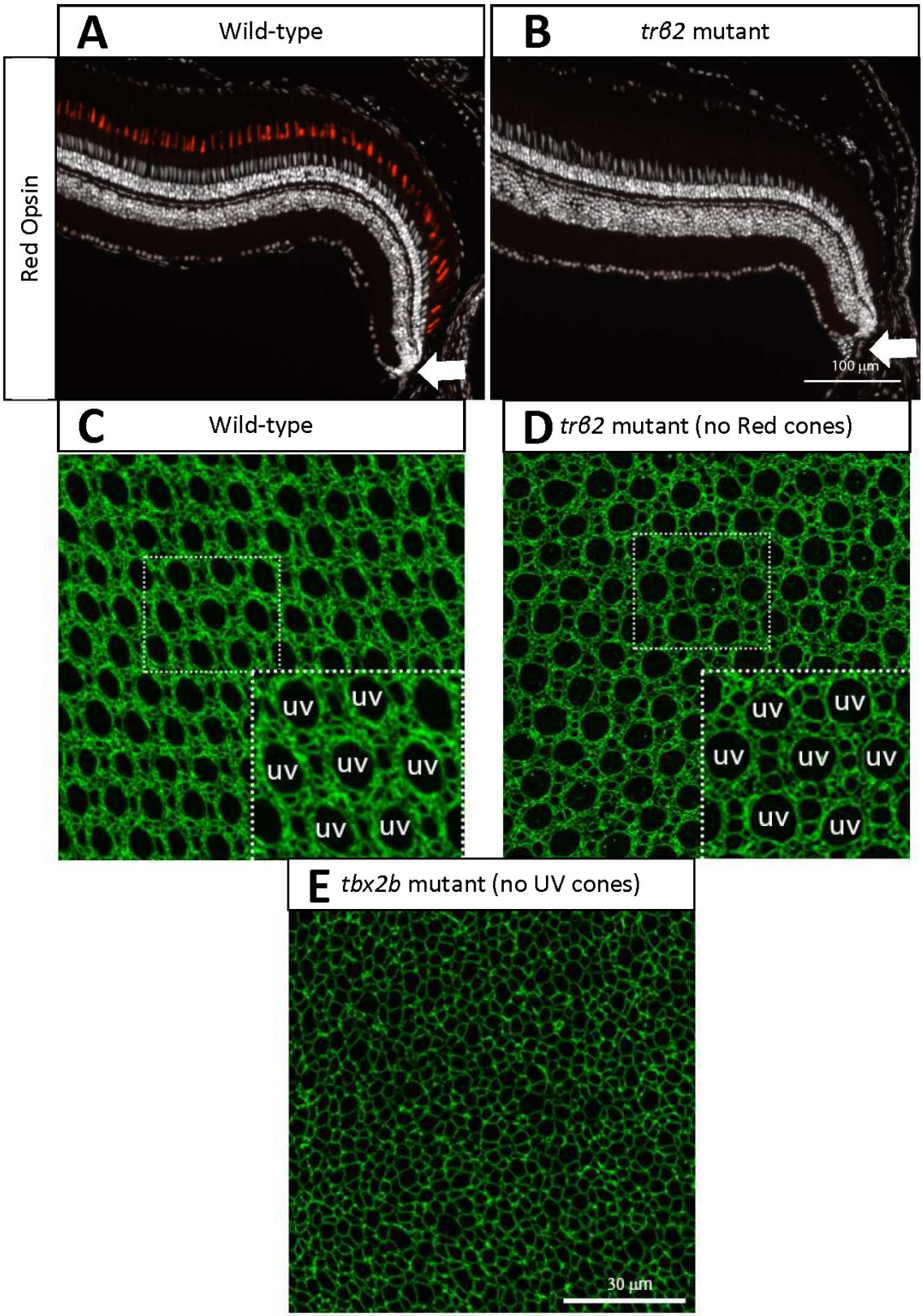
A
Wild-type
B
trβ2 mutant
Red Opsin
100 µm
C
Wild-type
D
trβ2 mutant (no Red cones)
uv
E
tbx2b mutant (no UV cones)
30 µm

Figure 2.7 **Phase-field crystal model of cone mosaic formation. A)** Schematic of contact-interaction model in which fate-committed cones interact homotypically and form an anisotropic lattice. UV cones (magenta circles) interact with nearest neighbors of same subtype. White arrows: contact interactions. New fate-committed cones are incorporated to right of ordered region. **B)** In the phase-field crystal model, continuum field describes positions of, in this case, UV cones. Peaks in density (white regions) are regions where a UV cone likely exists; troughs in density (dark regions) are the opposite. Gray regions are regions in which UV cone positions are disordered and in which new UV cones are incorporated. **C)** Image of flat-mounted retina (same as Fig. 2.3A-D) in which UV cones express a transgenic reporter under control of UV cone opsin promoter. Yellow dots: Y-Junctions. Red dots: reverse Y-Junctions. **D)** Simulation of phase-field crystal model on surface of a cone. The number of initial rows and number of total columns and defect density are comparable values in retinae. Degree of anisotropy of the triangular lattice is constrained by the anisotropy measured in live-imaging experiments. Yellow dots: Y-Junctions. Red dots: reverse Y-Junctions.

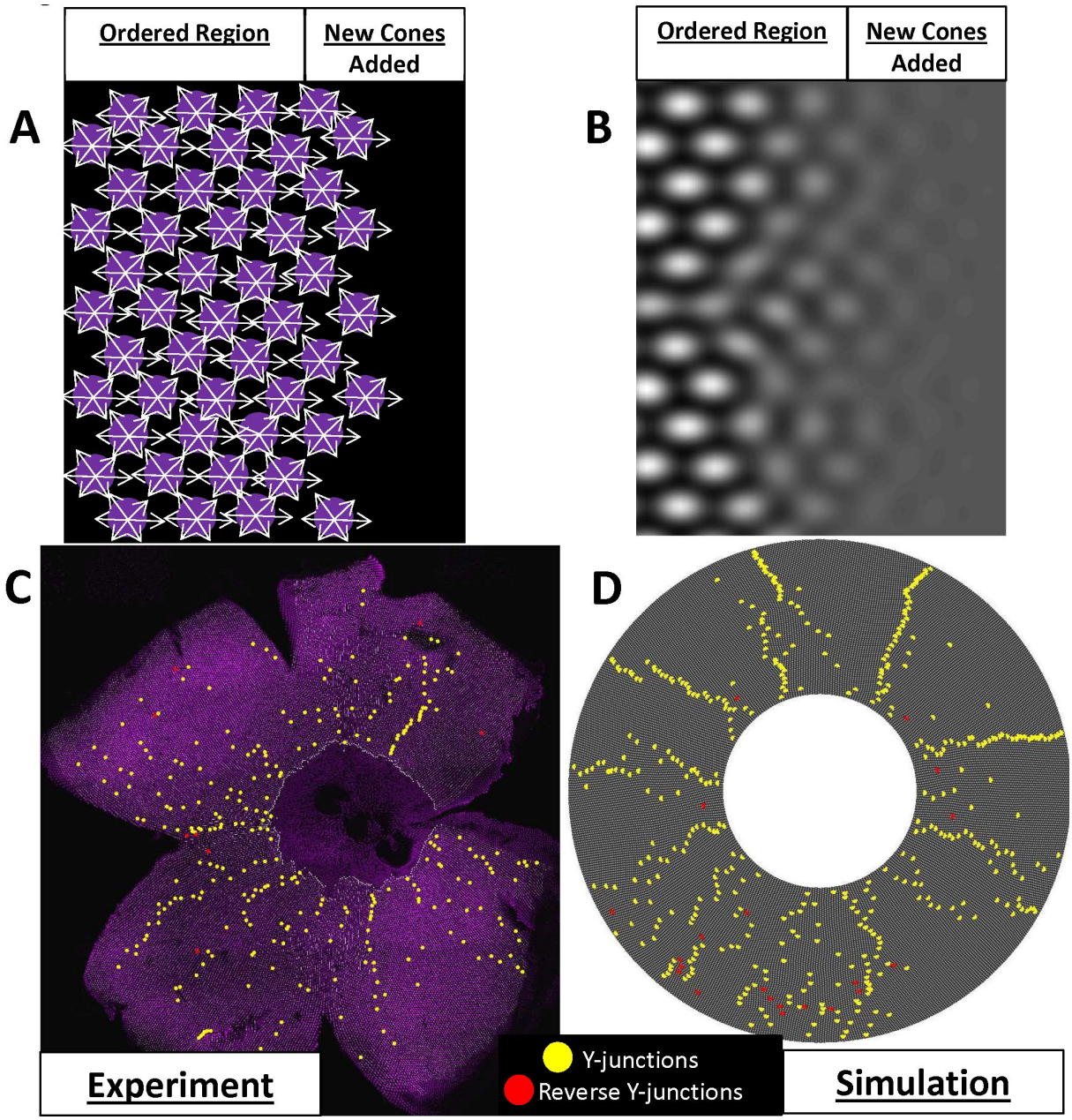

Model of repulsive interactions between fate-committed cells generates grain boundaries during initial cone mosaic formation

In building a model of cone mosaic formation, we hypothesize that cell motion is generated by repulsive interactions between fate-committed cones of the same subtype as they differentiate in a mechanically anisotropic medium. This model is motivated by cell mosaics in other vertebrate retinal layers [21, 73-75] and in the nervous system in *Drosophila* larvae [22]. For example, in mice, specific neuron subtypes disperse after fate commitment and during morphological differentiation [21, 75]. By cell ablation, previous investigators have established that for retinal horizontal cells in mice, the cells are fate-committed and homotypically interact via transient neurites (*i.e.*, cell processes) [21]. Similarly, in *Drosophila*, certain classes of peripheral sensory neurons tile the body wall. By ablation of dendritic processes, previous investigators have established that neurons of a specific class (class IV) interact homotypically to establish a tiling of the body wall by non-overlapping cell territories [22].

To model repulsive interactions between fate-committed cones of the same subtype, leading to a preferred spacing in the row and column directions, we employ a phase-field model of crystallization (Fig. 2.7A-B). These models are widely employed to describe various processes in physical crystals, including nucleation of crystalline domains in a supercooled fluid, epitaxial film growth from a neighboring liquid phase, and the mechanical hardness of a solid based on the microstructure of crystalline domains [87, 88].

Phase-field crystal models employ a continuum field, which corresponds to modulations in the particle density (Fig. 2.7B) [87-94]. Based on our simplification of the cone mosaic to a lattice of UV cones, the particle density represents the density of the UV cone subtype. If the field is homogeneous in space, the UV cones form a "liquid," with no clear periodicity. If the field is periodic in space, the UV cones form an ordered crystal. The field starts out entirely uniform except near the center of the simulation domain (see Methods). The crystalline region grows outward from the center, as fate-committed cones in the disordered region are incorporated (Fig. 2.7A-B).

This particle density field is evolved to minimize a free energy, while conserving the total number of particles [87-94] (see Methods). (Although there is no *a priori* reason that the dynamics of a biological system should be governed by a free energy, we expect that any model with symmetric, pairwise, repulsive interactions between cells can be mapped onto an effective free

energy.) This free energy incorporates the equilibrium two-point correlation function, which encodes the preferred spacing in the crystal and can be derived from the underlying cone-cone interactions [94, 95]. By imaging UV cones near the retinal margin, we know that the two-point correlation function must encode an anisotropic spacing such that the separation between UV cones along the row direction is elongated (Fig. A.2).

Given a two-point correlation function, there are only two free parameters within this free energy. The first parameter specifies the degree of undercooling; when the temperature is below the melting temperature (*i.e.*, the liquid is "undercooled"), the density field is unstable to the formation of periodic structures for a range of spatial frequencies. As there is no clear analogue to temperature in our system, we interpret this parameter as quantifying the strength of the interactions relative to the random noise in cone motion. The second parameter is the mean of the cone density field, which is conserved.

The values of these two free parameters, the interaction strength and the mean of the density modulation field, determine which phase (or phases) are stable. Depending on these parameters, this model can generate three phases: a constant ("liquid") phase, a striped phase, and a triangular phase [87, 90]. We can constrain these two free parameters to the region of the phase diagram in which the only stable phase is the triangular phase. We scan the parameters over a one-dimensional cut of this region of the phase diagram to ensure that our conclusions do not depend on fine-tuning of parameters (Fig. A.8; see Methods).

By simulating this model in a geometry of comparable size to the retina and with comparable defect densities, we find that this model generically produces spatial distributions of defects that are quantitatively similar to those observed in the flat-mounted retinae (Figs. 2.3, 2.7C-D, A.4, A.8). The fraction of defects in grain boundaries, as quantified by the measure that we applied to the flat-mounted retinae, is approximately sixty percent (Figs. 2.3E, A.8). In the eight flat-mounted retinae, approximately fifty percent of Y-Junctions are in grain boundaries (Figs. 2.3E). This model, for which there is supportive evidence in embryonic retinae [72], is consistent with observations of flat-mounted retinae (Fig. 2.7C-D).

Additional insights generated by model of cell-cell repulsive interactions

Armed with this cell-cell repulsion model, we now generate insights into cone mosaic formation. First, we address how the specific orientation of the cone mosaic lattice is selected and

how it is maintained as the crystal grows. With isotropic interactions in an isotropic medium, at the onset of ordering, crystallites form with random orientations. Additionally, as the crystal grows outward, the crystallites tend to rotate into an orientation that is misaligned with the orientation observed in the retinae by thirty degrees (*i.e.*, maximally misaligned) (Fig. A.9A). For an anisotropic crystal, as in the retinae, the correct crystallographic orientation is selected even without spatial ordering in the original cone positions, and that crystallographic orientation is maintained as the crystal grows (Fig. A.9B).

This model also suggests a mechanism by which grain boundaries form during initial mosaic formation. We consistently observe in our phase-field crystal simulations that the density profiles near a grain boundary remain poorly resolved even as neighboring regions of the crystal grow outward, leading to a characteristic V-shape of the crystal surface (Fig. A.9C). Our model predicts that there should be a lag in proper positioning of cones near a grain boundary.

Implausibility of lateral inhibition mechanism for cone mosaic formation

Before concluding our modelling of cone mosaic formation, we present a possible alternative model and explain its shortcomings in generating a crystalline mosaic. The alternative model is motivated by other biological lattices like sensory bristles and R8 photoreceptors in *Drosophila* [31, 33, 35-38, 57], where neural cells are selected through a process of lateral inhibition mediated by the Notch signaling system. In these examples, cell motion is largely absent during pattern formation. Mathematical models of motionless tissues in which cells differentiate, inhibiting neighboring cells within some range from committing to the same fate [33, 36, 37, 57], reproduce the observed patterns.

The lateral inhibition model that we adapt was originally developed in the context of sensory bristle patterning in *Drosophila* [57] (see Methods). An important difference between sensory bristle patterning in *Drosophila* and cone mosaic formation in zebrafish is that the lattice vectors in the cone mosaic are much shorter, in units of cell diameters, than the lattice vectors of the sensory bristle lattice. There are five to six cells between nearest-neighbor sensory bristle cells [57], but only one to two cells between nearest-neighbor UV cones. Therefore, we expect a cone mosaic lattice generated by lateral inhibition to be more sensitive to disorder in cell packing than is the sensory bristle lattice.

In Fig. A.10C, we provide an illustrative example of lateral inhibition with a short signaling range on a fixed cell packing (see Methods). As a wave of differentiation moves from the left side of the cell packing to the right, individual cells differentiate into the inhibiting cell fate, and these cells signal to their neighbors, causing them to adopt the alternative fate. The resulting fate pattern has many defects, disrupting the long-ranged crystalline order expected in the cone mosaic [51, 70]. Thus, the disordered cell packing prevents the formation of a precise triangular lattice, in contrast to the previous model in which fate specification occurs first and cells of known spectral fate then move into the correct lattice position.

Since the basic impediment to pattern formation by lateral inhibition in this model is the disorder in the cell packing, one might be tempted to consider a model in which lateral inhibition instead acts to impose a fate pattern on an ordered packing of equipotent cells. In such a model, however, there would have to be defects in the ordered packing to fit onto the retina's curved surface, and the pattern of defects in the eventual cone mosaic would be expected to follow the pattern of defects in the underlying packing. Thus, the problem would again be reduced to that of arranging cells (necessarily with some short-ranged repulsion, as they cannot overlap) into the surface of a growing hemisphere – that is, essentially to the same problem solved by our earlier phase-field model of cone mosaic formation.

Discussion

In this study, we characterize the properties of Y-junction defects in the zebrafish cone mosaic and their spatial distribution across the retina. Strikingly, we find that Y-junctions are organized into grain boundaries oriented perpendicular to the retinal margin, as would be expected if they were positioned to minimize the elastic energy of a physical crystal. We show, however, that unlike dislocations in most physical crystals, Y-junction motion is limited, implying that Y-junctions must be positioned within existing grain boundaries when they are created at the cone mosaic's growing margin. Inspired by these observations, as well as previous findings that cone photoreceptors in embryonic retinae are born from symmetric terminal divisions and then disperse to their final positions in the retina, we propose a model for cone mosaic formation based on interactions between fate-committed cells, generating cell motion. This model reproduces the major features of the Y-Junction distribution in the zebrafish retina.

Our model of cell motion contrasts with most previous pictures of pattern formation in sensory epithelia [31, 33, 35-38, 57, 96-98]. For example, in R8 photoreceptor specification, without invoking cell motion, one reproduces the observed patterns based on cell-cell signaling in a disordered tissue. Cells of an inhibiting fate prevent neighboring cells from adopting the same fate within some signaling range. In both R8 photoreceptor specification and the similar problem of sensory bristle patterning, the signaling range is larger than the typical cell diameter, resulting in approximately six cells between each inhibiting cell [31, 33, 35-38, 57]. These lateral inhibition systems are relatively insensitive to disorder in the cell packing.

We have argued, on the other hand, that if the lateral inhibition signaling range is on the order of the typical cell size in a disordered packing, one must invoke cell rearrangement to produce a crystalline mosaic. This finding is consistent with a very recent study by Cohen *et al.* of the patterning of outer hair cells in the mammalian inner ear [23]. The outer hair cells form a triangular lattice in a quasi-two-dimensional tissue where the lattice spacing is on the order of one cell [23, 34]. To produce a pattern consistent with the order observed in the inner ear, Cohen *et al.* first produce a fate pattern via lateral inhibition in a disordered packing. They, then, model rearrangements of the disordered packing: global shear forces and local repulsion between outer hair cells, followed by type-dependent edge tensions. Even with such significant rearrangements, their model produces excess defects in the triangular cell lattice of outer hair cells [23].

In contrast, our model of cone mosaic crystallization is based on interactions between cones of the same subtype (*e.g.*, UV cones) during their differentiation and incorporation into the retina. We hypothesize that these repulsive interactions are mediated by cellular appendages called telodendria [99, 100]. Previous investigators have suggested the potential role of telodendria in tangential dispersion after symmetric terminal cell division [72]. Though less ordered than the zebrafish cone mosaic, both the retinal horizontal cell mosaic in mice and class IV neural cell mosaic in *Drosophila* form via similar neurite-mediated interactions, demonstrating the importance of cell motion guided by repulsive interactions for forming neural cell mosaics [21, 22, 73-75].

It is tempting to speculate about the merits of cone mosaic formation via homotypic cell-cell repulsion between fate-specified cones as opposed to a more classic lateral inhibition pathway. For example, if the formation of defect-free crystalline domains (separated by grain boundaries) is functionally relevant, which aspects of fish retinae might allow our model to outperform lateral

inhibition on that merit? One possibility is that it is precisely the curvature of the retinal hemisphere and the resulting need for lattice defects that favor the homotypic repulsion mechanism over lateral inhibition. Indeed, we have argued that a cone mosaic formed in such a way will have many of the same features as a physical crystal. These features include, in particular, the presence of an effective long-ranged, elastic interaction between Y-Junctions that is absent in models of fate specification through signaling on a fixed cell packing. Such a long-ranged interaction likely makes it easier to position Y-Junctions correctly across the retina, as exemplified by the spontaneous appearance of grain boundaries in our phase-field crystal model.

Finally, this study highlights the importance of the kinetics of crystal growth in determining the observed spatial distribution of defects. Many studies of physical crystals focus on the agreement between theoretically predicted ground-state defect distribution and experimentally observed defect distributions [53, 54, 64] rather than on the kinetics of grain boundary formation. In the zebrafish retinae, we demonstrate the grouping of dislocations into grain boundaries during initial mosaic formation without requiring glide motion. Akin to work by Köhler *et al.* [78], the phase-field crystal simulations of cone mosaic formation suggest the following mechanism by which dislocations are grouped into grain boundaries: a delay of crystal growth near a grain boundary relative to growth of defect-free domains. Biological tests of this prediction await further investigation.

Materials and methods

Zebrafish

Fish were maintained at -28°C on a 14/10 h light/ dark cycle with standard husbandry procedures [101]. Zebrafish lines, *Tg(-5.5sws1: EGFP)kj9* [102], *Tg(-3.2sws2: mCherry)mi2007* [51], *Tg(trβ2: tdTomato)* [72], *Tg(-3.2sws2: EGFP)* [103], Tg(*gnat2*:H2A-CFP), and pigment mutant *ruby* carrying *albino (slc45a)*$^{b4/b4}$ and *roy*$^{a9/a9}$ were used. All animal procedures were approved by the Institutional Animal Care and Use Committee at the University of Michigan.

Histology

Retinal dissection, fixation and immunocytochemistry were performed as previously described [70, 104, 105]. Briefly, the isolated retina was fixed in 4% paraformaldehyde with 5%

sucrose in 0.1M phosphate buffer, pH 7.4, at 4C overnight. After antigen retrieval with 10 mM sodium citrate in 0.05% tween 20 (pH 6.0), retinas were incubated in blocking buffer for 2 hours followed by primary antibody incubation, mouse anti-Zonula Occludens (ZO1-1A1, 1:200, ThermoFisher Scientific, Waltham, MA) and rabbit anti-GFP (1:200, ThermoFisher Scientific) at room temperature overnight. Incubation with secondary antibodies (Alexa Fluor 555 and 649, ThermoFisher) were performed at room temperature overnight, and the retina was flat-mounted on a glass slide. For retinal cross sections, affinity-purified rabbit polyclonal opsin antibodies, a gift from Dr. David R. Hyde [106], were used. Images were acquired with a Zeiss AxioImage ZI Epifluorescent Microscope (Carl Zeiss Microimaging, Thornwood, NY) equipped with an ApoTome attachment for optical sectioning structured illumination, Leica DM6000 Upright Microscope System (Leica Microsystems, Werzlarm Germany) and a Leica TCS SP5 confocal microscope equipped with Leica 40X HCX PL APO CS Oil Immersion lens.

Generation of transgenic zebrafish with nuclear-localized photoconvertible (green-to-red) EOS protein expressed specifically in UV cones

Multi-Gateway-based *tol2* kit system was used to generate expression vectors [107]. In brief, the 5' entry clone, *p5E- 5.5sws1* [102], middle entry clone, *pME-nEOS* (gift from Dr. David Raible), and 3' Entry clone, *p3E-polyA*, were assembled into a destination vector, *pDestTol2pA* [107] using LR Clonase II Plus enzyme (Thermo Fisher Scientific). Embryos of the transparent *ruby* genetic background [70] at the 1-cell stage were injected with 1 nL of solution containing 25 pg plasmid DNA and 25 pg tol2 transposase mRNA [108]. Founders (F0) with germline transmission of the transgene were identified by outcrossing with wildtype animals, and their F1 progenies were screened for nEOS expression at 4 days post fertilization.

CRISPR-Cas9 mediated mutation in the *thrb* gene

A genetic mutation targeting the type 2 isoform of the *thrb* gene (synonym, *trß2*) was generated by CRISPR-Cas9 gene editing methods [109]. Briefly, pT7 gRNA vector (Addgene #46759) was used as a template to construct the *thrb2* gRNA [109]. PCR based method was performed using specific primers, 5'-GGGGTAATACGACTCACTATAGGCAACACAGCCAACCCTATGTTTTAGAGCTAGAA ATAGCAAG-3'; 5'-AAAAAGCACCGACTCGGTGCC-3'. The MEGAscript T7 Kit (Ambion

Inc., Austin, TX) was used to transcribe the gRNA. For the *nlsCas9nl* mRNA synthesis and purification, mMESSAGE mMACHINE T7 Transcription Kit (Ambion) and Qiagen RNeasy mini kit (Qiagen, Hilden, Germany) were used. For genotyping of the *thrb* mutation, PCR fragments of the *thrb* gene, amplified using specific primer set, 5'-CATGGTGTAAGTGGCGGATATG -3'; 5'-TCCACTGCATCTGAGAGAAATCC-3', were subjected to restriction with BstXI (New England Biolabs, Ipswich, MA).

nEOS photoconversion and imaging

Photoconversion of nEos protein was performed on *ruby; Tg(sws1:nEos)* fish [110]. Juvenile zebrafish (0.7 to 0.88 cm standard body length) were anesthetized with 0.672 mg/ml Tricaine S/ MS-222 (Western Chemical Inc., Ferndale, WA) and placed dorsal side down on a 50 mm glass bottom petri dish with a No. 1.5 coverslip (MarTek Corporation, Ashlan MA, see [70]) and held in place with damped Kimwipes. Imaging and photoconversion were performed with a Leica TCS SP8 LSCM (Leica Microsystems, Werzlar, Germany) equipped with Leica 40X PL APO CS2 Water Immersion lens, 1.1 NA with 650 μm working distance. Green to red photoconversion of nEOS protein was performed by a 405 Diode laser at 400 Hz scan speed with a resolution of 512 x 512 pixels in the *xy* dimension at a single optical plane. Pre and post photoconversion images were captured with the White Light Laser tuned to 506 nm for nEOS (green) and 573 nm for nEOS (red). Leica HyD hybrid detectors were tuned to 516-525 nm for nEOS (green) and 620-761 nm nEOS (red).

Large tile scans of flat-mounted retinae

Large tile scans of entire flat-mounted retinae from adult *Tg(sws1:EGFP)* zebrafish immunostained for ZO1 were acquired with a Leica TCS SP8 LSCM (Leica Microsystems) equipped with Leica 20X PL APO Dry lens. The GFP signal was recovered by immunostaining with anti-GFP antibody. The White Light Laser was tuned to 555 nm for Alexa Fluor 555 and 649 nm for Alexa Fluor 649. The Leica HyD hybrid detectors were tuned to 600-641 nm for Alexa Fluor 555 and 701-751 nm for Alexa Fluor 649. Images were acquired at 700 Hz scan speed with a resolution of 2048 x 2048 pixels in the *xy* dimension with a 2.0 μm interval between optical sections in the z-dimension.

Row tracing of flat-mounted retinae

We manually traced rows of UV cones, starting near the region coinciding with the disorder-to-order transition (Figs. 2.3A-E, A.4; Table A.1). The row tracing extends over approximately one hundred columns of UV cones from the larval remnant to the periphery, avoiding regions of the retinae which were damaged during flat-mounting. Based on the row-tracing, we identified where rows are inserted (*i.e.*, Y-Junctions) and where rows are removed (*i.e.*, reverse Y-Junctions, see Table A.1).

Detection of grain boundaries

In the flat-mounted retina, we have the positions of all Y-Junctions, which generate row insertions, in the traced regions. To define grain boundaries, we search for approximately linear chains of five Y-Junctions, which are nearest neighbors. To the image of all Y-Junctions in the traced regions (Fig. A.4), we apply the following algorithm:

1) Loop through all Y-Junctions one-by-one. We will build a chain of nearest neighbors, of five Y-Junctions, for each Y-Junction.
    a. Look for the Y-Junction's nearest neighboring Y-Junction, using a k-nearest neighbors search (knnsearch; MATLAB 2016B, MathWorks, Natick, MA). Add the nearest neighbor to the chain.
    b. For that nearest neighbor, add its nearest neighbor, excluding any Y-Junctions which already belong to the chain.
    c. Repeat b until you have a chain of five Y-Junctions, including the Y-Junction which initialized the chain.
2) Now, based on the calculation in step 1, every Y-Junction, indexed by i below, has a chain of five nearest neighbors, including the Y-Junction itself. We index the five defects in the chain by j. The position of the j^{th} defect in the i^{th} chain is $\overrightarrow{r_{i,j}}$. For each Y-Junction, we compute the following sum:

    $a_i = \frac{1}{4}\sum_{j=1}^{4} \frac{(\overrightarrow{r_{i,1}}-\overrightarrow{r_{i,5}})}{norm(\overrightarrow{r_{i,1}}-\overrightarrow{r_{i,5}})} \cdot \frac{(\overrightarrow{r_{i,j}}-\overrightarrow{r_{i,j+1}})}{norm(\overrightarrow{r_{i,j}}-\overrightarrow{r_{i,j+1}})}.$
3) Now, based on the calculations in steps 1 and 2, every Y-Junction, indexed by i, has a chain of five nearest neighbors, which is assigned a score a_i. If $a_i = 1$, the chain of

five Y-Junctions is perfectly linear. If $a_i > a_{gb}$, we call the i^{th} chain a grain boundary. We set the cutoff a_{gb} equal to seven-eighths.

4) We initialize an empty array, in which we will store Y-Junctions which belong to grain boundaries. Loop through all Y-Junctions, indexed by i, one-by-one.
    a. If $a_i > a_{gb}$, store (i.e., in the array of all Y-Junctions in grain boundaries) the five Y-Junctions which belong to this chain.

We recognize a couple of limitations of this approach as applied to the flat-mounted retina. First, for flattening the retina, the retina is sliced in four places. The cuts could physically separate one part of a grain boundary from another, leading us not to detect the grain boundary. Second, the flattening deforms the cone mosaic, which means that spatial relationship between Y-Junctions is somewhat different from the intact hemispheric retinae. Nevertheless, the algorithm performs well in identifying grain boundaries in the retina, as illustrated on three of the flat-mounted retinae in Fig. A.4.

We also perform this computation (steps 1-4) on the seven-coordinated particles in simulations of the phase-field crystal model. In that case, we map the cone frustum to the flat plane. This does not generate distortions because cones are isometric to the plane. We, then, calculate which dislocations form grain boundaries, respecting the periodic boundary conditions of the flattened cone frustum.

Tracking nuclear positions in photoconverted regions

In the photoconversion experiments, we observe the same region of the same retina at two different times in live fish. Given a nucleus at one time point, we want to find the same nucleus in the image at the other time point. One image of the region is taken immediately after photoconversion, which we call day 0. Across fish, we vary the time between photoconversion and the time of the second observation (i.e., two days after photoconversion at the earliest and four days after photoconversion at the latest). We call the second time point day 2-4.

At both times of observations for each fish, we have an image with two channels. One channel corresponds to the color of the photoconverted fluorescent protein. The other channel corresponds to the color of the non-photoconverted fluorescent protein. For the image analysis below, we use the photoconverted channel at both times. The image is three-dimensional, and the plane which contains the UV cone nuclei (i.e., where the fluorescent protein is localized) is mostly

parallel to the x-y plane. This fact allows us to perform most of the computations, for tracking each nucleus from one image to the other, based on two-dimensional projections.

For each z-stack, we compute a two-dimensional wiener filter (wiener2; MATLAB 2016B Image Processing Toolbox, MathWorks) with a filter size of eight pixels, which is approximately a micron. This filter removes noisy specks (i.e., spikes in intensity at small length scales). We, then, compute a two-dimensional projection by summing over z-stacks. The photoconverted UV cones are in the middle of the image. The intensity in the photoconverted channel is significantly weaker for UV cones near the edge of the image. This provides us the reference boundary by which we can identify common nuclei (i.e., which nucleus in the day 2-4 image corresponds to a specific nucleus in the day 0 image).

We perform an image registration, computing the combination of rotation and translation which optimizes the normalized cross-correlation between the two images (normxcorr2; MATLAB 2016B Image Processing Toolbox, MathWorks). Then, we segment nuclei in the two images. Because the intensity of UV cone nuclei varies significantly across the image, we use both adaptive thresholding (adaptthresh; MATLAB 2016B Image Processing Toolbox, MathWorks) and a low absolute threshold. We morphologically open the thresholded image, followed by morphological closing. We fill holes in the image (imfill; MATLAB 2016B Image Processing Toolbox, MathWorks) and clear the border of the image (imclearborder; MATLAB 2016B Image Processing Toolbox, MathWorks). We perform minimal manual correction of these segmentations. Given that we have aligned the two images and segmented the nuclei, we track each nucleus from one image to the other by computing for each nucleus in the day 0 image its nearest neighbor in the day 2-4 image (knnsearch; MATLAB 2016B, MathWorks). As a sanity check, for each nucleus in the day 2-4 we compute its nearest neighbor in the day 0 image to make sure that calculation returns the same answer for each nucleus. We manually correct any errors.

Following this segmentation and identification of common nuclei between the two images, we want to estimate the three-dimensional position of each nucleus based on the raw z-stacks rather than on a post-processed version. We identify a circular region, of radius two and a half microns, in the xy-plane centered on each of the segmented nuclei. This radius is larger in the xy-plane than the nuclear radius but small enough not to encompass other nuclei. This circular region corresponds to a pillar in the z-direction. To estimate the three-dimensional position of each nucleus in both images, we use the raw z-stacks, computing the center of intensity of each pillar

(i.e., weighted average of voxel positions in each pillar where the weights are the voxel intensities). At the end of this entire procedure, for each nucleus common to both images, we know its position at both time points.

Tracking UV cone positions in photoconverted regions and measuring glide motion

To identify the location of the Y-Junction, we need to calculate a triangulation over the nuclear positions. At both day 0 and at day 2-4, the UV cone nuclei positions in each experiment are well fit by a plane, which we fit by simple least-squares minimization (see RMSE information in Table A.2). For calculating the triangulation, we project the UV cone positions onto the plane of best fit. We, then, calculate the triangulation in that plane (delaunayTriangulation; MATLAB 2016B, MathWorks).

We want to track movement of UV cones near the Y-Junction core along the direction of glide motion. We systematically search for bond flips (*i.e.,* any change in nearest neighbor assignments as in Fig. 2.5C) between day 0 and day 2-4 for any bonds that could be flipped in glide motion (see Fig. 2.4C). Which UV cone bonds lie along the glide line is **always** unambiguous based on the triangulation. We never observe glide motion by more than one unit, as illustrated in Figs. 2.4C, 2.5A. We show an experimental example of glide motion by one unit in Fig. 2.5C (see Table A.2).

Statistical significance of growing grain boundaries in live fish

In Figure A.6, we show examples of images in which we can identify newly incorporated Y-Junctions lining up into grain boundaries. These are images of UV cone nuclei near the retinal margin (*i.e.*, where the layer grows by addition of post-mitotic cells). These images are oriented such that the margin is parallel to the y-axis. Because our field of view in these images is limited (*i.e.*, approximately forty rows of UV cones and forty columns of UV cones), it is difficult to apply our grain boundary measure that we use for flat-mounted retinae and simulations (see Detection of Grain Boundaries in Methods).

To identify grain boundaries which are already visible immediately after photoconversion, we trace rows of UV cones at the retinal margin. If immediately after photoconversion the row direction rotates about a group of defects by ten degrees or more at the margin, we call the group of Y-Junctions in-between the rotated rows a grain boundary. As a justification for this use of row

rotation to identify grain boundaries, see Figs. 2.3C-D, 2.5D, A.6. Based on this criterion, out of the eighteen samples, twelve samples have grain boundaries near the retinal margin at the time of photoconversion. Since some samples have two grain boundaries, in total we observe fifteen grain boundaries (Fig. 2.5E).

All subsequent analysis is based on the later image (*i.e.,* two, three, or four days later). We trace rows in the later image. We identify newly inserted rows (*i.e.,* newly incorporated Y-Junctions) in the later image, and we again identify the old defects within each grain boundary (*i.e.,* those not newly incorporated). We calculate a one-dimensional coordinate for the location of each grain boundary in the later image. This one-dimensional coordinate is the average of y-coordinates (*i.e.*, axis approximately parallel to the margin in the image) of all defects (*i.e.,* not newly incorporated) within each grain boundary. We are interested in how close, along the y-direction, newly incorporated Y-Junctions are to the nearest grain boundary in the image.

Suppose there is only one grain boundary in the image which is identifiable at the time of photoconversion and later imaging. Suppose this grain boundary is located at coordinate y_{gb}. The image spans from $y = 0$ to $y = y_{max}$. For each new Y-Junction, we generate one hundred thousand random Y-Junction positions, uniformly distributed from $y = 0$ to $y = y_{max}$ (rand; MATLAB 2016B, MathWorks). We calculate the distance between each of these one hundred thousand random Y-Junction positions and the grain boundary (at y_{gb}). We call the vector of distances between each random Y-Junction position and the grain boundary $\overrightarrow{\delta_{rand}}$. We also store the actual distance, which we call δ_{actual}, between each observed newly incorporated Y-Junction position in the image and the nearest grain boundary in the image.

Suppose there are two grain boundaries in the image which are identifiable at the time of photoconversion and later imaging. Suppose their coordinates are $y_{gb,1}$ and $y_{gb,2}$. The image spans from $y = 0$ to $y = y_{max}$. For each new Y-Junction, we generate one hundred thousand random Y-Junction positions, uniformly distributed from $y = 0$ to $y = y_{max}$ (rand; MATLAB 2016B, MathWorks). We calculate the distance between each of these one hundred thousand random Y-Junction positions and the nearest grain boundary (at either $y_{gb,1}$ or $y_{gb,2}$). We call the vector of distances between each random Y-Junction position and the nearest grain boundary $\overrightarrow{\delta_{rand}}$. We also store the actual distance, δ_{actual}, between each newly incorporated Y-Junction position and its nearest grain boundary.

Based on the procedure outlined above, for each new Y-Junction, we have a vector of length one hundred thousand and a scalar, $\overrightarrow{\delta_{rand}}$ and δ_{actual} (see Table A.3). If after random incorporation with respect to the grain boundaries in the image, a newly incorporated Y-Junction moves at a speed of one row per two days closer to the nearest grain boundary (with spacing between rows approximately equal to six microns as shown in Fig. A.2), the distribution of distances with respect to the nearest grain boundary becomes $\max\left(\overrightarrow{\delta_{rand}} - 3\frac{\mu m}{day}\Delta t * \vec{1}, \vec{0}\right)$, where Δt is the time between photoconversion and later imaging (*i.e.,* two, three, or four days).

We have a total of thirty-seven new Y-Junctions across the twelve samples with grain boundary at the retinal margin. We would like to compare the thirty-seven scalar values of δ_{actual} to a concatenated vector of $\max\left(\overrightarrow{\delta_{rand}} - 3\frac{\mu m}{day}\Delta t * \vec{1}, \vec{0}\right)$ across all thirty-seven defects. This concatenated vector is of length three million seven hundred thousand. We test whether the distribution of δ_{actual} has the same median as the concatenated vector of $\max\left(\overrightarrow{\delta_{rand}} - 3\frac{\mu m}{day}\Delta t * \vec{1}, \vec{0}\right)$ across all thirty-seven defects. We assign a p-value to that comparison via Mann-Whitney U-test (ranksum; MATLAB 2016B Statistics and Machine Learning Toolbox, MathWorks).

Numerical solutions of lateral inhibition on disordered cell packing

Starting with a Voronoi tessellation of uniformly (randomly) distributed points, we generated large, disordered, periodic cell packings (*e.g.*, 20,000 total cells in Fig. A.10) via vertex model simulations with equal tensions on all edges as described in [111, 112]. We model dynamics of individual cell fates on the static cell packing according to the model described in [57], but do not include noise in the dynamics ($D = 0$). Since we changed some aspects of the model, including the external signaling gradient and the noise in fate, we describe the model in [57] below for the sake of clarity. The fate of cell i, u_i, evolves as:

$$\tau \frac{du_i}{dt} = f(u_i, s_i) - u_i$$

where s_i is the signal each cell receives from other cells as well as from any external gradients. We interpret the $u = 1$ fate as the UV cone spectral subtype and the $u = 0$ fate to be other spectral subtypes. Also, $f(u, s)$ is sigmoidal: $f(u, s) \equiv f(u - s) = \sigma[2(u - s)] = \frac{\left(1+\tanh\left(2(2(u-s))\right)\right)}{2}$.

The signal that cell i receives, s_i, includes an external time-dependent signal $s_0(x,t)$ as well as signals from neighboring cells in a distance-dependent manner.

$$s_i = s_0(x_i,t) + \sum_j c_{ij} D^*(u_j)$$

The external signal provided to the cells has the following form: $s_0(x,t) = S_0\sigma\left(\frac{x-vt}{\epsilon\sqrt{A_0}}\right) \equiv S_0\left(\frac{1+\tanh\left(\frac{2(x-vt)}{\epsilon\sqrt{A_0}}\right)}{2}\right)$ where $S_0 = 1$ and $v = \frac{l}{4\tau}$ and $\epsilon = \frac{1}{50}$. τ is the timescale for cell fate dynamics, and l is the characteristic cell-cell signaling range. The distance-dependent coupling constant c_{ij} between cell i and cell j is of the form: $c_{ij} = e^{-{d_{ij}}^2/(2l^2)}$, where d_{ij} is the distance between the centroids of cell i and cell j. No cell signals to itself directly: $c_{ii} = 0$.

A cell of fate u_j produces signal $D^*(u_j) = a(u_j)D(u_j)$. The ligand level of cell j, $D(u_j)$, is directly proportional to the fate u_j. The ligand activity of cell j, called $a(u_j)$, is of the form: $a(u_j) = a_0 + \frac{3u^3}{2+u^2}a_1$. We use the same ligand activity levels for both the $u = 0$ fate and the $u = 1$ fate as in [57] ($a_0 = 0.05$; $a_1 = 1 - a_0$).

To explore the effects of cell-cell signaling range on the final fate pattern, we systemically change the signaling range l from $l = 3.0\sqrt{A_0}$ to $l = 1.75\sqrt{A_0}$ to $l = \sqrt{A_0}$, where A_0 is the mean cell area. All cells are initially in the $u = 0$ state. The sigmoidal signaling front, sharper than the characteristic cell size, starts at left side of the packing ($x = 0$ at $t = 0$) and moves to the right. In the wake of the front, individual cells differentiate into the $u = 1$ fate, inhibiting their neighbors from adopting the $u = 1$ fate within the specified cell-cell signaling range. We solve the differential equations for cell fates using ode45 (MATLAB 2016B, MathWorks).

Numerical solutions of anisotropic phase-field crystal model on cone

The free energy F for an anisotropic phase field ψ [87, 94, 95]:

$F = \int_S (\psi[r + (1+\nabla_s^2)^2]\psi + \frac{\psi^4}{4})d\vec{r}$

$\nabla_s^2 = b^2\frac{\partial^2}{\partial x^2} + \frac{1}{b^2}\frac{\partial^2}{\partial y^2}$; $b > 1$.

(stretched along the x direction)

$\nabla_s^2 = b^2\frac{1}{r}\frac{\partial}{\partial r}\left(r\frac{\partial}{\partial r}\right) + \frac{1}{b^2}\frac{1}{r^2}\frac{\partial^2}{\partial\theta^2}$; $b > 1$.

(stretched along the r direction in polar coordinates)

The particle density modulation field ψ is evolved to minimize the free energy F while conserving the mean of the particle density modulation field ($\psi_0 = \int_S \psi d\vec{r} \; / \int_S \; d\vec{r}$):

$$\frac{\partial \psi}{\partial t} = \nabla^2([r + (1 + \nabla_s^2)^2]\psi + \psi^3)$$

For solving this equation on the cone, we first map the cone to a flat plane, which does not generate distortions because the cone is isometric to the plane. We, then, use the Laplacian for polar coordinates, respecting the periodic boundary condition of the cone. We set up in the problem in terms of the variables u, v, ψ as defined in [113]. For computational efficiency, we take the Fourier transform along any direction which is periodic (e.g., along the θ direction on the cone). We use first-order implicit-explicit methods, as in [114], treating the non-linear term in ψ explicitly. We implement all derivatives by finite differences [115]. We use no-flux boundary conditions at each non-periodic boundary.

We evolve the system with a fixed step size in time ($\Delta t = 0.075$). The computational grid is such that there are approximately 25 grid points per lattice spacing along the circumferential direction in the initial row, and approximately 10 grid points per lattice spacing along the radial direction.

We systematically vary the parameters of the phase field crystal model as done in [87]; please note that stretching the crystal does not change the phase diagram as discussed in [90]. In short, we take a 1D cut of the phase diagram, setting $\psi_0 = -\frac{\sqrt{-r}}{2}$ as we vary the undercooling parameter r. For this cut, we also vary the strength of the noise in the initial conditions These three parameters are the parameters on which we do not have any quantitative handle (relative to experiments); therefore, we perform this robustness analysis on these three parameters. The results of this analysis are shown in Fig. A.8.

Geometry for cone mosaic growth

The retina is approximately hemispheric. A hemisphere might, thus, seem like the most obvious choice of geometry in which to test cone mosaic growth. It is important to note, however, that the retina is not a hemisphere of a fixed radius during development. Its radius increases as new retinal cells are incorporated. As the hemisphere dilates, the existing cone photoreceptor layer must be deformed. The exact way in which the existing pattern deforms, and how that affects subsequent

cone mosaic formation, is beyond the scope of this paper. Our aim is to choose a minimal geometry which allows us to test the phase-field crystal model's ability to form grain boundaries.

We choose a geometry in which we can easily tune the defect density. We choose a cone frustum, which is constructed by slicing off the top of a cone with a plane that is parallel to its base. By changing the level at which we slice the cone, we tune the number of UV cones in the initial column. We choose the top level such that there are approximately two hundred initial rows, which is consistent with the number of initial rows identified in flat-mounted retinae. By changing the opening angle of the cone, we can tune the number of Y-Junctions required to maintain constant cell-cell spacing per added column. We choose an opening angle such that two row insertions are required per added column, to maintain approximately constant cell spacing. The number of Y-Junctions necessary to maintain constant cell-cell spacing is comparable to the number of Y-Junctions observed in the retinae (Figs. 2.3E, A.4).

Initial conditions for cone mosaic growth

At the very top level of the cone frustum, we lay down one column of cones (see one-mode approximation in [87]). We add a white-noise mask to this initial column of cones. Because we do not have any quantitative handle on the noise in cell positions at the onset of patterning in the zebrafish retina, we vary the noise strength, exploring its effect on the subsequent pattern of defects (Fig. A.8).

Chapter 3 Apical Stress Fibers Enable a Scaling Between Cell Mechanical Response and Area in Epithelial Tissue

Acknowledgements: This manuscript results from a collaboration with Yohanns Bellaïche's lab. Jesús Lopez-Gay performed the vast majority of the experimental work. Many others, including Florencia di Pietro, Floris Bosveld, Olga Markova, performed experiments and analyzed data. Boris Guirao analyzed some experimental data. Meryl Spencer developed the vertex model for force balance in a tissue with apical stress fibers. I developed the phenomenological model of aSF nucleation and breakage and wrote the majority of the supplemental information for modelling.

Abstract

The scaling of the properties of biological systems with their size is central to organismal development and physiology. However, such scaling remains a poorly explored question in cell mechanics and mechanosensing. Here, by examining how a *Drosophila* epithelium responds to morphogenetic forces, we identified a class of apical stress fibers (aSFs) anchored to the adherens junctions. We found that aSF number scales with cell apical area and that this scaling prevents the elongation of larger cells under morphogenetic stress. Furthermore, aSFs promote the clustering of Hippo pathway components, thereby scaling Hippo/YAP activity with apical area to regulate epithelial proliferation. The scaling is mainly driven by tricellular junction number and distribution, which mediate an increase in aSF nucleation rate and lifetime in larger cells. Tissue development entails changes in epithelial cell area driven by mechanical forces; our work highlights how, in turn, cell mechanosensitivity scales with cell area during tissue dynamics.

Main text

Within epithelial tissues, cells generate mechanical forces, which are sensed by neighboring cells [13]. Numerous studies have explored the critical roles of cell mechanosensitivity in epithelial cell proliferation and the self-organizing properties of cells and tissues [13]. In epithelia, mechanical forces are sensed at the level of the adherens junctions (AJ),

in particular by the Hippo/Yap pathway [13, 116]. Cell geometry, including apical cell area, varies considerably among cells within a tissue. Yet, little attention has been given to whether and how epithelial cells adapt their mechanical response to their geometry or whether such adaptation is important for tissue dynamics and morphogenesis.

Figure 3.1 **Formation of aSFs in response to lateral tissue mechanical stress. A)** Pupal dorsal thorax labeled by E-Cadherin:3xGFP (E-Cad:3xGFP) imaged at 26 hAPF by multi-position confocal microscopy. Red line: midline. Dashed box: Posterior and central region where aSFs form and where proteins distributions and quantifications are reported at 26 hAPF, unless otherwise stated. Inset in A shows the cell resolution capacity of multi-position confocal microscopy. **B)** Medial-lateral (m-l) tissue elongation (mean ± SEM, blue) and inferred junctional mechanical stress anisotropy (mean ± SEM, red; positive values indicate tensile stress is higher along the m l axis) in the region boxed in A. N: number of animals at each timepoint. **C)** E-Cad:3xmKate2 and MyoII:3xGFP distributions within the region boxed in A at 18 hAPF (left) and 26 hAPF (right). Arrowheads: aSFs. **D)** Number of aSFs per cell (blue, mean ± SEM) and tissue stress anisotropy estimated by laser ablation (red, mean ± SEM) between 14 and 28 hAPF. n and N: minimum numbers of cells and ablations used at each time-point, respectively. **E)** Rose plot of the orientation of aSFs at 26 hAPF. n: aSF number. **F)** E-Cad:3xmKate2 and MyoII:3xGFP distributions before ablation (left) as well as at 1.3s (middle) and 9.2s (right) after aSF ablation. Dashed box: ablated region. Time at ablation is set to 0. Arrowheads: positions of the AJs prior to and after aSF ablation. **G, G')** E-Cad:3xmKate2 and MyoII:3xGFP distributions at level of the AJ (G) and along the cell apical-basal (a-b) axis (G'). Arrowheads in G indicate position of a-b section shown in G'. Conversely, the arrowheads in G' indicate the a-b position of the section shown in G. **H-J)** Distributions of Zyx:ChFP and MyoII:3xGFP (H), Ena:GFP and MyoII:3xmKate2 (I) and Actn:GFP and MyoII:3xmKate2 (J) at 26 hAPF. Arrowheads indicate some aSFs. **K, K')** E-Cad:3xmKate2 and MyoII:3xGFP distributions in the posterior central region in the *mirr-G4>LifeAct:GFP* (control, K) and *mirr-G4>zip^{DN}:YFP* (K') animals. *mirr*-G4 specifically drives expression in the lateral tissue domain. See also Fig. B.1M-M'. Arrowheads: aSFs. **L)** Graph of the m-l tissue recoil velocity upon a-p ablation (mean ± SEM,) in control *mirr-G4>LifeAct:GFP* versus *mirr-G4>zip^{DN}:YFP* tissues. N: number of ablations; p-value<10^{-3}. **M)** Graph of the number of aSFs per cell (mean ± SEM) in control *mirr-G4>LifeAct:GFP* versus *mirr-G4>zip^{DN}:YFP* tissues. n: number of cells; p-value<10^{-5}. **N)** Rose plot of the aSF orientation in control *mirr-G4>LifeAct:GFP* and *mirr-G4>zip^{DN}:YFP* tissues. n: number of aSFs; p-value<10^{-5}. **O, O')** MyoII:3xGFP distributions in uncompressed tissue (O) and in tissue compressed along the m-l axis (O'). See also, Fig. B.1N-N''. Arrowheads: aSFs. **P)** Graph of aSF number per cell in uncompressed tissue versus compressed tissue. n: number of aSFs; p-value<10^{-5}. **Q)** Rose plot of the aSF orientation in uncompressed tissue versus compressed tissue. n: number of aSFs; p-value<10^{-5}. Scale bars: 50 µm (A), 5 µm (C, K and O) and 2 µm (F, K, G and H and inset in A). Statistical tests: Kruskal-Wallis tests (L, M, and P). Levene tests for equality of variances (N and Q). ns: not significant. Statistically significant differences (p-value<0.05) are indicated by one asterisk.

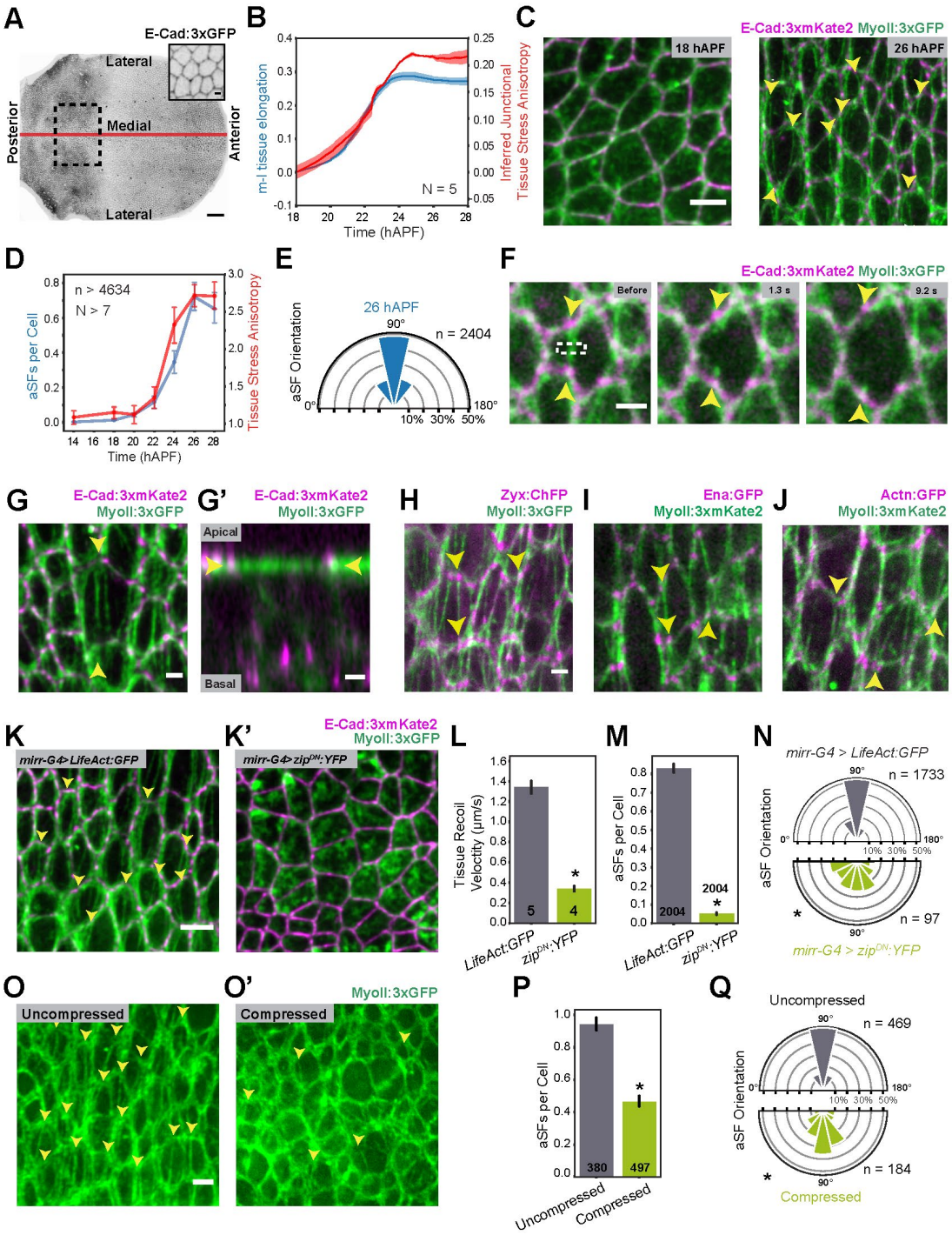

To investigate the possible interplay between cell geometry and cell mechanical response, we first aimed to better understand how epithelial tissues respond to endogenous morphogenetic forces. The *Drosophila* pupal dorsal thorax monolayered epithelium (notum) is a model to study cytoskeleton dynamics, mitosis, morphogenesis and mechanics [117-122]. In the posterior and central region of the dorsal thorax (dotted box in Fig. 3.1A, and Fig. B.1A, A'), the tissue

proliferates and elongates as tensile mechanical stress increases along the medial-lateral (m-l) axis and becomes highly anisotropic between 18 and 26 hours After Pupae Formation (hAPF, Fig. 3.1A,B and D, Fig. B.1B [117, 123]). In this region and prior to 18 hAPF, Myosin II (MyoII) is localized at the junctional cortex and in an apical medial pool (Fig. 3.1C, left). Between 18 and 26 hAPF, the MyoII apical pool changes its organization as MyoII fibers form at the cell apex (Fig. 3.1C, D). These fibers are oriented along the m-l axis and are under tensile stress as shown by laser ablation (Fig. 3.1E, F). The tips of the fibers are positioned at the level of the adherens junctions (AJs) (Fig. 3.1G, G' and Fig. B.1C-D''). Known components of stress fibers (SFs) including Zyxin (Zyx), Enable (Ena) and αActinin (Actn) are distributed along or at the tips of the MyoII fibers (Fig. 3.1H-J, Fig. B.1E-L and Table 3.1). Since we found that MyoII fibers are apical, connected to apical AJs, and tensile, we hereafter refer to them as apical stress fibers (aSFs). Myosin-rich fibers anchored at the level of AJs have been observed in other tissues and cells types [124-127]. Because the number of aSFs increases as mechanical stress increases in magnitude and anisotropy (Fig. 3.1D), we tested whether aSF formation is a response to mechanical stress. We thus reduced mechanical stress in the central domain of the tissue by two distinct approaches: by expressing a dominant negative form of MyoII heavy chain (zip^{DN} [128]) specifically in the lateral tissue region (Fig. 3.1K-L and Fig. B.1M, M') and by directly applying a 20% compressive mechanical strain in the plane of the tissue on the whole living animal (Fig. 3.1O, O' and Fig. B.1N-N''). Both approaches led to a reduction in the number of aSFs and a disturbance of the m-l orientation of the remaining ones at 26 hAPF (Fig. 3.1M, N and B.1P, Q). We conclude that an increase in mechanical stress promotes the formation of tensile aSFs aligned with the main tissue stress axis.

Figure 3.2 **Scaling between cell apical area and aSF number per cell.** Unless otherwise stated, protein distributions and quantifications are reported for the region boxed in Fig. 3.1A at 26 hAPF. **A)** Distribution of MyoII:3xGFP labelling aSFs in $actn^{RNAi}$ cells (outlined by orange dashed line) marked by Caax:tBFP accumulation (not shown) and in surrounding control cells. Arrowheads: some aSFs. **B)** Graph of aSF number per cell (mean ± SEM) in w^{RNAi} control and $actn^{RNAi}$ cells at 26 hAPF. n: number of cells; p-value<10^{-5}. **C)** Graph of m-l cell elongation (mean ± SEM) of w^{RNAi} control and $actn^{RNAi}$ clones at 26 hAPF. n: number of cells; p-value<10^{-5}. M-l cell elongation is defined as the ratio between the cell inertia matrix m-l axis component and a-p axis component. **D**) Graph of m-l tissue elongation (mean ± SEM) in control versus $actn^{RNAi}$ clones in the central posterior region of the tissue between 19 and 28 hAPF. N: number of clones; p-value<10^{-5}. **E)** Graph of m-l tissue recoil velocities upon a-p laser ablation (µm/s, mean ± SEM) in *pnr-G4*>w^{dsRNA} (control) versus *pnr-G4*>$actn^{dsRNA}$. *pnr-G4* specifically drives expression in the medial domain of the tissue. n: number of ablations. **F)** AJ (orange) and aSF (blue) ablation and recoil velocity measurement schematic. Upon AJ or aSF laser ablation, the l_0 and l_t distances (corresponding to distances at t=0 and t=1.3s) were used to calculate AJ or aSF recoil velocity, respectively. **G)** Graph of recoil velocity (µm/s, orange, mean ± SEM,) of ablated AJ without prior aSF ablation and 30s after aSF ablation was performed; (*n*: number of ablations; p-value<0.05); graph of recoil velocity (µm/s, blue, mean ± SEM) upon aSF ablation without prior junction ablation and 30s after prior ablation of a neighbouring AJ (*n*: number of ablations; p-value<10^{-5}). Only aSFs and AJs oriented between 72° and 118° relative to the a-p axis were used. See Fig. B.2E for junction and aSF velocity recoil after ablation as a function of their orientation relative to a-p axis. n: number of ablations. **H**) Graph of junction recoil velocity (µm/s, mean ± SEM) upon AJ ablation in w^{RNAi} control and $actn^{RNAi}$ cells at 18 hAPF (ns) and at 26 hAPF (p-value<10^{-4}). n: number of ablations. **I)** Schematic of the vertex model of a regular cell packing with aSFs under uniaxial stress (see Appendix B and Fig. B.3A-C). **J)** Cell elongation and tension distribution (γ, color scale) in vertex model without (top) or with (bottom) aSFs at fixed cell size and cell orientation and at fixed uniaxial tissue stress. Grey cells illustrate differential cell elongation, whereas colored cells illustrate the magnitude of tension at AJ and individual aSFs in high stress anisotropy case (at fixed tension per aSF). **K)** Number of aSFs per cell (at fixed tension per aSF) required for cells to remain regular under uniaxial stress as a function of cell apical area. See Fig. B.3I,J for vertex model parameter values. **L**) Graph of aSF number per cell (mean ± SEM) as a function of apical cell size in w^{RNAi} control and $actn^{RNAi}$ cells at 26 hAPF. n: number of cells. p-value< 10^{-5}. **M**) Graph of changes in cell elongation (percentage, mean ± SEM) without ablation, upon mock aSF ablation (i.e. ablation next to an aSF), and upon ablation of increasing number of aSFs in cells. p-value<10^{-4}. Cell elongation variations were determined for an interval of 9.2s in absence of ablation or between t=0s (time of ablation) and t=9.2s after ablation. n: number of cells without ablation, with mock ablations or with ablations on aSFs. **N)** Graphs of cell apical area (left, mean ± SEM) and aSF number per cell (right, mean ± SEM) 1h before and 1h after telophase in w^{RNAi} control cells (p-values<10^{-5} for area and p-values<10^{-5} for aSF number) and $auroraB^{RNAi}$ ($aurB^{RNAi}$) cells, ns for area and number of aSFs). n: number of cells. **O)** Graphs of cell apical area (horizontal axis, mean ± SEM) versus aSF number per cell (vertical axis, mean ± SEM) in control w^{RNAi}, $survivin^{RNAi}$ (svn^{RNAi}), $aurB^{RNAi}$, *tribbles overpression* ($trbl^{up}$) and $cdc2^{RNAi}$ cells. Number of cells w^{RNAi} (n: 2903), svn^{RNAi} (n: 872), $aurB^{RNAi}$ (n: 402) $trbl^{UP}$ (n: 356) and $cdc2^{RNAi}$ (n: 227). **P**) Graph of difference in cell elongation (mean ± SEM) upon ablation of all aSFs in a given cell as a function of apical area. Differences were measured 9.2s after ablation. n: number of cells. p-value<0.05 (25-35µm^2) and p-value<10^{-3} (+35µm^2) for differences with the first bin. **Q**) Graph of difference in m-l cell elongation between $actn^{RNAi}$ cells and w^{RNAi} control cells (mean ± SEM) as a function of apical cell size at 18, 20, 22, 24 and 26 hAPF. n: minimum number of cells used at each hAPF and condition. p-value<10^{-4}. Scale bars: 5µm (A). Statistical tests: Kruskal-Wallis tests (B, C, E, G, H and N), Kruskal-Wallis tests with Conover post hoc (M and P), Ancova tests (L and P) and mixed-ANOVA (D). ns: not significant. Statistically significant differences (p-value<0.05) are indicated by one asterisk. In the case of multiple pairwise comparisons, only maximum p- values (of the set of asterisked comparisons) are reported.

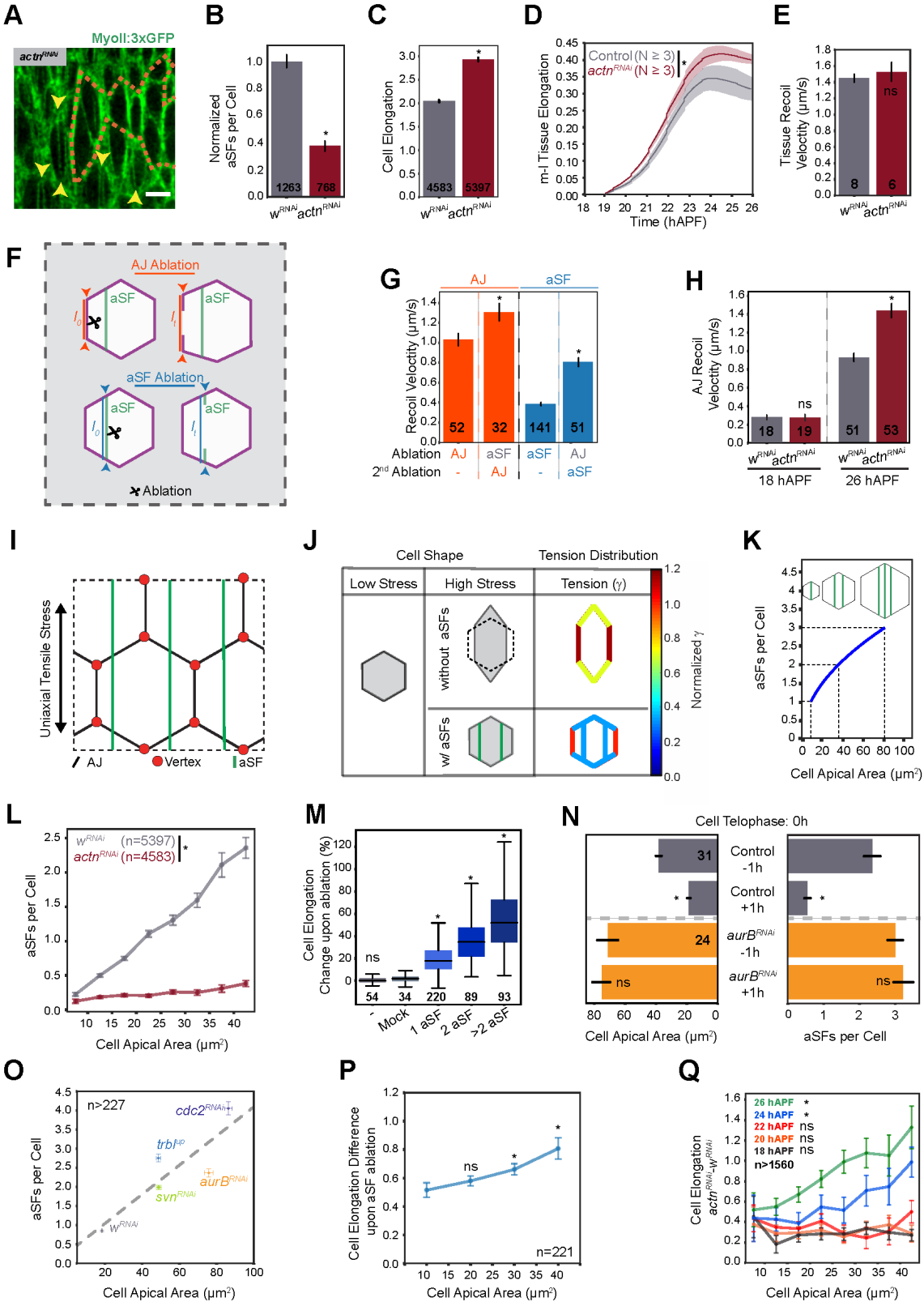
A
MyoII:3xGFP
actn^RNAi
B
Normalized aSFs per Cell
1263
768
w^RNAi
actn^RNAi
C
Cell Elongation
4583
5397
D
Control (N ≥ 3)
actn^RNAi (N ≥ 3)
m-I Tissue Elongation
Time (hAPF)
E
Tissue Recoil Velocity (μm/s)
ns
8
6
F
AJ Ablation
aSF Ablation
aSF
Ablation
G
AJ
aSF
Recoil Velocity (μm/s)
52
32
141
51
Ablation
2nd Ablation
H
AJ Recoil Velocity (μm/s)
ns
18
19
51
53
18 hAPF
26 hAPF
I
Uniaxial Tensile Stress
AJ
Vertex
aSF
J
Cell Shape
Tension Distribution
Low Stress
High Stress
Tension (γ)
without aSFs
w/ aSFs
Normalized γ
K
aSFs per Cell
Cell Apical Area (μm²)
L
w^RNAi (n=5397)
actn^RNAi (n=4583)
aSFs per Cell
Cell Apical Area (μm²)
M
Cell Elongation Change upon ablation (%)
ns
54
34
220
89
93
Mock
1 aSF
2 aSF
>2 aSF
N
Cell Telophase: 0h
31
Control -1h
Control +1h
24
aurB^RNAi -1h
aurB^RNAi +1h
ns
Cell Apical Area (μm²)
aSFs per Cell
O
n>227
cdc2^RNAi
trbl^ND
aurB^RNAi
svn^RNAi
w^RNAi
aSFs per Cell
Cell Apical Area (μm²)
P
Cell Elongation Difference upon aSF ablation
ns
n=221
Cell Apical Area (μm²)
Q
26 hAPF *
24 hAPF *
22 hAPF ns
20 hAPF ns
18 hAPF ns
n>1560
Cell Elongation actn^RNAi-w^RNAi
Cell Apical Area (μm²)

The mechanical contribution of cell-cell junctions and actomyosin cortex to tissue dynamics has been extensively studied [129-131]. However, the role of SFs is far less understood *in vivo,* and the respective contributions of cell-cell junctions and SFs in epithelial tissue mechanics are unexplored. We therefore investigated the roles of aSFs in cell and tissue morphogenesis by both experimental and modeling approaches. Since aSFs are under tension (Fig. 3.1F, Fig. B.2A), we tested whether aSFs regulate cell and tissue elongation. Towards this goal, we screened for loss of function mutants affecting aSF number at 26 hAPF (Table 3.1). Abrogating Actn function (using either RNAi or a CRISPR/Cas9 generated null allele) in the central posterior region of the tissue leads to a drastic decrease in aSF number per cell as well as an increase in cell and tissue elongation in the direction of mechanical stress (Fig. 3.2A-D and Fig. B.2B-E''). This increase in elongation occurred without a major change in global tissue mechanical stress as estimated by tissue-scale laser ablation (Fig. 3.2E); this indicates that aSFs prevent cell and tissue elongation in response to mechanical stress generated during tissue morphogenesis. To explore the respective mechanical roles of aSFs and AJs, we then used laser ablation to estimate the aSF and the AJ tensions (Fig. 3.2F). The recoil velocity upon aSF ablation was around one-third of that observed for AJs aligned with the m-l axis, suggesting that aSFs have lower tension than AJs aligned with the m-l axis (Fig. 3.2G, Fig. B.2A). By sequentially ablating an aSF and then an AJ for the same cell, we found that aSFs diminish the tension exerted on the AJ (Fig. 3.2G). Consistently, AJ recoil velocity upon laser ablation was increased in $actn^{RNAi}$ cells at 26 hAPF, but not at 18 hAPF when aSFs are absent (Fig. 3.2H). To further understand aSFs' contribution to cell and tissue morphogenesis, we considered a simple vertex model of a regular cell packing in mechanical equilibrium with or without aSFs (Fig. 3.2I, J, Appendix B, and Fig. B.3). As observed experimentally, the model shows that aSFs oriented along the main stress axis are able to limit cell and tissue elongation (Fig. 3.2J and Fig. B.3). Furthermore, mirroring the observation in $actn^{RNAi}$ cells, the model shows that at high stress anisotropies, aSFs are more efficient at limiting cell elongation than simply upregulating tension along AJs (Fig. 3.2J and Fig. B.3). The model moreover predicts that cells with a larger apical area require more aSFs (or more tension per aSF) to maintain the same aspect ratio and limit cell elongation (Fig. 3.2K, Appendix B and Fig. B.3).

Based on our model predictions, we investigated the relationship between individual aSF tension, aSF number per cell and cell apical area at 26 hAPF. First, laser ablation suggests that the tension supported by one aSF is independent of cell apical area (Fig. B.2F). Second, the number

of aSFs per cell scales with the cell apical area, and more weakly with cell volume (Fig. 3.2L and Fig. B.2G,H). Finally, when we ablated more than one aSF within a given cell, the cell elongated more with each additional aSF ablation (Fig. 3.2M). We then investigated whether a change in cell apical area leads to a change in the number of aSFs. We first analyzed whether the reduction in apical size upon cytokinesis modulates aSF number. Upon cytokinesis we observed a reduction in the number of aSFs per cell (Fig. 3.2N). Next, we prevented cell division or cytokinesis to increase cell area and observed an increase in aSF number per cell (Fig. 3.2N,O). Together, these experimental results validate that the number of aSFs increases with the cell apical area. We then tested whether, as predicted by our physical model, the scaling between cell area and aSF number is important for limiting cell elongation. We found that the cell elongation is independent of cell area in control cells (Fig. B.2I) and that aSF ablation leads to a cell elongation that increases with cell area (Fig. 3.2P). Accordingly, the cell elongation of $actn^{RNAi}$ cells increases with cell apical area as the stress anisotropy increases (Fig. 3.2Q and Fig. B.2I). Combining our modeling and experimental data, we propose that a scaling between aSF number and cell area helps to maintain cell elongation independent of cell area and thereby reduces tissue elongation under high anisotropic stress.

Figure 3.3 **Hippo component clustering and aSF formation.** Unless otherwise stated, protein distributions and quantifications are reported for region boxed in Fig. 3.1A at 26 hAPF. **A-B)** Distributions of Jub:GFP (A), Wts:GFP (B) and MyoII:3xmKate2 (A,B) at 26 hAPF. Arrowheads: aSF tips. **C)** Graph of the ratios of Jub:GFP and Wts:GFP in clusters versus along AJ ($ratio^{in/out}$ of cluster, mean ± SEM) at 18 hAPF (low stress) and 26hAPF (high stress). n: number of cells; p-values$<10^{-5}$ for comparison between 18 hAPF and 26 hAPF for both Jub:GFP and Wts:GFP. See Fig. B.4B-B''' for cluster identification and quantifications. **D-D')** Distributions of Jub:mKate2 and Wts:GFP at 18 hAPF (low stress, D) and at 26 hAPF (high stress, D'). Arrowheads: Jub:mKate2 and Wts:GFP co-clusters. **E**) Graph of colocalization (Pearson Correlation Coefficient, mean ± SEM) between Jub:mKate2 and Jub:GFP or between Jub:mKate2 and Wts:GFP at 18 hAPF (low stress) and 26 hAPF (high stress). Pearson coefficients were normalized by the mean of the Pearson coefficient between Jub:GFP and Jub:mKate2 at 18 hAPF. n: number of cells; Jub:mKate2 and Jub:GFP colocalization: ns; Jub:mKate2 and Wts:GFP colocalization: p-value$<10^{-5}$. **F-F')** Distributions of Jub:mKate2 (green, F and fire, F') and MyoII:3xGFP (F) during aSF formation. t=0 corresponds to aSF nucleation. Arrowheads: yellow aSF (F) and light green Jub:mKate2 cluster (F'). **G-G')** Distribution of Jub:GFP before and after (t=90s) ablation of the aSF labelled by MyoII:3xmKate2 (G). Time was set to 0 just before ablation (ablation at t~0.01s). Arrowheads: cluster prior to and after ablation. Graph of Jub:GFP cluster intensities (mean ± SEM) in mock ablated aSF (control) and upon aSF ablation (G'). n: number of ablations; p-value$<10^{-3}$ after timepoint 30s. **H-H')** Wts:CitFP (H) before and after (t=210s) ablation of aSF labelled by MyoII:3xmKate2. Time was set to 0 just before ablation (ablation at t~0.01s). Arrowheads: cluster prior to and after ablation. Graph of Wts:CitFP cluster intensities (mean ± SEM) in mock ablated aSF (control) and upon aSF ablation (H'). n: number of ablations, p-value$<10^{-2}$ after timepoint 120s. **I-J**) Distributions of Jub:GFP (I) and Wts:CitFP (J) in $actn^{RNAi}$ cells (marked by the expression of Caax:tBFP, not shown) outlined by orange dotted line and surrounding control cells. **K**) Graphs of the Jub:GFP and Wts:CitFP $ratio^{in/out}$ of clusters (mean ± SEM) in w^{RNAi} control and $actn^{RNAi}$ cells at 26 hAPF. n: number of cells; p-values$<10^{-5}$ for Jub:GFP and Wts:CiFP. **L**) Graph of normalized colocalization (Pearson Correlation Coefficient) of Jub:mKate2 and Wts:GFP (mean ± SEM) in w^{RNAi} control and in $actn^{RNAi}$ cells at 26h APF. n: number of cells; p-value$<10^{-4}$. **M)** Graph of *ban-nls:GFP* intensity (mean ± SEM) in w^{RNAi} control and $actn^{RNAi}$ cells at 18 hAPF and 26 hAPF. Average intensities were normalized by mean intensities of w^{RNAi} cells at 18hAPF. N: number of animals; 18 hAPF: ns; 26 hAPF: p-value$<10^{-3}$. **N)** Graph of the fraction of cells that divide (mean ± SEM) between 18 and 26 hAPF and between 26 hAPF and 34 hAPF in $pnr\text{-}G4>w^{dsRNA}$ (control) versus $pnr\text{-}G4>actn^{dsRNA}$ tissues; prior to 26 hAPF: ns; after 26 hAPF: p-value<0.05. N: number of animals. Scale bars: 2µm (A, D, F, G and H), 5µm (I-J) Statistical tests: Kruskal-Wallis test (C, E and K-M), Kruskal-Wallis tests with Conover post hoc (G', H') and One-tailed Wilcoxon signed rank test (N). ns: not significant. Statistically significant

differences (p-value<0.05) are indicated by one asterisk. In the case of multiple pairwise comparisons, only the maximum p-values (of the set of asterisked comparisons) are reported.

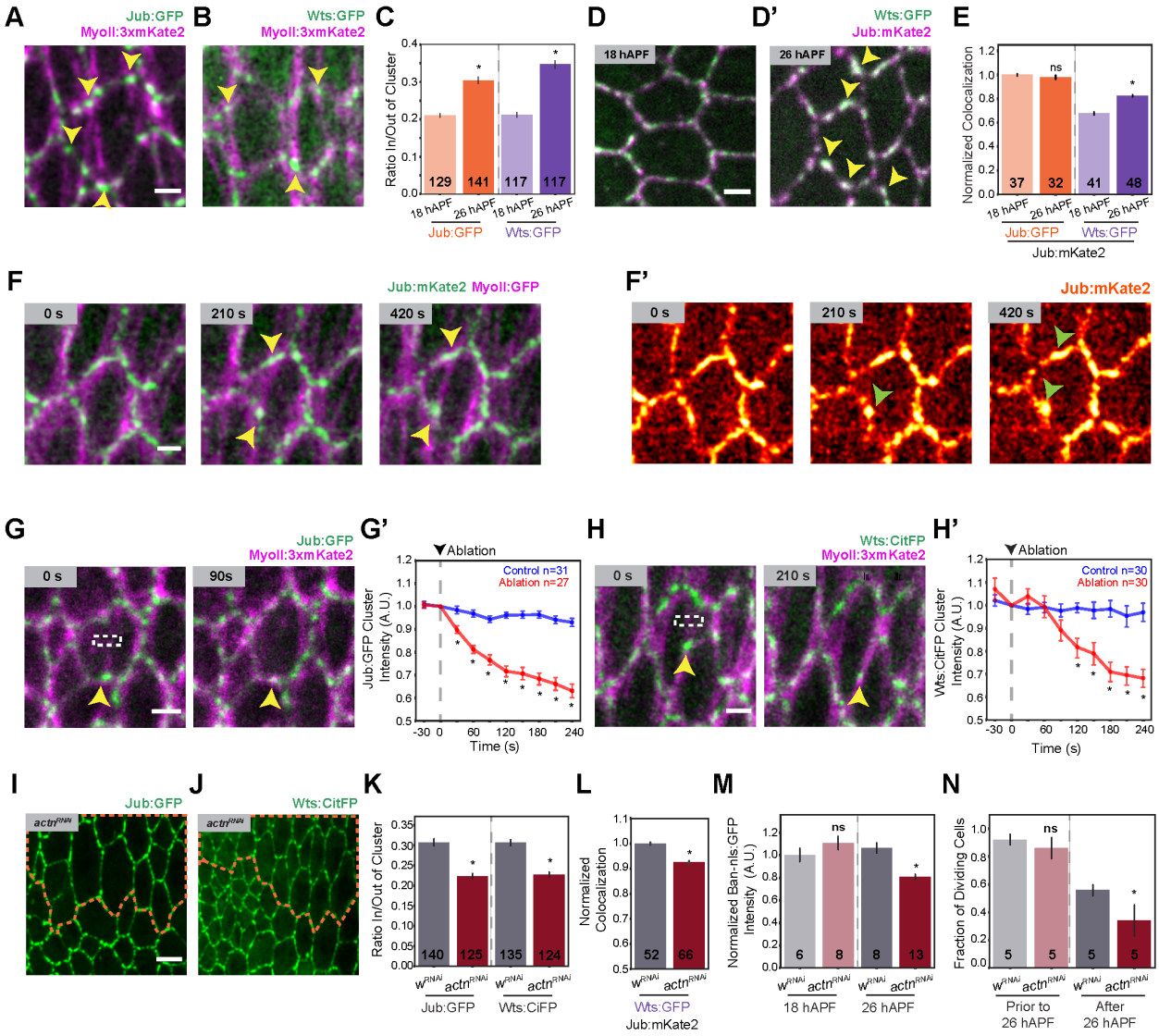

Before studying the origins of scaling between cell apical area and aSF number, we aimed to explore whether this scaling could also translate into a biochemical scaling under mechanical stress. In individual cells in culture, SFs regulate Yap/Taz (Yorkie, Yki in *Drosophila*) activity by directly deforming the nucleus [116, 132]. In this epithelial tissue, however, aSFs are located away from the nucleus (Fig. B.1C,C'). We therefore investigated alternative mechanisms through which aSFs might modulate Hippo/Yki activity in epithelial tissues. The LIM domain protein Ajuba (Jub) is a component of the Hippo/Yki pathway that binds to the Warts (Wts) kinase. Jub binding results in Wts inhibition and thus Yki activity upregulation [133, 134]. Previous findings indicate that an increase of MyoII contractility leads to the increased recruitment of Jub to the AJs and that this

recruitment promotes Hippo/Yki signaling [135-138]. In the dorsal thorax, we uncovered that at high mechanical stress (26 hAPF), Jub and Wts form clusters at the tips of the aSFs (Fig. 3.3A,B and Fig. B.4A). Furthermore, the quantitative analyses of the Jub and Wts distributions showed that the number of Jub and Wts clusters as well as the ratio of Jub and Wts intensity in clusters to that elsewhere along the AJ ($ratio^{in/out}$ of cluster) increases between low stress (18 hAPF) and high stress (26 hAPF) (Fig. 3.3C and Fig. B.4B-C). Accordingly, Jub and Wts colocalization increases under high mechanical stress (Fig. 3.3D-E). Thus, an increase in mechanical stress correlates with the formation of Jub and Wts co-clusters at the tips of the aSFs along the AJs. To determine whether Jub clustering modulates Hippo signaling, we used the Cry2Olig optogenetic clustering system [139] to induce Jub clustering independent of aSF formation. We found that the light-induced clustering of Jub is sufficient to co-cluster Wts and to upregulate Yki activity (Fig. B.4D-F). Next, we explored whether aSF formation and the associated tension modulate Jub and Wts clustering, Hippo/Yki activity, and cell proliferation. High-resolution time-lapse imaging showed that as an aSF forms or is displaced along the AJ, cortical Jub:mKate2 and Wts:CitFP flow and accumulate at the tip of the aSF (Fig. 3.3F, F', Fig. B.4G, G'). Conversely, upon ablation of a previously formed aSF, the Jub:GFP or Wts:CitFP clusters initially present at the tip of the aSF are strongly reduced (Fig. 3.3G-H'). While the loss of Actn function does not affect the total amount of Jub and Wts at the junction (Fig. B.4H, I), it decreases both the number of Jub and Wts clusters and their colocalization (Fig. 3.3I-L and Fig. B.4J). Last, we found that the loss of Actn function leads to a decrease of *ban-nls:GFP* Yki transcriptional reporter expression [140] and cell proliferation, specifically under high stress (Fig. 3.3M,N and Fig. B.4K,L). We conclude that aSFs promote the co-clustering of Jub and Wts at their tips, accounting for the downregulation of Wts activity and the upregulation of Yki transcriptional activity.

Figure 3.4 **Hippo signalling and scaling of aSF number with cell size.** Unless otherwise stated, protein distributions and quantifications are reported for region boxed in Fig. 3.1A at 26 hAPF. **A)** Graph of intensity of *ban-nls:GFP* and *Ubi-nls:GFP* (mean ± SEM) as a function of apical cell area. n: cell numbers. p-value<10^{-5}. **B)** Graph of *ban-nls:GFP* intensity (mean ± SEM) as a function of the Jub:mKate2 ratio$^{in/out}$ of cluster. n: number of cells. **C)** Graph of Wts:CitFP and Jub:GFP ratio$^{in/out}$ of cluster (mean ± SEM) as a function of apical cell area. n: number of cells. **D, E)** Graphs of Jub:GFP (D) and Wts:CitFP (E) ratio$^{in/out}$ of cluster (mean ± SEM) as a function of apical cell size in w^{RNAi} control and $actn^{RNAi}$ cells. n: number of cells; p-value<10^{-4}. **F)** Graph of the fraction of cells that divide between 22 hAPF and 34 hAPF as a function of apical cell size (mean ± SEM) in *pnr-G4>*w^{dsRNA} (control) versus *pnr-G4>*$actn^{dsRNA}$ tissues. N: number of animals (regions used of each animal contained on average 380 cells for w^{RNAi} and 243 cells for $actn^{RNAi}$, see M&M); p-value<0.05. **F)** Graph of the fraction of cells that divide between 22 hAPF and 34 hAPF as a function of apical cell size (mean ± SEM) in *pnr-G4>*w^{dsRNA} (control) versus *pnr-G4>*$actn^{dsRNA}$ tissues. N: number of animals (regions used of each animal contained on average 380 cells for w^{RNAi} and 243 cells for $actn^{RNAi}$, see M&M); p-value<0.05. **G)** Distribution of E-Cad:3xmKate2 and MyoII:3xGFP at aSF nucleation (t=0 min), as the aSF peels from the cortex (t=2 min to 14 min), reaching TCJs (t=22 min), at TCJs (t=34 min) and after breakage (t=42 min). Red arrowhead: nucleating TCJ; yellow arrowheads: aSF tips; blue arrowheads: breaking TCJs. Blue "x" marks absence of the aSF. **H)** Schematic of aSF nucleating at a TCJ (red arrowhead) and peeling from the cortex until aSF tips reach breaking TCJs (blue arrowhead). Orange arrows indicate the TCJ bisector, that makes an angle θ with the a-p axis ($\theta \approx 5°$ for nucleating TCJ at right; $\theta \approx 80°$ for breaking TCJ at bottom). **I)** Graph of proportion of aSF nucleation (red) and breakage (blue) events at TCJs. Each bar includes absolute number of aSFs observed in that group. n: total number of aSFs. **J)** Cumulative distribution of TCJ bisector orientations for TCJs where aSFs are observed to nucleate (red) and break (blue). See Appendix B.2 for our criterion for aSF breakage at a TCJ. n: number of nucleation and breakage events. **K-M)** Graphs of average aSF number per cell (K), aSF nucleation rate (L) and aSF lifetime (M) measured between 25 and 27 hAPF as a function of cell apical area. Dashed lines: best-fit linear regressions; n: number of cells. **N)** Graph of experimental (grey) and model-predicted (green) aSF number per cell (mean ± SEM) as a function of cell apical area. Our model explains approximately 75 percent of variance of aSF number with cell apical area. n: number of cells; see Fig. B.6, Fig. B.7 and Appendix B. **O)** Schematic based on a Jub:GFP confocal image illustrating positions of control cells (white) as well as the border (brown) and bulk (blue) $trbl^{UP}$ clone cells marked by Caax:tBFP accumulation. **P)** Graph of nucleating TCJs per cell (mean ± SEM) in $trbl^{UP}$ border and $trbl^{UP}$ bulk cells. n: number of cells; p-value<10^{-5}. **Q)** Graph of aSF number per cell (mean ± SEM) in $trbl^{UP}$ border and $trbl^{UP}$ bulk cells. n: number of cells; p-value<10^{-2} controlling for cell apical area differences (see Fig. B.9B,C and Appendix B.3). **R)** Graph of predicted aSF lifetime (mean ± SEM) in $trbl^{UP}$ border and $trbl^{UP}$ cells. n: number of cells. **S)** Graph of predicted aSF number per cell (mean ± SEM) in $trbl^{UP}$ border and $trbl^{UP}$ cells. n: number of cells; p-value<10^{-2} controlling for cell apical area differences (see Fig. B.9F,G and Appendix B.3). **T)** Schematic of elongated (top) and ortho-elongated (bottom) cells having same number of nucleating TCJs and same apical area; aSFs must travel farther between nucleating and breaking TCJs in the ortho-elongated case. **U)** Graph of aSF number per cell (mean ± SEM) in elongated and ortho-elongated cells. n: number of cells; p-value<10^{-5}. **V)** Graph of number of nucleating TCJs per cell (mean ± SEM) in elongated and ortho-elongated cells. n: number of cells. **W)** Graph of cell apical area (mean ± SEM) in elongated and ortho-elongated cells. n: number of cells. **X)** Graph of predicted aSF lifetime (mean ± SEM) in elongated and ortho-elongated cells. n: number of cells; p-value<10^{-5}. **Y)** Graph of predicted aSF number per cell (mean ± SEM) in elongated and ortho-elongated cells. n: number of cells; p-value<10^{-5}. Scale bars: 2μm (G). Statistical tests: Kruskal-Wallis tests (P-S and U-Y), Ancova tests for difference in regression slopes (A,C-F) and Mixed-ANOVA (F). r: Pearson correlation coefficients. ns: not significant. Statistically significant differences (p-value<0.05): one asterisk.

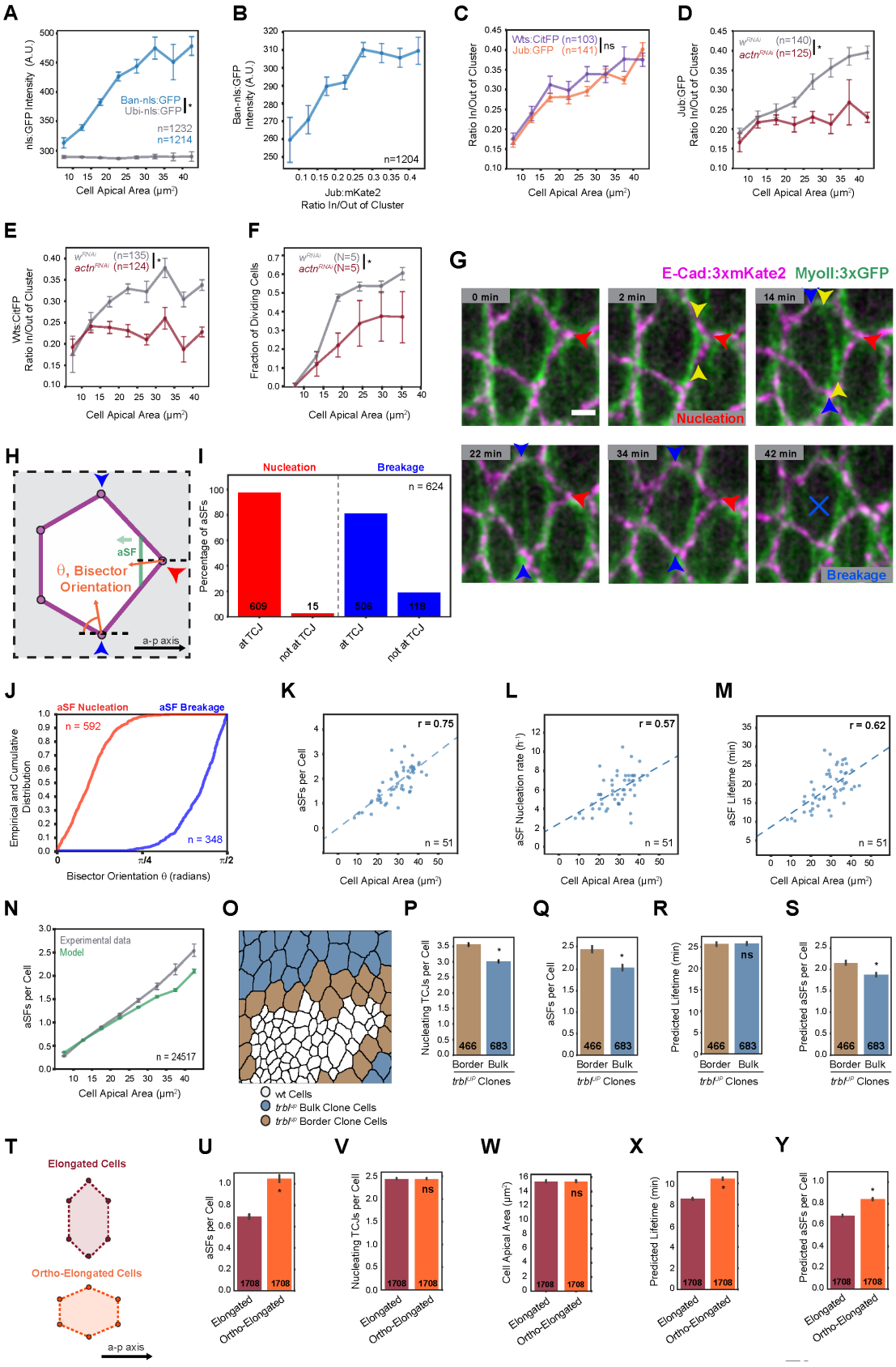
A
nls:GFP Intensity (A.U.)
Ban-nls:GFP
Ubi-nls:GFP
n=1232
n=1214
Cell Apical Area (μm²)
B
Ban-nls:GFP Intensity (A.U.)
n=1204
Jub:mKate2 Ratio In/Out of Cluster
C
Wts:CitFP (n=103)
Jub:GFP (n=141)
ns
Ratio In/Out of Cluster
Cell Apical Area (μm²)
D
wRNAi (n=140)
actnRNAi (n=125)
Jub:GFP Ratio In/Out of Cluster
Cell Apical Area (μm²)
E
wRNAi (n=135)
actnRNAi (n=124)
Wts:CitFP Ratio In/Out of Cluster
Cell Apical Area (μm²)
F
wRNAi (N=5)
actnRNAi (N=5)
Fraction of Dividing Cells
Cell Apical Area (μm²)
G
E-Cad:3xmKate2 MyoII:3xGFP
0 min
2 min
14 min
Nucleation
22 min
34 min
42 min
Breakage
H
aSF
θ, Bisector Orientation
a-p axis
I
Nucleation
Breakage
n = 624
Percentage of aSFs
609
15
506
118
at TCJ
not at TCJ
at TCJ
not at TCJ
J
aSF Nucleation
aSF Breakage
n = 592
n = 348
Empirical and Cumulative Distribution
Bisector Orientation θ (radians)
K
r = 0.75
n = 51
aSFs per Cell
Cell Apical Area (μm²)
L
r = 0.57
n = 51
aSF Nucleation rate (h⁻¹)
Cell Apical Area (μm²)
M
r = 0.62
n = 51
aSF Lifetime (min)
Cell Apical Area (μm²)
N
Experimental data
Model
n = 24517
aSFs per Cell
Cell Apical Area (μm²)
O
wt Cells
trblKD Bulk Clone Cells
trblKD Border Clone Cells
P
Nucleating TCJs per Cell
466
683
Border Bulk
trblKD Clones
Q
aSFs per Cell
466
683
Border Bulk
trblKD Clones
R
Predicted Lifetime (min)
ns
466
683
Border Bulk
trblKD Clones
S
Predicted aSFs per Cell
466
683
Border Bulk
trblKD Clones
T
Elongated Cells
Ortho-Elongated Cells
a-p axis
U
aSFs per Cell
1708
1708
Elongated
Ortho-Elongated
V
Nucleating TCJs per Cell
ns
1708
1708
Elongated
Ortho-Elongated
W
Cell Apical Area (μm²)
ns
1708
1708
Elongated
Ortho-Elongated
X
Predicted Lifetime (min)
1708
1708
Elongated
Ortho-Elongated
Y
Predicted aSFs per Cell
1708
1708
Elongated
Ortho-Elongated

Having characterized the link between aSF formation and Yki transcriptional activation at 26 hAPF, we explored whether the scaling between aSF number and cell apical area might result in the scaling of Yki activity with cell apical area. We quantified the intensity level of *ban-nls:GFP* as a function of cell apical area. *Ban-nls:GFP* levels increase as cell apical area increases from 10 to 32 μm^2 and then reach a plateau for cells between 32 and 40 μm^2 (Fig. 3.4A). In contrast, the level of *nls:GFP* under the control of a ubiquitin promoter (*Ubi-nls:GFP*) is independent of cell apical area (Fig. 3.4A). In full agreement with the proposed role of Jub clustering in Yki activity regulation, we found that the *ban-nls:GFP* signal increases with the Jub ratio$^{in/out}$ (Fig. 3.4B). Furthermore, we observed that under stress both the Jub and Wts ratios$^{in/out}$ of clusters increase with cell apical area, consistent with the notion that a larger fraction of Wts is inhibited in larger cells (Fig. 3.4C and Fig. B.5A,B). If aSFs contribute to the scaling between cell size and Hippo/Yki pathway activation, the impact of Actn loss of function on Wts and Jub clustering should be more pronounced in larger cells. Accordingly, Jub and Wts clustering is not affected in small *actn^{RNAi}* cells, whereas clear differences exist in large cells (Fig. 3.4D,E and Fig. B.5C). Furthermore, we observed that the impact of the Actn loss of function on cell proliferation mirrors the defects observed in Jub and Wts clustering in *actn^{RNAi}* cells (Fig. 3.4F). Finally, we increased cell apical area by preventing cytokinesis and observed a corresponding increase in both Jub ratio$^{in/out}$ of cluster and *ban-nlsGFP* level (Fig. B.5D,E). Together, these findings indicate that the scaling between cell area and aSF number leads to a scaling of the clustering of Jub and Wts with cell area, and thus to the scaling of Hippo/Yki signaling activity with apical cell size in epithelial tissues.

Having established the relevance of the scaling in the cell mechanical and biochemical responses under stress, we next explored the origins of the scaling of aSF number with cell apical area. SF formation is best studied in individual cells where the organization of the SFs depends on cell shape [141, 142]. Yet, even in this context, the mechanisms controlling SF number and dynamics are not fully understood [141, 142]. To investigate how the scaling between cell size and aSF number is achieved in epithelial tissues under anisotropic stress, we analyzed aSF dynamics at 26 hAPF. Via live imaging of aSFs, we found that aSFs form at curved regions of cell junctions aligned with the direction of anisotropic stress (Fig. 3.4G). In epithelial tissues, the tricellular junction (TCJ), the position where three cells meet, is often the most curved region of the cell apical contour [143]. Accordingly, aSFs mainly nucleate at TCJs (Fig. 3.4G-I). After nucleation,

aSFs sweep across the cell as they peel from the cortex, and aSFs most often break as they encounter another TCJ (Fig. 3.4G-I). Importantly, a TCJ's propensity to nucleate or to break aSFs varies simply as a function of the orientation of the TCJ bisector with respect to the main stress axis (Fig. 3.4J, Fig. B.6A-F, Fig. B.7A-K , M, N, Q and Appendix B). Thus, we could classify a TCJ as a "nucleating TCJ" or a "breaking TCJ" based on this orientation. While the exact mechanical and molecular mechanisms driving aSF nucleation and breakage at TCJs in tissues under uniaxial mechanical tension remain to be understood, the TCJs' role in both processes suggests a geometric mechanism for the scaling of aSF number with cell apical area based on the following trends: The larger cells in a tissue have more TCJs [144], and thus might have higher rates of aSF nucleation. TCJs in larger cells are also farther apart, so that aSFs in larger cells could be expected to take longer to travel from the nucleating TCJ to the breaking TCJ. Together, these two effects would lead to larger cells' having more aSFs due to an increase in both aSF nucleation rate and lifetime.

To test this hypothesis, we analyzed how aSF nucleation rates and lifetimes differ between small and large cells. Large cells on average have higher aSF nucleation rates and lifetimes, in agreement with our proposed geometric mechanism (Fig. 3.4K-M). Next, we performed computer simulations to quantitatively analyze how much of the observed scaling of aSF number with cell apical area could be explained by differences in TCJ number and positions. In these simulations, we considered a simple model where only the geometric effects are present; we did not include any explicit dependence on cell size (see Appendix B). We applied this model to cell shapes and orientations taken directly from experimental images at 26 hAPF. We found that our geometrical TCJ model explains around 75% of the observed variation of aSF number with cell apical area with one fitting parameter. This parameter can be interpreted as essentially the junctional cortex thickness, and the fitted value agrees well with direct thickness measurements (0.50±0.12 μm versus 0.51±0.12 μm; Fig. 3.4N, Appendix B and Fig. B.7L).

To further show that the number of aSFs within a cell depends on the properties of its TCJs, we sought to vary TCJ number and position independently of cell apical area and in a population of genetically identical cells. To accomplish this, we performed two distinct analyses. First, we took advantage of the fact that a large cell in contact with smaller cells typically has more TCJs than a large cell surrounded by other large cells [145]. To generate large cells with different local environments, we induced clones of large cells by blocking the G2/M transition through

overexpression of *trbl* (*trbl*^{UP} clones) and compared *trbl*^{UP} cells at the boundary of the clone (border cells) to cells within the clone (bulk cells, Fig. 3.4O). As anticipated, *trbl*^{UP} cells at the boundary of the clone have more nucleating TCJs (Fig. 3.4P), and thus might be expected to have more aSFs. To verify that no other differences in cell shape or TCJ distribution lead to a countervailing difference in predicted aSF lifetime between border and bulk cells, we simulated our geometric model of aSF nucleation and breakage on cell sizes and shapes taken from our images of *trbl*^{UP} clones; the model indeed predicts that *trbl*^{UP} cells at the boundary of the clone should have more aSFs per cell than *trbl*^{UP} bulk cells (Fig. 3.4S and Fig. B.8A-G). Further, we found experimentally that, controlling for any small difference in cell size between these two populations, cells at the boundary have on average more aSFs than cells within the clone (Fig. 3.4Q, R and Fig. B.8). Thus, these results substantiate our hypothesis that an increase in the number of TCJs correlates with an increase in the number of aSFs.

We then analyzed whether the distribution of TCJs modulates aSF number. If the distance between the nucleating TCJ and the breaking TCJ is critical to control aSF number, we predict that cells which are elongated orthogonal to the uniaxial mechanical stress (hereafter referred to as ortho-elongated) should have more aSFs than cells of a similar size elongated parallel to the main stress axis (Fig. 3.4T). By restricting our analysis to such ortho-elongated cells, we show that at constant nucleating TCJ number and cell size, the aSF number is higher in ortho-elongated cells as predicted (Fig. 3.4U-Y). Based on aSF dynamics, quantitative analyses of aSF nucleation and lifetime, modeling and experiments, we propose that the number and position of TCJs are major contributors to the scaling of aSF number with cell apical area in tissues under uniaxial tension. We conclude that TCJs play an unexpected role in the regulation of cell mechanical properties and signaling.

Scaling between body size and metabolic or biomechanical properties has been an intense field of study for decades [146, 147]. More recently, investigations of the scaling of morphogen gradients with tissue area or length have unveiled novel mechanisms of cell fate specification during development [148, 149]. Here, we have uncovered a scaling between the number of aSFs per cell and cell apical area in an epithelial tissue. We have furthermore provided evidence that this scaling is critical to control cell and tissue elongation as well as proliferation in response to epithelial morphogenetic forces. Existing work has emphasized the roles of SFs as anchors to extra-cellular matrix (ECM) via focal adhesions (FA) and the SFs' roles in cell locomotion, cell

mechanics and Hippo/YAP regulation [141, 150, 151]. Our work highlights the contributions of aSFs anchored to the AJ as regulators of both tissue morphogenesis and proliferation under physiological morphogenetic mechanical stress. We have also found that aSFs promote the co-clustering of Jub and Wts in the control of Hippo/YAP signalling. The full characterization of the molecular interactions between aSF components and Hippo/YAP regulators at the tips of the fibers will be critical to decipher how aSFs promote the recruitment of Jub to the aSF tips in response to tissue stress. Interestingly, mammalian Jub has been reported to be localized at ECM-integrin FA [152], suggesting that the recruitment of Jub to SF tips might provide a complementary mechanism of Hippo/YAP mechanical regulation in individual cells [116, 132, 150, 153-155]. Strikingly, cell cycle regulation is best predicted by a combination of cell area and cell tension in multicellular assemblies in culture [156]. Therefore, it will be useful to analyze whether the mechanisms that we have uncovered might generally explain the interplay between cell area and mechanical forces in the control of cell proliferation. Our characterization of the aSF dynamics illustrates that the scaling between apical area and aSF number can be in large measure accounted for by the number and distribution of TCJs. Thus, our work defines a functional link between TCJs and aSFs. As TCJ and SFs are preeminent biological structures [141, 143], the future molecular characterization of their interplay might shed light on numerous aspects of epithelial tissue mechanics, proliferation and morphogenesis.

Materials and methods

Fly stocks and genetics

Table 3.2 lists the *Drosophila melanogaster* stocks used in this study as well as the associated references. Loss-of-function and gain-of-function experiments were carried out using the FLP/FRT, the Gal4/UAS and Gal4/Gal80^{ts}/UAS systems [157-159]. Somatic clones were induced in the second instar or third instar larval stages by heat-shock (HS) at 37°C. When comparing gene function at 18 hAPF or 26 hAPF, the timing after clone induction (hACI) were identical to avoid possible confounding effect due to protein perdurance.

Molecular biology

The *actn*^{IG1} and *actn:GFP* alleles were generated by CRISPR/Cas9-mediated homologous recombination at their endogenous loci, using the vas-Cas9 line [160]. To generate the *actn*^{IG1} and *actn:GFP* alleles by CRISPR/Cas9-mediated homologous recombination, guide RNAs were cloned into the *pCFD5: U6:3-t::gRNA* vector [161]. For the *actn*^{IG1} allele, which deletes the amino-acid (aa) 841 to 2754, the following guide RNAs were used: 5'-TGCCTTGCGCTCTTACAAGTCGG -3', 5'- TGCTGAAGGACATGTAGTCCAGG -3', 5'-GGCAAAAACTGGGAAAGCACAGG-3', 5'-CCAAAACCGCTTGACTTCAATGG-3', 5'-AACTGGGAAAGCACAGGCCAAGG-3', 5'-CTTGACTTCAATGGAGTCCTTGG-3' ; while for the *actn:GFP* allele we used the following ones: 5'-GACCGACTTGTAAGAGCGCAAGG-3' and 5'-TGCAGTCCTTCGGATGCGGGTGG-3'. Homology sequences were cloned into homologous recombination vectors harboring a hs-miniwhite cassette either flanked by two loxP sites [122, 162] and an N-terminal GFP sequence for GFP tagging (vector and map available upon request) or flanked by two loxP to generate the *actn*^{IG1} sites and two attP sites for deletion allele [122, 162]. The two homologous regions (HR1 and HR2) flanking the site of CRISPR/Cas9 cuts were cloned using the following primers: (i) for the *actn*^{IG1} : (HR1) 5'-CCGGGCTAATTATGGGGTGTCGCCCTTCGCGCATCCGCAACTGCCAGATGC-3' and 5'-ACTCAAAGGTTACCCCAGTTGGGGCACTACGGGATTAGAATGCTCTAGCGAATTTGC-3'; (HR2) 5'- ACTCAAAGGTTACCCCAGTTGGGGCACTACAAGGACTGCATCGGCGAACCC-3' and 5'-ACTCAAAGGTTACCCCAGTTGGGGCACTACAAGGACTGCATCGGCGAACCC-3'; (ii) for actn:GFP : (HR1) 5'- TATGGGGTGTCGCCCTTCGGGTCTCTAGTTATTGTGAAGCAGCACCAGATCCC-3' and 5'- ACTGCCTGAAGAACCGCTGGACCCCGAACTCAAGTCGGTCTCGCCGTAGAG-3';

(HR2) 5'- GGAAGTGGTAGCTCAGGGTCTAGTGGATAGAAGGACTGCATCGGCGAACCC-3' and 5'- GCCCTTGAACTCGATTGACGCTCTTCGTCCGCCTGTGGGTGAATGTAGTGTGTTT-3'.

Jub:mKate2 was built based on the rescue construct described in [163] and was cloned by PCR ligation in pCaSpeR4 using the following primers: (Jub genomic region) 5'-TTAACGTTCGAGGTCGACTCTAGAGGATCCGCGTTGTTGTGGCTTCCTATGCTAAC-3', 5-GTGCATGTTCTCCTTAATCAGCTCGCTCACTCCCATATACTGGTACGAAGCGCAG-3' and (mKate2) 5'- GTGAGCGAGCTGATTAAGGAGAAC-3' and 5'-GCCTCTCCCAGCCACACTCCGTTCCGCTTATCTGTGCCCCAGTTTGCTAGGG-3'.

Cry2Olig:ChFP and Cry2Olig:ChFP:Jub were cloned in the pCaSpeR4 Ubiquitin promotor transgenesis vector (pUbi) in the following way: the pUbi-Cry2Olig:ChFP was first generated by cloning in the pUbi vector a PCR fragment of the Cry2 PHR Olig-mCherry (E490G) amplified from pCMV_Cry2PHROlig-mCherry(E490G) [139] using 5'-ATCCCCCGGGCTGCAGGAATTCACAGATCTATGAAGATGGACAAAAAGACTATAGTTTGG-3' and 5'-GCGCTCAGCTGGAATTGGGGTACGTCTAGAAGAAGAGCTCGCTCTTCTCTTGTACAGCTCGTCCATGCCG-3'. The genomic region of the jub gene [163] from the ATG to the STOP codons was then cloned in the resulting vector using the 5'-TCCACCGGCGGCATGGACGAGCTGTACAAGGGTTCGGGCTCGGGTAGTATGACCACCCAGCGGACGCAG-3' and 5'-GCGCTCAGCTGGAATTGGGGTACGTCTAGATTATCCCATATACTGGTACGAAGCGCAG-3' for PCR amplification and addition of a GSGSGS protein linker between mCherryFP and Jub. All embryo transgenesis injections were performed by Bestgene.

Live imaging microscopy

Pupae were prepared for dorsal thorax live imaging as described previously [117, 122]. Unless otherwise stated samples were imaged at 25°C or 29°C with an inverted confocal spinning disk microscope from Nikon or Zeiss, using either 60x NA1.4 OIL DIC N2 PL APO VC, 63x NA1.4 OIL DICII PL APO or 100x NA1.4 OIL DIC N2 PL APO VC objectives and sCMOS (Hamamtsu) camera. Additionally, images and movies were obtained with a confocal microscope Carl Zeiss (LSM880 NLO,) with 40x NA1,3 OIL DICII PL APO (UV) VIS-IR (optical zoom 2.5X) or a 63x NA 1.4 OIL DICII PL APO objective (optical zoom 5X or 7.5X). This confocal microscope was also used for laser ablations (see Laser ablations section) since it is equipped with

a two-photon Ti:Sapphire laser (Mai Tai DeepSee, Spectra Physics). In several experiments, a single image was acquired at 26 hAPF using confocal spinning disk or scanning microscopy. To record the long timescale dynamics of aSFs, E-Cad:3xmKate2, MyoII:3xGFP expressing pupae were imaged for 8 - 10 h every 5 min using confocal spinning disk microscopy. To image the short timescale dynamics of aSFs, E-Cad:3xmKate2, MyoII:3xGFP animals were imaged every 30 seconds or every 2 min using confocal spinning disk microscopy.

PDMS tissue compression

22 hAPF pupa were glued on a pre-stretched PDMS membrane mounted on a custom-made stretcher (Markova *et al., in preparation*). By releasing the PDMS membrane using a micrometric screw while imaging the pupa, a compressive strain of 20% was applied in the plane of the tissue. Images were acquired at 26 hAPF through the PDMS membrane on an inverted confocal spinning disk microscope from Nikon using a dry Nikon 40x NA 0.95 AIR PL APO objective.

Image processing and segmentation

Unless otherwise stated, images were denoised using the Fiji Gaussian Blur 3D plugins to improve signal-to-noise ratio and time-lapse movies were bleached-corrected using the Fiji Bleach Correction Histogram Matching function. For single time-point z-stack images and time-lapse movies, z-stacks were projected using a custom MatLab code [123, 164]. The custom MatLab code automatically determines an apical z-map using the E-Cad:3xmKate2, E-Cad:GFP, Jub:GFP or Jub:mKate2 signal. The apical z-map can then be used to project the relevant z-sections above and below the AJ. Maximum projections were used for aSF number quantification, aSF dynamics and segmentation, whereas average projections were used for fluorescent intensity quantification. 2D cell segmentation and tracking was achieved using previously published Matlab codes [123]. Segmentation errors were corrected through several iterations between manual and automatic segmentation rounds [123]. 3D cell segmentation was performed in Fiji by manually delineating the cell contour along the cell apical basal axis using the membrane PH:GFP marker. To quantify the nls:GFP nuclear signal two distinct image processing pipelines were applied. If an AJ marker was also acquired with the nls:GFP signal, the AJ z-map (see above) was used to compute an average projection of the nls:GFP signal between 0 µm to 10 µm below the AJ z-map. We verified that this procedure projects the entire nls:GFP signal. In absence of an AJ marker, the apical-basal

positions of the nls:GFP were defined as follows: the z-stacks were filtered by a 2D Gaussian Blur of 40 sigma using Fiji and the resulting stacks were resliced to obtain y-stacks along the apical-basal axis. The y-stacks were binarized using Fiji Mean threshold. The binarized y-stacks were then resliced back to binarized z-stacks. The resulting z-stacks were then manually corrected and used to define the apical-basal position of the nls-GFP nucleus signal. The binarized z-map was then used to perform an average projection of the nls:GFP signal. Each nucleus was manually segmented in Fiji to determine its average nls:GFP signal.

Quantification of number of aSFs and aSF orientation

In order to rigorously compare the aSFs number in different experimental conditions, the region harboring aSFs was defined using precise landmarks based on the position of the two posterior scutellar macrochaetae. The region enriched in aSF (aSF region) was defined as a box located 22µm anterior to the two posterior scutellar macrochaetae, centered on the midline and of size 122.5µm (anterior-posterior, a-p axis) by 127.5µm (medial-lateral, m-l axis). Quantifications of aSF number per cell were performed on projections (7 z-slices, 3µm) using MyoII:3xGFP or MyoII:3xmKate2 to label aSF. aSF were manually marked in Fiji and cell contours were obtained by E-Cad:3xmKate2, MyoII:3xGFP or Jub:3xmKate2 signal segmentation. Each marked aSF was then automatically assigned to a given cell using a custom MatLab code. To compare the scaling between aSF numbers per cell and cell apical area versus cell volume, aSF number, cell apical area and volume were determined in Fiji using manual aSF counting, 2D cell contour segmentation and the 3D cell segmentation, respectively. Subsequent aSF quantifications and data analysis were performed using custom MatLab and Python codes (see below). In wt tissue, the quantification of cell apical area versus aSF number per cell was independently checked by 3 persons. aSF orientations were obtained by manually segmenting each aSF in Fiji and then determining their orientation using the Fiji Analyze Particles tool.

To analyze the role of lateral tissue contraction on aSF number in the central domain of the tissue, the *mirr-Gal4* (*mirr-G4*) driver was used to express the MyoII heavy chain dominant negative transgene (*UAS-zip^{DN}:YFP,* [128]) or the F-Actin maker as control (*UAS-LifeAct:GFP*) in the lateral domain of the dorsal thorax. To restrict the expression of *zip^{DN}:YFP* or *LifeAct:GFP* to late pupal stage, the animals were initially kept at 18°C, shifted to 25°C at 1 hAFP ±1 hour and imaged at 26 hAPF. To analyze the impact of tissue compression on aSF number, pupal epithelial

tissues were compressed (see PDMS Tissue Compression) and aSF numbers were compared in compressed and non-compressed animals. aSF number per cell was also quantified at 26 hAPF in (i) Gal4 flip-out clones labeled by the expression of UAS-Caax:tBFP and expressing the relevant dsRNA or transgenes under UAS control ; (ii) $actn^{IG1}$ mutant clones labelled by loss of nls-GFP expression.

Measurements of aSF dynamics

To study the aSF dynamics on the timescale of minutes, E-Cad:3xmKate2 and MyoII:3xGFP time-lapse movie stacks were projected (7 z-slices, 3µm). The E-Cad:3xmKate2 signal was used to define each cell contours and the position of the cell tricellular junctions (TCJs). The MyoII:3xGFP labelled aSFs were manually annotated at every time-point and tracked from nucleation to breakage. aSF nucleation was defined when an aSF MyoII:3xGFP signal is clearly separated from the MyoII:3xGFP junctional cortical signal. aSF breakage was defined as the time-point at which the aSF no longer connects to the two opposing junctions. Using the E-Cad:3xmKate2 signal, the positions of the TCJs were manually annotated at the aSF nucleation time, mid-lifetime and breakage time. "Nucleating TCJ" and "breaking TCJ" were also annotated and defined as the TCJs at which the aSF nucleates and breaks, respectively. "Nucleating TCJ" were also tracked during the entire aSF lifetime. Additionally, aSF velocities were also measured from the position where the aSF originally nucleates to its breakage.

Protein clustering

To determine the ratio of Jub and Wts integrated intensity in clusters relative to that elsewhere along the junction ($ratio^{in/out}$ of cluster, see also Fig. B.4B)), z-stack of single cells expressing Jub:mkate2, Wts:GFP or Wts:CitFP were cropped and sum-projected (17 z-slices centered around the AJs and corresponding to 3.2µm). Three fluorescent intensity measurements were then performed: (i) The mean fluorescent intensity in cluster (Ic) : Clusters were automatically identified using the Fiji FindFoci plugin [165] (Fig. B.4B'') using the following parameters: background:2; search:0.15; search method: Fraction of peak – background; peak:0.15; maximum peaks:50; fraction:0.50; minimumsize:5. The resulting mask was used to measure the intensity in each cluster (Ic) and the area occupied by each cluster (Ac); (ii) The total integrated intensity along the AJ, (Iaj): the AJ cell contour was selected using Fiji segmented line tool (blue,

in Fig. B.4B''') and used to measure (Iaj) and the total area of the cell junction (Aaj) and; (iii) The fluorescent background intensity (Ib) was measured by selecting the apical medial region of the cells (red, Fig. B.4B''') and measuring the average intensity level. The signal in cluster was defined as $in^{cluster} = \frac{\sum_{each\ cluster}((Ic-Ib)*Ac)}{(Iaj-Ib)*Aaj}$ and the signal on the junction as $out^{cluster} = 1 - in^{cluster}$. The ratio$^{in/out}$ of cluster as $\frac{in^{cluster}}{out^{cluster}}$. Measurements were done in the aSF region as well as in region devoid of aSFs at both 18 hAPF or 26 hAPF in control tissues as well as in w^{RNAi}, $actn^{RNAi}$, svn^{RNAi} and $aurB^{RNAi}$ clones in the aSF region.

Optogenetics

Cry2Olig:ChFP:Jub or Cry2Olig:ChFP expressing pupae were kept at 18°C in the dark, and mounted as in [117, 122] but under red light exposure. Cry2Olig:ChFP light activation was performed by 491nm laser illumination and the dynamics of Cry2Olig:ChFP and Cry2Olig:ChFP:Jub were recorded using the 561nm laser line. All optogenetic experiments were performed in a region devoid of aSF, located between the two dorsocentral macrochaetae and adjacent to the midline. Clustering was induced by two initial steps of high blue laser illumination (see below for different activation times) and then maintained at low laser power for GFP imaging. During the 491nm illumination, Wts:GFP, Jub:GFP, MyoII:GFP were imaged every 50s. To analyze whether the 491nm illumination of Cry2Olig:ChFP:Jub or of Cry2Olig:ChFP modulates the level of the *dIAP1*-nls:GFP transcriptional Yki reporter, the nls:GFP signal intensities were compared in "dark" and "light" experimental conditions: (i) "light" condition : upon an initial 491nm illumination, the *dIAP1*-nls:GFP was acquired by 491nm illumination every 5min for 4h; (ii) "dark" condition: a single image was acquired using the 491nm laser at the beginning of the experiments, and then animals were kept in dark for 4 h until a second acquisition of the nls:GFP signal was performed using the 491nm laser line. Upon acquisition, the stacks were average-

projected and the average nls:GFP signal and background were measured. The changes in *dIAP1*-nls:GFP expression due to illumination were measured as:

$$\frac{dIAP-nls{:}GFP^{light,4h}\ (Cry2Olig{:}ChFP{:}Jub)}{dIAP-nls{:}GFP^{light,0h}\ (Cry2Olig{:}ChFP{:}Jub)} / < \frac{dIAP-nls{:}GFP^{light,4h}(Cry2Olig{:}ChFP)}{dIAP-nls{:}GFP^{light,0h}\ (Cry2Olig{:}ChFP)} >$$

corrected for background signals, and similarly for dark condition.

Laser ablations

Tissue recoil velocity.

To measure tissue recoil velocity upon laser ablation, E-Cad:GFPx3 or Jub:GFP labelled tissue was imaged using a two-photon laser-scanning microscope (LSM780 or LSM880 NLO, Carl Zeiss) equipped with a 40x NA1,3 OIL DICII PL APO (UV) VIS-IR objective (zoom 2.5X) in single-photon bidirectional scan mode lasting δt=756 ms every 5s. A rectangular region (length 0.83 µm x width 41.5 µm) was ablated at t=0s using the Ti:Sapphire laser (Mai Tai DeepSee, Spectra Physics) at 805 nm with < 100 fs pulses with a 80 MHz repetition rate typically set at 30% power. Ablations were performed parallel or orthogonal to the midline region to measure tissue recoil velocity along the a-p or m-l, respectively. Upon ablation, images were acquired every 5s for 60 seconds. Recoil velocity was estimated by measuring the displacement of the tissue at the edge of the ablation between t=0s and 25s. The ablations were performed in pupae at different time-points between 14 hAFP and 28 hAPF to determine the evolution of the recoil velocity during development. In a similar manner, tissue recoil velocities were measured in *pnr-G4>actn*^{RNAi} and *pnr-G4>w*^{RNAi} tissues at 26 hAPF. Tissue stress anisotropy (Fig. 3.1D) was defined as the ratio of the mean recoil velocity along the m-l axis to the mean recoil velocity along the a-p axis. The error on the difference in mean elongations was obtained through standard error propagation of the SEMs on the two means at each time-point. Error propagation was performed by using the uncertainties package in Python.

aSF and AJ recoil velocities.

To measure junction recoil velocity upon aSF or AJ ablations, E-Cad:3xmKate2, MyoII:3xGFP tissues were imaged at 26 hAPF as described above except that images were acquired at the following time-points: -1.1s, -0.1s, 0.65s, 1.3s, 2.2s, 3.2s, 4.2s, 5.2s, 6.2s, 7.2s, 8.2s and 9.2s.

Ablation was performed at t=0. Regions to be ablated (ROI) were precisely defined to cover the aSF, AJ (see Fig 3.2F for ablation schema), or a region adjacent to the aSF in case of mock ablations. The ROI was ablated using the Ti:Sapphire laser (Mai Tai DeepSee, Spectra Physics) at 805 nm with < 100 fs pulses with a 80 MHz repetition rate typically set at 35% power. aSF recoil velocity was deduced from the displacement of the junction to which the aSF was anchored between t=0 and t=1.3s. AJ recoil velocity was calculated by the displacement of the two vertexes of the AJ between t=0 and t=1.3s. The ablation of a second MyoII structure, aSF or junction, was performed 30s following initial ablation. AJ ablation was also performed in $actn^{RNAi}$ and w^{RNAi} flip-out clones at 18 hAPF and 26 hAPF in tissue labeled by Jub:GFP and MyoII:3xmKate2.

Jub and Wts cluster dynamics upon aSF ablation:

To determine Jub:GFP, Wts:GFP or Wts:CitFP clusters dynamics upon aSF ablation, aSF labelled by MyoII:3xmKate2 were ablated as described above except that a single time-point was acquired prior to ablation and that images were acquired every 30s upon aSF ablation. In addition, in cases where the given aSF was connected to another aSF, both aSFs were ablated. Upon acquisition, the intensities of Jub or Wts clusters were measured as follows: a ROI corresponding to the cluster of Jub:GFP, Wts:GFP or Wts:CitFP prior to ablation was manually delineated using the Fiji Polygon selection tools; the average fluorescent intensities in the ROI were then measured at each time-point by manually tracking the position of the cluster at each time-point. The average background fluorescence intensity was determined by averaging 5 intensity measurements performed in the medial region of the surrounding cells. Similar results were obtained for Wts:GFP and Wts:CitFP (not shown).

Cell and tissue elongations, stress inference and rate of cell division

Cell elongation.

Upon cell segmentation, we determined the cell elongation as follows. First, we determined the geometric center of the cell (x_c,y_c). Then, for each pixel i within the cell, we computed $\Delta x_i = x_i - x_c$, $\Delta y_i = y_i - y_c$ and the cell inertia matrix as:

$$I = \begin{bmatrix} I_{xx} & I_{xy} \\ I_{xy} & I_{yy} \end{bmatrix} = \sum_{pixels\ within\ cell} \begin{bmatrix} {\Delta x_i}^2 & \Delta x_i \Delta y_i \\ \Delta x_i \Delta y_i & {\Delta y_i}^2 \end{bmatrix}.$$

The cell elongation along the m-l axis was defined as the ratio between cell inertia matrix component I_{yy} (m-l axis component) and the I_{xx} component (a-p axis component). Ortho-elongated versus elongated cells was defined as cells with a larger I_{yy} (versus smaller) component than I_{xx} component, respectively.

Upon aSF ablation (t=0s), the changes in cell elongation were measured as the difference between the cell elongation at t=-0.1s and t=9.2s. The differences in cell elongation between $actn^{RNAi}$ and w^{RNAi} cells were calculated for each cell apical area bin at the indicated developmental times. The errors on the mean elongation differences were obtained by standard error propagation of the SEMs of the $actn^{RNAi}$ and w^{RNAi} means of each bin. Error propagation was performed by using the uncertainties package in Python. A ± 1.5 IQR (InterQuartile Range) filter was applied to only consider cells without outlier value of cell elongation. This filter was applied to w^{RNAi} and $actn^{RNAi}$ cell elongations as well as to the difference of cell elongation upon ablation.

Tissue elongation, rate of cell division and stress inference:

Upon cell segmentation and tracking, tissue elongation rate, cell division rate, fraction of dividing cells and junctional stress were determined in wt and mutant clones. Tissue properties can be heterogeneous in this region of the tissue, and clone position and size cannot be controlled, thereby making the comparison between a mutant clone behavior in our ROI and its control challenging. Therefore, for each mutant clone we analyzed, we first cropped it to its intersection with the ROI, and we applied this exact same zone of analysis (ZOA) onto the corresponding wt control tissue to make sure that the exact same region would be analyzed in the mutant clone and its corresponding control, thereby making the comparison of their respective analyses relevant. This was made possible thanks to prior time and space registration of each movie as described in [123]. Then, the rate of tissue elongation at a given time point along the m-l axis (y) in this ZOA was directly determined by determining the slope fitting data points giving cell velocity along the m-l or axis (V_y) versus cell position along this axis (y), namely $\partial_y V_y = \dot{\varepsilon}_{yy}$, as described in [166]. Then, cumulative tissue elongation along the m-l axis over a time period of T could be calculated: $\int_0^T \dot{\varepsilon}_{yy}\, dt$, dt being the time duration between two frames. The cell division rate (h^{-1}, Fig. B.4L) in a ZOA at a given time was determined by counting the number of divisions occurring over an hour normalized by the initial number of cells in the ZOA. The fraction of dividing cells in Fig. 3.3N is

the number of cells dividing in a given time range divided by the initial number of cells in the ZOA. The fraction of dividing cells in Fig. 3.4F is the ratio between the number of cells achieving a second division and the total number of cells in each size bin. Each cell size is determined by averaging its mother cell size over 6h. Inference of the junctional stress in the ZOA was performed as described in [123]. The junctional stress tensor was then renormalized by dividing it by its trace to make it truly dimensionless. Finally, the junctional stress anisotropy along the m-l axis was determined by taking the yy component of the traceless part of the renormalized stress tensor. Analyses were performed in wt, w^{RNAi} and $actn^{RNAi}$ tissues.

Scutellum adult shape:

Upon hatching, adult flies were aged for 3 days at 25°C. They were then preserved in Glycerol:Ethanol (3:1). Animals were mounted in Glycerol:Ethanol (3:1) and imaged with a Zeiss SteREO Discovery V20, using a PlanApo S 1.0x FWD 60mm objective and Axio CAM ICc 1 camera. Scutellum elongation was determined as the ratio between maximum m-l length of the scutellum length and the a-p length of the scutellum (Fig B.2E-E''). The elongation measurements were performed in male and females yielding similar results (not shown). Analyses were performed in *pnr-G4>*w^{dsRNAi} and *pnr-G4>*$actn^{RNAi}$ animals.

Hippo/Yki component localization and signaling

Hippo pathway component distributions around the aSF along the AJ.

To determine the distribution of PH:GFP, Jub:GFP, Wts:CiFP or Wts:GFP along the AJ centered at the tips of the aSF, tissues expressing PH:GFP, Jub:GFP, Wts:CiFP or Wts:GFP and MyoII:3xmKate2 were imaged and average projected (7 z-slices, 3µm) at the AJ level. Using the Fiji Segmented Tool, the intensity profile of PH:GFP, Jub:GFP, Wts:CiFP or Wts:GFP along the AJ was determined and the position of aSF tips (marked by MyoII:3xmKate2) was annotated. The background intensity was measured in the medial apical region of the cells. Each intensity profile was then registered using the position of the annotated aSF tips as a landmark and then averaged

to obtain the PH:GFP, Jub:GFP, Wts:CiFP or Wts:GFP distribution along the AJ centered around the aSF tips. Similar results were obtained for Wts:CiFP or Wts:GFP (not shown).

Jub and Hippo Pathway component colocalization.

Upon imaging of pupal tissue expressing Jub:mKate2 (or Jub:GFP) and Wts:GFP (or Wts:CiFP), single cells were cropped and average-projected (11 z-slices corresponding to 2µm). The Jub signal was then binarized using the Otsu algorithm in Fiji to create a mask used for calculating the Pearson correlation coefficient between the Jub signal and either Jub itself or Wts signals. Analyses were performed in $actn^{RNAi}$ mutant cells and w^{RNAi} control cells. Similar results were obtained for Wts:GFP and Wts:CiFP (not shown).

Ban-nls:GFP level measurements.

The level of transcriptional activation of Hippo/Yki pathway in a given mutant clone (marked by the expression of Caax:tBFP) was defined as the ratio between the *ban-nls:GFP* signal inside and outside the clone. The ratio was measured as follows: upon projection of the *ban-nls:GFP* nuclear signal (see above), each *ban-nls:GFP* nuclear signal was manually segmented using the ROI selection function of Fiji. The inside and outside *ban-nls:GFP* signals were defined as the average *ban-nls:GFP* signal within a layer of two nuclei along the clone boundary inside and outside the clone. The background fluorescence signal was measured by averaging the GFP fluorescence signal in 5 regions located between *ban-nls:GFP* marked nuclei. The level of transcriptional activation of Hippo/Yki pathway was normalized to the one of control w^{RNAi} clones at 18 hAPF. Similar measurements were performed for $actn^{IG1}$ mutant clones marked by the absence of nls:ChFP. To compare the level of transcriptional activation of Hippo/Yki pathway at 18 and 26 hAPF without possible confounding effects due to protein perdurance, the *ban-nls:GFP* signal measurements were performed 72h ± 4h after clone induction in both cases.

Quantification of nuclear GFP signal as a function of cell size or Jub ratio$^{in/out}$ of cluster.

To quantify *ban-nls:GFP* or *ubi-nls:GFP* signals as a function of cell apical area, a maximum E:Cad:3xmKate2 signal projection and the average-projection of the nls:GFP signal were obtained (see above). The E:Cad:3xmKate2 and the nls:GFP signals were then segmented (see above). Each nls:GFP signal was associated with a given E-Cad:3xmKate2 segmented cells using the cKDTree

tool of the package scipy.spatial in Python. The associations were manually validated and corrected, if necessary. To exclude non-epithelial cells, the nls:GFP segmented data were filtered by excluding nls:GFP nuclei, whose signals are lower or higher than the mean nls:GFP nucleus intensity ± 3 standard deviations. In a similar way, apical Jub:mKate2 maximum and average projections were used to determine the cell apical area and Jub ratio$^{in/out}$ of cluster, respectively.

Junctional cortex thickness

We estimated the junctional cortex thickness around 2 min prior to the nucleation of an aSF at a given TCJ using the Cad:3xmKate2 and MyoII:3xGFP time-lapse movies. Upon projection of the time-lapse movies, Cad:3xmKate2 and MyoII:3xGFP intensity profiles were measured along a line of 5 pixels wide (0.13µm per pixel) passing by the TCJ and orthogonal to the prospective aSF. All line profiles were then re-aligned using the position of the TCJ. Once, re-aligned, intensity profiles of 0.5 µm before TCJ and 2.0 µm after TCJ were considered and normalized between 0 (minimum value) and 1 (maximum values). The junctional cortex thickness was estimated by two different approaches. First, we performed a cross-correlation analysis to determine the distance between the average Cad:3xmKate2 and MyoII:3xGFP maximal signal intensities, which correspond to half of the estimated cortex thickness. Alternatively, we estimated the junctional cortex thickness by determining the distance between the position of the maximal MyoII:3xGFP peak and the position corresponding to 2/3 of the MyoII:3xGFP intensity maximal value. Both measurements give similar junctional cortex thickness values: 0.52 µm versus 0.51 µm ± 0.12 (n=90) (see also Fig. B.7L).

Statistics

Sample sizes vary in each experiment. The experiments were repeated, at least, three independent times, except for the data shown in Fig. 3.4A-B, which were repeated two times. Number of aSF, ablation, animals or cells used in each experiment are indicated in figures or figure legends. All error bars in graphs are standard error of the mean (SEM) and the statistical tests used to assess significance are stated in the figure legends. Statistical significance between sample distributions were typically analyzed by Nonparametric ANOVA (Kruskal-Wallis test) with Conover post hoc tests (using a step-down method using Bonferroni adjustments). Mixed-Anova and 1-tailed Wicoxon signed rank test were used for cell division evolution and cell division

dependency on cell apical area. Nonparametric Levene Test was used to analyze aSF orientations for equality of variances. Alternatively, Ancova test, which combines ANOVA and regression, was used to test differences in regression slopes and intercepts between different conditions. Statistical differences are indicated by one asterisk and *p*-values are indicated in the corresponding figure legends. Statistical analyses were performed using scipy.stats, scikit_posthocs and uncertainties statistical packages as well as the MATLAB 2016B Statistics and Machine Learning Toolbox, MathWorks.

Table 3.1 aSF component localizations and functions. (a): References describing the localization and the function of the associated proteins. (b): To avoid identifying indirect regulators of aSF formation, only components harboring an aSF localization were qualitatively tested. At least two distinct dsRNA lines either from *Drosophila* TRiP [1] or VDRC [2] collections were used, except for Vinc and Ena analyses for which a dsRNA and a mutant allele were studied.

Proteins and References[a]	***Drosophila* names**	**aSF localizations**	**loss of function phenotypes [b]**
PDLIM1/LDB3 [167, 168]	Zasp52	Fibers and Tips	No loss of aSF
Zyxin [169]	Zyxin	Fibers and Tips	No loss of aSF
α-Actinin [170-172]	Actn	Fibers and Tips	Loss of aSF
β-Spectrin [173]	Kst	Fibers and Tips	Junction and aSF breakage
Filamin A [174]	Cher	Fibers and Tips	No loss of aSF
β-Integrin [175]	Mys	Tips	No loss of aSF
Paxilin [169]	Pax	Tips	No loss of aSF
Talin [176]	Rhea	Tips	No loss of aSF
Vasp [177, 178]	Ena	Tips	No loss of aSF
Vinculin [179]	Vinc	Tips	No loss of aSF
Anillin [180]	Scra	-	Not tested

Arp3 [181]	Arp3	-	Not tested
Dystrophin [182]	Dys	-	Not tested
Fascin [183]	Fascin	-	Not tested
Fimbrin [170, 172, 184]	Fim	-	Not tested
mDiaphanous 2 [185]	Dia	-	Not tested
p130CAS [186]	p130CAS	-	Not tested
PDLIM1/LDB3 [167, 168]	Zasp66	-	Not tested
Septin 2 [187]	Sep2	-	Not tested
Septin 4 [188]	Sep4	-	Not tested
Tropomyosin 1 [189, 190]	Tm1	-	Not tested
Tropomyosin 2 [190]	Tm2	-	Not tested

Table 3.2 Alleles and transgenes used in this study of aSFs.

Drosophila stock	*Reference or Source*
***mirr*-Gal4**	[191], BDSC (#29650)
***pnr*-Gal4**	[192], BDSC (#3039)
HsFlp, Ubi-nls:mRFP, FRT19	BDSC (#31418)
Tub-Gal80^{ts}	BDSC (#7017)
Ubi-nls:GFP	BDSC (#5629)
Ban-nls:GFP	[140]
Ubi-PH:GFP	[193]
Act>CD2>Gal4	BDSC (#3953)
Act>y+>Gal4	BDSC (#4780)

UAS-Caax:tBFP (Chr III)	[194], made using BDSC (#55090)
UAS-Caax:tBFP (Chr II)	[194], made using BDSC (#55082)
Jub:GFP	[163], BDSC (#56806)
Wts:GFP	[137], BDSC (#56808)
Zasp52:GFP	BDSC (#58790)
UAS-Act5c:GFP	BDSC (#9258)
UAS-zip^{DN}:YFP	[128]
UAS-trbl	[195]
UAS-zyx:ChFP	BDSC (#28875)
UAS-cdc2^{dsRNA}	BDSC (#28368)
UAS-aurB^{dsRNA}	BDSC (#28691)
UAS-w^{dsRNA}	BDSC (#33644)
UAS-actn^{dsRNA}	BDSC (#34874)
UAS-svn^{dsRNA}	VDRC (#43112)
UAS-zasp52^{dsRNA}	VDRC (#106177 and #58198)
UAS-zyx^{dsRNA}	BDSC (#29591 and BDSC (#36716)
UAS-kst^{dsRNA}	VDRC (#37075) and BDSC (#33933)
UAS-cher^{dsRNA}	VDRC (#107451) and BDSC (#26307)
UAS-mys^{dsRNA}	VDRC (#103704) and BDSC (#33642)
UAS-pax^{dsRNA}	VDRC (#107789) and BDSC (#28695)
UAS-rhea^{dsRNA}	BDSC (#40399, #32999 and #33913)
UAS-ena^{dsRNA}	VDRC (#106484)
FRTG13 *ena^{210}*	BDSC (#25404)
UAS-vinc^{dsRNA}	VDRC (#105956)
vinc$^{\Delta 3}$	[122]

UAS-LifeAct:GFP	BDSC (#35544)
UAS-GFP:scra	BDSC (#51348 and #51349)
UAS-Arp3:GFP	BDSC (#39722 and #39723)
Dys:GFP	BDSC (#59782)
Fascin:GFP	[196]
UAS-Dia:GFP	BDSC (#56751)
Fim:GFP	BDSC (#59838 and #51562)
p130CAS:GFP	BDSC (#60508)
Zasp66:GFP	BDSC (#6824)
Sep2:GFP	BDSC (#26257)
UAS-Sep4:GFP	BDSC (#51345)
Tm1:GFP	BDSC (#51537)
Tm2:GFP	BDSC (#6829)
Ubi-Ena:GFP	BDSC (#28798)
E-Cad:GFP	[162]
Mys:GFP	[197]
Rhea:GFP	[197]
Vinc:GFP	[197]
Cher:YFP	Kyoto Stock Center (#115123)
Kst:YFP	Kyoto Stock Center (#115518)
Pax:YFP	Kyoto Stock Center (#115540)
Dlg:YFP	[198]
E-Cad:3xGFP	[122]
E-Cad:3xmkate2	[122]
MyoII:3xGFP	[122]

MyoII:3xmKate2	[122]
Actn:GFP	This work
***actn*^{IG1} FRT19A**	This work
Jub:mkate2	This work
Ubi-Cry2Oligo:ChFP	This work
Ubi-Cry2Oligo:ChFP:Jub	This work
Wts:CitFP	[199]
dIAP1(3.5):GFP	[200]

Chapter 4 Generation of Fate Patterns via Intercellular Forces

Acknowledgements: This manuscript results from a collaboration with Jianping Fu's lab. Xufeng Xue performed the experimental work. His earlier work motivated this project [17].

Abstract

Studies of embryonic fate patterning often focus on diffusible chemical signals. Intercellular forces' role in generating fate patterns in epithelia remains poorly understood. Recent experiments in stem cell colonies on elastic substrates demonstrated that a key patterning event, neural induction, can occur without exogenous chemical gradients and is affected by mechanical stretching. Inspired by these finding, here we propose a model of mechanics-guided patterning: cell contractility depends on fate, and in-plane mechanical pressure biases fate. The cells at the colony boundary, more contractile and more spread than bulk cells, generate a fate pattern by transmitting forces to bulk cells. In agreement with previous observations, we find that in this model the outer fate domain's width is independent of colony diameter. We further predict and experimentally confirm that the outer fate domain's width depends non-monotonically on substrate stiffness. By modeling and experiments, we demonstrate that in-plane mechanical pressure itself can act as a morphogen, under the control of substrate stiffness.

Introduction

Proper embryonic development depends on fate specification events in which initially equivalent cells differentiate in a spatially controlled manner [3, 5, 9, 11, 13, 30]. A key example is neural induction: in the vertebrate ectoderm, a strip of cells assumes the neural plate (NP) fate as cells on either side differentiate into neural plate border (NPB) (Fig. 4.1A) [17, 201-204]. *In vivo,* this pattern of two fates is induced at least in part by the secretion of diffusible chemicals from cells in the underlying mesoderm [202, 203].

Recent experiments have probed the same fate specification process *in vitro* (Fig. 4.1B) [17]. In these experiments, human pluripotent stem cell (hPS) colonies bind to micro-patterned circular regions on elastic substrates. In uniform neural induction medium, cells near the colony center differentiate into NP; they are surrounded by a ring of NPB cells extending to the colony border (Fig. 4.1B). Since motion of individual cells is limited, patterned differentiation must rely on some form of positional information [17]. This differentiation does not depend on endogenous expression of BMP4 or NOGGIN, chemical signals relevant for neural induction *in vivo* [17, 201, 204], but is affected by mechanical stretching. These findings suggest that mechanical interactions between stationary cells generate NP-NPB patterning *in vitro*.

Inspired by these findings, we build a phenomenological model of NP-NPB pattern formation based on a coupling between in-plane mechanical pressure and cell fate. Our model is distinct from mechanics-guided patterning models that require chemical advection [205, 206] or cell motion [207, 208]. Although it shares some mathematical features with models of strain-activated contractility [208, 209], our model differs by explicitly considering cell fate and by operating in a parameter regime where it produces a single NPB domain rather than traveling waves or periodic patterns. By combining modelling and experiments, we argue that intercellular forces act like a morphogen to set the NPB domain size and mediate pattern formation. The substrate's mechanical properties, rather than biasing the fate of individual cells directly [14], controls the propagation of these intercellular forces [210, 211].

Intercellular force transmission is well described by existing formalisms [212-214]. These models treat cell layers as thin, actively contractile elastic sheets bound to passive elastic substrates. Cell layers "leak" stress by substrate deformation [212, 214]. In one dimension on thin substrates, the in-plane stress $\sigma(x)$ in the cell layer couples to the substrate displacement $\vec{u}$:

$$div \cdot \sigma \propto \vec{u} \Rightarrow {l_l}^2 \frac{d^2\sigma}{dx^2} - h_c B_c P(x) = \sigma(x) \qquad \text{[Eq. 1]}$$

where $-h_c B_c P(x)$ is an active stress. The target strain $P(x)$ is the strain necessary for cells to be stress-free [214]. h_c and B_c are cell height and elastic modulus, respectively, and l_l is a length scale set by a balance of cell layer and substrate stiffnesses [211-216]; for stiff cell-substrate adhesions, ${l_l}^2$ is inversely proportional to substrate stiffness [212-214].

We apply these mechanical models to our system by coupling $\sigma(x)$ to a phenomenological fate variable w. Similar phenomenological approaches to fate specification driven by chemical signals

have had considerable success [57, 217]. Our model of mechanics-guided neural induction relies on two experimental observations: NPB cells are more contractile than NP cells, and extensile stress biases cells to NPB fate [17]. These findings imply signs of couplings that do not generate a Turing-like, linear instability [30, 218]; instead, NPB domain formation is driven by forces from highly contractile cells at the colony boundary [219, 220].

Our model reproduces the observation that the NPB domain width is insensitive to colony diameter and correctly predicts that this width depends non-monotonically on substrate stiffness. Although diffusible chemicals control the length scales of many tissue patterns [3, 5, 9, 30, 201-204, 221-225], the tissue patterning toolbox contains more than chemical mechanisms: cells can communicate with each other via force transmission to bias each other's fates.

Results

In vitro model of mechanics-guided neural induction

After seeding hPS cells on elastic substrates with circular micropatterned regions, the cells proliferate in conditioned medium for two days. After these two days, we initiate neural induction by supplying a medium that contains dual SMAD inhibitors [226]; we also briefly supplement the medium with a β-catenin stabilizer, that actives WNT [227, 228]. Both BMP and WNT signaling within individual cells are known to play a role in neural induction [201].

In vivo, the BMP-SMAD signaling level within individual cells mediates fate decisions between NP and NPB [17, 201-204]. Similarly, *in vitro,* NPB cells have nuclear-localized p-SMAD 1/5, transcriptional modulators activated by BMP; NP cells do not [17]. Instead of directly monitoring BMP-SMAD signaling, we label NP and NPB cells by immunostaining for the nuclear markers Pax6 and Pax3, respectively (Fig. 4.1C) [17].

We previously demonstrated experimentally that cell spread area and cell layer stretching modulate BMP-SMAD signaling, thereby biasing fate [17]. We hypothesize that boundary cells transmit in-plane forces to neighboring cells and that neighboring cells respond to this mechanical stretching (Fig. 4.1D). Below we detail the experimentally observed coupling between fate and stress.

Figure 4.1 ***In vitro* model of neural induction. A)** Schematic of neural induction in vivo. Astrip of cells in the embryonic ectoderm differentiates into neural plate (NP, red). Cells on either side form the neural plate border (NPB, cyan). **B)** Schematic of neural induction in vitro. Human pluripotent stem (hPS) cells bind to circular regions of elastic substrate (tan). Seven days after neural induction initiation, we stain for NP (red) and NPB (cyan). Schematics are Voronoi

tessellations of nuclear positions before and after neural induction initiation. **C)** Representative immunofluorescence images of colony at day 9. DAPI counterstains nuclei. PAX3 and PAX6 staining label nuclei of NPB cells and NP cells, respectively. Scale bar, 20 μm. **D)** Schematic of cell-cell communication via intercellular forces. Edge cells generate contractile forces (black arrows), perceived by other cells. Importantly, cells exert traction forces (magenta) on the substrate, and this interaction shapes the spatial pattern of intercellular forces.

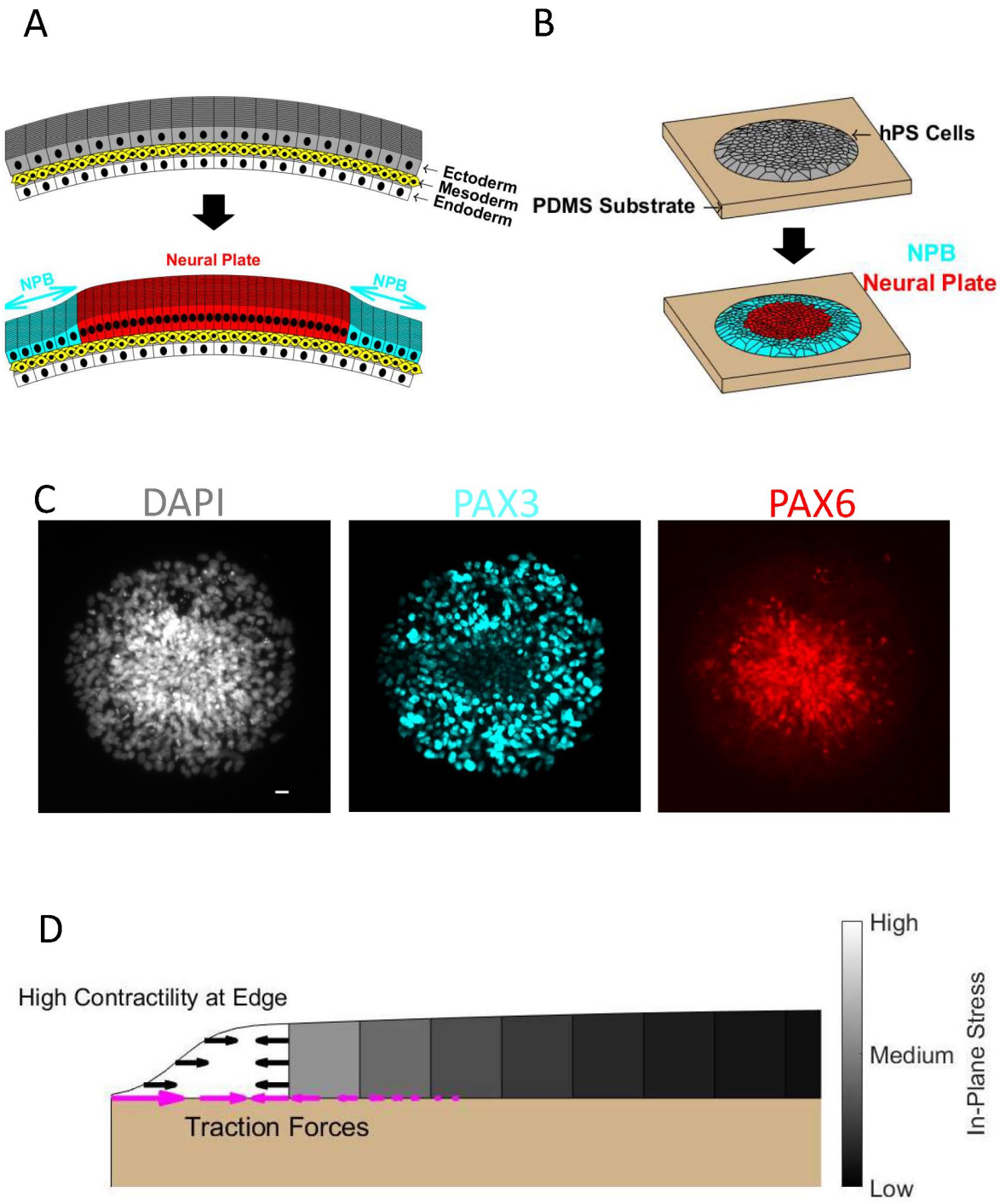

Figure 4.2 **Evidence for role of mechanics in neuroectoderm patterning *in vitro.* A)** Cell colony on micropost array. Two days after neural induction initiation, we measure cell-substrate forces via micropost displacements. Cells near colony edge are more contractile than cells near colony center. Colony diameter, 300 μm. **B)** Posts from white box in A. Cells displace (magenta arrows) posts. Post diameter, 2.2 μm. Post-to-post spacing, 4.0 μm. **C)** Concentrically averaged radial post displacements (from A) and radial traction stress T_r versus radial coordinate. Black line is three-domain fit (see Appendix C). We interpret the outermost domain as a ring of spread cells at the colony edge, the intermediate domain as a contractile domain of bulk cells, and the inner domain as group of non-contractile bulk cells. **D)** Radial post displacement profiles averaged over n=42 colonies. Since the position of the elbow-like feature in C shifts from sample to sample, this feature smooths out in average over all colonies. **E)** Schematic of control experiments (left) in which hPS cell colonies differentiate into two domains: NP (red) and NPB (cyan). Schematic of experiment (right) in which cell layer is stretched by microfluidic chamber (below colony). Stretching biases cells near colony center to the NPB fate (cyan).

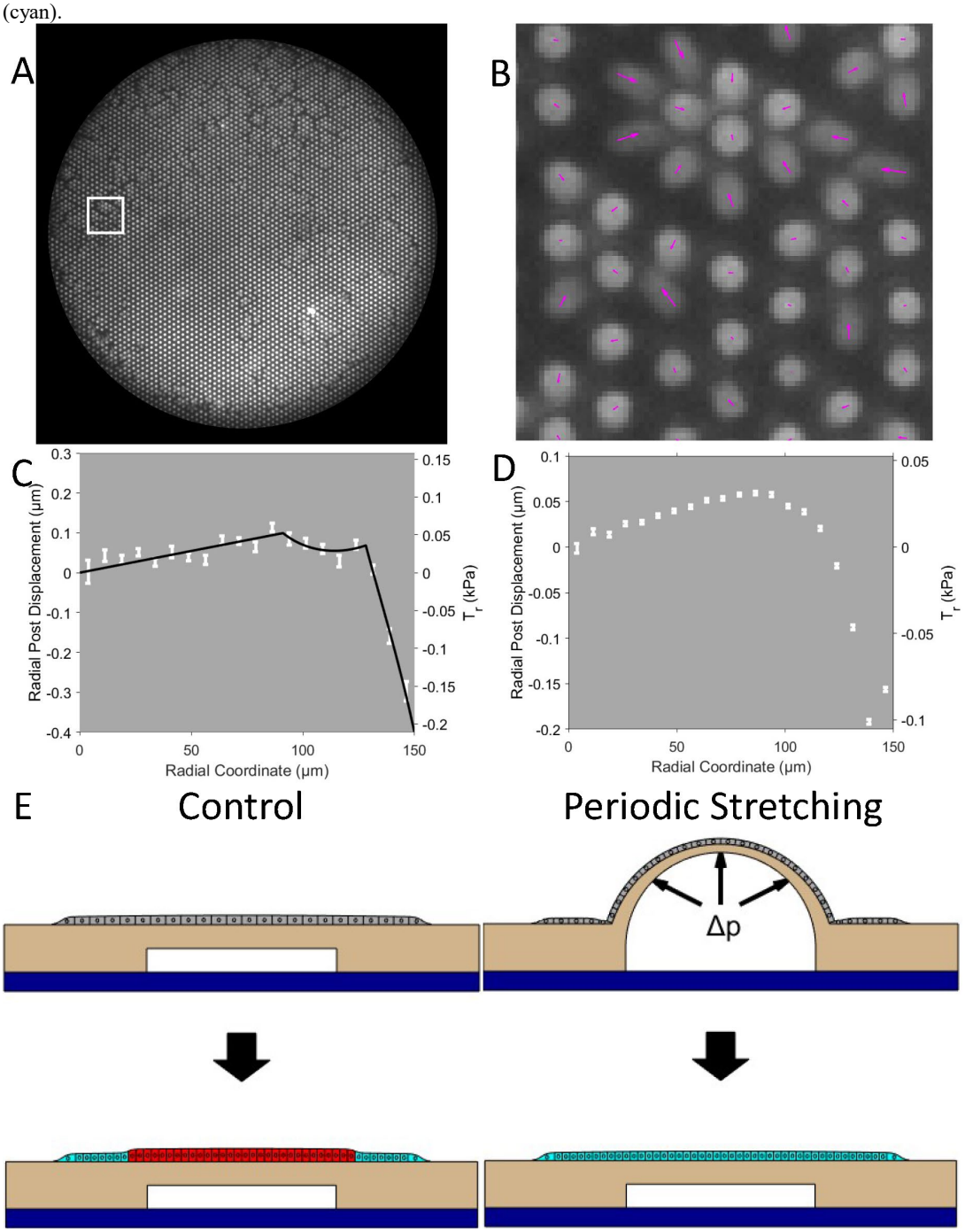

Experimental evidence for feedback between mechanical stress and fate

It is well known that patterns can originate from reciprocal feedback between two or more scalar fields, as in activator-inhibitor systems of reacting chemicals [30, 218]. Based on our hypothesis that coupling fate to an in-plane mechanical pressure could generate patterning, we test experimentally if cell fate regulates active stress generation and if mechanical pressure regulates fate.

To quantify if cell fate regulates active stress generation, we measure forces between cells and micropost substrates by measuring micropost deflections (Fig. 4.2A-D) [16, 17, 214, 229, 230]. Averaging radial post deflections, we determine which regions of the colony extend and which contract (Fig. 4.2C-D). We observe three distinct regions: a non-contractile central region surrounded by two concentric contractile regions (Fig. 4.2C, Appendix C.2). The extensile region coincides with the region that expresses Pax6, and the two contractile regions coincide with the region that expresses Pax3 [17]. Based on fits to the post displacement data [212, 214], we explain the mechanical difference between the two distinct NPB regions in the next section and the supporting information (Appendix C.2). We expected two regions (NPB and NP) rather than three; nonetheless, we conclude that NPB cells are more contractile than NP cells.

To test if mechanical pressure itself biases fate, we stretch the central region during differentiation. Stretching biases the central region to be Pax3$^+$ (*i.e.*, positive for Pax3 expression) rather than Pax6$^+$ (Fig. 4.2E) [17]; similarly, single cells constrained to larger areas have more nuclear p-SMAD 1/5 [17]. Compared to other estimates of cell layer stress *in vitro* [231-233], cell layer stresses during differentiation in our control conditions fall within a biologically realistic range (see Appendix C.2, Fig. C.1). Micropost and stretching experiments reveal that NPB cells generate more contractile stresses than NP cells and that mechanical stretching bias cells to the NPB fate.

Figure 4.3 **Phenomenological model of mechanics-guided fate patterning. A)** Schematic of differentiation from unstable cell state (gray) to stable cell state (red or cyan). **B)** Schematic of feedbacks between fate w and the trace of stress $tr\left(\underline{\underline{\sigma}}\right)$. NPB cells are more contractile than NP cell (positive feedback of w onto $tr\left(\underline{\underline{\sigma}}\right)$). Stretching of cell layer biases cells to NPB fate (positive feedback of $tr\left(\underline{\underline{\sigma}}\right)$ onto w). Fate w is bistable (self-positive feedback). Cells "leaks" stress into substrate (self-negative feedback of $tr\left(\underline{\underline{\sigma}}\right)$). **C)** Square root of cell area versus radial coordinate. In neural induction medium (DSI) and in conditioned medium (CM), cell area is large near colony boundary (magenta line) relative to colony bulk. Day 3 is 3 days after cell seeding; for DSI, day 3 is 1 day after neural induction initiation. **D)** Example of colony at day 3, immuno-stained for DAPI (green) and E-Cad (magenta), in DSI. White circle: micropatterned colony edge. **D')** Same colony as in D with Voronoi tessellation (white lines) over nuclei (green). Colony diameter, 400 μm. **E-F)** Initial condition (E) and fixed point (F) for phenomenological model. All parameters, except for α and w_{mid} (see Table C.6 for values), are from fit to micropost data in 4.2A-C. We fit σ^* to control fate boundary position. We plot target

strain (left), radial post displacement profile (center), and stress profile (left). Initially, outermost cell, which has large area, is contractile (cyan background, E). Highly contractile cells at colony boundary generate stress in their neighbors. The fate boundary moves inward until stress at fate boundary reaches a specified value, the coexistence stress. Note that fate boundary (between cyan and red backgrounds, E-F) moves from outermost cell toward colony center.

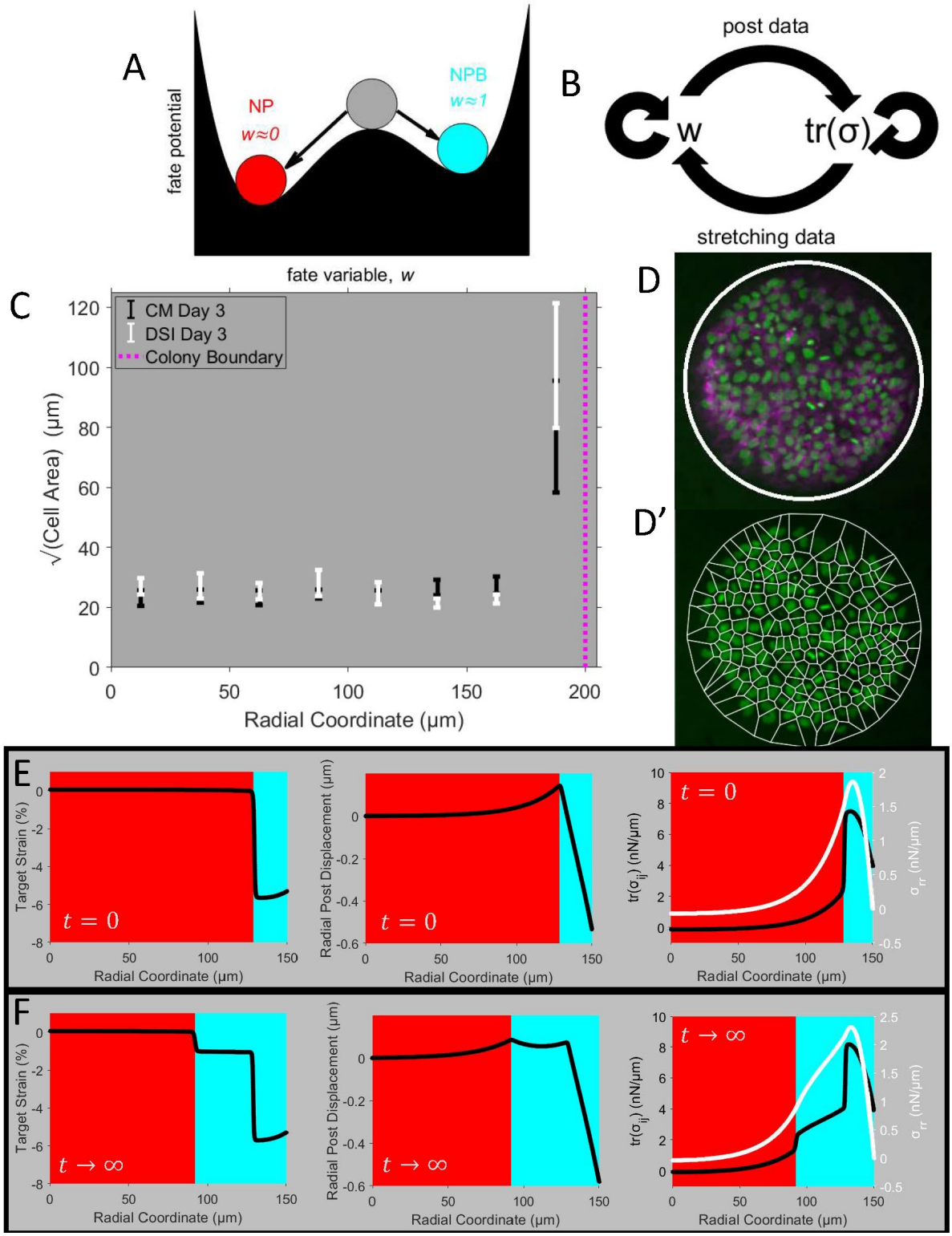

Constructing a phenomenological model of mechanics-guided fate patterning

Because we are interested in a binary fate decision, it is natural to map fate to a single variable w evolving in a bistable potential with minima corresponding to NP ($w \approx 0$) and NPB ($w \approx 1$) (Fig. 4.3A) [217]. In the spirit of including all allowed couplings at lowest order, we make two additional simplifying assumptions:

1. Active contractility is directly proportional to w, $P(\vec{r}) = \tilde{P}\, w(\vec{r})$.
2. In-plane mechanical pressure $-tr\left(\underline{\underline{\sigma}}\right)$ linearly biases w.

Here $\underline{\underline{\sigma}}$ is the two-dimensional in-plane stress tensor for the cell layer. w obeys:

$$\tau_w \frac{\partial w}{\partial t} = f\left(w, tr\left(\underline{\underline{\sigma}}\right)\right) + D\tau_w \nabla^2 w(r,\theta,t) \qquad \text{[Eq. 2]}$$

$$f\left(w, tr\left(\underline{\underline{\sigma}}\right)\right) = w(w - w_{mid})(1-w) + \alpha\left(tr\left(\underline{\underline{\sigma}}\right) - \sigma^*\right);\ \alpha > 0\ . \qquad \text{[Eq. 3]}$$

The signs of all couplings are determined by the micropost data and the stretching data — together with the assumption of bistability (Fig. 4.3B). τ_w is the time scale of fate evolution. w_{mid} determines the asymmetry of the potential in the absence of stress feedback (Fig. 4.3A). $\alpha\left(tr\left(\underline{\underline{\sigma}}\right) - \sigma^*\right)$ is the linearized feedback of stress onto w. σ^* is a constant value that tunes the position of the NPB domain. As in a previous study of mechanics-guided patterning [224], to regularize spatial variation of w, we introduce a diffusive term in Eq. 2; $\sqrt{D\tau_w}$ determines the smoothness of the NP-NPB boundary. To avoid artificially driving patterning at the free boundary in a stress-independent manner, we assume no-flux boundary conditions ($\frac{\partial w}{\partial \boldsymbol{n}} = 0$).

To calculate the in-plane mechanical stress that biases fate w, we treat the cell layer as an elastic medium [212-214]. Cell-substrate force balance dictates the behavior of $tr\left(\underline{\underline{\sigma}}\right)$ via a generalization of Eq. 1 to more than one dimension:

$$div \cdot \underline{\underline{\sigma}} \propto \vec{u} \Rightarrow l_l^2 \nabla^2 \left(tr\left(\underline{\underline{\sigma}}\right) + \frac{h_c B_c}{2}\tilde{P}w\right) + g\left(w, tr\left(\underline{\underline{\sigma}}\right)\right) = 0 \qquad \text{[Eq. 4]}$$

$$g\left(w, tr\left(\underline{\underline{\sigma}}\right)\right) = -\left(tr\left(\underline{\underline{\sigma}}\right) + \frac{h_c B_c}{2}\tilde{P}w\right) - \frac{1+\nu}{1-\nu}\frac{h_c B_c}{2}\tilde{P}w \qquad \text{[Eq. 5]}$$

(See Appendix C.4 for derivation of Eq. 4-5). ν is Poisson's ratio of the cell layer. We assume that $\underline{\underline{\sigma}}$ normal to the free boundary goes to zero at the boundary ($\sigma_{ij} n_j = 0$).

We ask whether our model (Eq. 2-5) with given boundary conditions generates an NPB domain at the boundary. Since the fate-stress couplings are of common sign ($\frac{\partial g}{\partial w}\frac{\partial f}{\partial (tr(\underline{\sigma}))} > 0$), no Turing-like, linear instability exists [30, 218]. Since cells at a tissue boundary often sense the boundary and develop distinct mechanical properties [219, 220, 224, 234, 235], we hypothesize that a mechanical inhomogeneity in the cell layer near the boundary drives the formation of NPB domain. Immunostaining of nuclei and adherens junctions during differentiation reveals that cells at the boundary occupy more area than bulk (*i.e.*, non-boundary) cells (Fig. 4.3C-D'). The region of boundary cells coincides with the outermost contractile regions discussed above (Fig. 4.2C, see Appendix C.2). This outermost ring of NPB cells is more contractile than NPB cells in the colony bulk (see Appendix C.2). We introduce boundary inhomogeneity into the model via a spatial dependence of the fate-contractility proportionality:

$$\tilde{P}(r) = \tilde{P}_1 + \left(\tilde{P}_2 - \tilde{P}_1\right)\theta\left(r - (r_0 - \Delta r)\right);\ \tilde{P}_2 < \tilde{P}_1 \qquad \text{[Eq. 6]}$$

where r_0 is the colony radius and Δr is the radial extent of the boundary cells.

In our model (Eqs. 2-6), a ring of highly contractile cells at the boundary generates in-plane stresses in neighboring cells (Fig. 4.3E). Experiencing in-plane stretching from boundary cells, neighboring bulk cells increase w, upregulating contractility. The fate boundary moves inward until the stress at the fate boundary equals the coexistence stress, that is model-parameter-dependent (Fig. 4.3F). The coexistence stress depends particularly strongly on σ^*, that must fall within a particular range in order for a stable pattern of both NP and NPB to exist. We can analytically determine the position of the fate boundary if we assume that the fate boundary is typically sharper than l_l (*i.e.*, $\frac{D\tau_w}{{l_l}^2} \ll 1$) (see Appendix C.5) [236-238].

Our phenomenological model (Eq. 2-6), based on experimentally motivated assumptions, reproduces measured traction forces (compare example in Fig. 4.2C to Fig. 4.3F). We test this model by, first, checking that it reproduces the previously reported weak dependence of NPB domain width on colony diameter [17]. Then, based on a model prediction, we probe how the NPB domain width depends on substrate stiffness.

Figure 4.4 **Effect of colony diameter and substrate stiffness on concentric width of NPB domain. A)** Box plot of NPB domain size versus colony diameter. Note that the median width of the NPB domain is independent of colony diameter. Red points: outliers. n=21 (300 μm). n=28 (400 μm). n=20 (500 μm). n=28 (800 μm). **B)** Representative examples of colonies immunostained for PAX3 (cyan) and DAPI (gray). Scale bar, 40 μm. **C)** Box plot of NPB domain size versus substrate stiffness (for colony diameter=400 μm). n=19 (3000 kPa). n=17 (1200 kPa). n=23 (560 kPa). n=16 (120 kPa). n=14 (30 kPa). Note that NPB domain size depends non-monotonically on substrate stiffness. **D)** Representative examples of cell colonies immunostained for PAX3 (cyan) and DAPI (gray). Scale bar, 40 μm.

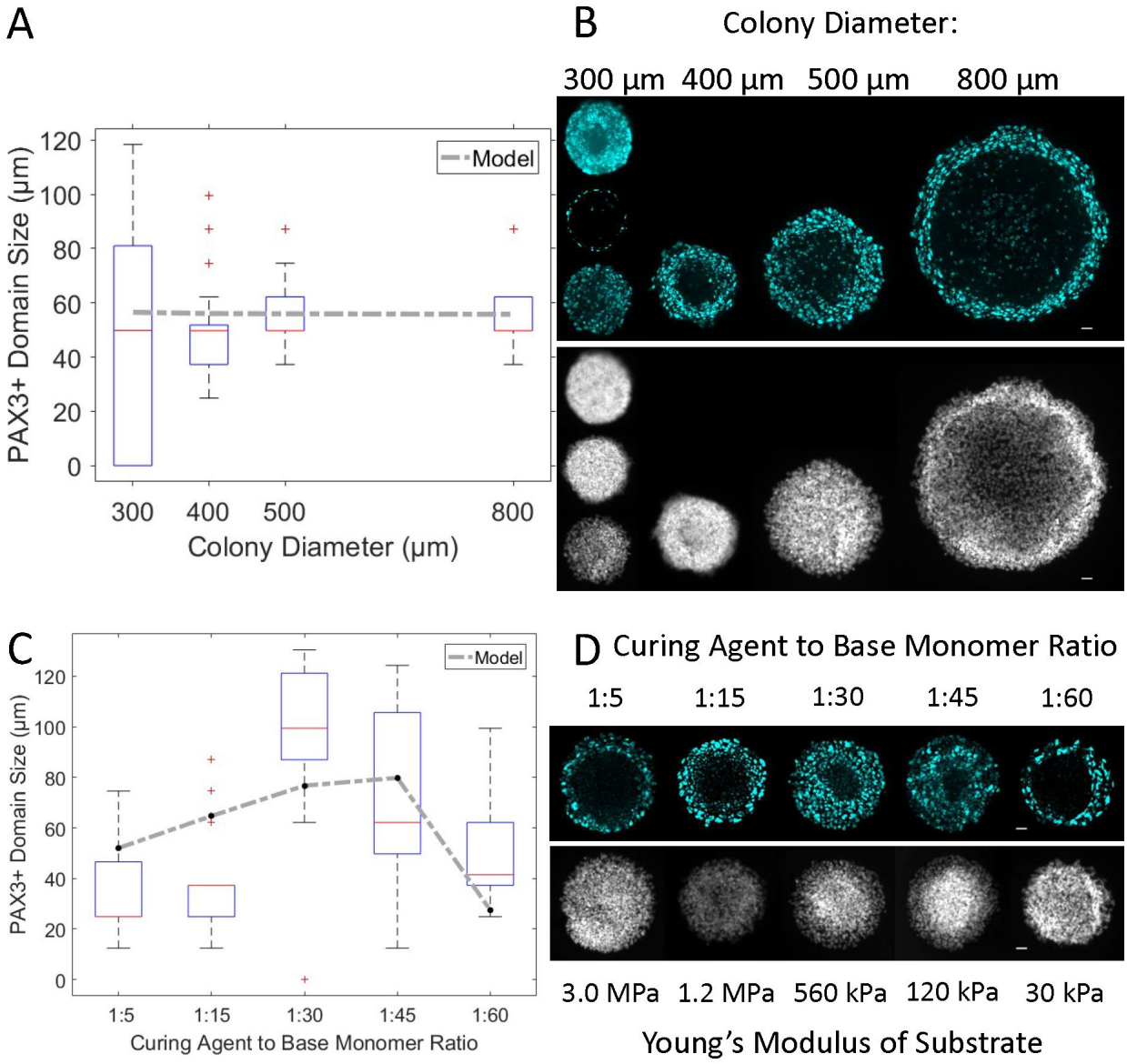

We previously reported that, as the colony diameter varies from 300 µm to 800 µm, the width of the NPB domain does not change (Fig. 4.4A-B). Our phenomenological model recapitulates this independence of NPB domain width on colony diameter (see Appendix C.3 for modelling on continuous substrate). To test our model further, we seek to change NPB domain width by changing experimental conditions. The most obvious condition to change is the substrate stiffness since cell-substrate forces tune intercellular forces [210, 211].

A previous mechanical model of a one-dimensional cohesive cell layer showed that intercellular force transmission is non-monotonic in substrate stiffness [211]. We test if our model

of fate patterning via force transmission predicts a non-monotonic dependence of NPB domain width on substrate stiffness. Indeed, our model predicts a non-monotonic dependence due to two competing factors: the magnitude of stress transmitted from outermost cells to bulk cells and the length scale over which that stress propagates l_l. l_l increases with decreasing substrate stiffness [211-214], while the magnitude of stress transmitted from outermost spread cells to the bulk decreases with decreasing substrate stiffness [211].

Experiments confirm this model prediction (Fig. 4.4C-D). Decreasing substrate stiffness from 3 MPa to 30 kPa at constant colony diameter, the NPB domain width changes from ≈40 μm to ≈100 μm to ≈25 μm. The largest NPB domain width occurs at a substrate stiffness value that is of the same order as previously reported physiological stiffnesses [14, 212-214, 230, 239-242]. This non-monotonic dependence of NPB domain width on substrate stiffness strongly suggests that mechanical forces play a key role in positioning the NP-NPB boundary *in vitro*.

Discussion and Outlook

Previous studies have experimentally demonstrated mechanical stresses' effects on tissue patterning [18, 20]. By constructing a mathematical model of fate patterning via intercellular forces, we show that stress-fate couplings can generate fate domains with a width that depends non-monotonically on substrate stiffness. Our results leave many open questions, including the molecular pathways that mediate mechanical influences on the NP-NPB decision. Recent studies in other contexts suggest that WNT/β-catenin is an appealing candidate [201, 224, 243-245].

In vivo differentiation depends on diffusible chemical signals released from mesodermal cells [202, 203]. Our study suggests that, *in vivo*, ectodermal cells differentiate into NP or NPB by combining information from both external chemicals and cell-cell forces. Due to the signs of stress-fate couplings, without a boundary or cell layer inhomogeneity, mechanical feedback alone would not drive patterning.

It is tempting to speculate about the functional significance of mechanical feedback in NP-NPB patterning. Since the ectoderm later folds at the NPB domains, generating a neural tube, mechanical feedback could possibly ensure that NPB domains coincide with the sites of force generation and tissue folding [244, 246].

Materials and methods

Cell culture

H1 human embryonic stem cell line (WiCell) were maintained on mitotically inactive mouse embryonic fibroblasts (MEFs; Thermo Fisher Scientific) in KSR medium consisting of DMEM/F12 (GIBCO) with 20% Knockout Serum Replacement (GIBCO), 0.1 mM β-mercaptoethanol (GIBCO), 2 mM Glutamax (GIBCO), 1% non-ssential amino acids (GIBCO), and 4 ng/ml human recombinant basic fibroblast (bFGF, Thermo Fisher Scientific). The cells were passaged using the STEMPRO EZPassage Disposable Stem Cell Passaging Tool (Invitrogen) as described previously [17]. The cell line was tested negative for mycoplasma contamination using LookOut Mycoplasma PCR Detection Kit (Sigma-Aldrich).

To induce neuroectoderm differentiation, cells were seeded on micropatterned PDMS substrate in KSR medium on day 0 at a density of 20,000 cells/cm^2. 10 μM ROCK inhibitor Y-27632 (R&D Systems) was added to prevent cell dissociation-induced apoptosis. On day 1, cell culture medium was replaced with fresh KSR medium without Y-27632. Cells were cultured in neural induction medium consisting of KSR medium supplemented with TGF- β inhibitor SB 431542 (10 μM; Stemcell Technologies) and BMP4 inhibitor LDN 193189 (500 nM; Stemcell Technologies) from day 2 to day 9. On day 3, CHIR99021 (3 μM; Stemcell Technologies) was added to the neural induction medium and was withdrawn on day 4.

Microcontact printing

PDMS stamps were fabricated using soft lithography from silicon molds, as described previously [16]. To generate micropatterned adhesive islands, a thin layer of PDMS was first spin-coated onto a glass coverslip at 1000 r.p.m for 30 s and cured at 110 °C for 24 h before use. Base-to-curing agent ratios of 5:1, 15:1, 30:1, 45:1 and 60:1 generated PDMS with Young's moduli of 3 MPa, 1.2 MPa, 560 kPa, 120 kPa, and 30 kPa, respectively, as measured by an Instron tensile testing machine (Illinois Tool Works Inc). PDMS membrane thicknesses were measure using a stylus profilometer (Dektak XT, Bruker Corporation). Then, PDMS stamps were soaked in a vitronectin solution (20 μg/ml, Stemcell Technologies) for 1 h. PDMS spin-coated coverslips were activated using ultraviolet ozone and then placed in contact with Vitronectin-coated PDMS stamps. Coverslips were then immersed in 0.2% pluronics solutions (BASF) for 30 min and washed with

PBS before cell seeding. PDMS stamps containing circular patterns with diameters of 300, 400, 500 and 800 μm were used.

Immunocytochemistry

hESCs were fixed in 4% paraformaldehyde for 30 min and permeabilized in 0.1% sodium dodecyl sulfate (SDS, Sigma Aldrich) for another 30min. Cells were then incubated in 10% goat serum (Thermo Fisher Scientific) for 1 h to block nonspecific binding, followed by primary and secondary antibodies for 1 h. 4,6-diamidino-2-phenylindole (DAPI, Thermo Fisher Scientific) was used for counterstaining cell nucleus. All primary antibodies are listed in Table 4.1.

Traction force measurements

Traction force was measured using PDMS micropost arrays (PMAs) as described previously [16]. Vitronectin was first coated onto the top surface of PMAs using microcontact printing. Then PMAs were incubated in 5μg/ml DiI (Invitrogen) for 1 h to label vitronectin coated PMAs. PMAs were then immersed in 0.2% pluronics solutions (BASF) for 30 min and washed with PBS before cell seeding. Live cell imaging was performed using Zeiss Axio Observer Z1 inverted epifluorescence microscope enclosed in the XL S1 incubator.

Determination of Pax3$^+$ domain width from colonies stained for DAPI and Pax3

We threshold the DAPI image to identify the region where nuclei are. We, then, morphologically close the thresholded DAPI image. In this closed image, we identify all pixels that delineate the boundary of the colony. Then, for each pixel within the colony, we compute its shortest distance to the colony boundary. To obtain a Pax3 intensity profile as a function of distance from the colony boundary, we average over pixels that are approximately equidistant from the colony boundary (*i.e.,* between some distance $|\vec{r}|$ and $|\vec{r}| - \Delta r$ from the colony boundary). We choose the averaging window's width to be approximately ten microns.

Then, for each colony, we use its Pax3 intensity profile as a function of distance from the colony boundary to calculate the width of the Pax3$^+$ domain. For each experimental condition indexed by i (fixed substrate mechanical properties and fixed colony diameter), we compute the average maximal Pax3 intensity (called $\overline{Pax3^{max}}_i$) and the average minimal Pax3 (called $\overline{Pax3^{min}}_i$). From these averages, we compute a midpoint (called $\overline{Pax3^{mid}}_i \equiv \frac{\overline{Pax3^{max}}_i + \overline{Pax3^{min}}_i}{2}$).

Then, for each experimental condition i, we loop through all colonies, calculating the distance from the colony boundary to the position where the Pax3 intensity profile crosses $\overline{Pax3^{mid}}_i$. That distance to the crossing point for each colony is its $Pax3^+$ domain width. Notably, this analysis method can identify which colonies are entirely $Pax3^-$, entirely $Pax3^+$, as well as patterned colonies (that have both $Pax3^-$ and $Pax3^+$ regions).

Table 4.1 Antibody staining.

Protein	Vendor	Catalog number	Dilution
PAX6	Abcam	ab78545	1:200
PAX3	Novus	NBP1-32944	1:400
PAX3	R&D systems	MAB2457-SP	1:200
E-cadherin	BD-Biosciences	610181	1:100

Chapter 5 Conclusion

Problems in developmental biology are inherently complex; every developmental process most likely involves both chemical mechanisms and mechanical forces. The point of a model, though, is to identify a simple representation of a process that can reproduce experimental observations and generate testable predictions. Every model is a falsification, yet some models are more useful than others are.

Across these three developmental systems, from cone crystallization in zebrafish retina to apical stress fiber generation in the *Drosophila* dorsal thorax to neural induction in stem cell colonies, we have argued for a strong role of intercellular forces in morphogenesis. In zebrafish retinae, we found that a model based on homotypic repulsive interaction is sufficient to reproduce the spatial pattern of defects in the mosaic. In the *Drosophila* dorsal thorax, we showed that a simple geometric model based on aSF nucleation and breakage at TCJs is sufficient to explain approximately two-thirds of the scaling of aSF number with cell apical area. Importantly, this scaling controls the final aspect ratio of the entire tissue by allowing larger cells to resist elongation under uniaxial stress. In our stem-cell-based model of neural induction, we showed that a phenomenological model based on reciprocal stress-fate coupling successfully predicts the non-monotonic dependence of the NPB domain width on substrate stiffness.

Definitively ruling out more traditional chemical mechanisms frequently requires further experimental tests. For example, if we could reliably identify differentiating UV cones in the precolumn area, we could ablate cellular processes that mediate contacts between UV cones. These ablations would allow us to test whether disrupting homotypic contacts disrupts cone mosaic formation. As another example, if we could use optogenetic tools to upregulate contractility in an individual stem cell in a colony, we could observe cells neighboring the optogenetically targeted cell to establish the link between intercellular forces and nuclear pSMAD1/5 localization.

Even if mechanical forces do play a dominant role in tissue patterning in a given system, the external chemical environment is not necessarily insignificant. For example, in our stem-cell-based model of neural induction, we know that the (uniform) chemical medium has been tuned to

allow cells to be competent to differentiate into either neural plate or neural plate border. A significantly higher concentration of dual SMAD inhibitors forces all cells to be neural plate, and significantly lower concentration of dual SMAD inhibitors forces all cell to be neural plate border.

A fuller appreciation of the role of mechanical forces in development requires future models to tease out the relative contributions of intercellular chemical signaling and intercellular mechanical forces. Our neural-induction model system carries perhaps the most promise in this regard. By gradually tuning the concentration of dual SMAD inhibitors in the medium, we could characterize how the underlying bias between the two fates changes, dictated by the midpoint of the fate potential, based on the chemical media. A detailed, quantitative marriage of the *in vitro* system and our phenomenological model could generate insights into how individual cells weight chemical and mechanical stimuli to make informed fate decisions.

Appendix A Supplementary Figures for Chapter 2

Figure A.1 **Defects other than Y-Junctions observed in live fish. A)** In this image, the nuclear-localized, photoconverted protein in UV cones is pseudo-colored magenta. White bonds: triangulation connecting nearest neighbors. The seven- and five- coordinated UV cones: seven- and five-sided stars, respectively. A Y-Junction exists near the reverse Y-Junction. Gray oval encloses the reverse Y-Junction. Row counts are annotated on each side of image. **B)** Example of double-row insertion and a Y-Junction. Double-row insertion, enclosed by gray oval, is a five- and seven-coordinated particle that are not connected in the lattice. Note that this double-row insertion does not disrupt cone mosaic patterning. Row counts are annotated on each side of image.

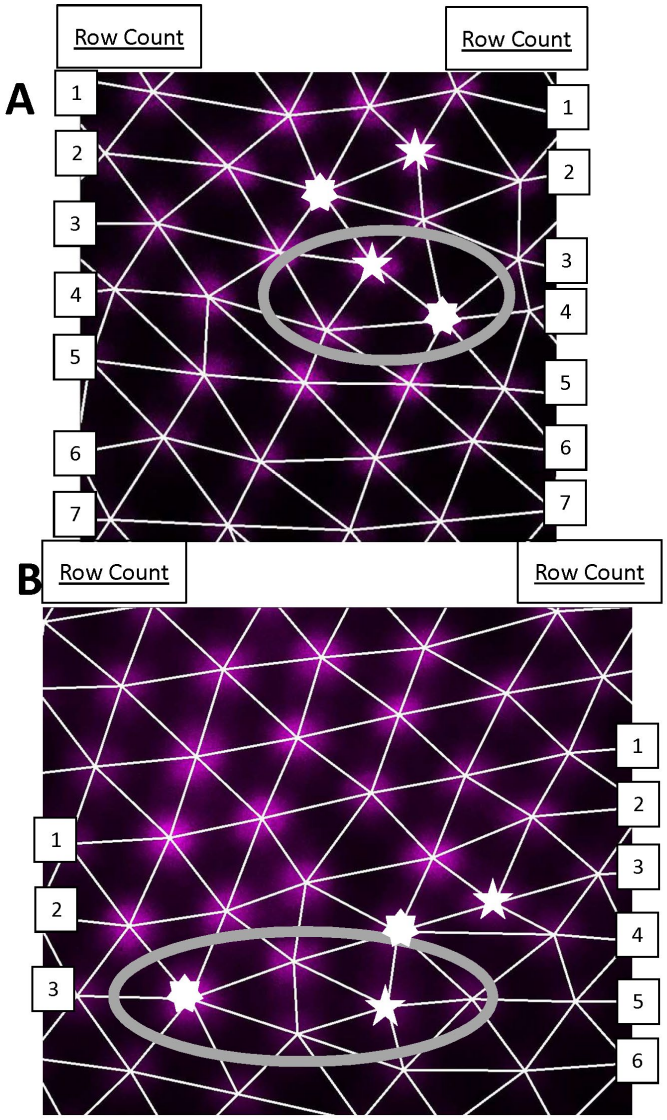

Figure A.2 **In live-imaging experiments, we quantify anisotropy of UV cone triangular lattice. A)** Patch of photoconverted UV cones near retinal margin. Patch of UV cones, that express nuclear-localized fluorescent protein, does not contain a Y-Junction. We use this patch, and two others, to quantify spacing between UV cones. **B)** The triangulation corresponding to patch of UV cones in panel A. In this triangulation, bonds connecting UV cones in the same row are black lines. Bonds along the other two principal directions of lattice are blue and red bonds. **C)** Scatter plot of bond length versus bond orientation in triangulation from panel B. The same color scheme denotes bonds along the row direction and along the two other principal directions. **D)** For three photoconverted patches with no Y-junctions, we calculated mean bond length (and standard deviation of mean bond length) along three principal directions. Same color-scheme is used such that the black points correspond to mean bond length along row direction, and red and blue points correspond to mean bond length along other two principal directions. **E)** The column direction is NOT a principal direction in the triangular lattice, meaning that UV cones in same column are not each other's nearest neighbors. Using a section of triangulation from panel B, we illustrate spacing along the row direction by black arrows, and the spacing along column direction by gray arrows. For an isotropic lattice, the column spacing is a square root of three times the row spacing. For this lattice, we can calculate the column spacing, given mean bond lengths in the three principal directions. We find that the column spacing is approximately twelve and a quarter microns, as compared to a row spacing of approximately ten and a quarter microns. This column to row spacing ratio is less than square root of three, meaning that row bonds are elongated relative to an isotropic lattice.

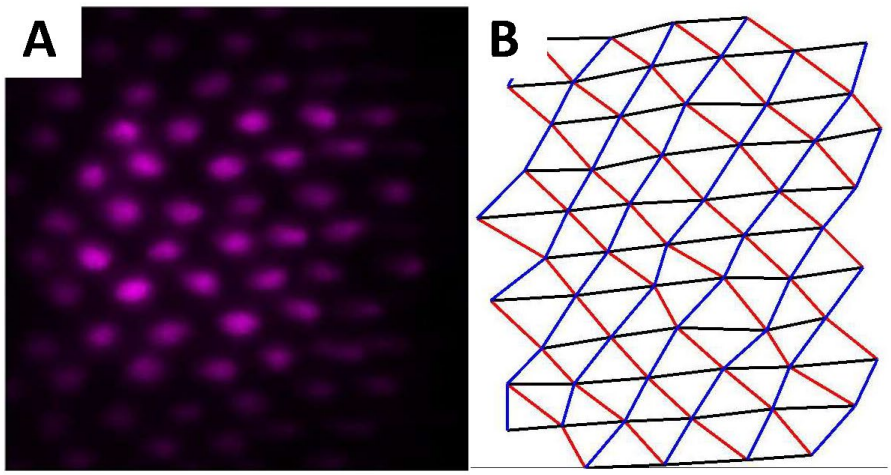
A
B

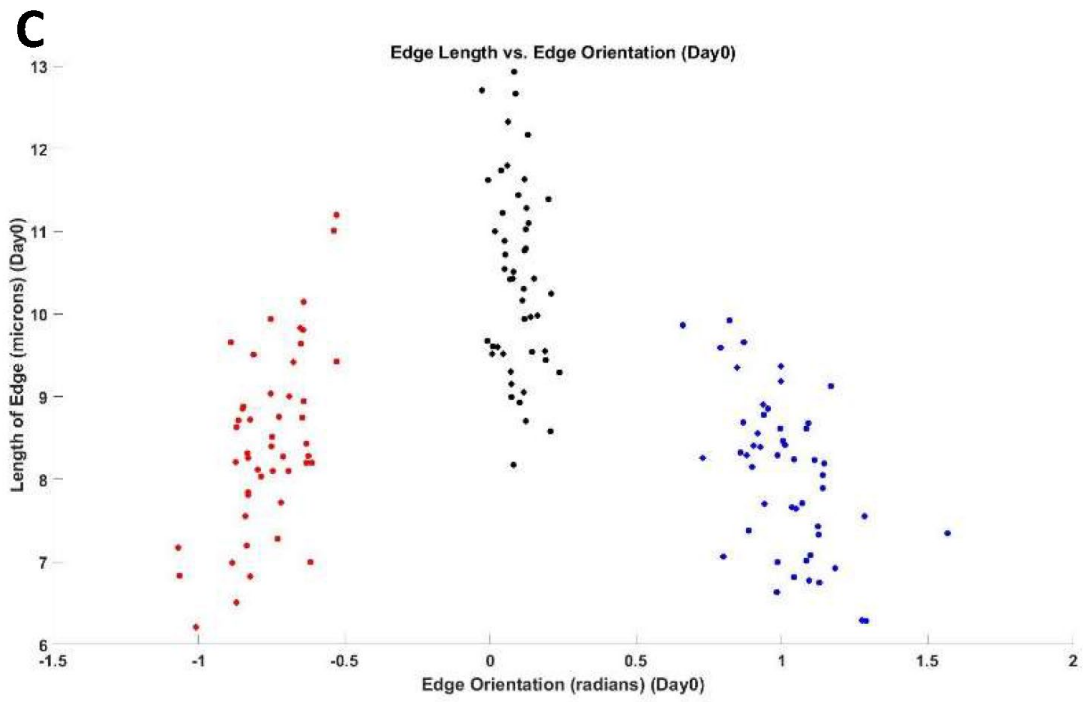
C
Edge Length vs. Edge Orientation (Day0)
Length of Edge (microns) (Day0)
Edge Orientation (radians) (Day0)
13
12
11
10
9
8
7
6
-1.5
-1
-0.5
0
0.5
1
1.5
2

Figure A.3 (Continued)

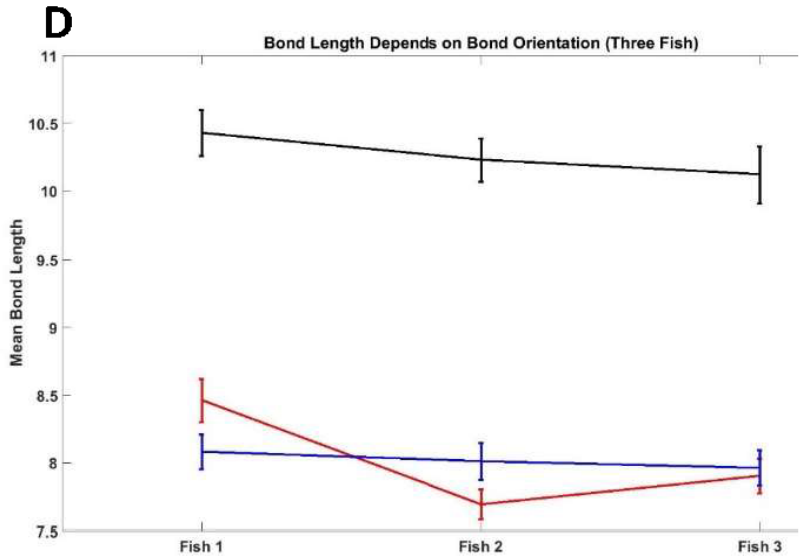

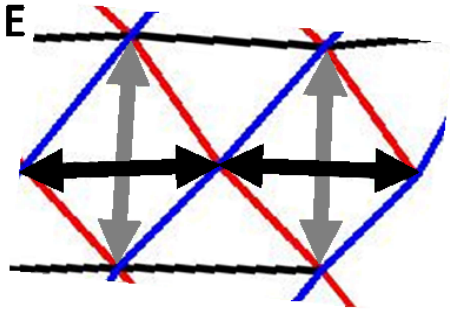

$$\frac{Gray\ arrow}{Black\ arrow} = \frac{Column\ spacing}{Row\ spacing} \approx \frac{12\frac{1}{4}\ \mu m}{10\frac{1}{4}\ \mu m} < \sqrt{3}$$

Figure A.4 **Distribution of Red and Green cones near Y-Junction core. A)** Two Y-Junctions (asterisks) in flat-mount retinal preparation from an adult, triple transgenic (Tg[*sws2:GFP*; *trβ2:tdTomato*; *gnat2:CFP*]) fish. Blue cones express a fluorescent reporter (pseudo-colored blue) under control of the Blue opsin promoter *sws2*, and Red cones express a fluorescent reporter (pseudo-colored red) under control of the *trβ2* promoter. All cones express an additional fluorescent reporter under control of the *gnat2* promoter. Although UV and Green cones do not express different fluorescent reporters, these two cone subtypes are morphologically distinguishable. **B)** Nodes of graph are Red cones from panel A, and edges connect nearest neighbors in honeycomb lattice. Note the existence of a heptagon-pentagon pair (*i.e.*, a 'glide' dislocation) in both defect cores. **C)** Nodes of graph are Green cones from panel A, and edges connect nearest neighbors in honeycomb lattice. Note the existence of an octagon (*i.e.*, a 'shuffle' dislocation) in both defect cores. **D-F)** Another example of a Y-Junction from flat-mount retinal preparation from same double transgenic line (akin to panels A-C).

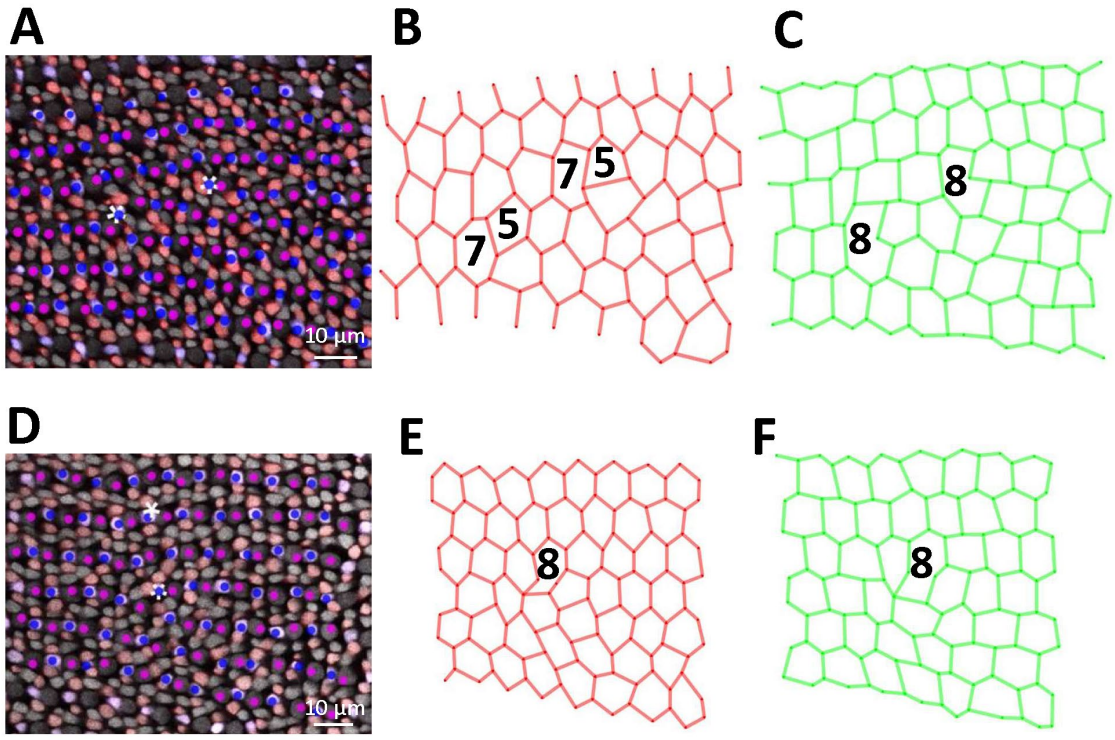

Figure A.5 **Algorithm for identification of grain boundaries. A-C)** For each of three flat-mounted retinae, image on left-hand side is of all identified Y-junctions, (yellow dots). Image on right-hand side is all Y-junctions that our algorithm identified as in a grain boundary. Panel A is fish 3 (total number of Y-Junctions = 221; number of Y-Junctions in grain boundaries = 105). Panel B is fish 4 (total number of Y-Junctions = 275; number of Y-Junctions in grain boundaries = 132). Panel C is fish 8 (total number of Y-Junctions = 285; number of Y-Junctions in grain boundaries = 144), the retina in Figs. 2.3, 2.6.

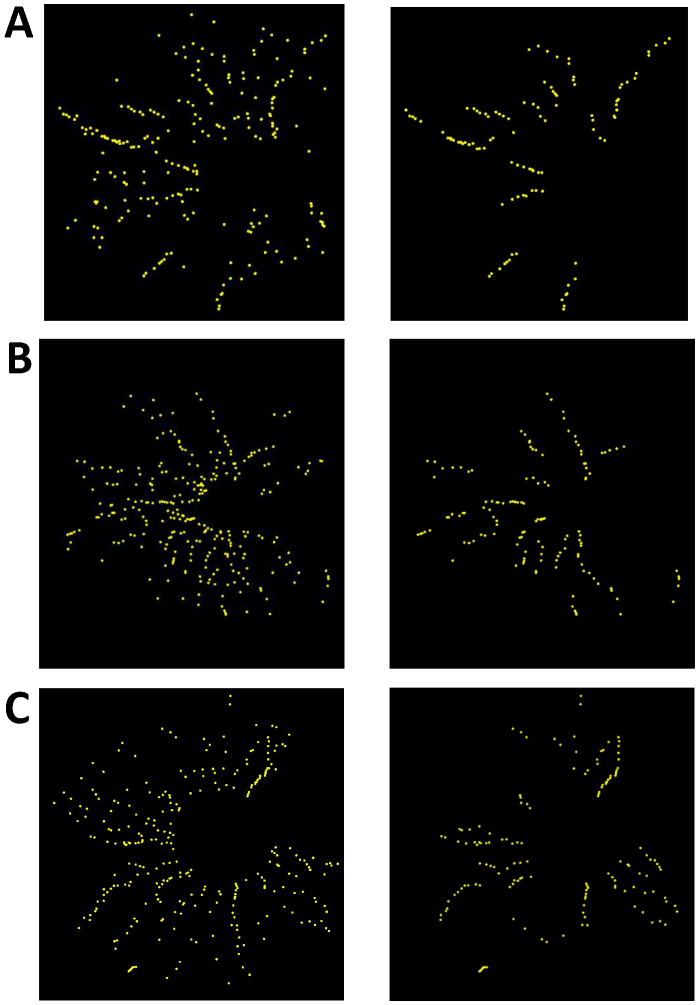

Figure A.6 **Climb motion requires creation or annihilation of vacancies or interstitials, that have no analog in the cone mosaic. A)** The creation of a vacancy allows dislocation to climb (i.e., move perpendicular to Burgers vector). The lattice in panel 1 has a dislocation. Photoconverted UV cones are magenta, and non-photoconverted UV cones are yellow. Panel 2 is triangulation in panel 1 with a new vacancy. Gray arrow is where the vacancy will hop, to create distribution

in Panel 3. Gray arrow in Panel 3 is where the vacancy will hop, to create distribution in Panel 4. As the vacancy hops, the defect core moves (i.e., perpendicular to the Burgers vector). **B)** Vacancy in the cone mosaic (two missing Red cones, two missing Green cones, one missing Blue cone, and one missing UV cone) can be destroyed. Red cone in Panel 1 must move as indicated by gray arrow to create distribution in Panel 2. Movements denoted by gray arrows in Panel 2 allow for vacancy to close, and for defect to move. Panel 3 corresponds to distribution of cones after destruction of vacancy. **We never observe a vacancy (involving two missing Red cones, two missing Green cones, one missing Blue cone, and one missing UV cone) in the cone mosaic, and thus consider climb motion to be irrelevant to be irrelevant for our system.**

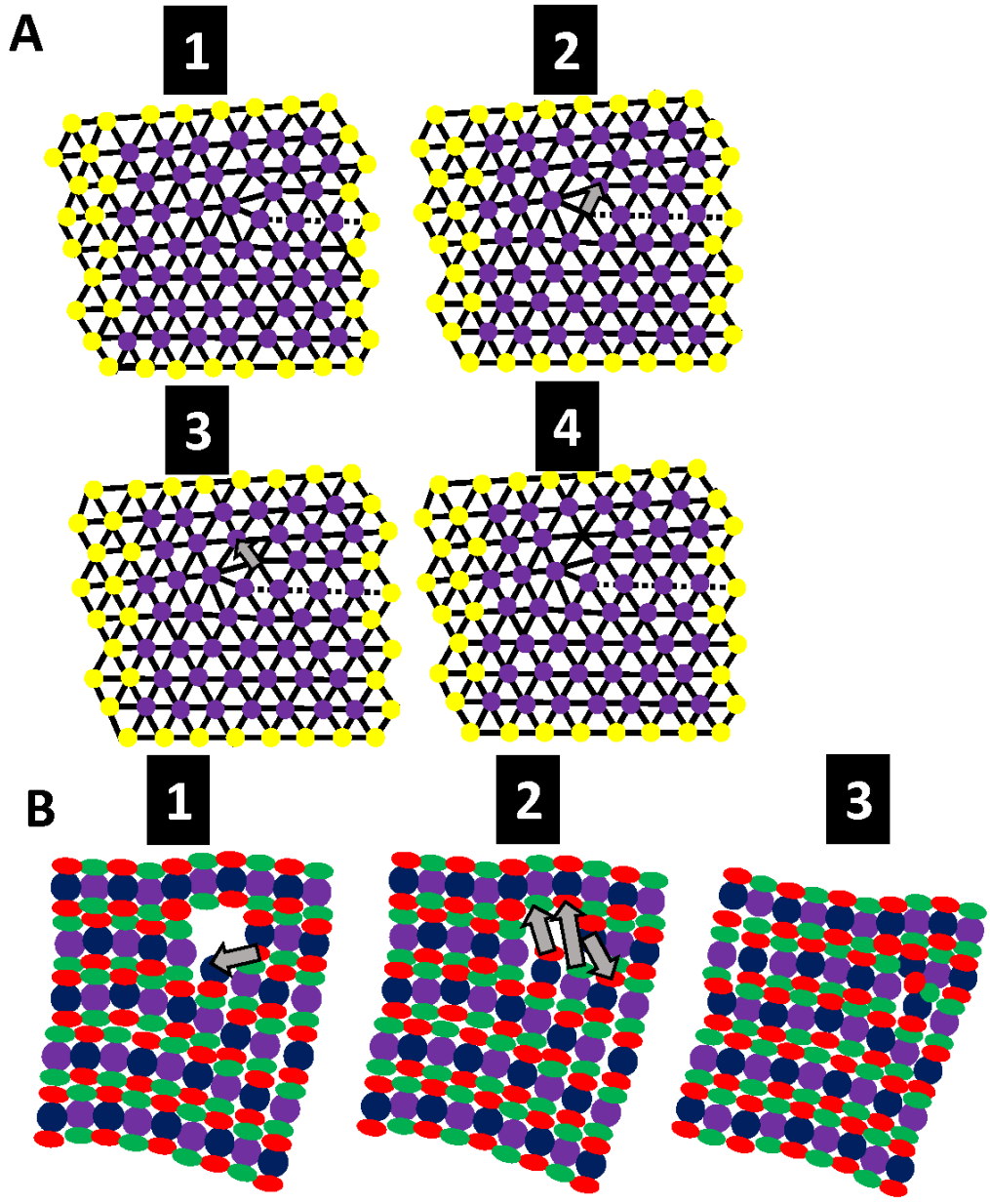

Figure A.7 **Examples of photoconverted retinae with grain boundaries growth during initial cone mosaic formation. A)** We trace rows of UV cones (white dashed lines) near Y-Junctions. Yellow dots: Y-Junctions observed immediately after photo-conversion. White dots: Y-Junctions observed in newly incorporated after two days (newly incorporated). Double-sided black arrow: newly incorporated UV cone columns. This is grain boundary 1 in Fig. 2.5E. **B)** Grain boundaries 4-1 and 4-2 in Fig. 2.5E.All row tracing and Y-Junctions denoted in same way as in panel A.

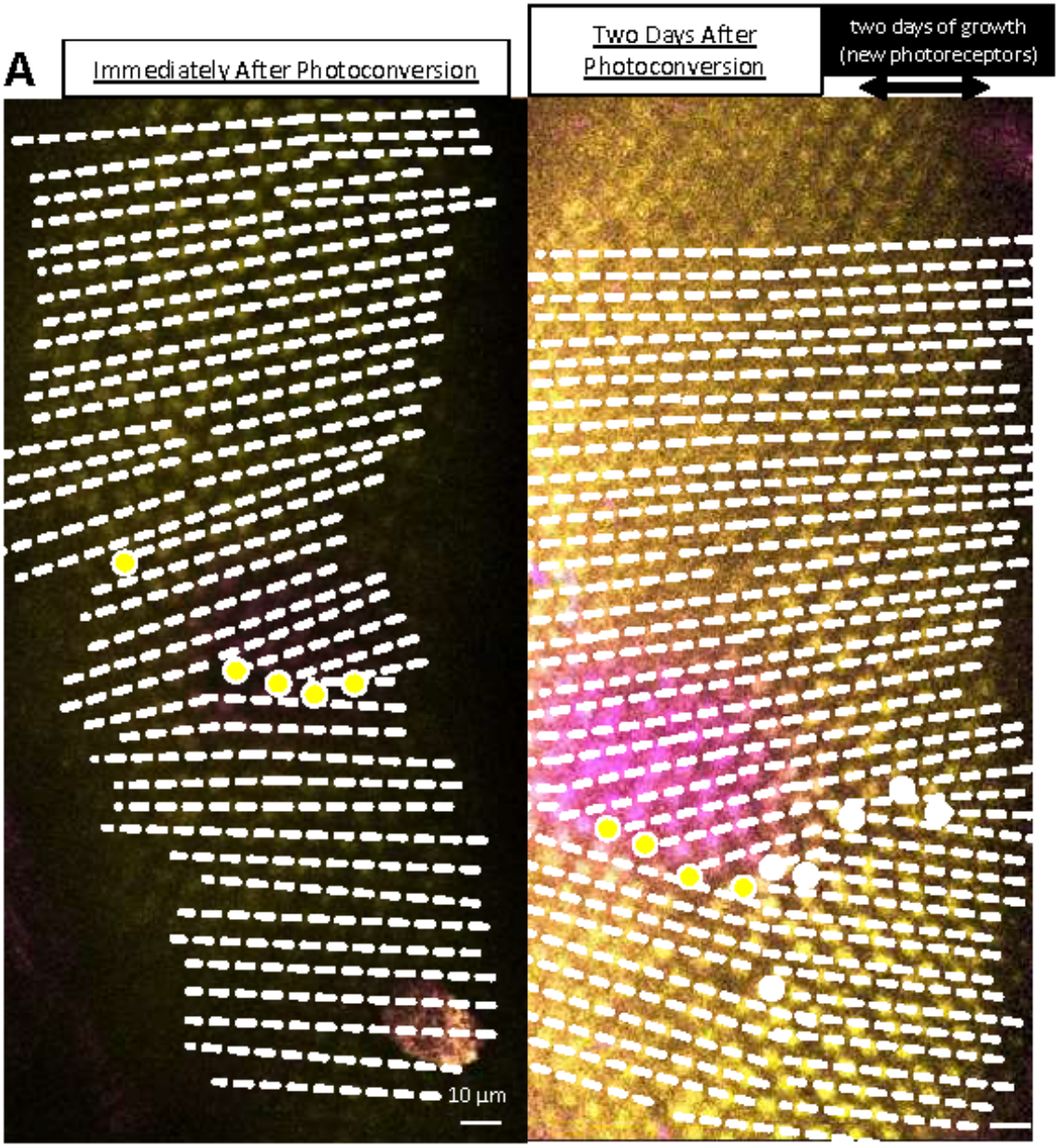

Figure A.8 **Mutation in the *trβ2* deletes Red cones, but not other cone subtypes. A)** Immunocytochemistry for cone subtype specific opsins, including Red opsin (red), Green opsin (green), Blue opsin (blue), and UV opsin (yellow) in wild-type and *trβ2* mutant retinas. **B)** Flat-mount retinal preparation of *trβ2* mutant immunostained with ZO1 (green). Profiles of UV cone are large and rounded (see Fig. 2.6C-D). White dashed lines: some rows of UV cones .

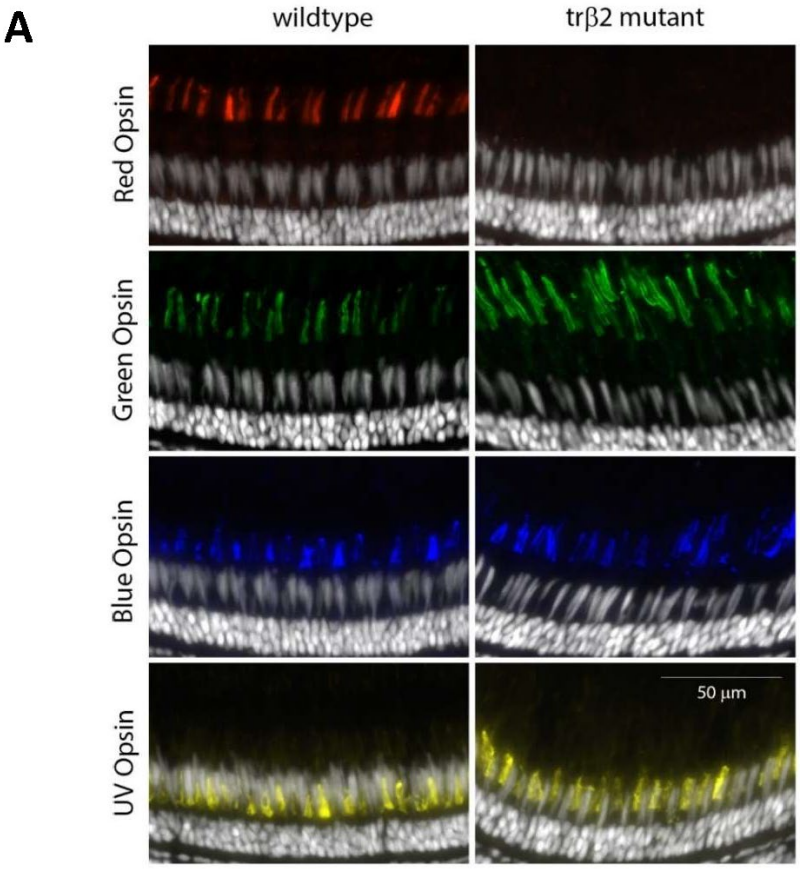

Figure A.9 (Continued)

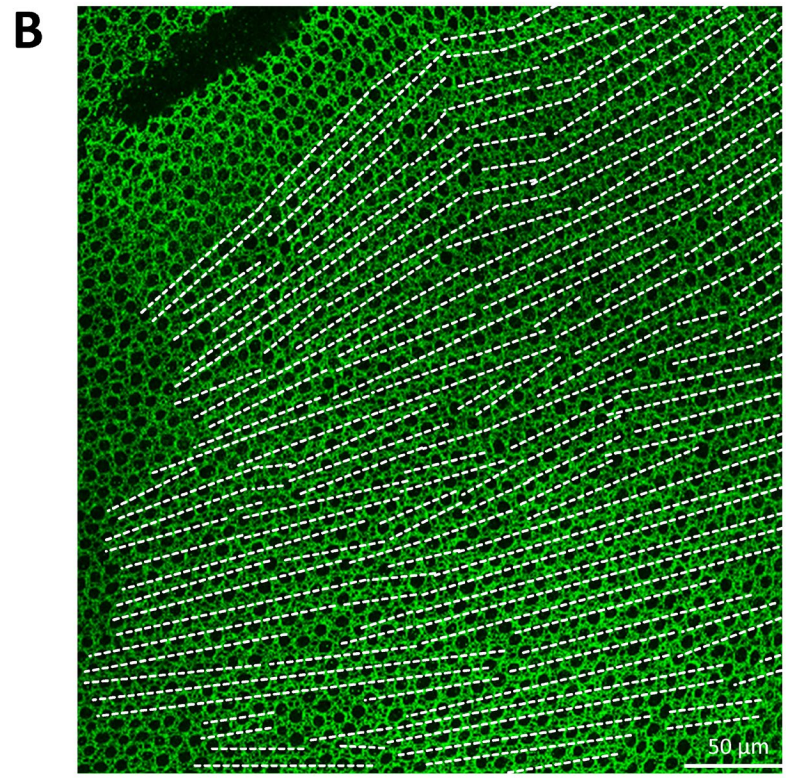

Figure A.10 **Scanning Parameters of Phase-Field Crystal Model.** We take a one-dimensional cut of two-dimensional phase diagram of phase-field crystal model ($\psi_0 = \frac{-\sqrt{-r}}{2}$), where ψ_0 is the mean of density modulation field and where r is the undercooling parameter. The number of initial rows on the cone frustum is two hundred. Approximately ninety-five columns exist from top of the cone frustum to bottom. About two row insertions per added column are necessary to maintain constant cell-cell spacing. The degree of anisotropy is constrained by Fig. A.2. **A)** Standard deviation of white noise field, added to the first two columns, in these simulations is three-quarters. Along the one-dimensional cut of PFC phase diagram, we measure the fraction of seven-coordinated particles in grain boundaries. **B)** Standard deviation of white noise field in these simulations is one. Along the one-dimensional cut of PFC phase diagram, we measure the fraction of seven-coordinated particles in grain boundaries. **C)** For same simulations in panel A, we plot the number of seven-coordinated particles. **D)** For same simulations in panel B, we plot the number of seven-coordinated particles.

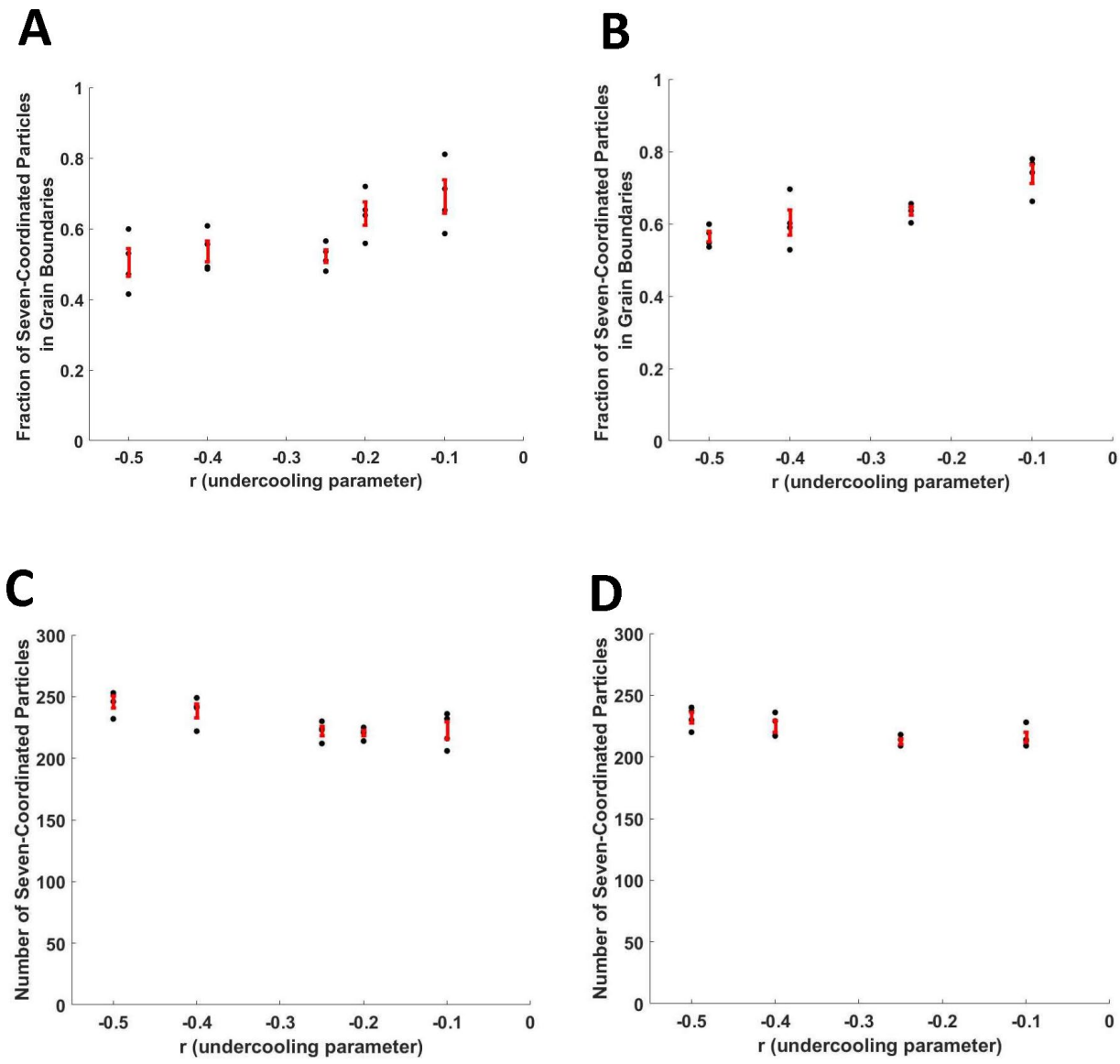

Figure A.11 **Additional insights generated by phase-field model of cone mosaic formation. A)** Example of isotropic crystal growth on cone frustum with an initial column as prepattern. All seven-coordinated particles are yellow dots. Note the lines of seven-coordinated particles that do not radiate from the center of the cone to the periphery (example within red oval). These non-radiating lines of seven-coordinated particles result from a rotation of crystallographic orientation during growth of the isotropic crystal, not observed in zebrafish retinae. **B)** Example of anisotropic crystal growth on cone frustum with no initial column as prepattern. With only white noise at the top of the cone in initial conditions, the anisotropy of the crystal (*i.e.*, in the phase-field crystal free energy) selects and maintains the orientation during growth (in contrast with panel A). Even when a domain forms with improper orientation (example within red oval), the domain rotates to proper orientation during growth. **C)** Zoomed-in snapshot of an anisotropic phase-field crystal simulation on a cone. Note that near grain boundaries (*i.e.*, where the domain rotation rotates), there is a lag in proper positioning of UV cones (*i.e.*, density field remains poorly resolved) relative to growth of neighboring domains. This results in a characteristic V-shape.

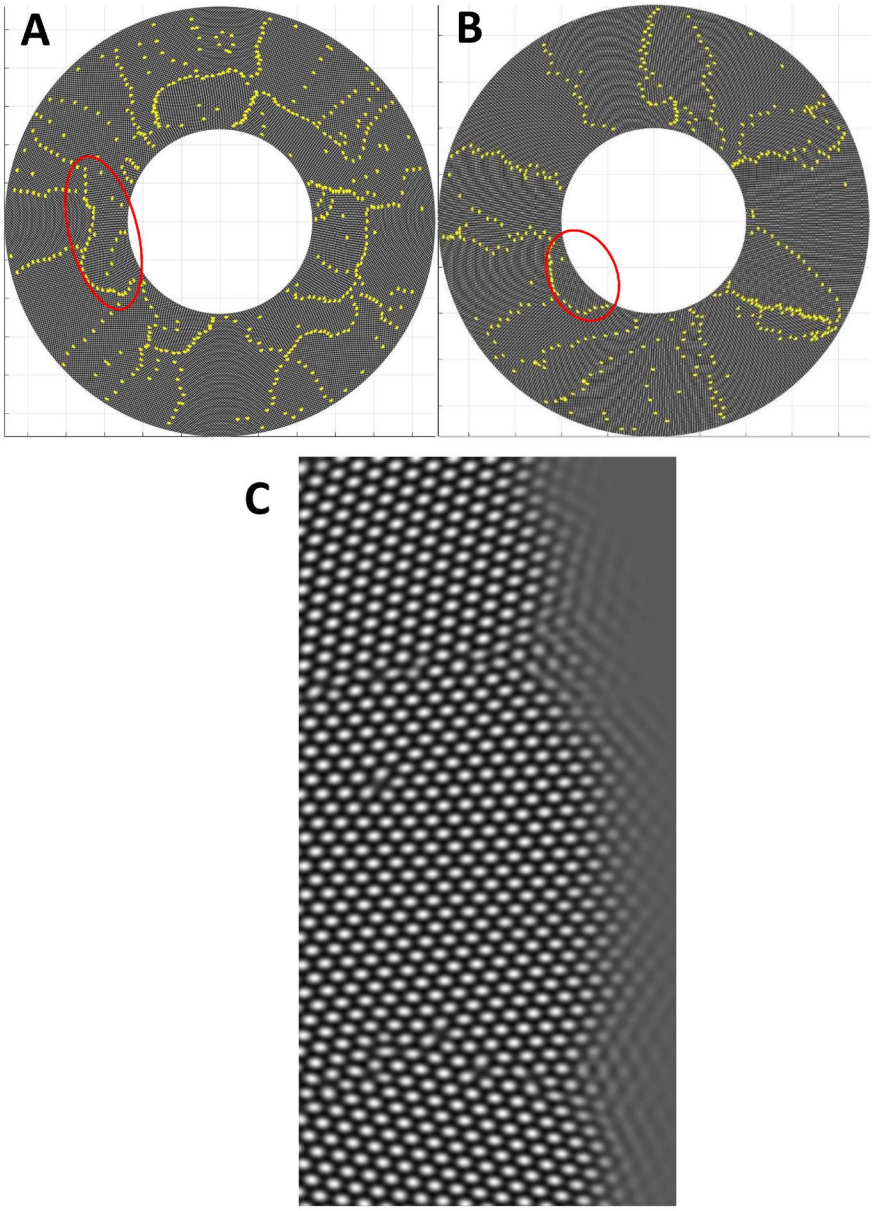

Figure A.12 **Lateral inhibition, with varying signaling ranges, in a disordered cell packing.** Triangular lattice of $u \approx 1$ cells forms on a square packing of 20000 cells with periodic boundary conditions. Defects (i.e., seven-coordinated) in

triangular lattice of $u \approx 1$ cells are yellow dots. Initially, all cells are in state ($u = 0$) because an external inhibiting signal is provided to all cells. Starting at $t = 0$, a wave of de-inhibition moves from left to right (see Methods). The wave moves at a speed $v = \frac{l}{4\tau}$ where τ is the timescale of cell differentiation and l is the range of cell-cell signaling. In each panel, black arrow is the direction of wave propagation. **A)** The signaling range is $3\sqrt{A_0}$, where A_0 is the mean cell area. This signaling range results in seven to eight $u \approx 0$ cells between each pair of neighboring $u \approx 1$ cells in the final pattern. Note that some defects are generated early in pattern formation (i.e., left side of packing), but the right side of the packing contains no defects. **B)** The signaling range is $1.75\sqrt{A_0}$. This results in about five $u \approx 0$ cells between each pair of neighboring $u \approx 1$ cells in the final pattern. The entire packing contains defects. **C)** The signaling range is $1\sqrt{A_0}$, comparable to lattice spacing in the cone mosaic. This results in one to two $u \approx 0$ cells between each pair of neighboring $u \approx 1$ cells in the final pattern. The entire packing contains defects. This image is enlarged relative to panels A-B for the sake of clarity.

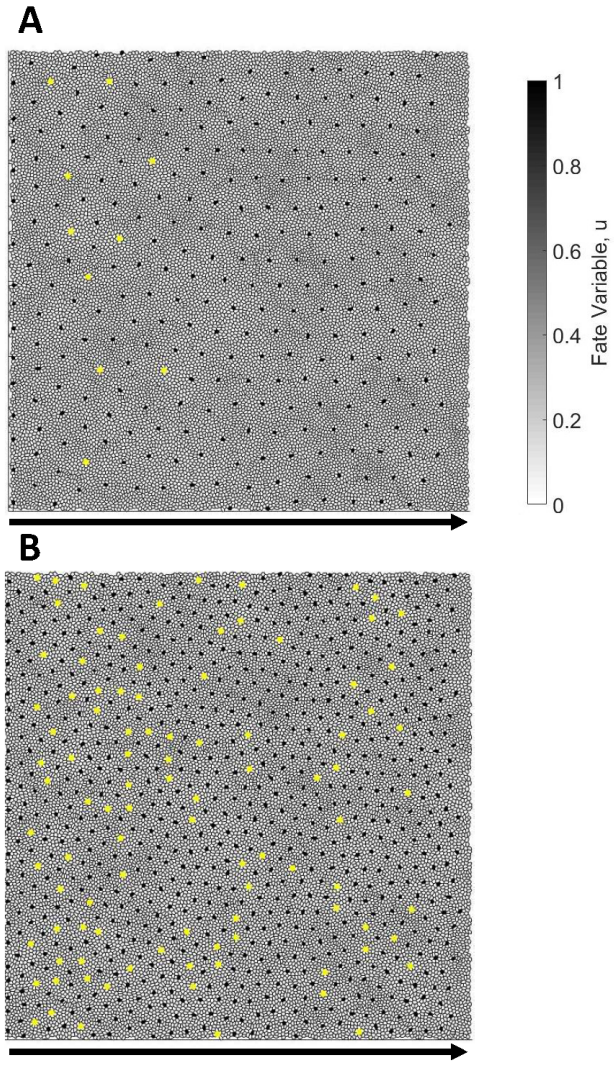

Figure A.13 (Continued)

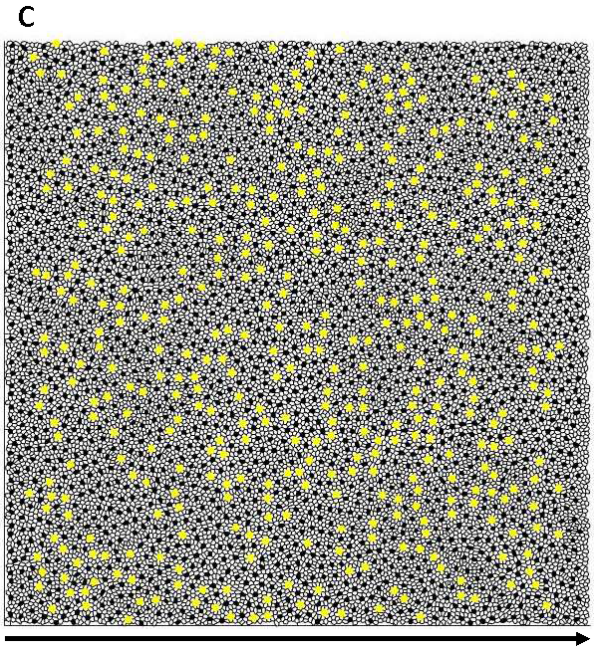

Table A.1 Counts of reverse Y-Junctions (i.e., row deletions) in regions of the retinae in which we traced rows. The same fish numbers are in Fig. 2.3E. ***There is a large-angle grain boundary in this retina, where patterning of the cone mosaic is slightly disrupted. There are potentially 10 additional reverse Y- Junctions associated with that large-angle grain boundary.**

Fish #	Number of (forward) Y-Junctions	Number of reverse Y-Junctions
1	155	0
2	166	5
3	221	0
4	275	5
5	249	14
6	184	2
7	182	10*
8	285	7

Table A.2 Motion of Defects within Photoconverted Region. Here we quantify the motion of Y-Junctions in photoconverted regions. The fish labels are the same as in Fig. 2.5E. Note that some fish are missing from this list (e.g., 4 and 8). These are fish that have grain boundaries in neighboring non-photoconverted regions, but do not have defects in the photoconverted region itself. For each fish, we fit UV cone nuclei positions in the photoconverted regions to a plane in order to compute a triangulation. Because the photoconverted region is small relative to the radius of curvature of the retina, the UV cone nuclei positions are well fit (as quantified by RMSE) by a plane at both imaging times. In UV cone triangulations, we check for bond flips near the defect core between photoconversion and later imaging (see Methods). If a Y-Junction glides by one row, we denote that with a 1, and if a Y-Junction does not glide, we denote that with a 0.

Fish Label	# of Y-Junctions in Photoconverted Region	Days between Photoconversion and Later Imaging	RMSE for Fit Plane at Day 0 (μm)	RMSE for Fit Plane at later imaging (μm)	Glide Motion of Defect(s) In Units of Rows
1	2	2	0.85	0.63	(0, 0)
2	1	2	0.76	0.55	0
3	2	2	0.50	0.42	(0, 0)
5	1	2	0.70	0.26	1
6	1	2	1.0	0.59	0
7	1	2	0.48	0.63	1
9	1	2	0.96	0.53	0
10	2	3	1.1	0.62	(0, 1)
11	1	4	1.8	0.82	0
12	1	4	1.5	0.74	1
13	1	2	0.85	0.31	1
14	1	2	0.90	1.1	0
15	1	2	1.2	0.45	1

Table A.3 New Y-Junctions are incorporated preferentially near existing grain boundaries in live fish. Fish labels are same as in Fig. 2.5E and A.3. We list the number of Y-Junctions incorporated between photoconversion and later imaging (within the whole image, not just within grain boundary). We list the expected average distance along the margin axis between a new Y-Junction and its nearest grain boundaries if new Y-Junctions positions are uncorrelated with positions of existing grain boundaries. We, then, list the actual distances along the margin axis between each newly incorporated Y-Junctions and its nearest existing grain boundary in the image. Fish 8 is omitted because, within the image, no new Y-Junctions are added between photoconversion and subsequent imaging.

Fish Label	# of Y-Junctions Added Between Photoconversion and Later Imaging	Mean Distance Between New Y-Junction and Nearest GB if Uncorrelated (μm)	Median Distance Between New Y-Junction and Nearest GB if Uncorrelated (μm)	Actual Distance Between new Y-Junctions and GB (μm)
1	6	84	73	[9, 2, 15, 12, 12, 46]
2	2	91	73	[24, 4]
3	3	87	73	[1, 2, 65]
4	4	45	44	[24, 1, 5, 1]
5	1	73	73	1
6	2	75	73	[4, 1]
7	3	74	73	[11, 123, 42]
9	2	73	73	[18, 20]
10	2	94	78	[2, 2]
11	8	43	39	[12, 23, 45, 1, 0, 95, 20, 69]
12	3	39	36	[5, 11, 36]

Appendix B Further Discussion of Apical Stress Fibers in Drosophila

In this supporting text, we describe biophysical models that we have developed to understand the behavior of apical stress fibers (aSFs) in epithelia and some experimental tests of the models' predictions. Section B.1 introduces a model of how aSFs affect the force balance in epithelial tissues under uniaxial stress and thereby help cells to resist elongation. We use this model to predict that for large cells to resist elongation as effectively as small cells, the total aSF tension per cell (proportional to the number of aSFs) must increase with apical area (Fig. 3.2K). We experimentally confirmed this increase of aSF number with apical area in wild-type tissues (Fig. 3.4N).

Based on the results of our time-lapse imaging, in Section B.2 we develop a geometrical model of aSF nucleation and breakage. This geometrical model, based on the role of tricellular junctions (TCJs) in aSF nucleation and breakage, explains approximately 75 percent of the observed increase of aSF number with cell apical area at 26 h APF. In Section B.3, we test this geometrical model by generating cells of similar apical area but with different numbers of TCJs; we find that, as the model predicts, a dependence of aSF number on the number of TCJs, not just on cell apical area, is required to explain the data. We also show that our model is consistent with observations on cells of a peculiar geometry: those elongated orthogonal to the tensile uniaxial stress. In Section B.4, we discuss biophysical hypotheses for the mechanisms leading to aSF nucleation primarily at TCJs with a certain orientation.

1. Mechanical model for the role of aSFs in resisting cell elongation

To gain a physical understanding of the implications of adding aSFs to epithelial cells under uniaxial mechanical stress, we build on an existing 2D mechanical model of epithelial tissues. The mechanical model that we modify, called a vertex model [247-249], has been successfully used to describe a diverse set of developmental processes in *Drosophila* and other model organisms [24, 51, 86, 247, 248, 250, 251]. In vertex models, the epithelium is represented as a tiling of the plane by polygonal cells; each polygon edge has a contractile tension, which

provides resistance against external mechanical stresses. Here, to model the presence of aSFs, we incorporate additional contractile structures that span the cell and are aligned with the axis of imposed high tensile stress (Fig. 3.2I and Fig. B.3A,B).

Specifically, we focus on the simplest case of a regular packing of identical, hexagonal cells. Similarly simplified geometries have provided useful insights into cell-cell mechanical interactions in past studies [112, 164, 211], and in our case this model's analytic tractability will allow us to extract a prediction for the aSF tension per cell necessary to resist elongation as a function of apical area. Importantly, we assume that, because aSFs are mobile, they can align with other aSFs or with contractile junctions in neighboring cells (Fig. B.3A,B); this mobility is central aSFs' superiority to junctional tension in limiting cell elongation. It is easy to verify that, if all aSFs are aligned with an appropriate structure in adjacent cells, the same results are obtained whether the aSF tension is all carried by one aSF or is split among multiple aSFs per cell (Fig. 3.2I). Our calculations are thus carried out in terms of the total aSF tension γ_f per cell. Depending on the context, we can thus phrase our results either in terms of γ_f or in terms of the number of aSFs per cell with some fixed tension per aSF (with the latter language, as discussed below, probably a better description of what actually occurs in the dorsal thorax).

With these assumptions, our tissue geometry is specified by two edge lengths and the angle of one edge with the horizontal (Fig. 3.2I and Fig. B.3A,B). In general, the cell packing's response to an imposed uniaxial tension depends on the cells' orientation with respect to the axis of high stress [112]. We perform our calculations for the two distinct limiting cases of this orientation, which we term the 'cable-forming orientation' (CFO) and the 'non-cable-forming orientation' (NCFO) (Fig. B.3A,B). Cells in the CFO become brick-shaped under tensile stress, which favors the formation of supracellular actomyosin cables. Cells in the NCFO elongate under tensile stress and do not form supracellular actomyosin cables. (For a detailed discussion of the response of the CFO and NCFO to uniaxial stress, see [112].) For each orientation we can describe the tissue in terms of six variables: two edge lengths l_i, an edge angle θ or ϕ, two edge tensions γ_i, and the total aSF tension γ_f.

By ablation of aSFs, we estimate that the tension per aSF is roughly independent of cell apical area (Fig. B.2F); therefore, we conclude that cell-to-cell variability in total aSF tension depends primarily on differences in aSF number rather than on differences in individual aSF tensions. However, as discussed above, in the model we keep track only of the total aSF tension

γ_f, and we view multiple aSFs in the same cell as behaving the same as a single, lumped aSF with the corresponding γ_f. Although our model simplifies the dynamics and organization of aSFs, it will provide a testable prediction for the relationship between cell apical area and the number of aSFs per cell required for cells to remain regular under uniaxial stress.

Mathematical formulation of vertex model with tensile aSFs

There are four physical constraints relating the six variables that describe each cell (Fig. B.3A,B). We assume that the cells are incompressible with a constant, given apical area A:

$A = 2\, l_1 \sin(\theta)\, (l_2 + l_1 \cos(\theta))$ (CFO); [Eq. 1]

$A = 2\, l_4 \cos(\phi)\, (l_3 + l_4 \sin(\phi))$ (NCFO). [Eq. 2]

For the tissue to be in mechanical equilibrium, tension forces at each vertex must balance:

$\cos(\theta) = \frac{\gamma_2}{2\,\gamma_1}$ (CFO); [Eq. 3]

$\sin(\phi) = \frac{\gamma_3 - \gamma_f}{2\,\gamma_4}$ (NCFO). [Eq. 4]

(Please note that because all cells are identical, any pressures conjugate to cell area drop out of the force balance equations and can be neglected.) We assume that the tension on each edge and aSF is proportional to the concentration of Myosin II (MyoII) on that edge and that the total amount λ of MyoII per cell is fixed per cell but may be redistributed from one edge or aSF to another. This assumption is certainly an oversimplification but reflects the essential fact that cell resources are limited and thus infinite reservoirs of MyoII are not available to counteract imposed mechanical stresses. This assumption implies the constraint:

$\lambda = 2\,\gamma_1 l_1 + \gamma_2 l_2 + \gamma_f (2 l_1 \sin(\theta))$ (CFO); [Eq. 5]

$\lambda = 2\,\gamma_4 l_4 + \gamma_3 l_3 + \gamma_f (l_3 + 2 l_4 \sin(\phi))$ (NCFO). [Eq. 6]

Finally, the difference $\sigma_D = \sigma_{yy} - \sigma_{xx}$ between the externally imposed vertical and horizontal stresses on the tissue is viewed as a fixed parameter and is related to the other six variables by (Fig. B.3C):

$\sigma_D = \frac{\gamma_1 \sin(\theta) + \gamma_f}{l_2 + l_1 \cos(\theta)} - \frac{\gamma_2}{2\, l_1 \sin(\theta)}$ (CFO); [Eq. 7]

$\sigma_D = \frac{\gamma_3 + \gamma_f}{2\, l_4 \cos(\phi)} - \frac{\gamma_4 \cos(\phi)}{l_3 + l_4 \sin(\phi)}$ (NCFO). [Eq. 8]

Given these four constraints, we have two free parameters in the model, which we generally take to be the aSF tension and one of the two edge tensions.

We are interested in the relation between cell elongation and aSF number. Our measure of elongation is $S = P/\sqrt{A}$, where P is the cell perimeter [252-254]. In this packing of identical, hexagonal cells, larger values of S imply that a polygon is more elongated. S is a mathematically convenient measure of cell elongation because S has a physically relevant global minimum when the hexagons are neither elongated along the uniaxial stress nor elongated orthogonal to this stress. If we had chosen a measure that tracks elongation specifically along the uniaxial stress, minimizing that measure of cell elongation would maximally elongate cells orthogonal to the uniaxial stress, generating a singular and physically irrelevant cell geometry. For cells in the CFO,

$S(\gamma_2, \gamma_f; \sigma_D, A, \lambda) = \frac{\lambda - A\sigma_D}{\sqrt{A}\gamma_2} + \frac{\lambda + A\sigma_D}{\sqrt{A}\,(\tan(\theta) + 2\gamma_f)}\left(\frac{2 - \cos(\theta)}{\sin(\theta)}\right)$, where $\tan(\theta) = \frac{\lambda^2 - A^2{\sigma_D}^2}{2{\gamma_2}^2 A} - 2\frac{\gamma_f}{\gamma_2}$. [Eq. 9]

For cells in the NCFO,

$S(\gamma_3, \gamma_f; \sigma_D, A, \lambda) = \frac{\lambda + A\sigma_D}{\sqrt{A}\,(\gamma_3 + \gamma_f)} + \frac{(\lambda - A\sigma_D)\tan(\phi)}{\sqrt{A}\,(\gamma_3 - \gamma_f)}\left(\frac{2}{\cos(\phi)} - \tan(\phi)\right)$, where $\tan(\phi) = \frac{2A({\gamma_3}^2 - {\gamma_f}^2)}{\lambda^2 - A^2{\sigma_D}^2}$. [Eq. 10]

The maximum value of the stress anisotropy allowed in our model is $\sigma_{max} = \lambda/A$. This is a consequence of having restricted both the apical cell area and the total amount of MyoII, which effectively limits the tension per unit length that can be obtained in the system.

Mechanical model predicts increase of aSF number with apical area

At a fixed apical area, we determine the minimal cell elongation as a function of the tissue stress anisotropy and total aSF tension per cell by minimizing $S(\gamma_i, \gamma_f; \sigma_D, A, \lambda)$ with respect to the value of the tension on the high-tension edge γ_i. We show the results of this minimization in Fig. B.3D-H, where we have normalized the cell elongation by the elongation of a regular hexagon ($S_{reg,hex} = \frac{P}{\sqrt{A}} = 6/\sqrt{\frac{3\sqrt{3}}{2}}$) and the stress anisotropy σ_D by σ_{max}; note that the results expressed in this nondimensionalized fashion are independent of A and λ. Under uniaxial stress, if cells have no aSFs, it is not possible for cells to remain regular hexagons (Fig. B.3F). In both the CFO and the NCFO, we find that the presence of aSFs reduces elongation at fixed total MyoII λ; that is, aSFs are more effective in resisting cell elongation than simply upregulating tension on cell-cell junctions. For minimizing cell elongation, cells in the NCFO benefit more from redistributing junctional MyoII to aSFs than cells in the CFO do (Fig. B.3F).

In both orientations and for any allowable stress anisotropy, there exists some distribution of MyoII between the edges and aSFs such that the cell is a regular hexagon (*i.e.*, normalized elongation parameter equal to one). At minimal cell elongation, we can exploit the following geometric constraints:

$l_1 = l_2$ and $\theta = \pi/3$ (CFO); [Eq. 11]

$l_3 = l_4$ and $\phi = \pi/6$ (NCFO). [Eq. 12]

to find an analytic solution for the distribution of MyoII between the edges and the aSFs. In the NCFO,

$$\gamma_3 = \sqrt{\frac{\sqrt{3}}{6}}\frac{\lambda}{\sqrt{A}}; \quad \text{[Eq. 13]}$$

$$\gamma_{fNCFO} = \sqrt{\frac{\sqrt{3}}{6}}\sqrt{A}\sigma_D; \quad \text{[Eq. 14]}$$

$$\gamma_4 = \gamma_3 - \gamma_{fNCFO}. \quad \text{[Eq. 15]}$$

In the CFO,

$$\gamma_1 = \gamma_2 = \sqrt{\frac{\sqrt{3}}{6}}\left(\frac{\lambda - A\sigma_D}{\sqrt{A}}\right); \quad \text{[Eq. 16]}$$

$$\gamma_{fCFO} = \sqrt{\frac{\sqrt{3}}{2}}\sqrt{A}\sigma_D. \quad \text{[Eq. 17]}$$

In both orientations (Eq. 14 and Eq. 17), for the cells to remain regular hexagons under uniaxial stress, the total aSF tension per cell must be proportional to $\sqrt{A}\sigma_D$. Since in the dorsal thorax the tension per aSF does not depend on apical area (Fig. B.2F), large cells need more aSFs per cell than small cells to resist elongation under the same stress anisotropy. This finding is reminiscent of the fact that a dry foam of large bubbles is less resistant to extensional shear than a dry foam of small bubbles [255, 256]. Since two-dimensional stress is a measure of force per length (Fig. B.3C), to remain regular hexagons, larger cells must compensate for the greater distance between edges by increasing the number of aSFs.

In summary, our mechanical model provides three predictions. First, at constant apical area and stress, cells with no aSFs will be less elongated in the CFO than in the NCFO [257]. Second, at constant apical area, stress, and orientation, cells with more aSFs are less elongated along the axis of high tensile stress than cells with fewer aSFs. Lastly, at constant stress and minimal cell elongation, larger cells will have more aSFs. Since the tissue of interest (Fig. 3.1C) is disordered, it is difficult to apply these predictions directly to experimental data. We do, however, test a broad

claim of the model: for cells to resist elongation due to tensile stress, the number of aSFs per cell must increase linearly with the square root of the apical area (Fig. B.3I). Over the range of observed wild-type cell sizes, the square root of the apical area is linear in the area to a very good approximation (Fig. B.3J), so we use cell apical area, the more biologically intuitive measure of cell size, to test this model claim.

We confirm in Fig. 3.4N that the number of aSFs per cell linearly increases with apical area at 26 h APF. The 95% confidence interval for the linear regression coefficient is $(0.058\ \frac{aSF}{\mu m^2}, 0.061\ \frac{aSF}{\mu m^2})$. Via an F-test [258, 259], we find that the regression coefficient is significantly different than zero ($p < 10^{-50}$). Based on our vertex model with aSFs (Eq. 14 and Eq. 17), we hypothesize that the wild-type linear increase of aSF number with cell apical area is necessary for large cells to resist cell elongation as effectively as small cells; in the main text, we test this hypothesis by showing that cell elongation is independent of apical area in control w^{RNAi} cells at 26 h APF (Fig. B.2I). Then, as predicted by our mechanical model, we show that when the scaling of aSF number with apical area is much weaker than the control w^{RNAi} scaling (Fig. 3.2L), larger cells elongate more than smaller cells (Fig. 3.2Q and Fig. B.2I).

2. Geometrical model of aSF nucleation and breakage

In this section we use time-lapse imaging of cells in the tissue of interest to develop a phenomenological model of how cell geometry affects the number of aSFs in individual cells. In these time-lapse images, MyoII:GFP marks the junctional cortex and aSFs, and E-Cad:3xmKate2 marks the adherens junctions (AJs). We find that aSFs nucleate from TCJs in an orientationally dependent manner: if a TCJ's bisecting vector in a cell points mostly along the anterior-posterior axis, aSFs tend to nucleate from that TCJ into that cell (Fig. 3.4G-J). Based on this aSF nucleation criterion, we first construct a model in which the aSF nucleation rate in a cell is proportional to the number of aSF-nucleating TCJs and in which all aSFs have the same mean lifetime. As observed in time-lapse imaging (Fig. 3.4L), this model predicts that larger cells have higher aSF nucleation rates per cell. However, the model shows that nucleation effects alone only account for approximately 15 percent of the wild-type scaling of aSF number with apical area (Fig. B.6I).

Since a model of aSF nucleation rates alone cannot adequately explain the wild-type scaling of aSF number with cell apical area, we analyze how aSF breakage rates depend on cell apical area. We find that aSFs in larger cells have longer lifetimes, on average, than aSFs in smaller

cells (Fig. 3.4M). To build a coarse-grained model of aSF breakage, we track aSFs from nucleation to breakage. We find that aSFs tend to break at TCJs (Fig. 3.4G-J). For the TCJs at which aSFs break, the bisecting vectors within the cell of interest point mostly along the medial-lateral axis (Fig. 3.4G-J). Based on these observations of aSF nucleation and breakage at TCJs, we construct a phenomenological model in which aSFs move at a constant speed along the anterior-posterior axis from an aSF-nucleating site to aSF-breaking sites. We experimentally constrain all but one of the model parameters. The one free parameter is the average signed distance between the leading aSF tip and breaking TCJ at the time of breakage (see Fig. B.7Q). This cell-autonomous model, with one free parameter, explains approximately 75 percent of the experimentally observed wild-type scaling of aSF number with apical area (Fig. 3.4N); encouragingly, the best-fit value of the one free parameter is on the order of the junctional cortex thickness and is, thus, amenable to a reasonable physical interpretation (Fig. B.7Q).

It is worth emphasizing that all the models in this section are intended to describe cells in tissues where aSF nucleation occurs at an appreciable rate. In *Drosophila* pupal dorsal thorax, such nucleation appears to happen only when the tissue is under substantial uniaxial mechanical tension. Thus, we do not suggest that all TCJs, in any tissue, obeying our geometric criteria can nucleate aSFs. Rather, our models claim that TCJs with an appropriate bisector orientation *and* in a tissue with the requisite mechanical stress will tend to serve as nucleating TCJs. In this section, we do not delve into the question of why mechanical stress together with TCJ orientation favor aSF nucleation, but we discuss some hypotheses and speculations on this point in Section B.4.

aSF nucleation at TCJs

One mechanism by which aSF number in a cell could be controlled by cell geometry is if cells produced aSFs at different rates based on apical area. More specifically, if certain sites act as sites of aSF nucleation, aSF number per cell could be controlled by changing the number of nucleating sites. In time-lapse images of individual cells, we find that aSFs nucleate from the cell cortex near TCJs. Over more than 600 nucleation events, we find that more than 95 percent of aSFs nucleate from a TCJ (Fig. 3.4I). Less than 5 percent of the nucleation events are due to apoptosis or division of a neighboring cell (Fig. 3.4I). In the cases of aSF nucleation during division of a neighboring cell, the cell-cell junction shared with the dividing cell becomes curved,

and the aSF nucleates from the curved region of the cell-cell junction. Indeed, this curved region will become a TCJ after cytokinesis is completed.

Although the association of other force-generating structures with TCJs is well-documented [118, 143, 164, 260-263], to the best of our knowledge, we are the first to describe TCJs as sites of SF nucleation. Contrary to many other examples of SFs, which are mostly stationary [28, 142, 183, 264-270], these aSFs, that nucleate at a TCJ, move along cell-cell junctions towards the center of the cell. Before discussing the dynamics of aSFs after nucleation, we would like to know if specific geometric properties of TCJs determine from which TCJs aSFs nucleate and from which TCJs aSFs do not nucleate.

In this study, to characterize TCJ geometry as a predictor of aSF nucleation, we measure two angles for each pair of adjacent edges that meet at the TCJ: the opening angle, α, between the adjacent edges and the orientation of the bisecting vector, θ, relative to the anterior-posterior axis (Fig. B.6A). We calculate α and θ immediately prior to nucleation for more than 600 nucleation events. We exclude nucleation events due to mitosis or apoptosis of a neighboring cell.

In a mechanically isotropic tissue, rotational symmetry must be respected, so nucleation rates per TCJ must only depend on differences between edge orientations (*i.e.*, opening angle between two edges). Because the dorsal thorax is under anisotropic stress, we expect that the nucleation rate is not simply a function of opening angle but likely also has some θ dependence. Additionally, we expect the results to be invariant under $\theta \to -\theta$ and $\to \pi - \theta$. For this reason, we define θ as $\left|tan^{-1}(\frac{\vec{\mu}\cdot\hat{y}}{\vec{\mu}\cdot\hat{x}})\right|$, where $\vec{\mu}$ is the bisecting vector of the TCJ. The anterior-posterior (a-p) axis corresponds to $\theta = 0$; the axis of medial-lateral (m-l) stress corresponds to $\theta = \frac{\pi}{2}$. Given this definition, we compare the angles α and θ for nucleation events to the angles α and θ of all pairs of adjacent edges, meeting at a TCJ, from still images of the same region of the *Drosophila* dorsal thorax at the same time in development. We quantify whether aSF nucleation events are restricted to certain regions of this two-dimensional space, α and θ.

In Fig. B.6B, we compute the fraction of pairs of adjacent edges, which meet at a TCJ, with angles α and θ in the region of interest in approximately 25,000 cells at 26 h APF. As expected, there is a correlation between α and θ in these tissues under anisotropic stress because cells tend to elongate along the axis of stress [112, 271]. Fig. B.6C shows the fraction of nucleation events as a function of α and θ. In Fig. B.6D, we show the nucleation rate from pairs of adjacent edges

of given α and θ (*i.e.*, the ratio of data from Fig. B.6C to data from Fig. B.6B). In Fig. B.6D, we exclude, indicated by hatching, values of α and θ which are very rarely observed (*i.e.*, value of less than 0.01% in Fig. B.6B).

The nucleation rates from Fig. B.6D appear to be relatively insensitive to opening angle α but strongly dependent on bisector orientation θ relative to the a-p axis. To test the sensitivity of nucleation rate to these two angles, we linearly regress the nucleation rates from Fig. B.6D on both α and θ. Via a *t*-test for the α regression coefficient in this bivariate regression [258, 259], we find that the nucleation rate per TCJ is insensitive to α ($p = 0.07$). Via a *t*-test for the θ regression coefficient [258, 259], we find that nucleation rate per TCJ is sensitive to θ (*i.e.*, the corresponding coefficient in the regression is non-zero; $p < 10^{-15}$). For the remaining analysis, we reduce this problem to one dimension, tracking only θ for each aSF nucleation event.

In Fig. B.6E, we plot the empirical cumulative distribution of the aSF nucleation data versus θ (*i.e.*, the fraction of aSF nucleation events at TCJs with $\theta' < \theta$). Given an image of a cell in the dorsal thorax, based on the θ value of each pair of adjacent edges, we want to predict which TCJs nucleate aSFs and which do not. For the sake of simplicity, we caricature the observed θ-dependence of aSF nucleation as a cutoff, which we calculate based on the 95th percentile of aSF nucleation events shown in Fig. B.6E. This calculation returns a cutoff for aSF nucleation at $\theta \approx \frac{2}{3}$. After reducing the problem of aSF nucleation in epithelia to a one-dimensional cutoff based on TCJ bisector orientation θ, we ask whether and how strongly the number of aSF-nucleating TCJs depends on cell apical area.

Large cells have more nucleating TCJs than small cells

To reach a steady state in which large cells have more aSFs than small cells, large cells could have higher aSF nucleation rates and/or lower aSF breakage rate. Below, we will explore how the tendency of aSF to break at TCJs implies that breakage events are less frequent in larger cells. In this section, however, we first calculate what percentage of the scaling of aSF number with cell apical area can be explained by differences in the number of aSF-nucleating sites alone.

We estimate the rate of aSF nucleation for each cell by counting the number of TCJs that satisfy the aSF nucleation criterion (Fig. B.6E-H). Encouragingly, in our tracking of aSF nucleation in time-lapse imaging, we find that aSF nucleation rate per cell *is* proportional to the number of nucleating TCJs (Fig. B.6G). We assume that the rate of aSF nucleation per nucleating

TCJ is independent of cell apical area. If we further assume that aSFs break at a constant rate γ per time, independent of both cell apical area and of their distance from TCJs, the mean number of aSFs in a cell should be directly proportional to the number of nucleating TCJs in that cell. The constant of proportionality is k_{nuc}/γ, where k_{nuc} is the aSF nucleation rate per nucleating TCJ.

To test this "nucleation-only" model, we use snapshots of approximately 25,000 cells, for which we count the number of nucleating TCJs and the number of aSFs, across 35 dorsal thoraces in the region boxed in Fig. 3.1A. We use a standard technique for determining the incremental contributions of variables to explaining variance [258] . In this case, we want to know how much of the variance of aSF number is explained by cell apical area beyond the variance of aSF number explained by the number of aSF-nucleating TCJs. We find that the nucleation-only model, based on differences in aSF nucleation rates alone, explains approximately 15 percent of the observed scaling of aSF number with apical area.

We illustrate the physical content behind the method in [258] in Fig. B.6I. To estimate k_{nuc}/γ, we linearly regress aSF number in each cell versus the number of nucleating TCJs, constraining the intercept to zero, as demanded by the model. This fit returns that k_{nuc}/γ is approximately one aSF per four nucleating TCJs (95% CI: $(0.28\ \frac{aSF}{nucleating\ TCJ}, 0.29\ \frac{aSF}{nucleating\ TCJ})$). To illustrate the scaling of aSF number with cell apical area predicted by the model, we bin the cells by apical area. In each bin, to estimate the mean aSF number predicted by the model, we calculate the mean number of nucleating TCJs multiplied by our fit parameter k_{nuc}/γ. We also calculate the experimentally observed mean number of aSFs for cells in each bin.

As illustrated in Fig. B.6I, the nucleation-only model produces a scaling of aSF number with cell apical area of approximately $0.01\ \frac{aSF}{\mu m^2}$. The observed scaling of aSF number with cell apical area is approximately $0.06\ \frac{aSF}{\mu m^2}$. The nucleation-only model thus produces a scaling of aSF number with apical area that is approximately 15 percent of the scaling observed in wild-type tissues at 26 h APF (Fig. B.6I).

The limited ability of this nucleation-only model to explain the scaling of aSF number with cell apical area suggests to us that aSF breakage is also influenced by cell geometry. If, in addition to aSF nucleation rates, aSF lifetime is positively correlated with cell apical area, that correlation could help to explain the scaling of aSF number with apical area that is observed. As shown in Fig.

3.4M, by tracking aSF lifetimes in time-lapse images in 51 distinct cells, we find that aSF lifetime is correlated with cell apical area. To search for a mechanism which explains this correlation between aSF lifetime and cell apical area, we proceed to track the aSF movement and aSF breakage, in a similar manner to our tracking of aSF nucleation. We will find that the cell apical area dependence of lifetimes can largely be explained if, as observed, aSF tend to break at appropriately oriented breakage TCJs.

aSF breakage at TCJs

As shown in Fig. 3.4M, we find that aSF lifetime is correlated with cell apical area, which possibly explains why our nucleation-only model only accounts for about 15 percent of the scaling of aSF number with cell apical area. To search for a mechanism that could cause a correlation between aSF lifetime and cell apical area, we track positions of 624 aSFs at midlife and at breakage (Fig. 3.4G and Fig. B.7A). We test if aSFs tend to break at certain sites in a cell. The existence of aSF-breaking sites could generate a correlation between cell apical area and aSF lifetime if the distance between the sites at which aSFs nucleate and the sites at which aSFs break increases with cell apical area.

In the time-lapse images, we find two facts about aSF positions at breakage that are not mutually exclusive:

(1) aSFs break near the cell center.

(2) aSFs break with endpoints near at least one TCJ.

Before demonstrating that TCJs are sites of aSF breakage, we examine point (1). Since the aSFs are mostly aligned with the m-l axis (Fig. 3.1E), to quantify how far an aSF penetrates into a cell, we calculate the distance along the a-p axis between the nucleating TCJ and the leading tip of the aSF (*i.e.*, the endpoint which penetrates farther into the cell from the nucleating TCJ) (Fig. B.7B). This penetration distance is the y-coordinate of Fig. B.7C-D. Along the x-axes of Fig. B.7C-D, we plot the separation along the a-p axis between the cell centroid and the nucleating TCJ (Fig. B.7B).

We find that if the distance between the nucleating TCJ and cell centroid is larger, the aSF penetrates farther, on average, into the cell (the regression coefficient is non-zero; *F*-test, $p < 10^{-50}$) (Fig. B.7D). The 95 percent confidence interval for the slope of the regression is (*0.74, 0.93*), and the 95 percent confidence interval for the y-intercept is (*-0.21 μm, 0.32 μm*) (Fig. B.7D).

We conclude that by the time of aSF breakage, aSFs penetrate, on average, about 85 percent of the distance from the nucleating TCJ to the cell centroid (Fig. B.7D).

We ask whether aSFs are stationary from midlife to breakage or whether they are, on average, moving towards the cell centroid. For each aSF, we calculate the difference between how far the aSF has penetrated at midlife and at breakage; we find that aSFs move $0.69 \pm 0.03\ \mu m$ (mean $\pm$ SEM) towards the cell centroid from midlife to breakage. At aSF midlife, we find that aSFs penetrate, on average, about 55 percent (as compared to 85 percent) of the distance from the nucleating TCJ to the cell centroid (Fig. B.7C). (The 95 percent confidence interval for the slope of the regression is (*0.46, 0.62*), and the 95 percent confidence interval for the y-intercept is (*-0.01 μm, 0.44 μm*).) We conclude that aSFs do not stall for an appreciable amount of their lifetimes before breakage; this is consistent with a picture in which an aSF constantly move away from its nucleating TCJ until it reaches a breaking site (Fig. 3.4H).

We now test whether TCJs are sites of aSF breakage (*i.e.*, point (2)). Specifically, we would like to show that aSFs are not only likely to break near TCJs, but that they are more likely to do so than would be expected solely from a bias towards breaking near the cell centroid. For example, in Fig. B.7E,F, each aSF is aligned with two TCJs, and each aSF breaks after aligning with the TCJs. However, the two TCJs with which the aSF is aligned also happen to be near the cell centroid. We need to make sure that such observations of aSF breakage at TCJs do not simply arise due to a correlation between TCJ positions and cell centroid positions.

Because the two aSF tips are on opposite sides of the cell (*i.e.*, along the m-l axis about the nucleating TCJ position), each aSF tip encounters a different set of TCJs as the aSF moves from the nucleating TCJ to the cell centroid. We identify which aSF tip has penetrated farther into the cell from the nucleating TCJ. We, then, calculate the distance along the a-p axis between that aSF endpoint and its nearest TCJ (*i.e.*, on the same side of the cell as the leading aSF endpoint). We store all these distances (one per aSF) in a vector called $\vec{\delta}^{aSF-TCJ}$. We seek to test whether the leading aSF tip is closer to its nearest TCJ at the time of breakage than would be expected in a model in which leading aSF tip positions are simply correlated with the cell centroid position (Fig. B.7D).

To test whether aSFs tend to break at TCJs and not just near the cell centroid, we develop a procedure for identifying pairs of aSFs which have similar distances from nucleating TCJ to cell centroid but different cell geometries. First, we build a vector of distances along the a-p axis

between each nucleating TCJ and cell centroid (*i.e.*, x-coordinate in Fig. B.7D), which we call $\vec{x}$. We also build a vector of penetration distances (*i.e.*, y-coordinate in Fig. B.7D), which we call $\vec{y}$. In each of these vectors, there is one entry per aSF. Looping through the vector $\vec{x}$, for each aSF j, we find an aSF $i \neq j$ within another cell such that $|x_i - x_j|$ is minimized. Once aSF i has been matched with aSF j, we enforce that aSF i cannot be matched with any other aSFs. For an example of aSFs (in different cells) which have the same separation between nucleating TCJ and cell centroid, see Fig. B.7E,F. Since this procedure depends on the order in which we loop through the list of aSFs, we repeat the procedure with random permutations of the looping order several times, generating different bijective maps.

Given a bijective map from each aSF j to an accompanying aSF i, we want to test whether each aSF's breakage position depends on TCJ positions within a cell, not only on the position of the cell center. To test this, we swap aSF i into the cell which contains aSF j (*i.e.*, a different cell with different TCJ positions) (Fig. B.7G). To swap aSF i into another cell, we calculate the coordinate (along the a-p axis) of the leading edge of the aSF i, which we call $pos_{a-p}^{aSF\ i,swapped}$, in the cell which contains aSF j:

$$pos_{a-p}^{aSF\ i,swapped} = pos_{a-p}^{nuc\ j} + y_i * sign(pos_{a-p}^{aSF\ j} - pos_{a-p}^{nuc\ j}). \quad \text{[Eq. 18]}$$

In Eq. 18, $pos_{a-p}^{nuc\ j}$ is the coordinate (along the a-p axis) of the TCJ at which aSF j nucleated, and $pos_{a-p}^{aSF\ j}$ is the coordinate (along the a-p axis) of the leading edge of the aSF j in its original cell. We translate the one-dimensional coordinate $pos_{a-p}^{aSF\ i,swapped}$ into a two-dimensional coordinate by computing the intersections between a line (along the m-l axis) at $pos_{a-p}^{aSF\ i,swapped}$ and the cell outline (represented as a polygon – with straight edges) (polyxpoly; MATLAB 2016B Mapping Toolbox, MathWorks, Natick, MA). The swapped leading tip of aSF i is on the same side of the cell as the leading tip of aSF j (*i.e.*, we choose the intersection on that side of the cell). For example, if the leading tip of aSF j is "above" (along the m-l axis) the nucleating TCJ, the swapped leading tip of aSF i is also "above" (along the m-l axis) the nucleating TCJ (Fig. B.7G).

Now, we can compute how close this swapped aSF tip is to its nearest TCJ in the cell into which it has been swapped (Fig. B.7G). This swapped aSF tip comes from a cell with a different distribution of TCJs but with the same distance from nucleating TCJ to cell centroid; therefore, as our null model, we can use the distance between the swapped aSF and its nearest TCJ in the cell

into which it has been swapped. Our null model is that aSFs break near the cell centroid, but that their positions at breakage are otherwise uncorrelated with TCJ positions.

We store these distances (*i.e.*, one per aSF) between each swapped aSF and its nearest TCJ in the cell into which it has been swapped in a vector called $\vec{\delta}^{aSF-TCJ\ swapped}$. Now, we compare $\vec{\delta}^{aSF-TCJ}$ to $\vec{\delta}^{aSF-TCJ,swapped}$ (Fig. B.7H and B.7I at midlife; Fig. B.7J and B.7K at breakage). For example, in Fig. B.7F, the leading tip of the aSF is approximately 0.1 μm from its nearest TCJ. When we swap an aSF from another cell, the leading tip of the swapped aSF is approximately 0.8 μm from its nearest TCJ (Fig. B.7G). Via a Mann-Whitney U-test, we compare the medians of $\vec{\delta}^{aSF-TCJ}$ and $\vec{\delta}^{aSF-TCJ\ swapped}$ at aSF breakage (Fig. B.7J and B.7K, respectively). The two distributions have different medians ($p < 10^{-9}$). The median of $\vec{\delta}^{aSF-TCJ}$ is 0.46 μm, and the median of $\vec{\delta}^{aSF-TCJ\ swapped}$ is 0.67 μm.

We have shown that aSF leading tips tend to be near TCJs at the time of breakage, but to associate TCJs with aSF breakage, we must show that aSF leading tips are *not* near TCJs at midlife. We repeat the procedure outlined above, using the cell geometries at midlife (*i.e.*, the data in Fig. B.7C rather than the data in Fig. B.7D). We build two vectors $\vec{\delta}^{aSF-TCJ}$ and $\vec{\delta}^{aSF-TCJ\ swapped}$ for aSF positions at midlife (Fig. B.7H and B.7I, respectively). We compare the medians of $\vec{\delta}^{aSF-TCJ}$ and $\vec{\delta}^{aSF-TCJ,swapped}$ via a Mann-Whitney U-test, and find that their medians are not statistically significantly different ($p > 0.5$). The medians of both distributions are approximately 0.7 μm.

In conclusion, we have shown the following:

(1) A large majority of aSFs originate from a nucleating TCJ.

(2) aSFs move from the nucleating TCJ towards the cell center.

(3) At midlife, the leading aSF tip is not statistically significantly close to a TCJ.

(4) At breakage, the leading aSF tip is statistically significantly close to a TCJ.

We proceed to analyze geometric properties of TCJs which are close to the leading tip of the aSF at the time of breakage. Given a snapshot of a cell outline with the positions of the TCJs, we would like to predict the TCJs at which aSFs break.

We associate an aSF breakage event with a specific TCJ if, at the time of breakage, the leading aSF tip is plus or minus 0.5 μm from the TCJ (*i.e.*, approximately four pixels), along the a-p axis. Our physical justification for this 0.5 μm cutoff is that the average cortex thickness is 0.5 μm (Fig. B.7L). If an aSF tip is less than 0.5 μm from a TCJ, the aSF can link up to the cortex in

the neighboring cell. Based on this criterion, a majority of the aSFs break when the leading tip of the aSF is at a TCJ. We report the geometric properties of these TCJs associated with aSF breakage in Fig. B.7M,N.

To characterize aSF nucleation, we computed the fraction of pairs of adjacent edges, which meet at a TCJ, with angles α and θ in the region of interest (Fig. B.6B). We, then, calculated the fraction of nucleation events as a function of α and θ (Fig. B.6C). We estimated the nucleation rate from pairs of adjacent edges of given α and θ (*i.e.*, the ratio of data from Fig. B.6C to data from Fig. B.6B). We *cannot* repeat that procedure to estimate the propensity of aSF breakage at TCJs of given α and θ. To estimate the propensity of breakage at TCJs with given α and θ, we need an estimate of how many aSFs per unit time encounter TCJs with given α and θ; then, we could compare the actual count of aSF breakage events to the number of times that aSFs reach TCJs with given α and θ. Nonetheless, by comparing Fig. B.6B to Fig. B.7M, we find that aSF breakage events occur at TCJs with large bisector orientation θ and that aSF breakage at TCJs appears to be insensitive to opening angle α.

In the same way that we calculated a cutoff for aSF-nucleating TCJs in Fig. B.6E, we plot the empirical cumulative distribution of the aSF breakage data versus θ (*i.e.*, the fraction of aSF breakage events for TCJs with $\theta' < \theta$) (Fig. B.7N). We calculate a cutoff based on the 5th percentile of aSF breakage events (Fig. B.7N). The cutoff for aSF-breaking TCJs is at $\theta \approx 1$ radian. Given this cutoff, we proceed to develop a phenomenological model of aSF movement and breakage.

Phenomenological model of aSF movement and breakage

In the preceding subsection, we discussed that the correlation between aSF lifetime and cell apical area might arise because of aSF breakage at specific TCJs. We have not specified how breakage at TCJs would explain this correlation. Now we propose a phenomenological model for aSF movement and breakage. We will, then, employ this model to quantify how much of a correlation between aSF lifetime and cell apical area that it generates. The model of aSF movement and breakage is as follows:

(1) All TCJs that meet the aSF nucleation criterion (Fig. B.6E-G) nucleate aSFs at the same rate, which we call k_{nuc}. aSFs do not nucleate at TCJs that do not meet the criterion.

(2) aSFs nucleate a distance x_0 away, along the midline axis, from the center of a nucleating TCJ. x_0 is equal to the cortex thickness (Fig. B.7L).

(3) aSF endpoints move at constant velocity v_x, along the midline axis, towards the cell center. The speed of aSFs along the midline is independent of cell area (Fig. B.7O).

(4) If a cell has only one breaking TCJ (Fig. B.7N), we assume the aSF breaks as it approaches its endpoint approaches that TCJ, a distance Δx before reaching the breaking TCJ as it links up to cortex in the neighboring cell. (We expect Δx to be approximately equal to, but not necessarily exactly equal to, the cortex thickness.) The aSF lifetime is determined by the separation between the breaking TCJ and the nucleating TCJ.

(5) Suppose the cell has more than one breaking TCJ (*i.e.*, at least one breaking TCJ on both sides of the cell so that each aSF tip can reach a breaking TCJ). It is possible that the aSF could break when one aSF tip reaches its breaking TCJ. It is also possible that the aSF could break as the other aSF tip reaches its breaking TCJ. We assume that the aSF lifetime is determined by the average of the separations between the nucleating TCJ and each of the two breaking TCJs.

As suggested by this model, we characterize aSF movement as one-dimensional (*i.e.*, along the a-p axis) since the aSFs are aligned with the m-l axis (Fig. 3.1E). Given the geometry of the cell at the time of aSF breakage and the TCJ from which the aSF nucleated, our model makes a specific prediction about the lifetime of each aSF. The lifetime of each aSF is determined by how far it moves from its nucleating TCJ before breakage (Fig. B.7P). Given this phenomenological picture of aSF dynamics (Fig. B.7Q), we proceed to estimate model parameters from time-lapse imaging.

Experimental estimates of parameters of aSF motion and breakage

Before we calculate how much of the scaling of aSF number with cell apical area can be explained by this model, we specify estimates for the model parameters. We have experimental estimates for the criteria for nucleating TCJs and breaking TCJs (Fig. B.6E,F and Fig. B.7N). This means that given a snapshot of a cell, we can predict at which TCJs aSFs nucleate and at which TCJs aSFs break. We additionally have an estimate of x_0, which is the cortex thickness (Fig. B.7L).

There are three parameters in the model, including k_{nuc} and v_x and Δx, that we have not yet estimated from time-lapse imaging. k_{nuc} is the nucleation rate per nucleating TCJ. v_x is the speed of aSF tips along the a-p axis. The average signed distance between the leading aSF tip and its breaking TCJ at the time of breakage is Δx (positive if the aSF breaks as its endpoint approaches the breaking TCJ, negative if the aSF breaks after its endpoint passes the TCJ) (see Fig. B.7Q). As we will see in the next subsection, k_{nuc} and v_x appear in the model as a single parameter, $\frac{k_{nuc}}{v_x}$. We estimate k_{nuc} by counting aSF nucleation events across 51 cells over 2 hours. For each of these cells, we calculate the average number of nucleating TCJs (*i.e.*, TCJs with bisector orientations that satisfy the aSF nucleation criterion) over the same time period. The average aSF nucleation rate per nucleating TCJ is $0.031 \pm 0.001\ min^{-1}$ (mean $\pm$ SEM). The average aSF speed along the a-p axis for tracked aSFs for these 51 cells is $0.111 \pm 0.003 \frac{\mu m}{min}$ (mean $\pm$ SEM) (Fig. B.7O). Thus, $\frac{k_{nuc}}{v_x}$ is $0.29 \pm 0.01\ \mu m^{-1}$ (mean $\pm$ SEM).

For the remaining parameter Δx, we do not have an estimate from time-lapse imaging. We will leave Δx as a free parameter. After using this parameter to fit our model to wild-type aSF counts per cell, we will check whether the best-fit value of the Δx is physically reasonable. Equipped with this model of aSF nucleation and breakage for which all but one parameter is constrained, we will compare our model's prediction for the scaling of aSF number with cell apical area to the experimentally observed scaling of aSF number with cell apical area.

Explanatory power of cell-autonomous model: scaling of aSF number with apical area

Based on our knowledge that aSFs tend to nucleate at TCJs and break at TCJs, we seek to quantify what fraction of the scaling of aSF number with cell apical area can be explained by our phenomenological model. From skeletonized images of the region of interest at 26 h APF, we define the TCJs and cell-cell junctions. To these still packings, we apply our model of aSF nucleation and breakage. Let us denote the separation (along the a-p axis) between nucleating TCJ (indexed by j) and the first breaking TCJ by ${x_{nuc-break1}}^j$. Let us denote separation (along the a-p axis) between the nucleating TCJ and the second breaking TCJ by ${x_{nuc-break2}}^j$.

Suppose a cell has only one breaking TCJ. Our model predicts that the lifetime of an aSF nucleated by TCJ (indexed by j) is equal to $\frac{\max({x_{nuc-break1}}^{j}-(\Delta x+x_0),0)}{v_x}$. The mean aSF number in cell i from nucleating TCJ j is:

$$\overline{N_{ij}} = \frac{k_{nuc}*\max({x_{nuc-break1}}^{j}-(\Delta x+x_0),0)}{v_x} \quad \text{[Eq. 19]}$$

Suppose the cell has more than one breaking TCJ (*i.e.*, at least one breaking TCJ on both sides of the cell so that each aSF tip can reach a breaking TCJ). Our model predicts that the lifetime of an aSF nucleated by TCJ (indexed by j) is equal to $\frac{\max(\text{mean}({x_{nuc-break1}}^{j}, {x_{nuc-break2}}^{j})-(\Delta x+x_0),0)}{v_x}$. The mean aSF number in cell i from nucleating TCJ j is:

$$\overline{N_{ij}} = \frac{k_{nuc}*\max(\text{mean}({x_{nuc-break1}}^{j}, {x_{nuc-break2}}^{j})-(\Delta x+x_0),0)}{v_x} \quad \text{[Eq. 20]}$$

The mean aSF number in cell i (from all its nucleating TCJs) is:

$$\overline{N_i} = \sum_{nucleating\ TCJ\ (j)} \overline{N_{ij}} \quad \text{[Eq. 21]}$$

Changing $(\Delta x + x_0)$ in the model shifts the mean aSF number per cell up or down with little effect on the slope of aSF number versus cell apical area. We are mostly interested in the slope of aSF number versus cell apical area rather than in uniform shifts of aSF number per cell; we leave $(\Delta x + x_0)$ as a free parameter. For 25,000 cells in 35 distinct samples, we calculate the sum of squared errors as a function of $(\Delta x + x_0)$. The value of $(\Delta x + x_0)$ that minimizes the sum of squared errors (cell-by-cell) between the model prediction and actual aSF counts is 1.01 ± 0.01 μm (error estimated via bootstrapping; bootstrp; MATLAB 2016B Statistics and Machine Learning Toolbox, MathWorks). This is approximately two times the cortex thickness (*i.e.*, $(\Delta x + x_0) \approx 2x_0$); the experimental value of the cortex thickness is approximately 0.51 ± 0.12 μm (Fig. B.7L).

Using the value of $(\Delta x + x_0)$ that minimizes the sum of squared errors, we plot the mean aSF number predicted by our model for all cells of a given apical area in Fig. 3.4N. The mean aSF number for a given apical area is an average over the sum in Eq. 21 for all cells of a given apical area. Using the same technique for determining incremental contributions of variables to explaining variance as above [258], we find that this model, with the nucleating and breaking TCJ cutoffs constrained by experimental data, explains approximately 75 percent of the scaling of aSF number with cell apical area at 26 h APF (Fig. 3.4N). This cell-autonomous model predicts that

the slope of aSF number versus cell apical area should be approximately $0.05\ \frac{aSF}{\mu m^2}$, whereas the observed scaling is approximately $0.06\ \frac{aSF}{\mu m^2}$ (Fig. 3.4N).

The fundamental physical content of this model is that TCJs set the average aSF number per cell on a largely cell-autonomous basis. The role that a given TCJ plays in determining the number of aSFs in a cell depends on the orientation of its bisector relative to the uniaxial stress. If the bisecting vector of a TCJ points along the a-p axis (Fig. B.6E), the TCJ is a nucleation site for aSFs in the cell. If the bisecting vector of a TCJ points along the m-l axis (Fig. B.7N), the TCJ is a site at which aSFs break in the cell. The assumptions that aSF number is set entirely cell-autonomously likely underlies the model's inability to completely explain the variation in the data. Indeed, the model is blind to many details of the mechanical environment of cells, which we expect to affect MyoII accumulation and activity [272-275]. Nevertheless, our model, based solely on individual cell geometries, with one free parameter explains approximately 75 percent of the experimentally observed scaling of aSF number with cell apical area (Fig. 3.4N). Encouragingly, the value of the fit parameter which best fits the experimental data is approximately equal to the cortex thickness (Fig. B.7L), suggesting a physical picture in which aSFs break near TCJs as they link up with cortex in a neighboring cell (Fig. B.7Q).

3. Experimental tests of cell-autonomous, geometric model

Testing the model by varying TCJ number: comparing clone boundary to clone bulk

Since the geometric model helps to explain the scaling of aSF number with cell apical area in wild-type dorsal thoraces at 26 h APF (Fig. 3.4N), we seek to test the model directly. The geometric model, based on the role of TCJs in aSF nucleation and breakage, suggests that manipulating the number of TCJs could affect aSF number, independent of cell apical area. To change the average number of TCJs in a set of cells, we generate clones of cells that are larger than the wild-type cells (Fig. 3.4O). Large cells in a tissue of small cells have more TCJs, on average, than large cells in a tissue of large cells [144, 276].

To accomplish an increase in cell apical area, we prevent division in a subset of cells ($trbl^{UP}$). To study the effect of a differing number of TCJs per cell at approximately the same cell

apical area (Fig. B.8A), we compare *trbl*^{UP} cells at clone boundaries to *trbl*^{UP} cells in the clone bulk (Fig. 3.4O).

Having generated and segmented images of tissues harboring large *trbl*^{UP} clones, we divide the clone cells into two groups, *trbl*^{UP} cells which contact at least one wild-type cell (466 cells, *trbl*^{UP} clone border cells) and *trbl*^{UP} cells which contact no wild-type cells (683 cells, *trbl*^{UP} clone bulk cells). Both groups have approximately the same apical area per cell; the mean difference in cell apical area is $5.0 \pm 1.5\ \mu m^2$ (mean $\pm$ SEM) (Fig. B.8A). Although *trbl*^{UP} border cells are of approximately the same apical size as *trbl*^{UP} bulk cells, *trbl*^{UP} border cells have roughly one more TCJ per cell than *trbl*^{UP} bulk cells (Fig. B.8D,E).

Since our *trbl*^{UP} manipulations lead to more TCJs per cell in border cells than in bulk cells, we ask whether we observe differences in aSF number per cell between border and bulk cells as a result of this difference in cell geometry. As shown in Fig. 3.4Q, without controlling for differences in cell apical area, the mean difference in aSF number per cell between *trbl*^{UP} border cells and *trbl*^{UP} bulk cells is 0.4 ± 0.1 aSF (mean $\pm$ SEM). The *trbl*^{UP} group with more TCJs has more aSFs per cell (Fig. B.8B-E).

We would like to know if the observed mean aSF number difference between clone boundary and clone bulk in the *trbl*^{UP} cells can explained solely by the small difference in mean cell apical area between *trbl*^{UP} border cells and *trbl*^{UP} bulk cells. If not, we would like to know if our geometrical model explains the difference in mean aSF number per cell between the two groups of *trbl*^{UP} cells (Fig. 3.4Q).

To test whether the observed mean aSF number difference between *trbl*^{UP} clone boundary cells and *trbl*^{UP} clone bulk cells can be explained by a difference in mean apical area, we perform an analysis of covariance [258]. We linearly regress the aSF count in each cell on two independent variables. One independent variable is categorical, zero for *trbl*^{UP} cells in the clone bulk and one for *trbl*^{UP} cells at the clone boundaries. The other independent variable is the cell apical area. The 95% confidence interval for the scaling of aSF number with cell apical area is ($0.028\ \frac{aSF}{\mu m^2}$, $0.035\ \frac{aSF}{\mu m^2}$) (Fig. B.8B,C).

The 95% confidence interval for the regression coefficient of the categorical variable is (0.10 aSF, 0.43 aSF). Thus, controlling for cell apical area differences, *trbl*^{UP} cells at the clone boundaries have, on average, about 0.25 more aSF than *trbl*^{UP} cells in the clone bulk (Fig. B.8B,C).

The p-value for the *t*-statistic that the regression coefficient of the categorical variable is non-zero is 0.001 (fitlm; MATLAB 2016B Statistics and Machine Learning Toolbox, MathWorks)[258].

We now turn to the cell-autonomous, geometric model to see if the model predicts the difference in mean aSF number between $trbl^{UP}$ border cells and $trbl^{UP}$ bulk cells. We simulated aSF nucleation and breakage in the geometric model on cell sizes and shapes taken from our images of $trbl^{UP}$ clones. Performing an analysis of covariance on the model predictions, we linearly regress the predicted aSF number count in each cell on the same two independent variables. The 95% confidence interval for the regression coefficient of the categorical variable is (0.05 aSF, 0.21 aSF) (Fig. B.8F,G); controlling for cell apical area differences, the model predicts that $trbl^{UP}$ boundary cells have on average 0.15 aSF more than $trbl^{UP}$ bulk cells.

Our geometric model thus accounts for approximately 60% of the observed effect (*i.e.*, 60% of the increased aSF number per cell in $trbl^{UP}$ boundary cells relative to the $trbl^{UP}$ bulk cells). For the model prediction, the p-value for the *t*-statistic that the regression coefficient for the categorical variable is non-zero is 0.001 (Fig. B.8F,G) (fitlm; MATLAB 2016B Statistics and Machine Learning Toolbox, MathWorks) [258]. In summary, increasing the number of TCJs per cell in $trbl^{UP}$ border cells, while controlling for differences in cell apical area, increases the mean aSF number in a statistically significant way, in agreement with expectations from our geometrical model.

In conclusion, our model, applied to the still images of $trbl^{UP}$ clone cells, predicts the following $trbl^{UP}$ effect: increasing the number of TCJs in a cell tends to increase the number of aSFs in a cell. This is due to an increase in predicted aSF nucleation rate (Fig. 3.4P) without any difference in predicted aSF lifetime between $trbl^{UP}$ border cells and $trbl^{UP}$ bulk cells (Fig. 3.4R). Although our model is cell-autonomous and relies on a few simple assumptions, motivated by the time-lapse imaging of aSF nucleation and breakage, the phenomenological model is powerful enough to predict the effect of changing the number of TCJs at fixed cell apical area in these $trbl^{UP}$ clone experiments.

Ortho-elongated cells tend to have more aSFs, as predicted by cell-autonomous, geometric model

The number of aSFs per cell is determined by a balance of aSF nucleation and aSF breakage. We have tested our model in $trbl^{UP}$ cells by analyzing whether increasing the number of TCJs would lead to an increase in nucleation rate and thus of aSF number, as predicted by our

model (Fig. 3.4P,S). We now test our model on cell geometries that are expected to promote long aSF lifetimes. In our geometrical model, aSF lifetime is proportional to the distance between a nucleating TCJ and breaking TCJs along the a-p axis (Fig. B.7P,Q). To test this second characteristic of our model, in this section we seek a group of cells that are elongated orthogonal to the uniaxial tensile stress such that expected nucleating TCJs and breaking TCJs are far from each other (Fig. 3.4T).

We define ortho-elongated cells based on the moment of inertia tensor [118]. First, we compute the geometric center of the cell, ($x_{geocent}$,$y_{geocent}$). Then, for each pixel i within the cell, we compute $\Delta x_i = x_i - x_{geocent}$, $\Delta y_i = y_i - y_{geocent}$. Since, by convention, the m-l axis corresponds to the y-axis, ortho-elongated cells are those with $\frac{\sum_{i\ pixels\ within\ cell}(\Delta y_i)^2}{\sum_{i\ pixels\ within\ cell}(\Delta x_i)^2} \leq 1$; elongated cells are those with $\frac{\sum_{i\ pixels\ within\ cell}(\Delta y_i)^2}{\sum_{i\ pixels\ within\ cell}(\Delta x_i)^2} > 1$.

In comparing ortho-elongated cells to elongated cells, we control for cell apical area and for the number of nucleating TCJs per cell (proportional to the predicted aSF nucleation rate per cell). For each ortho-elongated cell (indexed by i with number of nucleating TCJs n_i and cell apical area A_i), we find an elongated cell (indexed by j) with the same number of nucleating TCJs and with approximately the same apical area (*i.e.,* $|A_i - A_j|$ minimized for $n_i = n_j$). Once elongated cell j has been matched with ortho-elongated cell i, we enforce that elongated cell j cannot be matched with any other ortho-elongated cells. We compare the aSF number per ortho-elongated cell to the aSF number per elongated cell. We find that the group of ortho-elongated cells have more aSFs than the group of elongated cells (Fig. 3.4U).

Since we control for the number of nucleating TCJs (Fig. 3.4V), the predicted aSF nucleation rates per cell are the same for the group of elongated cells and the group of ortho-elongated cells. In our geometric model, the increased aSF lifetime leads to a greater predicted aSF number per cell in the group of ortho-elongated cells relative to the group of elongated cells (Fig. 3.4X,Y). The analysis of ortho-elongated cells and *trbl*^{UP} cells demonstrate that at fixed cell apical area, the number and spatial distribution of TCJs significantly impact the number of aSFs per cell.

4. Possible biophysical mechanisms for the distinction between nucleating and breaking TCJs

In this section, we state hypotheses that could account for the fact that aSF nucleation rate depends so strongly on TCJ bisector orientation (see Appendix B.2). We explain in this section how a model for aSF nucleation based solely on the orientation of the two adjacent edges that meet at the TCJ disagrees with our empirical observations. Then, we use our observations of cell geometries under increasing uniaxial tensile stress to motivate a proposal in which aSFs appear in response to *increases* in the opening angle of a TCJ over time. Additionally, we discuss specific proteins that could plausibly be responsible for aSF nucleation at TCJs. Although we do not attempt to verify these proposed mechanisms directly in the current paper, they provide at least some suggestion of how our observed dependence of nucleation and breakage on TCJ orientation could plausibly arise.

aSF nucleation model based solely on edge orientation

The role of TCJs in aSF nucleation arises quite naturally in a very simple model of aSF formation inspired by the observation that aSF tend to peel off from the cortex and by similar models of membrane adhesion to surfaces [277]. We imagine that the actin, Myosin II, and other proteins that will form the aSF can exist in two states, as a proto-aSF still bound to the rest of the junctional cortex or as a detached, fully-formed aSF. When the proto-aSF is attached to the rest of the cortex, the proto-aSF gains an adhesion energy $-\sigma$ per unit length which favors its remaining attached. At the same time, both the proto-aSF and the detached aSF are contractile and thus can be modeled as having a line tension λ that favors peeling from the cortex in order to shorten the aSF: Peeling allows the (proto-)aSF to become shorter because, instead of following the curved cell-cell junction, upon peeling it can form a straight line between its two attachment points. Thus, we expect peeling to be most favorable where junctions are most highly curved and the decrease in line tension energy from peeling is correspondingly largest. As TCJs are regions of high junctional curvature, it, thus, makes sense that aSFs tend to nucleate at TCJs. Interestingly, this explanation of aSF nucleation at TCJs due to high junctional curvature is supported by the fact that aSFs also nucleate at cell-cell junctions which become curved during division of a neighbouring cell prior to completion of cytokinesis, as described in Section B.2.

Specifically, suppose an aSF nucleates from the two edges adjacent to a TCJ and moves in the direction of the TCJ bisecting vector. The change in energy due to peeling of a segment of proto-aSF initially of length $2s$ is:

$$\Delta U = U_f - U_i = 2s \sin\left(\frac{\alpha}{2}\right)\lambda - 2s(\lambda - \sigma). \quad \text{[Eq. 22]}$$

$$\Delta U < 0 \Leftrightarrow \sin\left(\frac{\alpha}{2}\right) < \frac{\lambda-\sigma}{\lambda} = 1 - \frac{\sigma}{\lambda}. \quad \text{[Eq. 23]}$$

For $\Delta U < 0$, it is energetically favorable for aSFs to nucleate from the cortex because the energetic favorability of length minimization overcomes the energetic cost of breaking attachments with the rest of the cell cortex. In this simplest model, nucleation thus occurs when the TCJ opening angle α is small enough.

A natural extension of this simple model, to account for externally imposed anisotropic tensile stress, is to make λ and/or σ dependent on the orientations of the two adjacent edges relative to the a-p axis (which, recall, is perpendicular to the uniaxial stress). For the sake of simplicity, let us consider cases in which the bisector of the pair of adjacent edges points either along the a-p axis or along the m-l axis. We will compare TCJs in the bin indicated by the red dot to the bin indicated by the blue dot in Fig. B.9A-B. Those in the bin indicated by the red dot have opening angle larger than $\frac{\pi}{2}$ (*i.e.*, $\alpha_{red} = \frac{\pi}{2} + \epsilon$; $\epsilon > 0$). Those in the bin indicated by the blue dot have opening angle smaller than $\frac{\pi}{2}$ (*i.e.*, $\alpha_{blue} = \frac{\pi}{2} - \epsilon$; $\epsilon > 0$). We observe that TCJs in the bin indicated by the red dot do nucleate aSFs, while TCJs in the bin indicated by the blue dot do not nucleate aSFs.

The notable fact about the TCJs in these two bins is that (assuming the same value of ϵ in both cases) the two edges adjoining each red TCJ are at the same angles with respect to the a-p axis as the two edges adjoining each blue TCJ, as shown in Fig. B.9C,C'. Thus, even if the parameters λ and α depend on edge orientation, they will be the same for the TCJs in the red and blue bins. Let us call the orientation of each of the edges with respect to the a-p axis $\delta = \delta_{red} = \delta_{blue}$. Although the edges have the same orientation with respect to the a-p axis, the TCJs in the red bin have a larger opening angle than the TCJs in the blue bin. This means that $\sin\left(\frac{\alpha_{red}}{2}\right) > \sin(\frac{\alpha_{blue}}{2})$. Based on Eq. 23, it is thus impossible for the TCJ defined by the red edges to nucleate aSFs (*i.e.*, to have $\sin\left(\frac{\alpha_{red}}{2}\right) < 1 - \frac{\sigma(\delta)}{\lambda(\delta)}$) if the TCJ defined by the blue edges does not (*i.e.*, $\sin\left(\frac{\alpha_{blue}}{2}\right) > 1 - \frac{\sigma(\delta)}{\lambda(\delta)}$), because $\sin\left(\frac{\alpha_{red}}{2}\right) > \sin(\frac{\alpha_{blue}}{2})$. Regardless of the choice of orientational

dependence for λ and/or σ, this edge-orientation-dependent framework hence cannot explain the fact that TCJs in the red bin nucleate aSFs while the TCJs in the blue bin do not nucleate aSFs (Fig. B.9A-C').

Dependence of opening angle on bisector orientation in tissue under uniaxial stress

It, thus, remains an open question how TCJs with certain bisector orientations "know" that they are supposed to nucleate aSFs while TCJs with the opposite orientations "know" that they are not. Here, we argue that one appealing possibility is that the cortex (or related factors) in the vicinity of the TCJ could have some memory of its history of deformation, so that aSF nucleation depends on the rate of change of TCJ opening angle rather than on instantaneous edge orientations. We also discuss specific molecular, mechanosensitive mechanisms that could be responsible for nucleation at TCJs for which the bisectors point perpendicular to the uniaxial stress.

To quantify the response of the tissue to the uniaxial tensile stress, we measure the correlation between TCJ bisecting angle θ and opening angle α (Fig. B.9D). In wild-type tissues at 18 h APF, before the increase in tensile stress, α does not depend on θ. Indeed, the mean opening angle, regardless of θ, is approximately $\frac{2\pi}{3}$, as one would expect in a mechanically isotropic tissue. Then, as the imposed uniaxial tensile stress increases from 18 h APF to 26 h APF (Fig. 3.1B-D), the opening angle α between adjacent edges develops a dependence on TCJ bisecting angle θ (Fig. B.9D).

If a TCJ's bisector into a cell points mostly along the a-p axis (Fig. B.9C), the opening angle α tends to increase in response to increasing tensile stress (Fig. B.9D). If the bisector points mostly along the m-l axis (Fig. B.9C'), α instead tends to decrease in response to increasing tensile stress (Fig. B.9D). Our observations of aSF nucleation in time-lapse images reveal that TCJ bisector orientation is strongly predictive of aSF nucleation (Fig. B.6B-F); for TCJs with bisectors pointing along the a-p axis, we hypothesize that aSFs nucleate at certain TCJs *because* their opening angle has recently increased in response to increased tensile stress.

Unlike a mechanism that depends only on instantaneous edge orientation, such a history-dependent mechanism is, thus, at least qualitatively consistent with the observation that a TCJ's nucleation rate depends primarily on its bisector orientation θ. Since the opening angle between adjacent edges increases in response to uniaxial tensile stress, we hypothesize that aSF nucleation could occur downstream of recruitment of medial MyoII at TCJs.

Recruitment of MyoII to TCJs in *Drosophila* epithelia is well-documented [164, 260, 261]. For example, during the stretching of the *Drosophila* pupal wing epithelium due to forces from the hinge, MyoII forms ring-like structures around TCJs during cell rearrangement [261]. Similarly, in germ-band extension during cell neighbor exchanges (*i.e.*, T1 transitions), pulses of medial MyoII near TCJs generate the lengthening of new cell-cell junctions [260]. In some existing mechanical models of simple epithelia, Myosin II recruitment to cell-cell junctions occurs when the junctions experience strain [275]. One could extend such models of active tension networks to allow recruitment of MyoII specifically at TCJs; this recruitment to TCJs would occur as the opening angle between adjacent junctions increases, straining actomyosin filaments at the TCJ.

Furthermore, we foresee that the dynamics of TCJ proteins might be modulated in response to uniaxial tissue stress. For example, the conserved Sidekick (Sdk) protein is localized at TCJs in multiple *Drosophila* epithelial tissues; an increase in junction tension or a change in cell geometry was proposed to modulate its level at TCJs [278-280]. This suggests that the composition of TCJs might depend on the orientation and anisotropy of tissue stress. Therefore, the detailed analysis of TCJ protein dynamics is a promising avenue to shed light on how the TCJ bisector angle defines nucleating and breaking TCJs.

Figure B.1 **Tissue mechanical stress and aSF organization.** Unless otherwise stated, protein distributions and quantifications are reported for the region boxed in Fig. 3.1A at 26 hAPF. **A-A')** Picture of the *Drosophila melanogaster* pupa (A) and close-up picture of the adult dorsal thorax (notum, A'). Orange region in A delineates the pupal dorsal thorax (notum). Dashed box: Posterior and central region where aSFs form and corresponding region in the adult. Red line: midline. **B)** Graph of the tissue recoil velocity (mean ± SEM) along the a-p axis (red) and m-l axis (blue) between 14 hAPF and 28 hAPF. Blue asterisks: calculated for the comparison of the recoiled velocities measured at 18 hAPF and at a later timepoint for a-p ablation, p-values<0.05 from 22 hAFP. Red asterisks: calculated for the comparison of the recoiled velocity measured along the a-p and m-l tissue axes, p-values<10^{-5} from 22 hAFP. n: minimum number of ablations at each timepoint and orientation. **C,C')** E-Cad:3xmKate2, nls:mRFP and MyoII:3xGFP distributions at the level of the AJ (C**)** and along the cell a-b axis (C'**)**. Yellow arrowheads in C indicate the position of a-b section shown in C'. Conversely, the yellow arrowheads in C' indicate the a-b position of the section shown in C. **D-D'')** Dlg:YFP and MyoII:3xmKate2 distributions at the level of the AJ (D), of the septate junction (D') and along the a-b axis (D''). Yellow arrowheads in D indicate the position of a-b section shown in D''. Yellow and blue arrowheads in D'' indicate the a-b position of the section shown in D and D', respectively. **E-L)** Localization of LifeAct:GFP and MyoII:3xmKate2 (E), Vinc:GFP and MyoII:3xmKate2 (F), Kst:YFP and MyoII:3xmKate2 (G), Zasp52:GFP and MyoII:3xmKate2 (H), Pax:YFP and MyoII:3xmKate2 (I), Cher:YFP and MyoII:3xmKate2 (J), Rhea:GFP and MyoII:3xmKate2 (K) and Mys:GFP and MyoII:3xmKate2 (L). **M-M')** MyoII:3xGFP and E-Cad:3xmKate2 in control *mirr-G4>LifeAct:GFP* (M) and in *mirr-G4>zip^{DN}:YFP* tissues (M'). The dotted green lines delineate roughly the medial domain where *mirr-G4* is not expressed (M, M'). The medial domain is less elongated along the m-l axis in *mirr-G4>zip^{DN}:YFP* in agreement with the reduced mechanical stress measured in the central domain (Fig. 3.1L). **N-N'')** Schematic of the pupal m-l compression. Arrowheads indicate the compression orientation (N and N''). Distributions of MyoII:3xGFP in uncompressed tissue (N') and in a tissue compressed by around 20% along the m-l axis (N''). The cyan lateral margins illustrate the magnitude of m-l compression. Scale bars: 200 µm (A, A') 20 µm (M, M' and N', N'') and 2µm (C, D, D'' and E). Statistical tests: Kruskal-Wallis test with Conover post hoc (B). ns: not significant. Statistically significant differences (p-value<0.05) are indicated by using one asterisk. In the case of multiple pairwise comparisons, only the maximum p-values (of the set of asterisked comparisons) are reported.

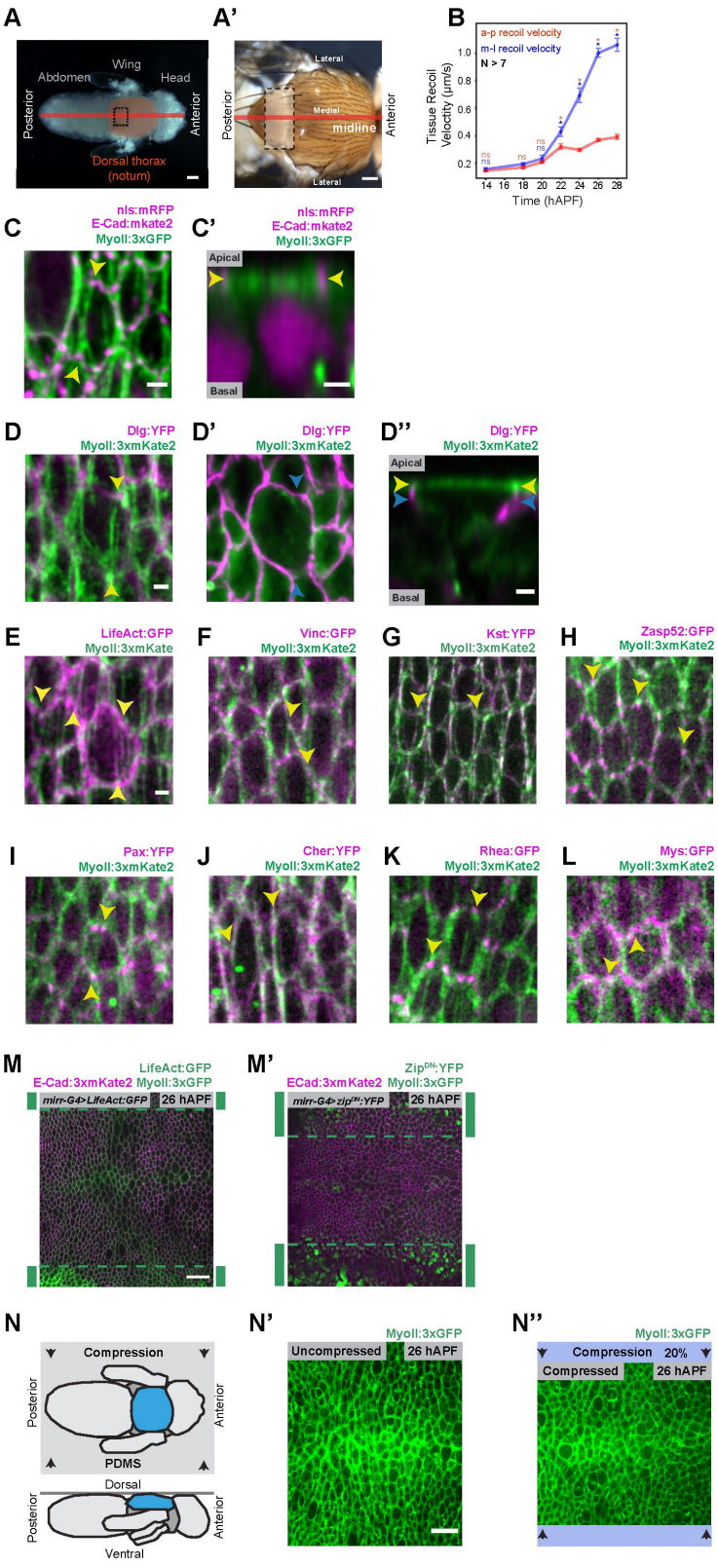
A
Wing
Abdomen
Head
Posterior
Anterior
Dorsal thorax
(notum)
A'
Lateral
Medial
midline
Lateral
Posterior
Anterior
B
a-p recoil velocity
m-l recoil velocity
N > 7
Tissue Recoil Velocity (μm/s)
Time (hAPF)
C
nls:mRFP
E-Cad:mkate2
MyoII:3xGFP
C'
nls:mRFP
E-Cad:mkate2
MyoII:3xGFP
Apical
Basal
D
Dlg:YFP
MyoII:3xmKate2
D'
Dlg:YFP
MyoII:3xmKate2
D''
Dlg:YFP
MyoII:3xmKate2
Apical
Basal
E
LifeAct:GFP
MyoII:3xmKate
F
Vinc:GFP
MyoII:3xmKate2
G
Kst:YFP
MyoII:3xmKate2
H
Zasp52:GFP
MyoII:3xmKate2
I
Pax:YFP
MyoII:3xmKate2
J
Cher:YFP
MyoII:3xmKate2
K
Rhea:GFP
MyoII:3xmKate2
L
Mys:GFP
MyoII:3xmKate2
M
LifeAct:GFP
E-Cad:3xmKate2 MyoII:3xGFP
mirr-G4>LifeAct:GFP
26 hAPF
M'
ZipDN:YFP
ECad:3xmKate2 MyoII:3xGFP
mirr-G4>zipDN:YFP
26 hAPF
N
Compression
Posterior
Anterior
PDMS
Dorsal
Posterior
Anterior
Ventral
N'
MyoII:3xGFP
Uncompressed
26 hAPF
N''
MyoII:3xGFP
Compression 20%
Compressed
26 hAPF

Figure B.2 **aSF scaling and role in cell and tissue elongation.** Unless otherwise stated, protein distributions and quantifications are reported for the region boxed in Fig. 3.1A at 26 hAPF. **A)** Radar plot of the recoil velocity (µm/s) upon junction (blue) and aSFs (red) ablations as a function of their orientation relative to the a-p axis at 26 hAPF. **B)** Distribution of MyoII:3xGFP in *actn*^{IG1} cells (orange dashed outline) marked by the lack of expression of *Ubi-nls:mRFP* (not shown) and in surrounding control cells. **C)** Graph of the normalized aSF number per cell (mean ± SEM) in control and *actn* cells. n: number of cells; *p*-value<10^{-5}. **D)** Graph of the normalized cell elongation (mean ± SEM) of control and *actn* cells. n: number of cells; *p*-value<10^{-5}. **E-E'')** *pnr-G4>w*^{dsRNA} (E) and *pnr-G4>actn*^{dsRNA} (E') adult scutella. H is the a-p length of the scutellum (blue line). V is the maximum length of the scutellum along the m-l axis (green line). (E'') Graph of scutellum elongation (V/H, mean ± SEM) in control *pnr-G4>w*^{dsRNA} and *pnr-G4>actn*^{dsRNA} animals. n: number of animals; *p*-value<10^{-5}. **F)** Graph of the recoil velocity (µm/s) upon aSF ablation as a function of cell apical area. n: number of cells. **G-H)** Graph of number of aSFs per cell as a function of cell apical area (F) or volume (H). n: number of cells. **I)** Graph of cell elongation (mean ± SEM) as a function of cell apical area in *w*^{RNAi} and *actn*^{RNAi} cells at 26 hAPF. n: number of cells; *p*-value<10^{-5}. Scale bars: 5µm (B). Statistical tests: Kruskal-Wallis tests (C, D and E'') and Ancova tests for difference in regression slopes (I). r: Pearson correlation coefficient. ns: not significant. Statistically significant differences (*p*-value<0.05) are indicated by one asterisk.

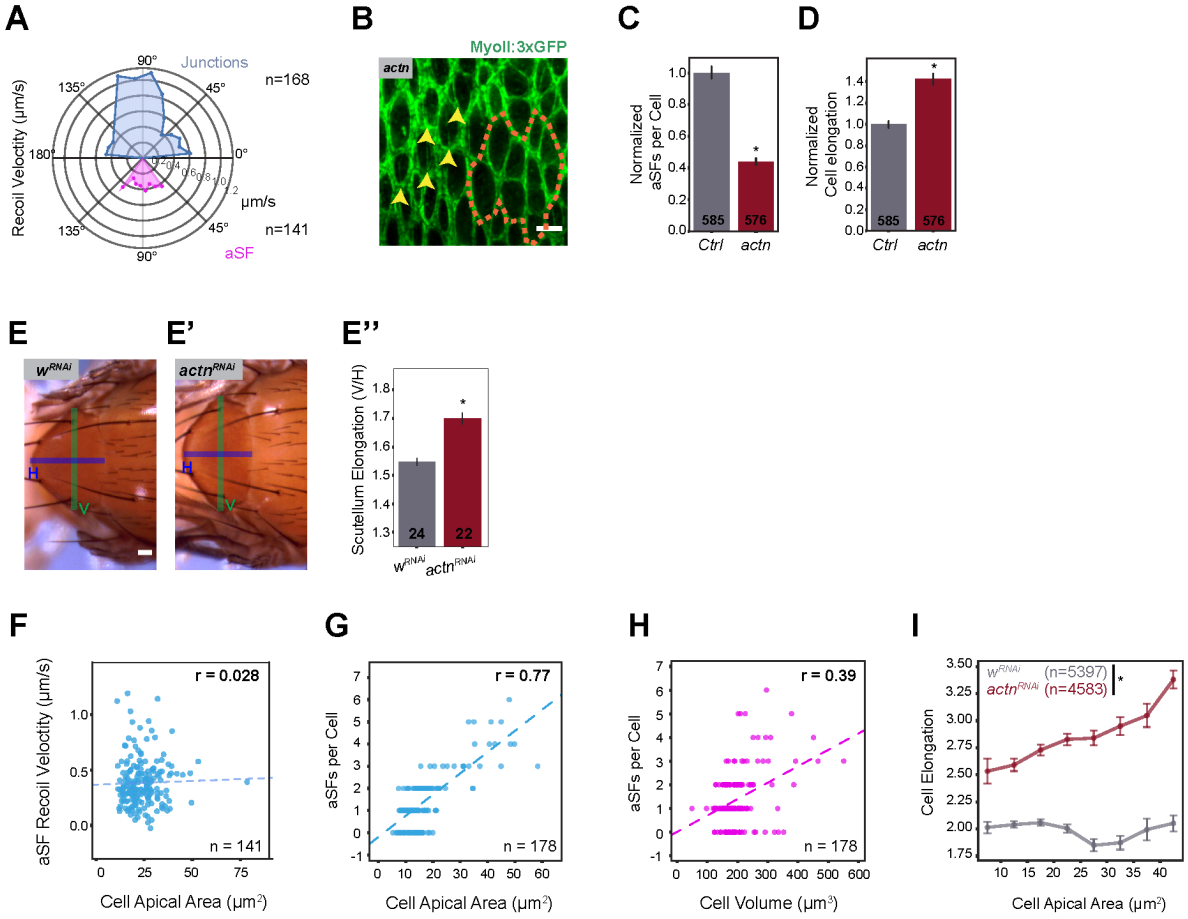

Figure B.3 **Theoretical modelling of cell elongation as a function of tissue stress anisotropy and aSF number.** *To gain a physical understanding of the contributions of aSFs to epithelial cells under anisotropic mechanical stress, we consider regular hexagonal epithelia under uniaxial tensile stress (by convention, along the vertical axis). The regular hexagonal epithelia are organized into one of two orientations, called the cable-forming (CFO) and non-cable-forming (NCFO) orientations, relative to the uniaxial stress (A-C). Tensile forces on cell-cell junctions and on aSFs allow these epithelial cells to resist elongation (D-H). Given that no cell has an infinite pool of MyoII, there is a finite bound on the stress anisotropy that the cells can resist ($\sigma_{max} > \sigma_D \equiv \sigma_{yy} - \sigma_{xx} > 0$). We ask whether cells resist elongation more or less effectively by redistributing junctional MyoII to aSFs (D-H). The vertex model with aSFs predicts that for cells to remain regular hexagons under uniaxial stress, the number of aSFs, or the total aSF tension, per cell must scale linearly with the square root of the cell apical area (I). Larger cells must compensate for the greater distance between edges (orthogonal to the uniaxial stress) by increasing the aSF number, or total aSF tension, per cell.* **A)** Schematic of hexagonal epithelium in the cable-forming orientation (CFO) with aSFs (green). Epithelial geometry is characterized by two edge lengths (l_1 and l_2) and one angle (θ). Edges of length l_1 have tension γ_1; edges of length l_2 have tension γ_2. Total aSF tension per cell is γ_f. **B)** Schematic of hexagonal epithelium in the non-cable-forming orientation (NCFO) with aSFs (green). Epithelial geometry is characterized by two edge lengths (l_3 and l_4) and one angle (ϕ). Edges of length l_3 have tension γ_3; edges of length l_4 have tension γ_4. Total aSF tension per cell is γ_f. **C)** Schematic of stress anisotropy calculation in epithelium from (B). Using linear cuts of the epithelium along axes parallel (magenta dashed line) or perpendicular (blue dashed line) to the aSFs, we sum projections (perpendicular to the cut) of tensile forces from edges and aSFs to calculate a tensile force per length (*i.e.*, 2D stress) along the cut. **D-E)** Schematics of cell shapes and edge tensions for fixed stress anisotropy ($\frac{\sigma_D}{\sigma_{max}}$ indicated in each panel) in the CFO (top) and NCFO (bottom). Edge and aSF widths correspond to magnitudes of tension. Cells with more aSFs (vertical lines in each cell) have a larger total aSF tension γ_f. As the number of aSFs increases, cell elongation in the direction of imposed tension decreases. Blue dashed lines form regular hexagons (see Appendix B Eqs. 11, 12). **F)** Graph of cell elongation normalized by the elongation $S_{reg,hex}$ of a regular hexagon ($\frac{S}{S_{reg,hex}}$) as a function of stress anisotropy ($\frac{\sigma_D}{\sigma_{max}}$). We compare cells in the CFO without aSFs to cells in the NCFO with total aSF tension (γ_f). **G-H)** Plot of normalized cell elongation ($\frac{S}{S_{reg,hex}}$) as a function of total aSF tension (γ_f) and stress anisotropy ($\frac{\sigma_D}{\sigma_{max}}$) for cells in the CFO and NCFO. Tension is scaled such that $\gamma_f = 1$ corresponds to the edge tension in the case of isotropic stress without aSFs. Note that large total aSF tensions (upper left-hand quadrant of plot) generate cells which are elongated orthogonal to the uniaxial stress. The elongation measure S does not distinguish between elongation along the uniaxial stress and elongation orthogonal to the uniaxial stress. **I)** Plot of aSF number per cell (at fixed tension per aSF) as a function of the square root of cell apical area in the vertex model. For this plot, $\sigma_D = \frac{2}{3}\sigma_{max}$ and the tension per aSF is equal to one third of the edge tension in the case of isotropic stress without aSFs. **J)** Graph of the cell apical area as a function of the square root of the cell apical area between 10 and 40μm, illustrating the linear relationship between these quantities for the sample of wt cells used in our analysis of aSFs in time-lapse imaging. n: cell number. r: Pearson correlation coefficients.

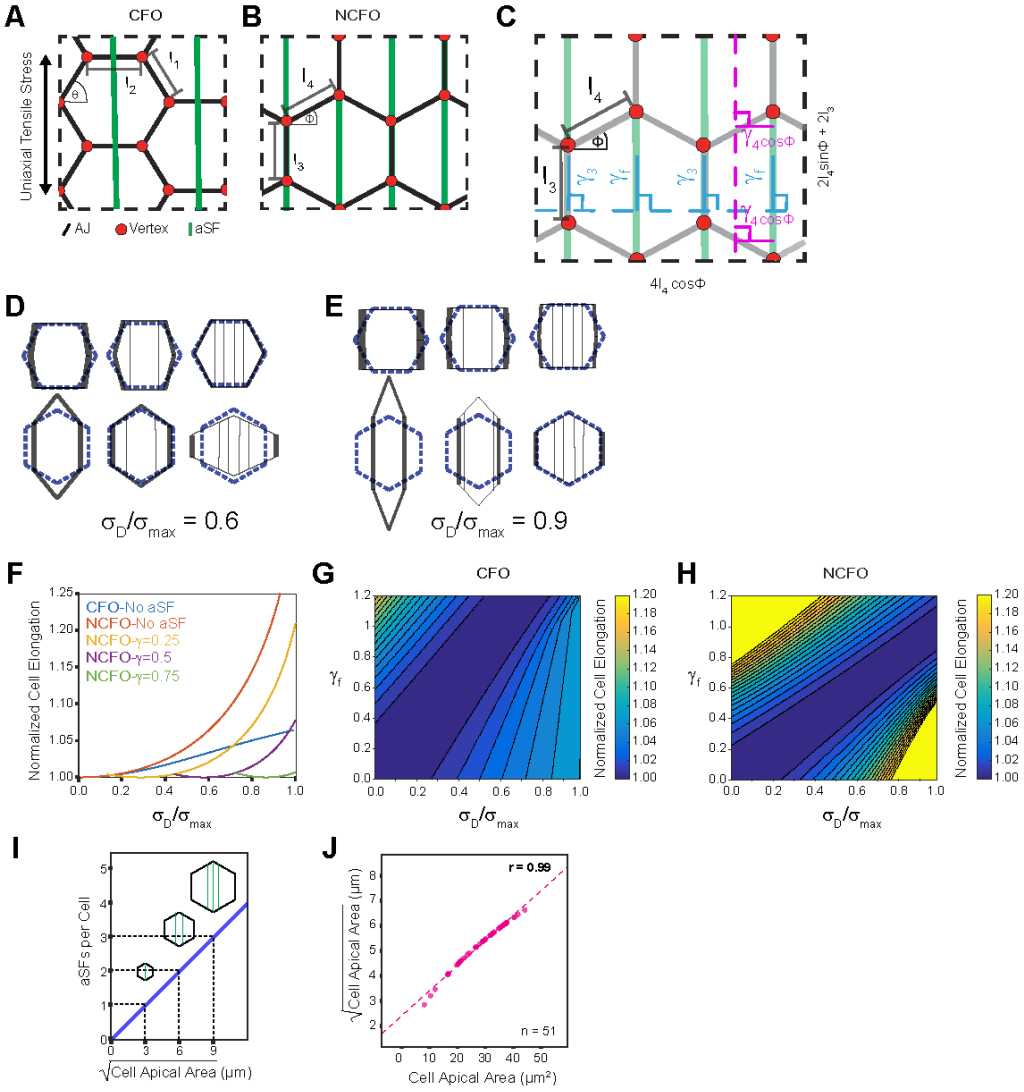
A
CFO
B
NCFO
C
Uniaxial Tensile Stress
AJ
Vertex
aSF
D
σD/σmax = 0.6
E
σD/σmax = 0.9
F
Normalized Cell Elongation
CFO-No aSF
NCFO-No aSF
NCFO-γ=0.25
NCFO-γ=0.5
NCFO-γ=0.75
σD/σmax
G
CFO
γf
Normalized Cell Elongation
H
NCFO
I
aSFs per Cell
√Cell Apical Area (μm)
J
r = 0.99
n = 51
√Cell Apical Area (μm)
Cell Apical Area (μm²)

Figure B.4 **Modulation of Hippo/Yki signalling by mechanical stress.** *In order to quantify the intensity of Jub and Wts distributed in clusters at different developmental timepoints or in different experimental conditions, we implemented a method based on the Fiji FindFoci plug-in allowing cluster identification (B-B'''). To determine whether Jub clustering could modulate Hippo signaling, we developed an optogenetic approach to induce Jub clustering independently of aSF formation. The Cry2Olig:ChFP protein forms clusters upon blue-light illumination. We generated a Cry2Olig:ChFP:Jub as well as a control Cry2Olig:ChFP, and expressed them ubiquitously. Blue-light illumination was sufficient to induce the clustering of both Cry2Olig:ChFP and Cry2Olig:ChFP:Jub in the absence of aSFs. While the light-induced clustering of control Cry2Olig:ChFP does not promote Wts:GFP clustering nor change of Yki transcriptional activity, the light-induced clustering of Cry2Olig:ChFP:Jub leads to the formation of Wts:GFP clusters colocalizing with Cry2Olig:ChFP:Jub and to an increase in Yki transcriptional activity (D-F).* Unless otherwise stated, protein distributions and quantifications are reported for the region boxed in Fig. 3.1A at 26 hAPF. **A)** Graph of intensities (mean ± SEM) of Wts:GFP (purple), Jub.GFP (orange) and PH:GFP (grey) along AJ centered at the aSF tip (arrowhead). n: number of junctions. *p*-values<10^{-5} for Wts:GFP and Jub.GFP. Statistical comparisons were performed between the intensities at the aSF tip (± 0.5 µm around the aSF tip) and the AJ intensities. **B-B''')** Schematic of protein clusters identification and ratio$^{in/out}$ of cluster measurement. Fluorescence signals were sum projected from eight z-sections above to eight z-sections below the AJs (B-B'). The sum projected image was used to determine: (i) The mean fluorescent intensity in cluster (Ic): Clusters were automatically identified using the Fiji FindFoci plug-in (B''). The resulting mask was used to measure the mean intensity in each cluster (Ic) and the area occupied by each cluster (Ac); (ii) The mean intensity along the AJ, (Iaj): the AJ cell contour was selected using Fiji segmented line tool (blue, B''') and used to measure (Iaj) and the total area of the cell junction (Aaj); (iii) The mean fluorescent background intensity (Ib) was measured by selecting the apical medial region of the cells (red, B'''). The signal in cluster was defined as $in^{cluster} = \frac{\sum_{each\ cluster}((Ic-Ib)*Ac)}{(Iaj-Ib)*Aaj}$ and signal on junction as $out^{cluster} = 1 - in^{cluster}$. The ratio$^{in/out}$ of cluster as $\frac{in^{cluster}}{out^{cluster}}$. **C)** Graph of the number of Jub:GFP and Wts:GFP clusters per cell (mean ± SEM) at 18 hAPF (low stress) and 26hAPF (high stress). n: number of cells; *p*-values<10^{-4} for the difference between 18 hAPF and 26 hAPF for both Jub:GFP and Wts:GFP. **D-D')** Distributions of Cry2Olig:ChFP and Wts:GFP at the time of blue light illumination at t=0s (D) and at t=950s upon blue light illumination every 50 s (D'). **E-E')** Distributions of Cry2Olig:ChFP:Jub and Wts:GFP at the time of blue light illumination at t=0s (E) and at t=950s upon blue light illumination every 50 s (E'). **F)** Graph of the intensity of the *DIAP1-nls:GFP* Yorkie reporter (mean ± SEM) in tissues expressing Cry2Olig:ChFP or Cry2Olig:ChFP:Jub in dark (ns) or light (*p*-value<0.01) conditions. Fluorescence intensities were measured at 0h (beginning of the experiment) and 4h. The fluorescence intensities measured at 4h were divided by fluorescence intensities measured at 0h, and the resulting ratios were normalized by the mean of the ratios calculated for Cry2Olig:ChFP of each condition. Clustering was induced by two initial steps of high blue laser illumination (491nm, interval 5 min), and then was maintained at low laser power for GFP imaging, every 5 min. N: number of experiments. **G-G')** Distributions of Wts:CitFP (green, G and fire, G') and MyoII:3xGFP during aSF displacement. Yellow arrowheads: aSF (G); light green arrowheads: Wts:CitFP cluster (G'). **H-I)** Graph of cortical Jub:GFP (H) and Wts:GFP (I) normalized integrated intensity (mean ± SEM) in w^{RNAi} control and $actn^{RNAi}$ cells. Integrated intensities of the w^{RNAi} control or $actn^{RNAi}$ cells were normalized by the mean integrated intensity of surrounding cells not juxtaposed with the w^{RNAi} control and $actn^{RNAi}$ cells, respectively. **J**) Graphs of the number of Jub:GFP and Wts:CitFP clusters (mean ± SEM) in w^{RNAi} control and $actn^{RNAi}$ cells at 26 hAPF. n: number of cells; *p*-values<10^{-3} for Jub:GFP and Wts:CiFP. **K)** Graph of *ban-nls:GFP* intensity (mean ± SEM) in control and $actn^{lGl}$ cells at 26 hAPF. Average intensities were normalized by mean intensities of control cells. N: number of animals; *p*-value<10^{-2}. **L)** Graph of cell division rate between 16 and 40 hAPF (mean ± SEM) in *pnr-G4*>w^{dsRNA} (control) and *pnr-G4*>$actn^{dsRNA}$ tissues. At the central and posterior region of the tissue (box in Fig. 3.1A), cell proliferation occurs as two successive waves. The first wave occurs between 18 and 24 hAPF, while the second one occurs after 24 hAPF. This second wave of division corresponds to cells that have progressed through the cell cycle under higher mechanical stress. The reduction of Actn function leads to a specific decrease in the number of cell divisions during this second wave. Average number of cells used per animal in w^{RNAi} is 218 and in $actn^{RNAi}$ is 148. N: number of animals. *p*-value<10^{-2}. Scale bars: 2 µm (D, G). Statistical tests: Kruskal-Wallis tests (A, C, F and H-K) and mixed-ANOVA test (L). ns: not significant. Statistically significant differences (*p*-value<0.05) are indicated by one asterisk.

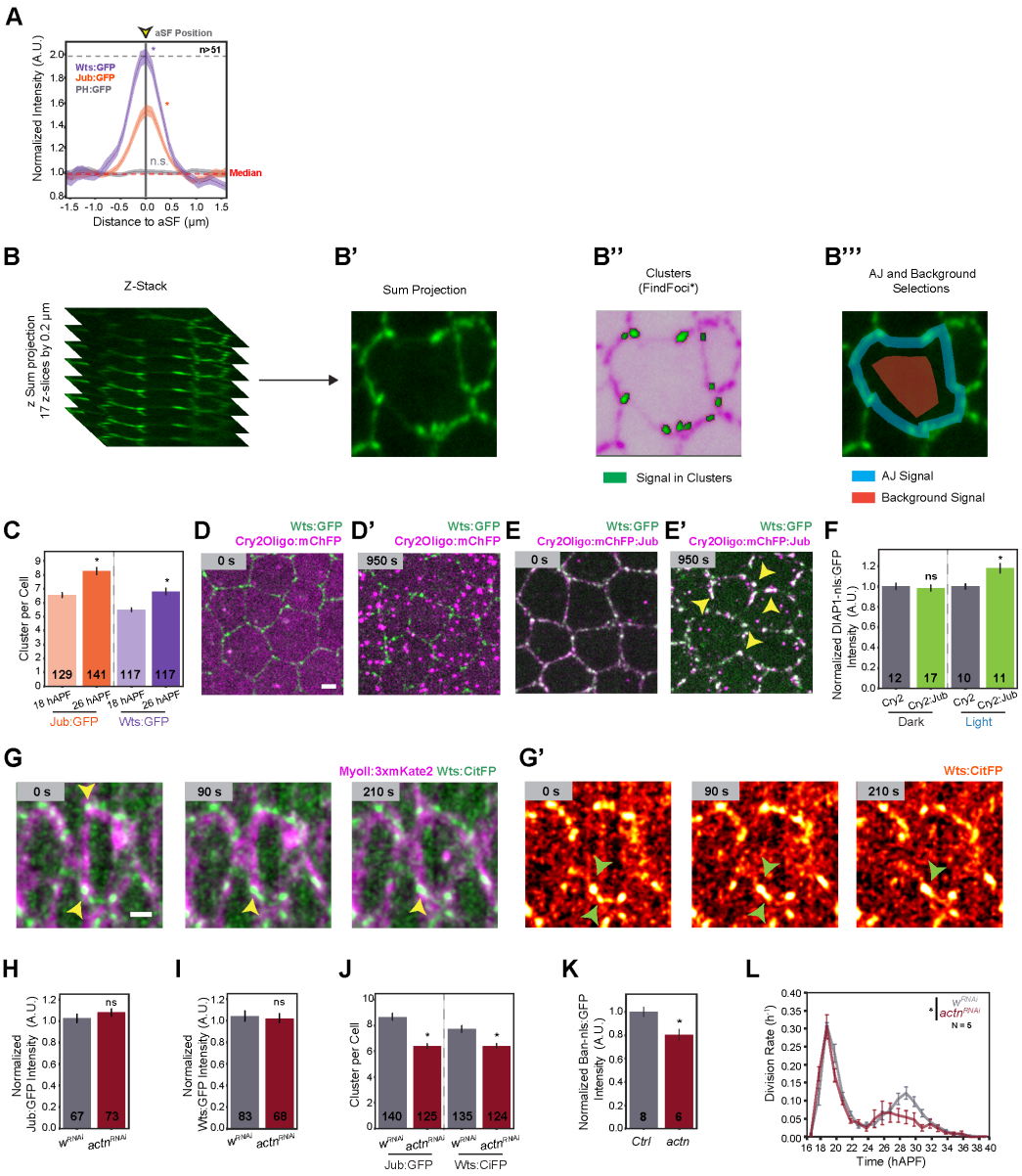
A
aSF Position
n>51
Wts:GFP
Jub:GFP
PH:GFP
Normalized Intensity (A.U.)
n.s.
Median
Distance to aSF (µm)
B
Z-Stack
z Sum projection
17 z-slices by 0.2 µm
B'
Sum Projection
B''
Clusters
(FindFoci*)
Signal in Clusters
B'''
AJ and Background
Selections
AJ Signal
Background Signal
C
Cluster per Cell
129
141
117
117
18 hAPF
26 hAPF
18 hAPF
26 hAPF
Jub:GFP
Wts:GFP
D
Wts:GFP
Cry2Oligo:mChFP
0 s
D'
Wts:GFP
Cry2Oligo:mChFP
950 s
E
Wts:GFP
Cry2Oligo:mChFP:Jub
0 s
E'
Wts:GFP
Cry2Oligo:mChFP:Jub
950 s
F
Normalized DIAP1-nls:GFP
Intensity (A.U.)
ns
12
17
10
11
Cry2
Cry2:Jub
Cry2
Cry2:Jub
Dark
Light
G
MyoII:3xmKate2 Wts:CitFP
0 s
90 s
210 s
G'
Wts:CitFP
0 s
90 s
210 s
H
Normalized
Jub:GFP Intensity (A.U.)
ns
67
73
wRNAi
actnRNAi
I
Normalized
Wts:GFP Intensity (A.U.)
ns
83
68
wRNAi
actnRNAi
J
Cluster per Cell
140
125
135
124
wRNAi
actnRNAi
wRNAi
actnRNAi
Jub:GFP
Wts:CiFP
K
Normalized Ban-nls:GFP
Intensity (A.U.)
8
6
Ctrl
actn
L
Division Rate (h-1)
wRNAi
actnRNAi
N = 5
Time (hAPF)

Figure B.5 **Hippo/Yki scaling with cell apical area.** Unless otherwise stated, protein distributions and quantifications are reported for the region boxed in Fig. 3.1A at 26 hAPF. **A)** Graph of Wts:GFP ratio$^{in/out}$ of cluster (mean ± SEM) as a function of apical cell size at 18 hAPF and 26 hAPF. n: number of cells; p-value<10^{-4}. **B)** Graph of Wts:CitFP and Jub.GFP ratio$^{in/out}$ of cluster (mean ± SEM) as a function of apical cell size at 18 hAPF. n: number of cells; p-value<0.05. **C)** Graph of the number of Jub:GFP clusters (mean ± SEM) as a function of apical cell size in w^{RNAi} control and $actn^{RNAi}$ cells at 26 hAPF. n: number of cells; p-value<10^{-5}. **D)** Graph of apical cell area (mean ± SEM) versus *ban-nls:GFP* intensity (mean ± SEM) in w^{RNAi}, $actn^{RNAi}$, $aurB^{RNAi}$ and svn^{RNAi} cells. Number of cells (n) used to calculate cell apical area (and clustering of Jub:GFP, in Fig. B.5E) and number of animals (N) *ban-nls:GFP* w^{RNAi} (n: 140 and N: 8), $actn^{RNAi}$ (n: 125 and N: 13), $aurB^{RNAi}$ (n: 45 and N: 9) and suv^{RNAi} (n: 140 and N: 10). Dotted line is the regression line for the w^{RNAi}, $aurB^{RNAi}$ and svn^{RNAi} data points. **E)** Graph of Jub:GFP ratio$^{in/out}$ of cluster (mean ± SEM) versus *ban-nls:GFP* intensity (mean ± SEM) in w^{RNAi}, $actn^{RNAi}$, $aurB^{RNAi}$ and svn^{RNAi} cells. Number of cells (n) used for Jub:GFP clustering (and cell apical area, in Fig. B.5D) and number of animals (N) *ban-nls:GFP* w^{RNAi} (n: 140 and N: 8), $actn^{RNAi}$ (n: 125 and N: 13), $aurB^{RNAi}$ (n: 45 and N: 9) and svn^{RNAi} (n: 140 and N: 10). Dotted line is the regression line for w^{RNAi}, $actn^{RNAi}$, $aurB^{RNAi}$ and svn^{RNAi} data points. Statistical tests: Ancova tests for difference in regression slopes (A-C). ns: not significant. Statistically significant differences (p-value<0.05) are indicated by one asterisk.

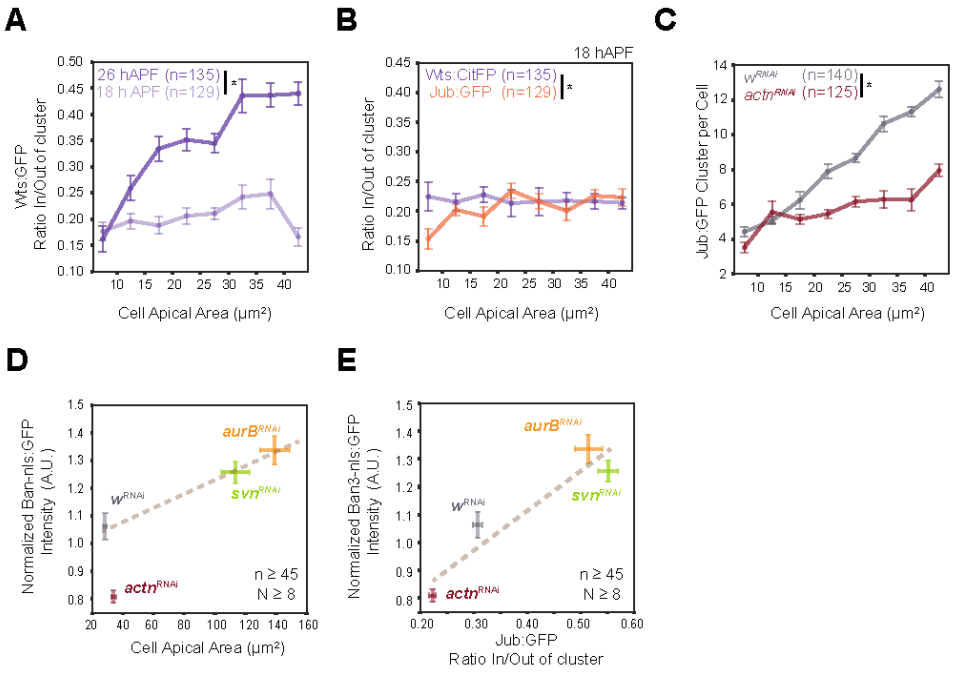

Figure B.6 **Quantitative characterization of aSF nucleation at TCJs.** *More than 95 percent of aSFs nucleate at a TCJ (n=624, Fig. 3.4I). For a given cell's shape, we would like to predict which TCJs are sites of aSF nucleation for that cell. When an aSF nucleates at a TCJ, we calculate both the TCJ's opening angle and the orientation of its bisector in that cell relative to the a-p axis (A); these are the angles for the pair of adjacent edges that meet at the TCJ (A). We compare the geometric properties of nucleating TCJs to the geometric properties of the set of all TCJs (B-C). The TCJ bisector orientation is strongly predictive of aSF nucleation; nucleating TCJs are TCJs with a bisector pointing mostly along the a-p axis (D-F). We check that the nucleation rate per cell is proportional to the number of nucleating TCJs (G). After verifying that the number of nucleating TCJs increases with cell apical area (H), we explore whether large cells have more aSFs because they have more nucleating TCJs. Using an aSF-nucleating TCJ criterion derived from the data, we*

find that a "nucleation-only" model (in which the nucleation rate per cell is proportional to the number of nucleating TCJs) generates a weak scaling of aSF number with cell apical area (I). Unless otherwise stated, protein distributions and quantifications are reported for the region boxed in Fig. 3.1A at 26 hAPF. **A)** Illustration of TCJ opening angle α and TCJ bisector orientation θ with respect to the a-p axis. **B)** Grey-coded plot of fraction of TCJs with opening angle (α) and bisector orientation (θ). n: pairs of adjacent edges (3 pairs of adjacent edges per individual TCJ). **C)** Grey-coded plot of fraction of aSF nucleation events as a function of opening (α) and bisector (θ) TCJ angles. n: number of nucleation events. **D)** Grey-coded plot of nucleation rate as a function of opening (α) and bisector (θ) TCJ angles. This relative nucleation rate is the ratio of the data in (C) to the data in (B). The white region with dashed lines corresponds to TCJs which are rarely observed (less than 0.01% in (B)). n: number of nucleation events. **E)** Empirical cumulative distribution of the aSF nucleation data as a function of bisector orientation θ (red curve). The aSF-nucleating TCJ cutoff (dashed magenta line) is based on the ninety-fifth percentile of aSF nucleation events. n: number of nucleation events. **F)** Graph of the nucleation rate as a function of TCJ bisector orientation θ. Within each bin of θ, we compute the ratio of the number of nucleation events to the fraction of the total number of adjacent edge pairs in that bin and normalize all bins by the largest ratio. The vertical (dashed magenta) line denotes the aSF nucleation cutoff in (D). n: number of nucleation events. **G)** Graph of aSF nucleation rate (h^{-1}) as a function of the average number of nucleating TCJs over 2h (25-27 hAPF). n: number of cells. **H)** Graph of number of TCJs per cell (grey, mean ± SEM) and number of aSF-nucleating TCJ per cell (red, mean ± SEM) as a function of cell apical area. n: number of cells. **I)** Graph of experimental (grey, mean ± SEM) and predicted (red, mean ± SEM) aSF number per cell as a function of cell apical area. The red line is the result of the "nucleation-only" model. n: number of cells. r: Pearson correlation coefficient. ns: not significant. Statistically significant differences (p-value<0.05) are indicated by using one asterisk.

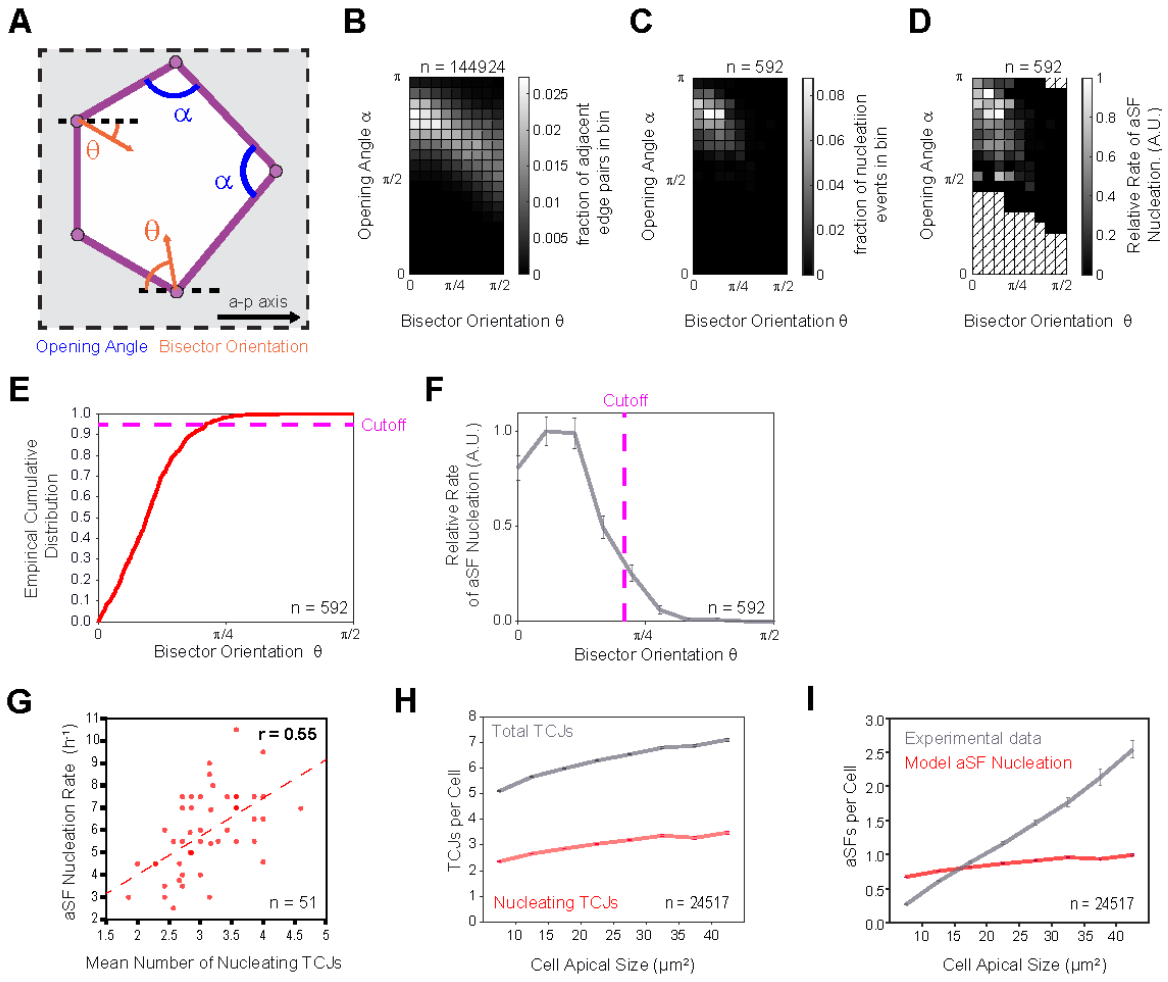

Figure B.7 **Quantitative characterization of aSF breakage at TCJs.** *To determine where aSFs break, we track aSF positions from midlife to breakage in E-Cad:3xmKate2 and MyoII:3xGFP time-lapse images. Since no aSF is perfectly aligned with the uniaxial stress, for each aSF we can define a leading tip and a lagging tip. The leading tip is the aSF tip that has moved farther from the nucleating TCJ along the a-p axis, and the lagging tip is the other aSF endpoint (A-B). To quantify the aSF position, we measure the distance along the a-p axis between the nucleating TCJ and the leading aSF tip (B). We, first, show that aSFs break near the cell centroid and that aSFs are closer to the cell centroid at breakage than at midlife (C-D). Furthermore, aSFs are more likely to break near TCJs than would be expected solely from a bias towards breaking near the cell centroid (E-I). We assign an aSF breakage event to a specific TCJ, if the distance between the leading aSF tip and the TCJ is less than the cortex thickness, estimated in (L). We determine the geometric characteristics of these aSF-breaking TCJs (M-N). After defining an aSF-breaking TCJ criterion (N), we develop a phenomenological model in which aSFs move at a constant speed (O) from aSF-nucleating TCJs to aSF-breaking TCJs. As validated by experimental data (P), our model assumes that aSF lifetime is proportional to how far each aSF moves from nucleation to breakage (Q).* Unless otherwise stated, protein distributions and quantifications are reported for the region boxed in Fig. 3.1A at 26 hAPF. **A)** Distribution of E-Cad:3xmKate2 and MyoII:3xGFP immediately before aSF breakage. In this example, both aSF tips are attached to TCJs at the time of aSF breakage. **B)** Schematic for calculation of aSF penetration distance (orange dashed line) and cell centroid position (red dashed line) along the a-p axis relative to the nucleating TCJ (red arrow). The aSF is green. aSF tips are indicated by yellow arrows. The cell centroid is indicated by a blue dot. **C)** Graph of aSF penetration distance as a function of the separation between the aSF's nucleating TCJ and the cell centroid position at aSF midlife. The dashed line is the line of best fit, which indicates that the extent of aSF penetration at midlife depends on the distance between the nucleating TCJ and the cell centroid (p-value$<10^{-5}$). n: number of aSFs. **D)** Graph of aSF penetration distance as a function of the separation between the aSF's nucleating TCJ and the cell centroid position at aSF breakage. The dashed line is the line of best fit, indicating that the extent of aSF penetration at the time of breakage depends on the distance between the nucleating TCJ and the cell centroid (p-value$<10^{-5}$). aSFs penetrate farther by the time of breakage than at midlife (see Appendix B.2). n: number of aSFs. **E-F)** Two examples of aSFs at the time of breakage in two distinct cells. In both cases, the aSF breaks near the cell centroid and is aligned with two TCJs. The red dashed line is the a-p distance between the aSF-nucleating TCJ (red arrows) and the cell centroid (blue circles), which is plotted in (D, x-coordinate). The orange dashed line is the distance between the position of the aSF nucleation and the leading aSF tip, which is plotted in (D, y-coordinate). Although the cell in (E) and (F) are distinct, the distances between the nucleating TCJ and the cell centroid are the same for both examples. **G)** To illustrate our procedure for defining a distance $\delta^{aSF-TCJ\ swapped}$ for each breakage event (see Appendix B), we swap the aSF from the cell in (E) into the cell in (F). $\delta^{aSF-TCJ\ swapped}$ (yellow line) is the distance along the a-p axis from the breaking TCJ to the leading tip of the swapped aSF. **H)** Histogram of distance between the leading tip of each aSF and its nearest TCJ at the time of aSF midlife. n: number of aSFs. **I)** Histogram of distance between the leading tip of each swapped aSF and its nearest TCJ in the cell into which it has been swapped at aSF midlife. n: number of aSFs. **J)** Histogram of distance between the leading tip of each aSF and its nearest TCJ at the time of aSF breakage. n: number of aSFs. **K)** Histogram of distance between the leading tip of each swapped aSF and its nearest TCJ in the cell into which it has been swapped at the time of aSF breakage. n: number of aSFs. **L)** Graph of E-Cad:3xmKate2 and MyoII:3xGFP intensities (mean ± SEM) as a function of the distance to a nucleating TCJ. E-Cad:3xmKate2 and MyoII:3xGFP intensity profiles were measured along a line of 5 pixels wide (0.13 µm per pixel), which passes through the nucleating TCJ (2 min before aSF nucleation) orthogonal to the nascent aSF. Positive distances correspond to pixels within the cell in which an aSF will nucleate; negative distances correspond to pixels on the other side of the TCJ. We selected pixels that are between -0.5 µm and 2.0 µm from the nucleating TCJ. We normalized both E-Cad:3xmKate2 and MyoII:3xGFP intensity profiles. Maximum intensity peaks were found for E-Cad:3xmKate2 (magenta arrow) and MyoII:3xGFP on the average intensity profiles. Junctional cortex thickness was estimated via a cross-correlation between average intensity profiles of E-Cad:3xmKate2 and MyoII:3xGFP (junctional cortex thickness estimation 0.52 µm). Alternately, individual MyoII:3xGFP and E-Cad:3xmKate2 intensity profiles of TCJs were used to estimated junctional cortex thickness by measuring, for each sample, the distance between MyoII:3xGFP maximum peak and E-Cad:3xmKate2 maximum peak and by also estimating junctional cortex thickness, using 66% (dotted blue line) of the maximum peak of MyoII:3xGFP as a limit to define cortex. Both measurements result in similar junctional cortex thickness values: 0.52 µm versus 0.51 ± 0.12 µm. n: number of TCJs. **M)** Grey-coded plot of the fraction of aSF breakage events as a function of the opening (α) and bisector angle (θ) of the breaking TCJ. n: number of aSFs. **N)** Empirical cumulative distribution of aSF breakage events as a function of TCJ bisector angle θ (blue curve). Dashed magenta line: θ cutoff for aSF-breaking TCJ. n: number of aSFs. **O)** Graph of average aSF velocity per cell (µm.min^{-1}) as a function of cell apical area. n: number of cells. **P)** Graph of average aSF lifetime (min) as a function of average aSF total distance travelled (µm) from the nucleating TCJ. n: number of cells. **Q)** Schematic for model of aSF lifetimes as a function of cell geometry. First, the aSF (green) nucleates a short distance (burgundy; shown in inset) from its nucleating TCJ (red arrow). The aSF moves away from its nucleating TCJ until its tips (green arrows) reach breaking TCJs (blue arrows). The aSF breaks when its tips (green arrows) are within a short distance (orange; shown in inset) from breaking TCJs. (Note that $x_0 < 0$ would correspond to aSF breakage *after* passing breaking TCJs.) The predicted aSF lifetime is proportional to the distance (along the a-p axis) that the aSF moves, on average, from its nucleation site to its breakage site(bracketed red dotted line). Statistical tests: *F*-test (C-D).

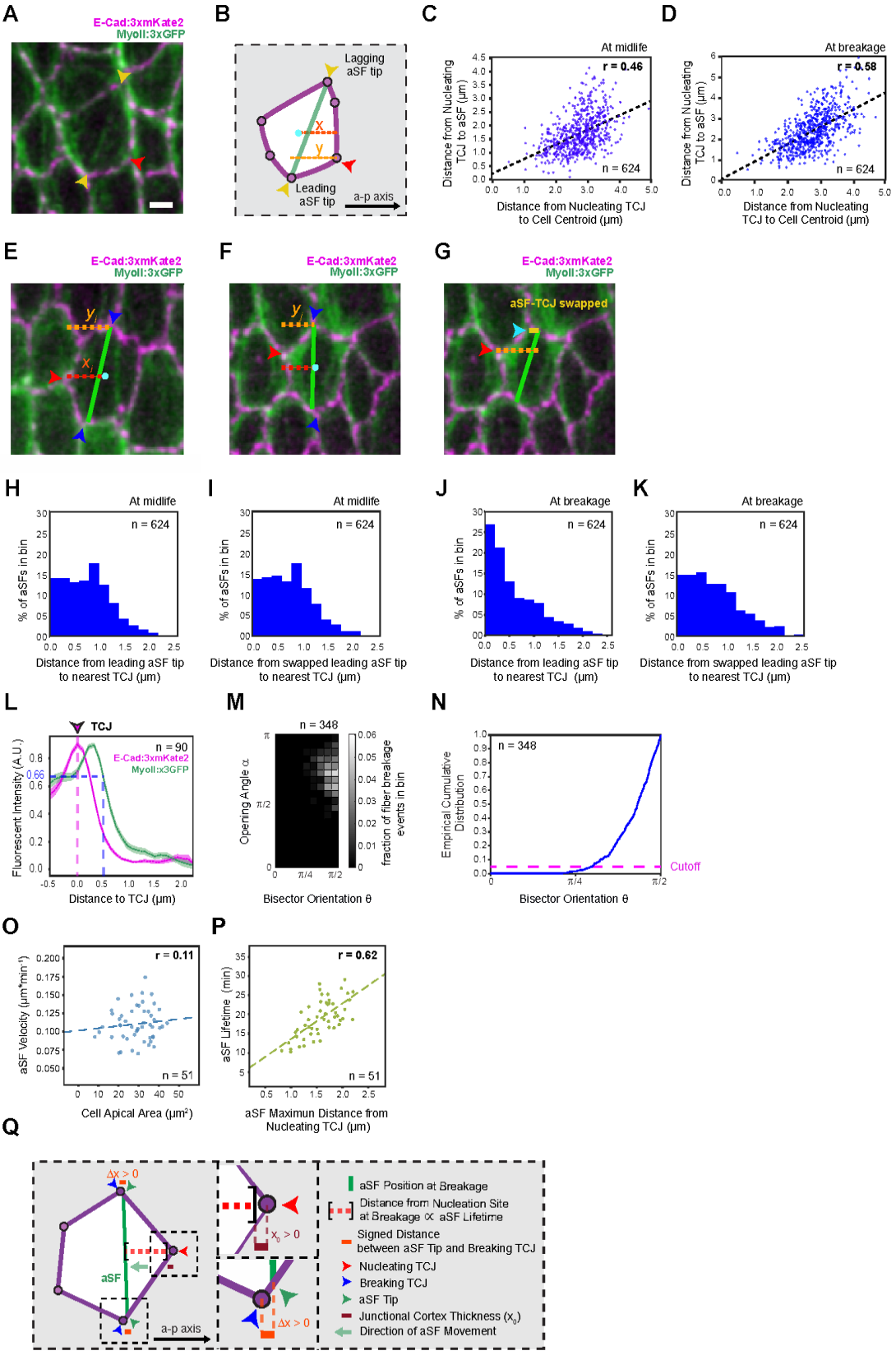
A
E-Cad:3xmKate2
MyoII:3xGFP
B
Lagging aSF tip
Leading aSF tip
a-p axis
C
At midlife
r = 0.46
n = 624
Distance from Nucleating TCJ to aSF (μm)
Distance from Nucleating TCJ to Cell Centroid (μm)
D
At breakage
r = 0.58
n = 624
E
F
G
aSF-TCJ swapped
H
At midlife
n = 624
% of aSFs in bin
Distance from leading aSF tip to nearest TCJ (μm)
I
Distance from swapped leading aSF tip to nearest TCJ (μm)
J
At breakage
K
L
TCJ
n = 90
Myoll:x3GFP
Fluorescent Intensity (A.U.)
Distance to TCJ (μm)
M
n = 348
Opening Angle α
fraction of fiber breakage events in bin
Bisector Orientation θ
N
Empirical Cumulative Distribution
Cutoff
O
r = 0.11
aSF Velocity (μm*min⁻¹)
Cell Apical Area (μm²)
P
r = 0.62
aSF Lifetime (min)
aSF Maximun Distance from Nucleating TCJ (μm)
Q
Δx > 0
aSF
a-p axis
aSF Position at Breakage
Distance from Nucleation Site at Breakage ∝ aSF Lifetime
Signed Distance between aSF Tip and Breaking TCJ
Nucleating TCJ
Breaking TCJ
aSF Tip
Junctional Cortex Thickness (x0)
Direction of aSF Movement

Figure B.8 **Analyses of *trbl*^{UP} cell clones.** Unless otherwise stated, protein distributions and quantifications are reported for the region boxed in Fig. 3.1A at 26 hAPF. **A)** Graph of cell apical area (mean ± SEM) for *trbl*^{UP} border and bulk cells. n: number of cells; *p*-value<10^{-3}. **B)** Graph of the experimental number of aSFs (mean ± SEM) as a function of cell apical area in *trbl*^{UP} border and bulk cells. n: number of cells. **C)** Graph of the experimental number of aSFs (mean ± SEM) and cell apical area (mean ± SEM) in *trbl*^{UP} border and bulk cells. n: number of cells; *p*-value<10^{-2}. For each group, the dashed line represents the scaling of aSF number with cell area given by the analysis of covariance. The scaling of aSF number with cell area is 0.031 $\frac{aSF}{\mu m^2}$. **D)** Graph of number of TCJs per cell (mean ± SEM) for *trbl*^{UP} border and bulk cells. n: number of cells; *p*-value<10^{-5}. **E)** Graph of the number of TCJs per cell (mean ± SEM) as function of cell apical area in *trbl*^{UP} border and bulk cells. n: number of cells. **F)** Graph of the predicted number of aSFs (mean ± SEM.) as a function of cell area in *trbl*^{UP} border and bulk cells. n: number of cells. **G)** Graph of the predicted number of aSFs (mean ± SEM) and cell apical area (mean ± SEM) in *trbl*^{UP} border and bulk cells. n: number of cells; *p*-value<10^{-2}. For each cell group, the dashed line represents the scaling of aSF number with cell area given by the analysis of covariance. The scaling of aSF number with cell area is 0.030 $\frac{aSF}{\mu m^2}$. Statistical tests: Kruskal-Wallis tests (A,D) and Ancova tests for difference in regression intercepts (C and G). ns: not significant. Statistically significant differences (*p*-value<0.05) are indicated by one asterisk.

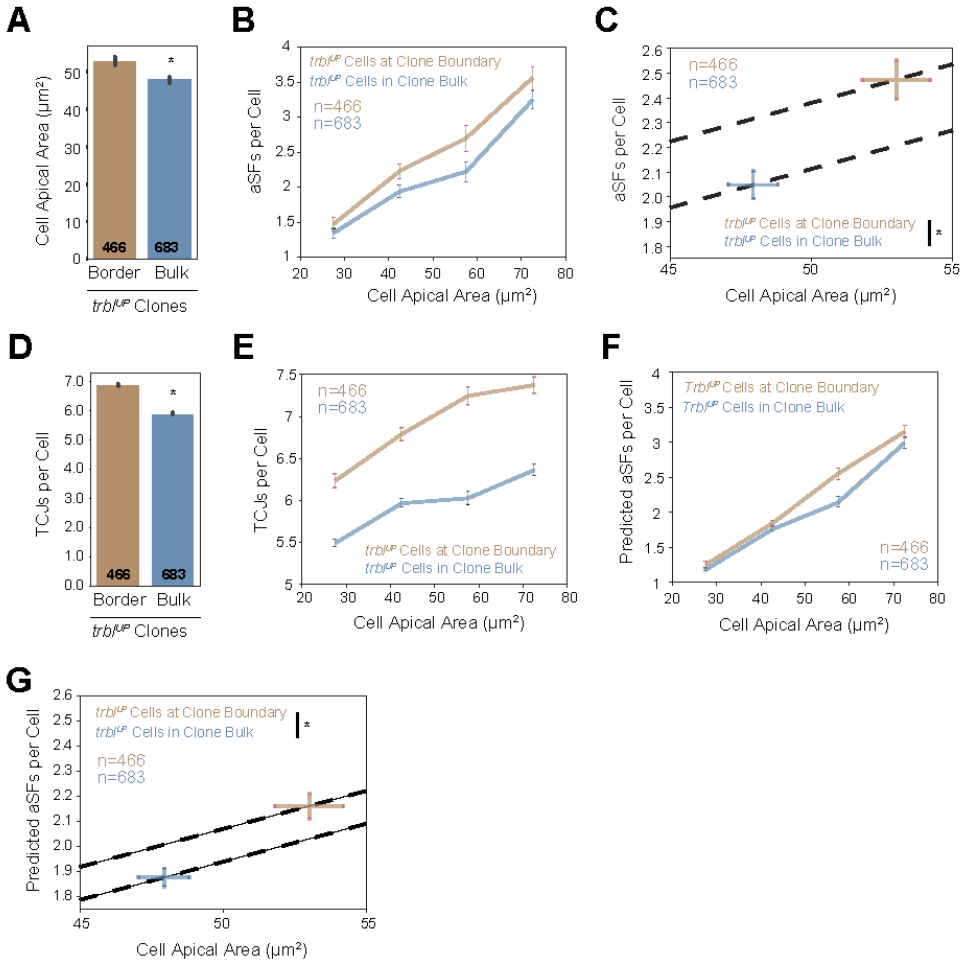

Figure B.9 **Dependence of aSF nucleation on TCJ bisector orientation.** *To investigate why TCJ bisector orientation is predictive of aSF nucleation at TCJs (A,B), we consider a model in which an aSF nucleates at a TCJ when the decrease in line tension energy overcomes the increase in energy due to detachment from the junctional cortex. To account for mechanical anisotropy, we allow both the line tension energy and the attachment energy to depend on the orientations of cell-cell junctions relative to the a-p axis. We find that this model is incapable of explaining why aSFs nucleate at TCJs like (C) while aSFs do not nucleate at TCJs like (C'). Searching for a possible physical reason for the dependence of aSF nucleation on TCJ bisector orientation, we analyse the relationship between TCJ opening angle and TCJ bisector orientation under uniaxial stress (D). Under increases in tensile uniaxial stress, TCJs for which bisectors point perpendicular to the a-p axis (C') tend to close (i.e., decrease in opening angle), and TCJs for which bisectors point along the a-p axis (C) tend to open (i.e., increase in opening angle). We propose a hypothesis in which aSFs nucleate at TCJs due to increases in TCJ opening angle; aSF nucleation could occur via a mechanosensitive mechanism as actomyosin filaments near a TCJ experience strain during increases in the TCJ opening angle. We also foresee that the TCJ composition might be modulated by mechanical stress since the level of the TCJ protein Sidekick was recently reported to be modulated by junction tension or cell geometry.* **A)** Grey-coded plot of fraction of TCJs with opening angle (α) and bisector orientation (θ) (adapted from Fig. B.6B). Red dot indicates a group of TCJs for which the bisector points along the a-p axis. Blue dot indicates a group of TCJs for which the bisector points perpendicular to the a-p axis. n: pairs of adjacent edges (3 pairs of adjacent edges per TCJ). **B)** Grey-coded plot of nucleation rate as a function of opening (α) and bisector (θ) TCJ angles (adapted from Fig. B.6D). The red dot indicates a group of TCJs for which the bisector points along the a-p axis and at which aSFs nucleate. The blue dot indicates a group of TCJs for which the bisector points perpendicular to the a-p axis and at which no aSFs nucleate. n: number of nucleation events. **C)** Schematic of TCJ for which the bisector points along the a-p axis and with an opening angle α larger than $\frac{\pi}{2}$ (*i.e.*, $\varepsilon > 0$). The angle of each cell-cell junction relative to the a-p axis is δ. **C')** Schematic of TCJ for which the bisector points perpendicular to the a-p axis and with an opening angle α smaller than $\frac{\pi}{2}$ (*i.e.*, $\varepsilon > 0$). The angle of each cell-cell junction relative to the a-p axis is δ. **D)** Graph of opening angle α (mean ± SEM) as a function of bisector orientation θ at 18 h APF, 22 h APF, and 26 h APF. n: pairs of adjacent edges (3 pairs of adjacent edges per TCJ).

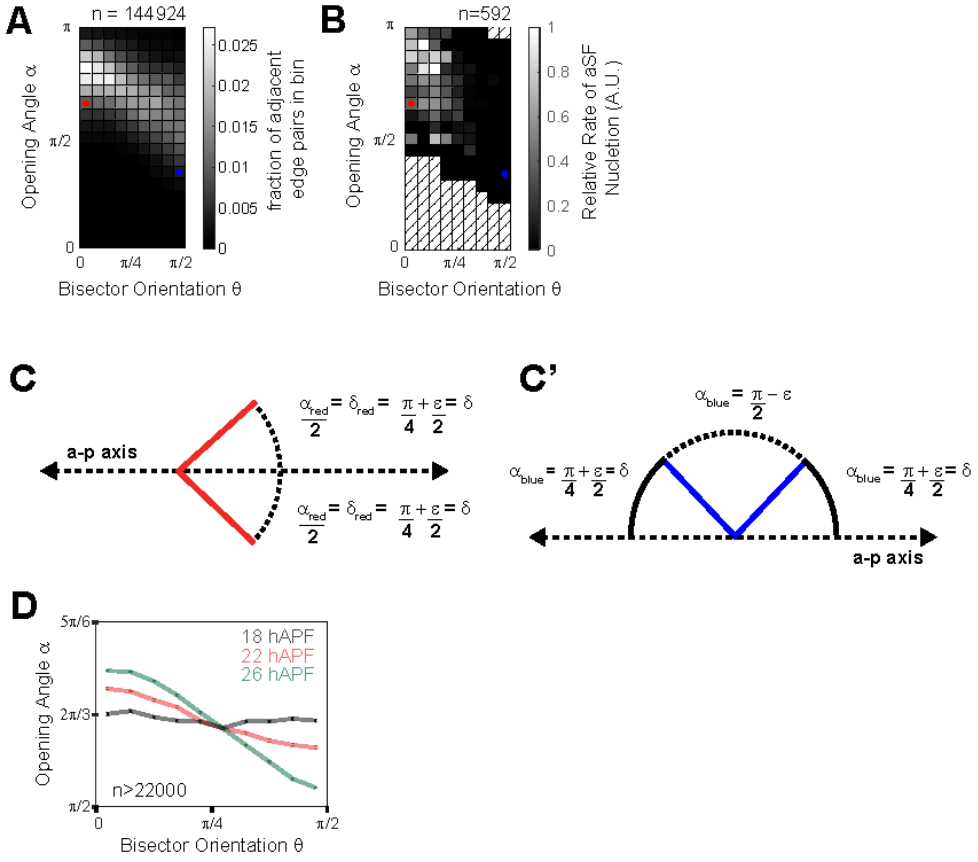

Appendix C Further Discussion of Mechanics-Guided Neural Induction

1. Estimating in-plane stress (without fitting post displacements to functional form)

First, we consider a rectangular cell layer that is much longer along one axis (y-axis) than the other (x-axis). This rectangular layer is thin (along the z-axis). One can estimate the in-plane stress via [233]:

$$\langle \sigma_{xx}(x) \rangle = \frac{1}{h_y} \int_0^x \int_0^{h_y} T_x(x', y') dx' dy' \quad \text{[Eq. 1]}$$

where T_x is the x-component of the traction force per cell area. h_y is the length of the cell layer (parallel to the free boundary) over which one averages. $x = 0$ corresponds to the free boundary of the cell layer (where $\langle \sigma_{xx}(x = 0) \rangle = 0$). σ_{xx} has units of force per length and corresponds to the stress integrated over the height of the cell layer.

In the remaining discussion, we use the formalism developed in [212, 214]; we predominantly adopt the notation from [214]. Since we are considering an array of posts that behave like Hookean springs,

$$T_x(x', y') = kNu_x(x', y') \quad \text{[Eq. 2]}$$

u_x is the x-displacement of the substrate caused by the contraction of the cell layer. k is the effective spring constant of the posts. N is the planar density of posts.

Our measurements of traction forces are for cell layers in a disc geometry rather than in a rectangular stripe geometry. To develop an estimate of in-plane stress, we first provide the equation for force balance in polar coordinates [212, 214]:

$$div \cdot \sigma = kN\vec{u} \quad \text{[Eq. 3]}$$

$$div \cdot \sigma = \left(\frac{\partial \sigma_{rr}}{\partial r} + \frac{1}{r} \frac{\partial \sigma_{r\theta}}{\partial \theta} + \frac{1}{r} (\sigma_{rr} - \sigma_{\theta\theta}) \right) \hat{r} + \left(\frac{\partial \sigma_{r\theta}}{\partial r} + \frac{1}{r} \frac{\partial \sigma_{\theta\theta}}{\partial \theta} + \frac{2}{r} (\sigma_{r\theta}) \right) \hat{\theta} = kN\vec{u} \quad \text{[Eq. 4]}$$

$$(div \cdot \sigma) \cdot \hat{r} = \frac{\partial \sigma_{rr}}{\partial r} + \frac{1}{r} \frac{\partial \sigma_{r\theta}}{\partial \theta} + \frac{1}{r} (\sigma_{rr} - \sigma_{\theta\theta}) = kNu_r \quad \text{[Eq. 5]}$$

We, then, average over the θ-direction. We use the notation $\frac{1}{2\pi} \int_0^{2\pi} (\dots) d\theta \equiv \langle \dots \rangle$,

$$\langle (div \cdot \sigma) \cdot \hat{r} \rangle = \langle \frac{\partial \sigma_{rr}}{\partial r} + \frac{1}{r}\frac{\partial \sigma_{r\theta}}{\partial \theta} + \frac{1}{r}(\sigma_{rr} - \sigma_{\theta\theta}) \rangle = kN\langle u_r \rangle \quad \text{[Eq. 6]}$$

Since $\int_0^{2\pi} \left(\frac{\partial \sigma_{r\theta}}{\partial \theta}\right) d\theta = 0$, this equation simplifies to:

$$\langle (div \cdot \sigma) \cdot \hat{r} \rangle = \langle \frac{\partial \sigma_{rr}}{\partial r} + \frac{1}{r}(\sigma_{rr} - \sigma_{\theta\theta}) \rangle = kN\langle u_r \rangle \quad \text{[Eq. 7]}$$

If the cellular contraction is isotropic, we find that:

$$\sigma_{rr} - \sigma_{\theta\theta} = kN(1-\nu)l^2(e_{rr} - e_{\theta\theta}) = kN(1-\nu)l^2\left(\frac{\partial u_r}{\partial r} - \frac{1}{r}\frac{\partial u_\theta}{\partial \theta} - \frac{u_r}{r}\right) \quad \text{[Eq. 8]}$$

where e_{rr} and $e_{\theta\theta}$ are elements of the strain tensor. ν is the Poisson's ratio of the cell layer. l is the localization length, which depends on the ratio of the cell stiffness to the substrate stiffness [212, 214].

Since $\int_0^{2\pi} \left(\frac{\partial u_\theta}{\partial \theta}\right) d\theta = 0$,

$$\langle \frac{1}{r}(\sigma_{rr} - \sigma_{\theta\theta}) \rangle = kN(1-\nu)l^2 \langle \frac{1}{r}\left(\frac{\partial u_r}{\partial r} - \frac{u_r}{r}\right) \rangle \quad \text{[Eq. 9]}$$

We conclude that:

$$\langle (div \cdot \sigma) \cdot \hat{r} \rangle = \langle \frac{\partial \sigma_{rr}}{\partial r} \rangle + \frac{kN(1-\nu)l^2}{r} \langle \left(\frac{\partial u_r}{\partial r} - \frac{u_r}{r}\right) \rangle = kN\langle u_r \rangle \quad \text{[Eq. 10]}$$

$$\frac{\partial}{\partial r}\langle \sigma_{rr} \rangle = \left(-\frac{kN(1-\nu)l^2}{r}\langle \frac{\partial u_r}{\partial r} - \frac{u_r}{r} \rangle + kN\langle u_r \rangle\right) = \left(-\frac{kN(1-\nu)l^2}{r}\left(\frac{\partial \langle u_r \rangle}{\partial r} - \frac{\langle u_r \rangle}{r}\right) + kN\langle u_r \rangle\right) \quad \text{[Eq. 11]}$$

Integrating from the boundary of the cell layer (at $r' = r_0$) to $r' = r < r_0$, we find:

$$\langle \sigma_{rr}(r) \rangle = kN\big(\xi_1(r) + \xi_2(r)\big) \quad \text{[Eq. 12]}$$

$$\xi_1(r) \equiv \int_{r_0}^{r} \langle u_r(r') \rangle \, dr' \quad \text{[Eq. 13]}$$

$$\xi_2(r) \equiv -(1-\nu)l^2 \int_{r_0}^{r} \frac{1}{r'}\left(\frac{\partial \langle u_r(r') \rangle}{\partial r'} - \frac{\langle u_r(r') \rangle}{r'}\right) dr' \quad \text{[Eq. 14]}$$

If we assume that $\xi_2(r) \ll \xi_1(r)$, then Eq. 12 reduces to the quasi-1D case (see Eq. 1):

$$\langle \sigma_{rr}(r) \rangle \approx kN\xi_1(r) \equiv kN \int_{r_0}^{r} \frac{1}{2\pi}\int_0^{2\pi} u_r(r', \theta') \, d\theta' \, dr' \quad \text{[Eq. 15]}$$

In this section, we do not fit post displacements to extract estimates of ν and l, so we would like to neglect $\xi_2(r)$ in Eq. 12 since $\xi_2(r)$ has an explicit dependence on ν and l (Eq. 14). In our experiments, the maximum value of $|\langle u_r \rangle|$ is of order 0.25 μm. The colony radius is 150 μm. The maximum value of $\left|\langle \frac{\partial u_r}{\partial r} \rangle\right|$ is of order 0.1. ν is approximately 0.5, and l^2 is typically of order 100 μm^2 [213, 214]. Near the colony boundary ($r \approx r_0$), $\frac{(1-\nu)l^2}{r}\left(\frac{\partial u_r}{\partial r} - \frac{u_r}{r}\right)$ is of order 0.01 μm, so we

expect that $\xi_2(r) \ll \xi_1(r)$ for $r \approx r_0$. In the subsequent analysis, we explicitly compute $\frac{\xi_2(r)}{(1-\nu)l^2}$ to check that $\xi_2(r) \ll \xi_1(r)$ for $r \approx r_0$.

Since we expect this approximation (Eq. 15) to break down for r small, we use Eq. 15 to approximate $\langle \sigma_{rr}(r) \rangle$ for $r \gtrapprox \frac{r_0}{2}$, where r_0 is the colony radius. After concluding from these samples that $\xi_2(r) \ll \xi_1(r)$ (Fig. C.1A-C), we provide our estimate of $\langle \sigma_{rr}(r) \rangle$ in Fig. C.1D. The magnitude of $\langle \sigma_{rr}(r) \rangle$ near the peak is approximately $2\frac{nN}{\mu m}$, which is consistent with estimates of cell layer stress in other contexts [156, 231-233, 241, 242]. For example, assuming a cell layer height of 5 μm, Trepat *et al.* estimate that the magnitude of $\langle \sigma_{xx}(x) \rangle$ in an expanding cell colony is on the order of $1\frac{nN}{\mu m}$ (see Fig. 3 in [233]). In measuring how traction forces scale with the size of cohesive cell colonies, Mertz *et al.* estimate that the active stress (integrated over the cell layer height) is approximately $1\frac{nN}{\mu m}$ [232]. Studying mechanotransduction in collective cell migration, Das *et al.* estimate mechanical stresses on the order of $1\frac{nN}{\mu m}$ (see Fig. 6 in [231]).

2. Estimating cellular material properties (by fitting post displacements to functional form)

We now ask whether we can extract estimates for cellular material properties like contractility and stiffness from fits to post displacement data. To model traction forces from single cells, one typically treats the single cell as a uniformly contractile medium with a uniform stiffness [215, 281]. Previous studies of cell colonies have assumed that all cells have the same mechanical properties, including both stiffness and contractility [211, 216, 232]. In our system, the cells in the colony are differentiating; we, thus, expect that a model of a uniform contractile medium will not fit our colony measurements well.

To fit the post displacements to some functional form, we assume that the cell layer is axisymmetric. We assume the cell layer is composed of distinct (concentric) domains with distinct cell stiffnesses and distinct contractilities. We propose three competing models to fit the post displacements. For each model, we use the formalism developed in [214]. As discussed in the supplementary note in [214], we assume that at the boundary between two domains, u_r and σ_{rr} are continuous.

Before introducing each of the three models, we would like to point out a few choices that we made to reduce model complexity. For each model, we only fit the post displacement from $r =$

$0\ \mu m$ to $r = 140\ \mu m$. The radius of the micropattern is $r_0 = 150\ \mu m$, so one would expect that the maximum $|\langle u_r(r)\rangle|$ would occur at the very edge ($r = 150\ \mu m$) [212, 214, 215] and that $|\langle u_r(r)\rangle|$ would abruptly collapse to zero for $r > 150\ \mu m$. However, in our experiments the maximal $|\langle u_r(r)\rangle|$ occurs near $r = 140\ \mu m$, and $|\langle u_r(r)\rangle|$ gradually transitions to zero from $r = 140\ \mu m$ to $r = 150\ \mu m$ (Fig. C.2-C.3). We could account for this in the model by introducing a region near the edge with different material properties, but that would unnecessarily increase the number of fit parameters.

A second simplifying assumption we make for models 1 and 2 is that the innermost tissue domain is stiff ($l' \to \infty$). This assumption is motivated by the fact that the post displacement profiles near the center are nearly linear (which occurs when l' is equal to or greater than the radius of the interior tissue domain) (Fig. C.2-C.3). This assumption ($l' \to \infty$) allows us to remove one extraneous free parameter and to focus our attention on mechanical interaction between cells in the vicinity of the fate boundary $r \gtrapprox \frac{r_0}{2}$.

The last simplifying assumption relates to Poisson's ratio for the cellular layer. For a 1D colony (e.g., a cell layer in a stripe geometry [214]), it is impossible to extract independent estimates of the preferred strain P and Poisson's ratio ν from the post displacements. These two values appear in the equation for post displacements as the product $(1 + \nu)P$ [212, 214]. As in other studies [215, 216, 231, 241], we choose a value for Poisson's ratio for the cell layer within a biologically relevant range. We choose $\nu = 0.43$ [215].

Model 1: The cell layer is uniform in both contractility and stiffness. The cell layer extends to $r = r' = 140\ \mu m$. $\langle \sigma_{rr}(r = r')\rangle = \tilde{\sigma}$; $\tilde{\sigma}$ is estimated as described in Appendix C.1. The cell layer has localization length l' and target strain P'.

$$u(r) = AI_1\left(\frac{r}{l'}\right); 0 \le r \le r' \qquad \text{[Eq. 16]}$$

$$A \equiv \frac{\left(\frac{1+\nu}{2}P' + \frac{1}{kN(l')^2}\tilde{\sigma}\right)}{\left(\frac{I_0\left(\frac{r'}{l'}\right)}{l'} + \frac{(\nu-1)I_1\left(\frac{r'}{l'}\right)}{r'}\right)} \qquad \text{[Eq. 17]}$$

The free parameters are l' and P'.

Model 2: The cell layer is composed of two distinct domains. One domain extends from $r = 0$ to $r = r'$; this domain has localization length l' ($l' \to \infty$) and target strain P'. The other domain extends from $r = r'$ to $r = r''$; this domain has localization length l'' and target strain P''. The cell

layer extends to $r = r'' = 140\ \mu m < r_0 = 150\ \mu m$. $\langle \sigma_{rr}(r = r'') \rangle = \tilde{\sigma}$; $\tilde{\sigma}$ is estimated as described in Appendix C.1.

$$u(r) = \begin{cases} \frac{P'r}{2}; 0 \le r \le r' \\ BI_1\left(\frac{r}{l''}\right) + CK_1\left(\frac{r}{l''}\right); r' \le r \le r'' \end{cases} \quad \text{[Eq. 18]}$$

$$B \equiv \frac{\left(kN\, l'' P' r' r'' K_0\left(\frac{r''}{l''}\right) + r''\left(kN(l'')^2(1+\nu)P'' + 2\tilde{\sigma}\right)K_1\left(\frac{r'}{l''}\right) - kN(l'')^2(-1+\nu)P' r' K_1\left(\frac{r''}{l''}\right)\right)}{2kN\, l''\left(\left(r'' I_0\left(\frac{r''}{l''}\right) + l''(-1+\nu) I_1\left(\frac{r''}{l''}\right)\right)K_1\left(\frac{r'}{l''}\right) + I_1\left(\frac{r'}{l''}\right)\left(r'' K_0\left(\frac{r''}{l''}\right) - l''(-1+\nu)K_1\left(\frac{r''}{l''}\right)\right)\right)} \quad \text{[Eq. 19]}$$

$$C \equiv \frac{\left(kN\, l'' P' r' r'' I_0\left(\frac{r''}{l''}\right) - r''\left(kN(l'')^2(1+\nu)P'' + 2\tilde{\sigma}\right)I_1\left(\frac{r'}{l''}\right) + kN(l'')^2(-1+\nu)P' r' I_1\left(\frac{r''}{l''}\right)\right)}{2kN\, l''\left(\left(r'' I_0\left(\frac{r''}{l''}\right) + l''(-1+\nu) I_1\left(\frac{r''}{l''}\right)\right)K_1\left(\frac{r'}{l''}\right) + I_1\left(\frac{r'}{l''}\right)\left(r'' K_0\left(\frac{r''}{l''}\right) - l''(-1+\nu)K_1\left(\frac{r''}{l''}\right)\right)\right)} \quad \text{[Eq. 20]}$$

The free parameters are l'', r', P' and P''.

Model 3: The cell layer is composed of three distinct domains. One domain extends from $r = 0$ to $r = r'$; this domain has localization length l' ($l' \to \infty$) and target strain P'. Another domain extends from $r = r'$ to $r = r''$; this domain has localization length l'' and target strain P''. The last domain extends from $r = r''$ to $r = r'''$; this domain has localization length l''' and target strain P'''. The cell layer extends to $r = r''' = 140\ \mu m < r_0 = 150\ \mu m$. $\langle \sigma_{rr}(r = r''') \rangle = \tilde{\sigma}$; $\tilde{\sigma}$ is estimated as described in Appendix C.1.

For the sake of simplicity (to reduce the number of free parameters), we assume $l'' = l'''$.

$$u(r) = \begin{cases} \frac{P'r}{2}; 0 \le r \le r' \\ BI_1\left(\frac{r}{l''}\right) + CK_1\left(\frac{r}{l''}\right); r' \le r \le r'' \\ DI_1\left(\frac{r}{l''}\right) + EK_1\left(\frac{r}{l''}\right); r'' \le r \le r''' \end{cases} \quad \text{[Eq. 21]}$$

The free parameters are l'', r', r'', P', P'' and P'''. The analytical expressions for B, C, D, E in terms of the fit parameters are rather cumbersome, so we do not explicitly state them here. We do provide our Mathematica code for calculating these coefficients.

We would like to compare Models 1-3 to see which is most correct based on goodness of fit to the data; more specifically, we would like to know the probability $Pr(M_j|D)$ that model M_j ($j = 1, 2, 3$) is correct for the data D. For the sake of clarity, we reproduce some of the discussion from [282, 283] below. The probability of the data D given the model M_j is

$$Pr\left(D\middle|M_j\right) = \int Pr\left(D\middle|\vec{\vartheta}_j, M_j\right) Pr\left(\vec{\vartheta}_j\middle|M_j\right) d\vec{\vartheta}_j \quad \text{[Eq. 22]}$$

where $Pr\left(D\middle|\vec{\vartheta}_j, M_j\right)$ is the likelihood of M_j with parameters $\vec{\vartheta}_j$. $Pr\left(\vec{\vartheta}_j\middle|M_j\right)$ is the prior probability of parameters $\vec{\vartheta}_j$ for the model M_j. One can compare two models (for example, M_1 and M_2) via:

$$\frac{Pr(M_2|D)}{Pr(M_1|D)} = \left[\frac{Pr(D|M_2)}{Pr(D|M_1)}\right]\left[\frac{Pr(M_2)}{Pr(M_1)}\right] = (ratio\ of\ likelihoods\ of\ models\ for\ data\ D)(prior\ ratio) \quad \text{[Eq. 23]}$$

If our prior is that both models are equally likely, then the ratios of the probabilities of the two models M_1 and M_2, given the data, is simply equal to the ratio $\left[\frac{Pr(D|M_2)}{Pr(D|M_1)}\right]$.

To compute $Pr\left(D\middle|M_j\right)$, we must compute $Pr\left(D\middle|\vec{\vartheta}_j, M_j\right)$. Suppose we have n distinct values of the independent variable $(r_1, r_2, \ldots, r_{n-1}, r_n)$; in this case, this variable is the radial coordinate. For each value of the radial coordinate r_i, we have a measured value of the dependent variable y_i, the concentrically averaged radial post displacement, and its error σ_i. For each value r_i, we also have a predicted value of the dependent variable $f_i(\vec{\vartheta}_j, M_j)$; the predicted value of the dependent variable depends on the value of fit parameters $(\vec{\vartheta}_j)$ and the Model M_j. The likelihood of observing dependent variables y_i, with normally distributed errors σ_i, given the predicted values $f_i(\vec{\vartheta}_j, M_j)$ from model M_j is:

$$Pr\left(D\middle|\vec{\vartheta}_j, M_j\right) = \prod_{i=1}^{n}\left[\frac{1}{\sqrt{2\pi}\sigma_i}\exp\left(-\frac{1}{2}\left(\frac{y_i - f_i(\vec{\vartheta}_j, M_j)}{\sigma_i}\right)^2\right)\right] \quad \text{[Eq. 24]}$$

$$\log\left(Pr\left(D\middle|\vec{\vartheta}_j, M_j\right)\right) = \sum_{i=1}^{n}\left[-\frac{1}{2}\log(2\pi) - \log(\sigma_i) - \frac{1}{2}\frac{1}{(\sigma_i)^2}\left(y_i - f_i\left(\vec{\vartheta}_j, M_j\right)\right)^2\right] \quad \text{[Eq. 25]}$$

To compare the likelihood values of models, we use the Bayesian information criterion (BIC), an approximation to the integral in Eq. 22 [282-284]. The assumptions behind the BIC are described in Section 4 of [282]. For a choice of "noninformative" prior distribution $Pr\left(\vec{\vartheta}_j\middle|M_j\right)$ described in [282],

$$\log\left(Pr\left(D\middle|M_j\right)\right) = -\frac{1}{2}BIC\left(M_j\right) + O\left(n^{-\frac{1}{2}}\right) \quad \text{[Eq. 26]}$$

$$BIC\left(M_j\right) = -2\log\left(Pr\left(D\middle|\hat{\vec{\vartheta}}_j, M_j\right)\right) + d_j\log(n) \quad \text{[Eq. 27]}$$

where d_j is the number of parameters in the model M_j and $\hat{\vec{\vartheta}}_j$ is the maximum-likelihood estimate of fit parameters $\vec{\vartheta}_j$ for model M_j $(j = 1, 2, 3)$. The error $O\left(n^{-\frac{1}{2}}\right)$ is such that $\lim_{n\to\infty} n^{\frac{1}{2}}O\left(n^{-\frac{1}{2}}\right) = constant.$

To compare two models (for example, M_1 and M_2), we compute the following ratio:

$$BF(M_2, M_1) = \frac{Pr(M_2|D)}{Pr(M_1|D)} = \exp\left(\frac{log\left(Pr(D|M_2)\right)}{log\left(Pr(D|M_1)\right)}\right) \approx \exp\left(\frac{\Delta BIC_{12}}{2}\right) \quad \text{[Eq. 28]}$$

where $\Delta BIC_{12} = BIC(M_1) - BIC(M_2)$.

The medians for Model 1, Model 2, and Model 3 are 5.9 μm, 8.2 μm, and 15.6 μm, respectively (see Table C.1-3). We can estimate the cell layer stiffness via [214]:

$$E_c = \frac{l^2 kN(1-\nu^2)}{h} \quad \text{[Eq. 29]}$$

Plugging in values for $kN\left(= 0.53\frac{nN}{\mu m^3}\right)$ and $\nu(\approx 0.43)$ and h$(\approx 5\ \mu m)$ [17, 233, 241, 242],

$$E_c \approx \frac{l^2(0.086\ kPa)}{(\mu m)^2} \quad \text{[Eq. 30]}$$

The cell layer stiffness is thus on the order of 10 kPa. Past studies have reported values of at least 1 kPa and at most 100 kPa for cell stiffness [211-214, 231, 241]. Direct estimates of stiffness of human cancer cells and of human smooth muscle cells are on the order of 1 kPa [239, 240]. By fitting substrate displacements to extract l, previous investigators have reported indirect estimates of stiffness of approximately 5 kPa for fibroblasts and MDCK cells [215, 216]. In conclusion, the localization lengths for each model (Table C.1-3) correspond to biologically realistic estimates of cell layer stiffness.

We conclude by discussing which model performs best (see Table C.4). We can categorically reject Model 1; it performs worse than Model 2 and Model 3 for each of the more than forty samples. Comparing the performance of Model 2 and Model 3 is more difficult. For some samples, Model 2 outperforms Model 3 ($\frac{Pr(M_2|D)}{Pr(M_3|D)} > 20$; Blue in Table C.4). For some samples, Model 3 outperforms Model 2 ($\frac{Pr(M_3|D)}{Pr(M_2|D)} > 20$; Maize in Table C.4).

3. Simulations of Tissue Patterning on Substrate of Finite Thickness

We experimentally validated that the size of the PAX3+ domain depends nonmonotonically on the substrate stiffness (controlled by the curing agent to base monomer ratio). Unfortunately, this method of controlling the substrate stiffness simultaneously changes the substrate thickness (see Table C.5). The mechanical model that we use in the main text [212, 214] does not include the effect of substrate thickness. For completeness, we modelled the effect of both substrate thickness and substrate Young's modulus on the size of the PAX3+ domain.

Banerjee and Marchetti developed a formalism for cell layers on finite-thickness substrates in [213]. They approximate the one-dimensional Green's function as:

$$G(x) = \frac{2}{\pi L E_s} K_0 \left[\frac{a+|x|}{h_s(1+\nu_s)}\right] \quad \text{[Eq. 31]}$$

In Eq. 31, the length of the cell layer is L, and a is a short distance cutoff that makes $\lim_{x\to 0} G(x)$ finite. In our case, $L = 400\ \mu m$. We choose $a \approx 0.5\ \mu m$, the approximate size of an adhesion complex [229, 285]. We choose a Poisson's ratio for the substrate $\nu_s = 0.4$ [213].

We slightly modify their notation. Our σ has units of $\frac{nN}{\mu m}$ rather than $\frac{nN}{\mu m^2}$ ($\sigma \to h_c\sigma$).

With no stress propagation through the substrate,

$$\sigma = \lambda^2 \frac{\partial^2 \sigma}{\partial x^2} + h_c \zeta_0 \Delta\mu;\ \ \lambda^2 = \frac{B_c h_c}{E_s};\ \sigma_a = h_c \zeta_0 \Delta\mu \quad \text{[Eq. 32]}$$

$$\zeta_0 \Delta\mu \approx 1\ kPa;\ h_c \approx 5\ \mu m \quad \text{[Eq. 33]}$$

$\zeta_0\Delta\mu$ is the active stress (with unit force / area) due to a chemical potential difference $\Delta\mu$ between ATP and its products [212]. A biophysical explanation for the order of magnitude of $\zeta_0\Delta\mu$ is provided in [232].

$$E_s \approx 1 \frac{kPa}{\mu m};\ B_c \approx 10\ kPa \quad \text{[Eq. 34]}$$

The integro-differential equation (including stress propagation through the substrate) for $\sigma(x)$ is:

$$l_a{}^2 \frac{\partial^2 \sigma}{\partial x^2} - \sigma + \sigma_a = -B_c L h_c \int_0^L dx' \frac{\partial G(|x-x'|)}{\partial x} \frac{\partial \sigma(x')}{\partial x'} \quad \text{[Eq. 35]}$$

$$l_a{}^2 = \frac{B_c h_c}{Y_a};\ Y_a = \frac{k_a}{L\ l_{c0}} \quad \text{[Eq. 36]}$$

In these expression (Eqs. 35, 36), l_a is controlled by the stiffness of the focal adhesions, and l_{c0} is the typical length of a cell in the cell layer [213].

We, first, reproduce the discussion in [213] on how to solve for in-plane stress $\sigma(x)$ in a cell layer bound to an infinitely thick elastic substrate. For an infinitely thick substrate, the Green's function (Eq. 31) becomes:

$$G(x) = \left(-\frac{2}{\pi L E_s}\right)\left(\gamma + \log\left(\frac{a+|x|}{L}\right)\right) \quad \text{[Eq. 37]}$$

where γ is the Euler-Mascheroni constant. We compute $\frac{\partial G(|x-x'|)}{\partial x}$

$$\frac{\partial G(|x-x'|)}{\partial x} = \left(-\frac{2}{\pi L E_s}\right)\frac{(x-x')}{|x-x'|(a+|x-x'|)} \quad \text{[Eq. 38]}$$

As discussed in the supplemental material of [213], we expand $\sigma(x)$ in a Fourier series. We know that $\sigma(x) = 0$ at $x = 0, L$ and that $\frac{d\sigma}{dx} = 0$ at $x = \frac{L}{2}$. Eq. 35 becomes:

$$\sigma_a(x) = \sum_{n=1,3,5,..} \sigma_n \sin\left(n\pi\left(\frac{x}{L}\right)\right)\left[(n\pi)^2\left(\frac{l_a}{L}\right)^2 + 1\right] -$$

$$B_c L h_c \int_0^L dx' \frac{\partial G(|x-x'|)}{\partial x} \sum_{m=1,3,5,\ldots} \sigma_m \cos\left(m\pi\left(\frac{x'}{L}\right)\right)\left(\frac{m\pi}{L}\right) \quad \text{[Eq. 39]}$$

Integrating both sides of Eq. 39 by $\frac{2}{L}\int_0^L dx \sin\left(n\pi\left(\frac{x}{L}\right)\right)$,

$$\frac{2}{L}\int_0^L dx \sin\left(n\pi\left(\frac{x}{L}\right)\right)\sigma_a(x) = \left[(n\pi)^2\left(\frac{l_a}{L}\right)^2 + 1\right]\sigma_n -$$

$$B_c L h_c \left(\frac{2}{L}\right) \sum_{m=1,3,5,\ldots} \sigma_m \left(\frac{m\pi}{L}\right) \int_0^L dx \int_0^L dx' \sin\left(n\pi\left(\frac{x}{L}\right)\right) \frac{\partial G(|x-x'|)}{\partial x} \cos\left(m\pi\left(\frac{x'}{L}\right)\right) \quad \text{[Eq. 40]}$$

Plugging in Eq. 38,

$$\frac{2}{L}\int_0^L dx \sin\left(n\pi\left(\frac{x}{L}\right)\right)\sigma_a(x) = \left[(n\pi)^2\left(\frac{l_a}{L}\right)^2 + 1\right]\sigma_n +$$

$$\frac{4B_c h_c}{\pi L E_s} \sum_{m=1,3,5,\ldots} \sigma_m \left(\frac{m\pi}{L}\right) \int_0^L dx \int_0^L dx' \sin\left(n\pi\left(\frac{x}{L}\right)\right) \frac{(x-x')}{|x-x'|(a+|x-x'|)} \cos\left(m\pi\left(\frac{x'}{L}\right)\right) \quad \text{[Eq. 41]}$$

Defining ${l_{s\infty}}^2 \equiv \frac{4B_c h_c L}{\pi E_s}$,

$$\frac{2}{L}\int_0^L dx \sin\left(n\pi\left(\frac{x}{L}\right)\right)\sigma_a(x) = \left[(n\pi)^2\left(\frac{l_a}{L}\right)^2 + 1\right]\sigma_n + \left(\frac{l_{s\infty}}{L}\right)^2 \sum_{m=1,3,5,\ldots} \sigma_m H_{mn} \quad \text{[Eq. 42]}$$

where $H_{mn} = m\pi \int_0^1 dx \int_0^1 dx' \sin(n\pi x) \frac{(x-x')}{|x-x'|(a/L+|x-x'|)} \cos(m\pi x')$ [Eq. 43]

where $n = 1,3,5, \ldots$

If instead we consider a cell layer bound to an elastic substrate of finite thickness h_s,

$$\frac{\partial G(|x-x'|)}{\partial x} = \left(-\frac{2}{\pi L E_s h_s (1+\nu_s)}\right) \frac{(x-x') K_1\left(\frac{a+|x-x'|}{h_s(1+\nu_s)}\right)}{|x-x'|} \quad \text{[Eq. 44]}$$

Plugging Eq. 44 into Eq. 40,

$$\frac{2}{L}\int_0^L dx \sin\left(n\pi\left(\frac{x}{L}\right)\right)\sigma_a(x) = \left[(n\pi)^2\left(\frac{l_a}{L}\right)^2 + 1\right]\sigma_n -$$

$$B_c L h_c \left(\frac{2}{L}\right)\left(-\frac{2}{\pi L E_s h_s (1+\nu_s)}\right) \sum_{m=1,3,5,\ldots} \sigma_m \left(\frac{m\pi}{L}\right) \int_0^L dx \int_0^L dx' \sin\left(n\pi\left(\frac{x}{L}\right)\right) \frac{(x-x') K_1\left(\frac{a+|x-x'|}{h_s(1+\nu_s)}\right)}{|x-x'|} \cos\left(m\pi\left(\frac{x'}{L}\right)\right) \quad \text{[Eq. 45]}$$

$$\frac{2}{L}\int_0^L dx \left(\sin\left(n\pi\left(\frac{x}{L}\right)\right)\sigma_a(x)\right) = \left[(n\pi)^2\left(\frac{l_a}{L}\right)^2 + 1\right]\sigma_n + \left(\frac{l_{s\infty}}{L}\right)^2 \sum_{m=1,3,5,\ldots} \sigma_m H_{mn} \quad \text{[Eq. 46]}$$

where $H_{mn} = \left(\frac{1}{(1+\nu_s)}\right)\frac{1}{Lh_s} m\pi \int_0^L dx \int_0^L dx' \sin\left(n\pi\left(\frac{x}{L}\right)\right)\frac{(x-x')K_1\left(\frac{a+|x-x'|}{h_s(1+\nu_s)}\right)}{|x-x'|}\cos\left(m\pi\left(\frac{x'}{L}\right)\right)$ [Eq. 47]

For both the case of an infinitely thick substrates and of finitely thick substrates, we can solve this problem as follows:

$$(\sigma_{a,1}\ \sigma_{a,3}\ \sigma_{a,5}\ \dots) = (\sigma_1\ \sigma_3\ \sigma_5\ \dots) \times \left[\begin{pmatrix} 1 & 0 & 0 \\ 0 & 1 & 0 \\ 0 & 0 & 1 \end{pmatrix} + \begin{pmatrix} (\pi)^2 & 0 & 0 \\ 0 & 9(\pi)^2 & 0 \\ 0 & 0 & 25(\pi)^2 \end{pmatrix}\left(\frac{l_a}{L}\right)^2 + \begin{pmatrix} H_{11} & H_{13} & H_{15} \\ H_{31} & H_{33} & H_{35} \\ H_{51} & H_{53} & H_{55} \end{pmatrix}\left(\frac{l_{s\infty}}{L}\right)^2\right] \quad \text{[Eq. 48]}$$

where $\sigma_{a,n} \equiv \frac{2}{L}\int_0^L dx \left(\sin\left(n\pi\left(\frac{x}{L}\right)\right)\sigma_a(x)\right)$ [Eq. 49]

To compute the elements H_{mn}, we use the fact that:

$$H_{mn} = 2\left(\frac{1}{(1+\nu_s)}\right)\frac{1}{Lh_s} m\pi \int_0^L dx \int_0^x dx' \sin\left(n\pi\left(\frac{x}{L}\right)\right)\frac{(x-x')K_1\left(\frac{a+|x-x'|}{h_s(1+\nu_s)}\right)}{|x-x'|}\cos\left(m\pi\left(\frac{x'}{L}\right)\right). \quad \text{[Eq. 50]}$$

We solve H_{mn} via integral2 in MATLAB. We solve the linear equation via linsolve in MATLAB.

In [213], they note that in one dimension, $\sigma(x) = h_c B_c \frac{\partial u}{\partial x} + \sigma_a$ [Eq. 51]

Instead of using σ_a, we define $\sigma_a \equiv h_c B_c(-P)$. Eq. 51 becomes:

$\sigma(x) = h_c B_c\left(\frac{\partial u}{\partial x} - P\right)$ [Eq. 52]

P is the preferred strain. Iff $\frac{\partial u}{\partial x} = P$, the cell layer has zero elastic stresses. $P < 0$ for a contractile medium.

4. Differential Equation for Trace of In-Plane Stress (Micropost Array)

We would like to derive a differential equation for the trace of the in-plane stress that only includes the trace of the stress and the active stress, proportional to fate w. Like the differential equation for the 1D cell layer stress (Eq. 32), we assume it will contain up to second derivatives:

$\left(\frac{\partial^2}{\partial x^2} + \frac{\partial^2}{\partial y^2}\right)(\sigma_{xx} + \sigma_{yy}) = \frac{\partial^2 \sigma_{xx}}{\partial x^2} + \frac{\partial^2 \sigma_{yy}}{\partial y^2} + \frac{\partial^2 \sigma_{yy}}{\partial x^2} + \frac{\partial^2 \sigma_{xx}}{\partial y^2}$ [Eq. 53]

We will systematically replace the terms on the right-hand side of (Eq. 53), testing if the equation reduces to the trace of the stress and the active stress itself.

The elements of the in-place stress σ_{ij} are:

$\sigma_{xx} = \frac{h_c B_c}{1-\nu^2}\frac{\partial u_x}{\partial x} + \frac{h_c B_c}{1-\nu^2}\nu\frac{\partial u_y}{\partial y} - \frac{(1+\nu)}{2}\frac{h_c B_c}{1-\nu^2}P$ [Eq. 54]

$\sigma_{yy} = \frac{h_c B_c}{1-\nu^2}\frac{\partial u_y}{\partial y} + \frac{h_c B_c}{1-\nu^2}\nu\frac{\partial u_x}{\partial x} - \frac{(1+\nu)}{2}\frac{h_c B_c}{1-\nu^2}P$ [Eq. 55]

$$\sigma_{xy} = \frac{(1-\nu)}{2}\frac{h_c B_c}{1-\nu^2}\left(\frac{\partial u_x}{\partial y} + \frac{\partial u_y}{\partial x}\right) \quad \text{[Eq. 56]}$$

Here h_c and B_c are the cell height and elastic modulus, respectively. ν is Poisson's ratio of the cell layer. P is the target strain.

The trace of the in-plane stress is:

$$tr(\sigma) = \sigma_{xx} + \sigma_{yy} = \frac{h_c B_c}{1-\nu^2}(1+\nu)\left(\frac{\partial u_x}{\partial x} + \frac{\partial u_y}{\partial y}\right) - \frac{h_c B_c}{1-\nu^2}(1+\nu)(P) \quad \text{[Eq. 57]}$$

To make a clear connection with the formalism in Appendix A.3 (Eq. 32, 51-52), the active stress σ_a is:

$$\sigma_a = -\frac{h_c B_c}{1-\nu^2}(1+\nu)(P) \quad \text{[Eq. 58]}$$

Force balance between the cell layer and the substrate ($div \cdot \sigma = kN\vec{u}$) demands that:

$$\frac{\partial \sigma_{xx}}{\partial x} + \frac{\partial \sigma_{xy}}{\partial y} = kNu_x \quad \text{[Eq. 59]}$$

$$\frac{\partial \sigma_{yy}}{\partial y} + \frac{\partial \sigma_{xy}}{\partial x} = kNu_y \quad \text{[Eq. 60]}$$

Here spring constant k and number density N characterize the micropost substrate to which the cell layer is bound.

Taking $\frac{\partial}{\partial x}$ and $\frac{\partial}{\partial y}$ of Eq. 59-60, respectively,

$$\frac{\partial^2 \sigma_{xx}}{\partial x^2} = kN\frac{\partial u_x}{\partial x} - \frac{\partial}{\partial x}\frac{\partial \sigma_{xy}}{\partial y} \quad \text{[Eq. 61]}$$

$$\frac{\partial^2 \sigma_{yy}}{\partial y^2} = kN\frac{\partial u_y}{\partial y} - \frac{\partial}{\partial y}\frac{\partial \sigma_{xy}}{\partial x} \quad \text{[Eq. 62]}$$

Plugging Eq. 61-62 into Eq. 53,

$$\left(\frac{\partial^2}{\partial x^2} + \frac{\partial^2}{\partial y^2}\right)\left(\sigma_{xx} + \sigma_{yy}\right) = kN\left(\frac{\partial u_x}{\partial x} + \frac{\partial u_y}{\partial y}\right) - 2\frac{\partial}{\partial x}\frac{\partial \sigma_{xy}}{\partial y} + \frac{\partial^2 \sigma_{yy}}{\partial x^2} + \frac{\partial^2 \sigma_{xx}}{\partial y^2} \quad \text{[Eq. 63]}$$

where $\frac{\partial}{\partial x}\frac{\partial \sigma_{xy}}{\partial y} = \frac{(1-\nu)}{2}\frac{h_c B_c}{1-\nu^2}\left(\frac{\partial}{\partial x}\frac{\partial^2 u_x}{\partial y^2} + \frac{\partial}{\partial y}\frac{\partial^2 u_y}{\partial x^2}\right)$ [Eq. 64]

and $\frac{\partial^2 \sigma_{yy}}{\partial x^2} = \frac{h_c B_c}{1-\nu^2}\frac{\partial}{\partial y}\frac{\partial^2 u_y}{\partial x^2} + \frac{h_c B_c}{1-\nu^2}\nu\frac{\partial^3 u_x}{\partial x^3} - \frac{1+\nu}{2}\frac{h_c B_c}{1-\nu^2}\frac{\partial^2 P}{\partial x^2}$ [Eq. 65]

and $\frac{\partial^2 \sigma_{xx}}{\partial y^2} = \frac{h_c B_c}{1-\nu^2}\frac{\partial}{\partial x}\frac{\partial^2 u_x}{\partial y^2} + \frac{h_c B_c}{1-\nu^2}\nu\frac{\partial^3 u_y}{\partial y^3} - \frac{1+\nu}{2}\frac{h_c B_c}{1-\nu^2}\frac{\partial^2 P}{\partial y^2}$ [Eq. 66]

$$-2\frac{\partial}{\partial x}\frac{\partial \sigma_{xy}}{\partial y} + \frac{\partial^2 \sigma_{yy}}{\partial x^2} + \frac{\partial^2 \sigma_{xx}}{\partial y^2} = \frac{h_c B_c}{1-\nu^2}\nu\left(\frac{\partial}{\partial x}\frac{\partial^2 u_x}{\partial y^2} + \frac{\partial}{\partial y}\frac{\partial^2 u_y}{\partial x^2} + \frac{\partial^3 u_x}{\partial x^3} + \frac{\partial^3 u_y}{\partial y^3}\right) - \frac{1+\nu}{2}\frac{h_c B_c}{1-\nu^2}\left(\frac{\partial^2}{\partial x^2} + \frac{\partial^2}{\partial y^2}\right)P$$

[Eq. 67]

$$\left(\frac{\partial^2}{\partial x^2} + \frac{\partial^2}{\partial y^2}\right)\left(\sigma_{xx} + \sigma_{yy}\right) = \frac{h_c B_c}{1-\nu^2}(1+\nu)\left(\frac{\partial^3 u_x}{\partial x^3} + \frac{\partial^2}{\partial y^2}\frac{\partial u_x}{\partial x} + \frac{\partial^3 u_y}{\partial y^3} + \frac{\partial^2}{\partial x^2}\frac{\partial u_y}{\partial y}\right) - \frac{h_c B_c}{1-\nu^2}(1+\nu)\left(\frac{\partial^2}{\partial x^2} + \frac{\partial^2}{\partial y^2}\right)(P) \quad \text{[Eq. 68]}$$

$$\left(\frac{\partial^3 u_x}{\partial x^3}+\frac{\partial^2}{\partial y^2}\frac{\partial u_x}{\partial x}+\frac{\partial^3 u_y}{\partial y^3}+\frac{\partial^2}{\partial x^2}\frac{\partial u_y}{\partial y}\right)=\frac{1-\nu^2}{h_c B_c(1+\nu)}\left(\frac{\partial^2}{\partial x^2}+\frac{\partial^2}{\partial y^2}\right)\left(\sigma_{xx}+\sigma_{yy}\right)+\left(\frac{\partial^2}{\partial x^2}+\frac{\partial^2}{\partial y^2}\right)(P)$$ [Eq. 69]

Plugging Eq. 69 into Eq. 67,

$$-2\frac{\partial}{\partial x}\frac{\partial \sigma_{xy}}{\partial y}+\frac{\partial^2\sigma_{yy}}{\partial x^2}+\frac{\partial^2\sigma_{xx}}{\partial y^2}=\frac{\nu}{1+\nu}\left(\frac{\partial^2}{\partial x^2}+\frac{\partial^2}{\partial y^2}\right)\left(\sigma_{xx}+\sigma_{yy}\right)+\frac{h_c B_c}{1-\nu^2}\nu\left(\frac{\partial^2}{\partial x^2}+\frac{\partial^2}{\partial y^2}\right)(P)-\frac{1+\nu}{2}\frac{h_c B_c}{1-\nu^2}\left(\frac{\partial^2}{\partial x^2}+\frac{\partial^2}{\partial y^2}\right)P$$ [Eq. 70]

Plugging Eq. 71 into Eq. 64,

$$\left(\frac{\partial^2}{\partial x^2}+\frac{\partial^2}{\partial y^2}\right)\left(\sigma_{xx}+\sigma_{yy}\right)=kN\left(\frac{\partial u_x}{\partial x}+\frac{\partial u_y}{\partial y}\right)+\frac{\nu}{1+\nu}\left(\frac{\partial^2}{\partial x^2}+\frac{\partial^2}{\partial y^2}\right)\left(\sigma_{xx}+\sigma_{yy}\right)-\frac{1-\nu}{2}\frac{h_c B_c}{1-\nu^2}\left(\frac{\partial^2}{\partial x^2}+\frac{\partial^2}{\partial y^2}\right)P$$ [Eq. 71]

The last step is to replace $kN\left(\frac{\partial u_x}{\partial x}+\frac{\partial u_y}{\partial y}\right)$. From Eq. 57,

$$kN\left(\frac{\partial u_x}{\partial x}+\frac{\partial u_y}{\partial y}\right)=kN\frac{1-\nu^2}{h_c B_c(1+\nu)}\left(\sigma_{xx}+\sigma_{yy}\right)+kNP$$ [Eq. 72]

Plugging Eq. 72 into Eq. 71,

$$\left(\frac{1}{1+\nu}\right)\left(\frac{\partial^2}{\partial x^2}+\frac{\partial^2}{\partial y^2}\right)\left(\sigma_{xx}+\sigma_{yy}\right)=kN\frac{1-\nu^2}{h_c B_c(1+\nu)}\left(\sigma_{xx}+\sigma_{yy}\right)+kNP-\frac{1-\nu}{2}\frac{h_c B_c}{1-\nu^2}\left(\frac{\partial^2}{\partial x^2}+\frac{\partial^2}{\partial y^2}\right)P$$ [Eq. 73]

$$\left(\frac{\partial^2}{\partial x^2}+\frac{\partial^2}{\partial y^2}\right)\left(\sigma_{xx}+\sigma_{yy}\right)=\frac{1}{{l_l}^2}\left(\sigma_{xx}+\sigma_{yy}\right)+kN(1+\nu)P-\frac{h_c B_c}{2}\left(\frac{\partial^2}{\partial x^2}+\frac{\partial^2}{\partial y^2}\right)P$$ [Eq. 74]

$$\left(\frac{\partial^2}{\partial x^2}+\frac{\partial^2}{\partial y^2}\right)\left(\sigma_{xx}+\sigma_{yy}+\frac{h_c B_c}{2}P\right)=\frac{1}{{l_l}^2}\left(\sigma_{xx}+\sigma_{yy}+\frac{h_c B_c}{2}P\right)+\frac{(1+\nu)^2}{2}kNP$$ [Eq. 75]

Recall that $P=\tilde{P}w$.

5. Domain-Wall Approximation

The simplifying assumption ($\frac{D\tau_w}{{l_l}^2}\ll 1$) allows us to easily determine the position of the fate boundary based on the value of the stress at the fate boundary. In this limit, $\left(tr(\sigma)+\frac{h_c B_c}{2}\tilde{P}w\right)$ varies smoothly from one side of the fate boundary to the other, while w varies sharply. By "smooth", we mean variation on length equal to l_l; by "sharp", we mean variation on length equal to $\sqrt{D\tau_w}$. Here we call $\sigma_{smooth}\equiv\left(tr(\sigma)+\frac{h_c B_c}{2}\tilde{P}w\right)$ the smooth stress.

$$f\left(w,tr(\sigma)\right)=w(w-w_{mid})(1-w)+\alpha(tr(\sigma)-\sigma^*)+\alpha\frac{h_c B_c}{2}\tilde{P}w-\alpha\frac{h_c B_c}{2}\tilde{P}w$$ [Eq. 76]

$$\bar{f}(w,\sigma_{smooth})=w(w-w_{mid})(1-w)-\alpha\frac{h_c B_c}{2}\tilde{P}w+\alpha(\sigma_{smooth}-\sigma^*)$$ [Eq. 77]

Near the fate boundary, σ_{smooth} is approximately constant. We call that constant value ${\sigma_{smooth}}^{FB}$. The position of the fate boundary is determined by the following constraint:

$$D\tau_w\int_{-\infty}^{\infty}\kappa(r,\theta)\left(\frac{dw(r)}{dr}\right)^2dr=\int_{w_{s1}}^{w_{s3}}-\bar{f}(w,{\sigma_{smooth}}^{FB})dw=-\int_{w_{s1}}^{w_{s3}}\left(w(w-w_{mid})(1-w)-\alpha\frac{h_c B_c}{2}\tilde{P}w+\alpha({\sigma_{smooth}}^{FB}-\sigma^*)\right)dw$$ [Eq. 78]

Here, r is the (signed) distance from the fate boundary. θ is the coordinate that traces the path of the fate boundary. $\kappa(r,\theta)$ is the curvature of the line that is a constant distance r from the fate boundary at coordinate θ. The infinite limits of integration signify that the boundaries of integration are far from the fate boundary (relative to $\sqrt{D\tau_w}$).

w_{s1} and w_{s3} are the values of the fate variable w far from the fate boundary on each side. w_{s2} is the value of the fate variable at the fate boundary.

$w_{s1} = w(r \to -\infty);\ w_{s2} = w(r = 0);\ w_{s3} = w(r \to \infty)$

$D\tau_w \int_{-\infty}^{\infty} \kappa(r) \left(\frac{dw(r)}{dr}\right)^2 dr$ is of order $\frac{\sqrt{D\tau_w}}{R}$ where R is the radius of curvature of the fate boundary.

Figure C.1 **Estimates of σ_{rr} from colonies on micropost substrates at day 4. A)** ξ_1 (see Appendix C Eqs. 12,13) versus radial coordinate. Gray lines: individual cell colonies. Black: mean ± SEM. **B)** $\frac{\xi_2}{-(1-\nu)l^2}$ (Appendix C Eqs. 12,14) versus radial coordinate. Gray lines: individual cell colonies. Red: mean ± SEM. **C)** ξ_2 (mean ± SEM). Here we assume $l^2 \approx 100\ \mu m^2$ and $\nu \approx 0.4$. Note: $\xi_2(r) \ll \xi_1(r)$. **D)** Approximation of $\langle \sigma_{rr}(r) \rangle$ (mean ± SEM) based on $\xi_1(r)$ alone.

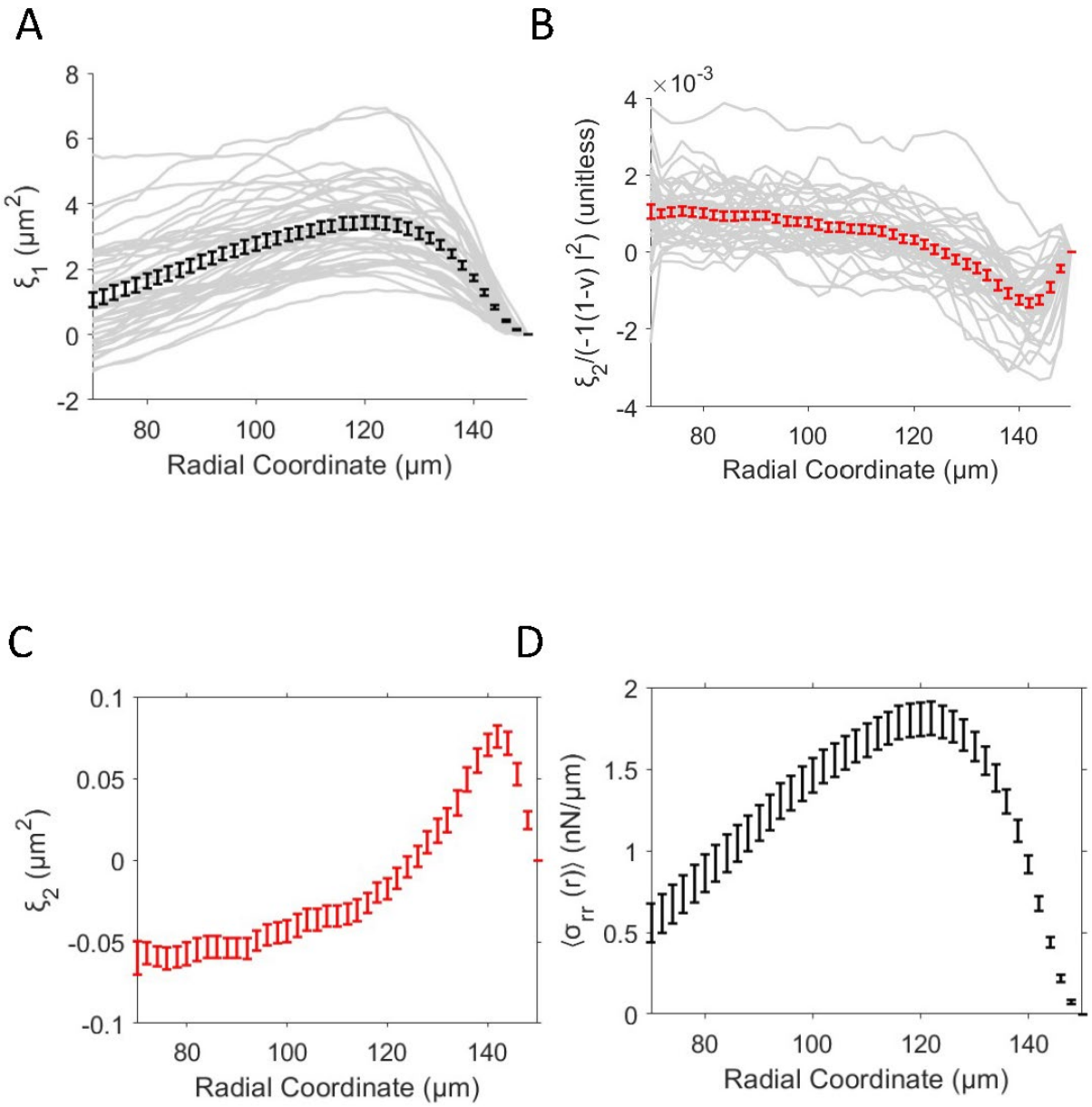

Figure C.2 **Examples of concentrically averaged radial post displacement profiles with three domains. A-D)** Examples of colonies for which Model 3 is more likely than Model 2. Yellow double-headed arrow: extent of intermediate domain **A)** Colony 23; **B)** Colony 17; **C)** Colony 37; **D)** Colony 8. (See Appendix C, Tables C.1-C.4).

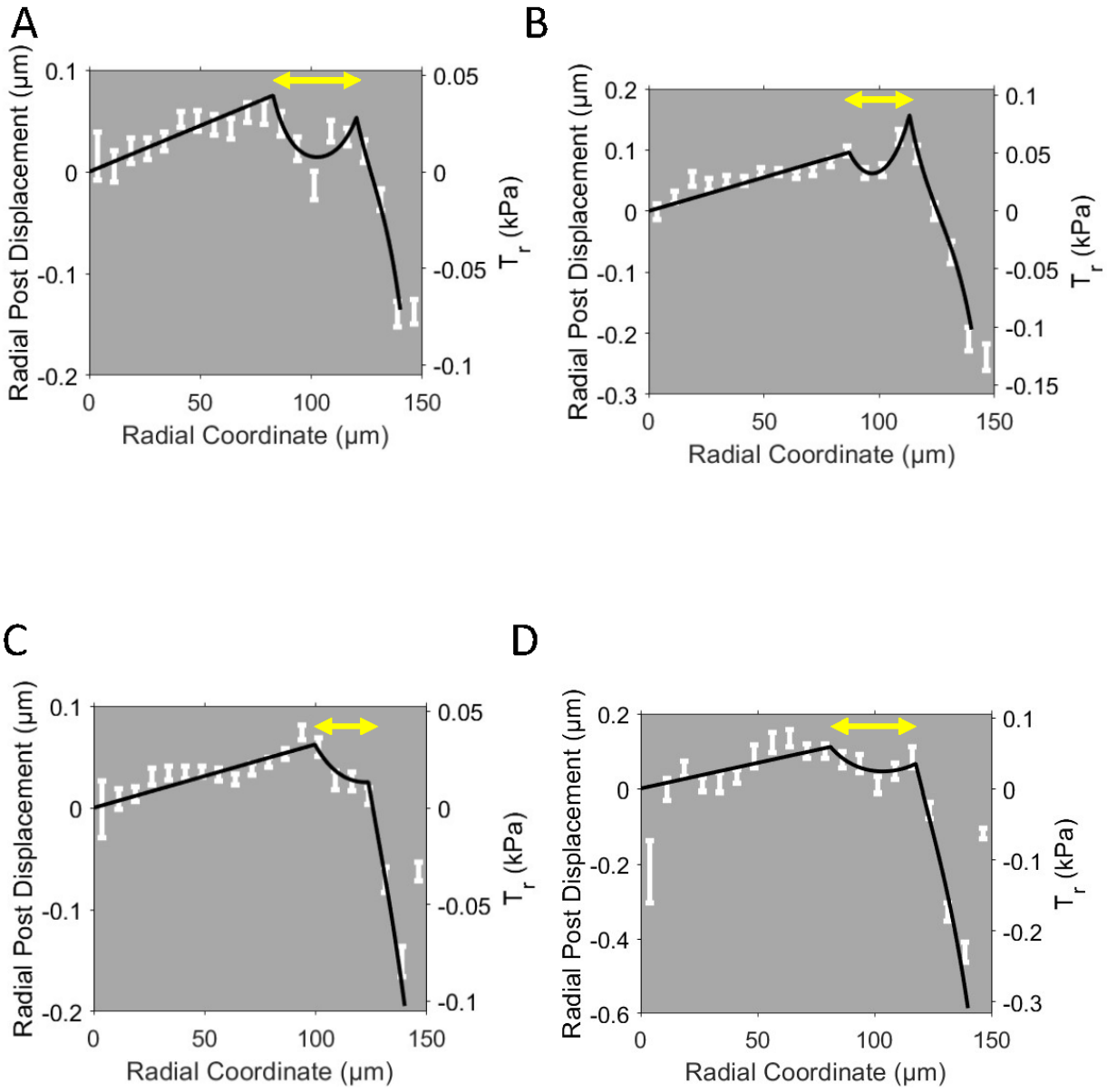

Figure C.3 **Examples of concentrically averaged radial post displacement profiles with two domains. A-D)** Examples of colonies for which Model 3 is less likely than Model 2. **A)** Colony 38; **B)** Colony 32; **C)** Colony 30; **D)** Colony 15. (See Appendix C, Tables C.1-C.4).

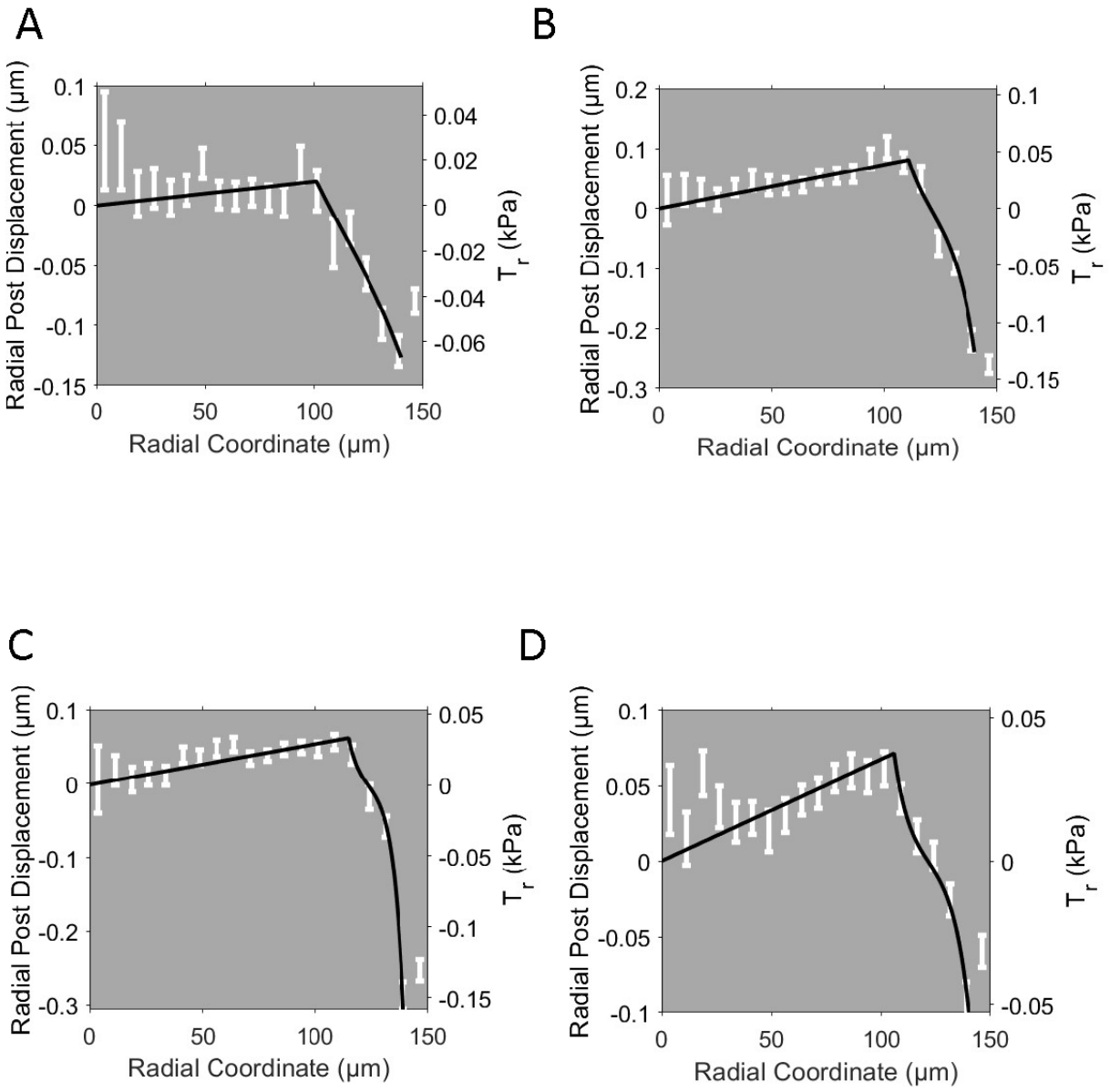

Table C.1 Best-fit parameters for Model 1 (see Appendix C.2) for each sample.

Number	$\tilde{\sigma}\left(\frac{nN}{\mu m}\right)$	$l'(\mu m)$	P'
1	0.40	24.9	-0.01
2	1.78	6.3	-0.23
3	0.84	4.4	-0.20
4	1.25	4.1	-0.37
5	1.42	2.4	-0.82
6	0.78	5.0	-0.14
7	0.68	5.9	-0.11
8	0.92	7.7	-0.16
9	0.81	9.2	-0.07
10	0.86	6.2	-0.12
11	0.83	4.9	-0.15
12	1.34	6.4	-0.17
13	0.84	6.1	-0.14
14	0.62	4.4	-0.15
15	0.36	4.7	-0.08
16	1.21	4.2	-0.27
17	1.36	3.7	-0.38
18	0.94	5.0	-0.16

19	1.29	4.7	-0.30
20	0.81	6.3	-0.13
21	0.58	5.2	-0.10
22	0.68	6.5	-0.06
23	0.81	3.5	-0.26
24	0.55	4.8	-0.13
25	1.12	4.8	-0.20
26	0.64	6.6	-0.07
27	1.41	5.0	-0.26
28	1.08	6.6	-0.13
29	0.76	9.2	-0.06
30	1.52	4.2	-0.37
31	0.94	9.7	-0.05
32	1.43	5.9	-0.17
33	0.90	9.1	-0.07
34	0.97	6.4	-0.12
35	0.86	9.2	-0.08
36	0.42	7.3	-0.05
37	0.41	4.9	-0.11
38	0.48	12.9	-0.02
39	0.82	5.2	-0.14
40	0.80	7.9	-0.06
41	0.41	7.8	-0.04

42	1.52	3.2	-0.52
Median	0.84	5.9	-0.14

Table C.2 Best-fit parameters for Model 2 (see Appendix C.2) for each sample.

Number	$\tilde{\sigma}\left(\frac{nN}{\mu m}\right)$	$l''(\mu m)$	$r'(\mu m)$	P'	P''
1	0.40	>100	87	0.0002	-0.01
2	1.78	8.2	105	0.0022	-0.15
3	0.84	5.3	101	0.0015	-0.13
4	1.25	5.5	118	0.0019	-0.22
5	1.42	>100	127	0.0016	-0.03
6	0.78	5.4	94	0.0014	-0.12
7	0.68	6.4	98	0.0022	-0.10
8	0.92	8.2	84	0.0028	-0.15
9	0.81	12.2	87	0.0023	-0.04
10	0.86	6.6	90.	0.0023	-0.10
11	0.83	6.7	113	0.0011	-0.09
12	1.34	7.1	92	0.0026	-0.14
13	0.84	9.3	109	0.0016	-0.07
14	0.62	5.6	106	0.0018	-0.10
15	0.36	7.2	106	0.0013	-0.04
16	1.21	6.1	102	0.0018	-0.14
17	1.36	4.4	117	0.0020	-0.28
18	0.94	5.0	99	0.0017	-0.17

19	1.29	4.9	101	0.0020	-0.28
20	0.81	9.9	102	0.0025	-0.06
21	0.58	7.8	104	0.0017	-0.05
22	0.68	>100	111	0.0009	-0.01
23	0.81	3.6	90.	0.0017	-0.24
24	0.55	5.6	109	0.0008	-0.10
25	1.12	4.9	97	0.0013	-0.19
26	0.64	9.5	107	0.0008	-0.04
27	1.41	8.2	117	0.0012	-0.12
28	1.08	>100	119	0.0010	-0.02
29	0.76	15.1	95	0.0012	-0.03
30	1.52	4.3	115	0.0011	-0.31
31	0.94	52.6	105	0.0011	-0.01
32	1.43	9.3	111	0.0015	-0.08
33	0.90	9.5	77	0.0014	-0.07
34	0.97	>100	121	0.0006	-0.02
35	0.86	13.1	103	0.0013	-0.05
36	0.42	10.8	96	0.0014	-0.03
37	0.41	5.7	104	0.0013	-0.09
38	0.48	28.6	101	0.0004	-0.01
39	0.82	6.0	112	0.0008	-0.11
40	0.80	>100	109	0.0013	-0.01
41	0.41	>100	103	0.0012	-0.01

42	1.52	>100	122	0.0014	-0.02
Median	0.84	8.2	104	0.0014	-0.08

Table C.3 Best-fit parameters for Model 3 (see Appendix C.2) for each sample.

Number	$\tilde{\sigma}\left(\frac{nN}{\mu m}\right)$	$l''(\mu m)$	$r'(\mu m)$	$r''(\mu m)$	P'	P''	P'''
1	0.40	86.1	98	108	0.0002	-0.02	0.00
2	1.78	>100	101	123	0.0022	0.00	-0.03
3	0.84	46.2	87	124	0.0016	0.00	-0.02
4	1.25	7.7	117	127	0.0019	-0.11	-0.14
5	1.42	20.0	92	129	0.0022	-0.01	-0.05
6	0.78	7.2	93	116	0.0014	-0.05	-0.07
7	0.68	9.8	91	115	0.0024	-0.04	-0.05
8	0.92	15.3	81	118	0.0027	-0.03	-0.07
9	0.81	10.4	56	80.	0.0022	-0.01	-0.05
10	0.86	6.2	90.	108	0.0023	-0.10	-0.12
11	0.83	7.4	77	110.	0.0018	-0.03	-0.07
12	1.34	10.9	89	114	0.0026	-0.05	-0.07
13	0.84	10.3	83	111	0.0023	-0.04	-0.06
14	0.62	12.6	99	121	0.0018	-0.02	-0.03
15	0.36	>100	89	116	0.0014	0.00	-0.01
16	1.21	4.6	101	114	0.0018	-0.18	-0.23
17	1.36	10.0	87	113	0.0022	-0.02	-0.07
18	0.94	8.0	98	129	0.0017	-0.06	-0.08

19	1.29	5.5	101	125	0.0020	-0.21	-0.22
20	0.81	12.0	81	104	0.0029	-0.02	-0.04
21	0.58	8.2	80.	102	0.0019	-0.01	-0.05
22	0.68	16.0	77	110.	0.0013	-0.01	-0.02
23	0.81	8.8	83	120.	0.0018	-0.03	-0.05
24	0.55	>100	81	126	0.0001	0.00	-0.02
25	1.12	6.8	94	121	0.0014	-0.09	-0.11
26	0.64	52.3	72	121	0.0010	0.00	-0.01
27	1.41	>100	55	117	0.0006	0.00	-0.02
28	1.08	32.9	64	119	0.0014	0.00	-0.02
29	0.76	27.6	91	115	0.0012	-0.01	-0.01
30	1.52	5.4	97	112	0.0011	-0.18	-0.22
31	0.94	19.8	67	109	0.0020	-0.01	-0.02
32	1.43	14.7	83	107	0.0014	-0.01	-0.04
33	0.90	16.8	75	121	0.0014	-0.02	-0.03
34	0.97	16.2	86	121	0.0009	-0.01	-0.04
35	0.86	17.0	87	111	0.0014	-0.02	-0.04
36	0.42	45.2	91	125	0.0015	0.00	-0.01
37	0.41	15.2	100.	124	0.0013	-0.01	-0.03
38	0.48	22.9	60.	101	0.0006	-0.01	-0.01
39	0.82	>100	99	131	0.0009	0.00	-0.03
40	0.80	40.8	99	109	0.0013	0.00	-0.01
41	0.41	36.2	93	105	0.0013	0.00	-0.01

42	1.52	42.1	64	120.	0.0002	0.00	-0.02
Median	0.84	15.6	88	116	0.0014	-0.01	-0.04

Table C.4 Comparing probability of each model via Bayesian Information Criterion for each sample. Color code: Maize $BF(M_3, M_2) \geq 20$; Blue $BF(M_2, M_3) \geq 20$.

Number	$\tilde{\sigma}$	$BIC(M_1)$	$BIC(M_2)$	$BIC(M_3)$	$BF(M_3, M_2)$
1	0.40	-235.	-256.	-271.	1150
2	1.78	1.	-237.	-244.	24.2
3	0.84	-13	-323.	-323.	1.16
4	1.25	379.	-314.	-309.	0.088
5	1.42	213.	-262.	-307.	6.0×10^9
6	0.78	-132.	-263.	-276.	744
7	0.68	139.	-297.	-289.	0.017
8	0.92	-7.	-138.	-164.	497000
9	0.81	-61.	-234.	-240.	23.4
10	0.86	-7.	-303.	-300.	0.16
11	0.83	-101.	-225.	-241.	4040
12	1.34	8.	-223.	-247.	173000
13	0.84	-71.	-257.	-278.	42000
14	0.62	617.	-350.	-355.	11.0
15	0.36	-68.	-307.	-300.	0.025
16	1.21	2.	-293.	-308.	2000
17	1.36	811.	-291.	-311.	32700
18	0.94	37.	-281.	-277.	0.12

19	1.29	-11.	-250.	-242.	0.022
20	0.81	188.	-264.	-272.	54.8
21	0.58	124.	-311.	-318.	31.3
22	0.68	-96.	-298.	-299.	1.97
23	0.81	-28.	-278.	-310.	6.5×10^6
24	0.55	-175.	-342.	-351.	73.8
25	1.12	-84.	-294.	-294.	0.92
26	0.64	-238.	-357	-365.	43.6
27	1.41	-35.	-314.	-324.	139.
28	1.08	-164.	-292.	-291.	0.49
29	0.76	-97.	-270.	-275.	12.8
30	1.52	-60.	-302.	-291.	0.004
31	0.94	-186.	-256.	-270.	1350
32	1.43	-113.	-282.	-274.	0.02
33	0.90	-144.	-206.	-203.	0.21
34	0.97	-220.	-266.	-263.	0.16
35	0.86	-155.	-221.	-220.	0.62
36	0.42	-44.	-341.	-338.	0.19
37	0.41	247.	-336.	-353.	5040
38	0.48	-261.	-272.	-265.	0.03
39	0.82	-150.	-309.	-305.	0.12
40	0.80	138.	-294.	-285.	0.010
41	0.41	-11.	-347.	-339.	0.019

42	1.52	691.	-377.	-372.	0.08

Table C.5 Young's modulus and substrate thickness for each value of curing-agent-to-base-monomer ratio.

Curing agent : base monomer	Thickness h_s (μm)	Young's Modulus E_s (kPa)
1 : 5	40	3,000
1 : 15	81	1,200
1 : 30	101	560
1 : 45	120	120
1 : 60	134	30

Table C.6 Parameter values for figures.

Fig. 3E-F	$\alpha * \tilde{P}_1 * k * N * {l_l}^2 * (1+\nu) = -0.05; \nu = 0.43; w_{mid} = \frac{1}{2}; {l_l}^2 = (20\ \mu m)^2;$ $\tilde{P}_1 = -0.01; \tilde{P}_2 = -0.05; \Delta r = (150-129)\ \mu m;\ \sigma^* = 1.865\frac{nN}{\mu m}; D\tau_w = 0.0125\ \mu m^2$
Fig. 4A	$h_c = 5.0\ \mu m; B_c = 300\ kPa;\ \nu_s = 0.4;\ Y_a = \frac{h_c B_c}{4\ \mu m^2};\ w_{mid} = \frac{1}{2};\ \Delta r = 25\ \mu m;$ $\tilde{P}_1 = -0.02; \tilde{P}_1 = -0.1;\ \sigma^* = 0.525 * h_c * B_c * (-1) * \tilde{P}_1; \alpha = \frac{0.8}{h_c B_c * -\tilde{P}_1};$ $D\tau_w = 0.0125\ \mu m^2; h_s = 81\ \mu m; E_s = 2100\ kPa$
Fig. 4C	$h_c = 5.0\ \mu m; B_c = 300\ kPa;\ \nu_s = 0.4;\ Y_a = \frac{h_c B_c}{4\ \mu m^2};\ w_{mid} = \frac{1}{2};\ \Delta r = 25\ \mu m;$ $\tilde{P}_1 = -0.02; \tilde{P}_1 = -0.1;\ \sigma^* = 0.525 * h_c * B_c * (-1) * \tilde{P}_1; \alpha = \frac{0.8}{h_c B_c * -\tilde{P}_1};$ $D\tau_w = 0.0125\ \mu m^2; see\ Table\ 5\ for\ h_s, E_s$

Bibliography

1. Perkins, L.A., et al., *The Transgenic RNAi Project at Harvard Medical School: Resources and Validation.* Genetics, 2015. **201**(3): p. 843-52.
2. Dietzl, G., et al., *A genome-wide transgenic RNAi library for conditional gene inactivation in Drosophila.* Nature, 2007. **448**(7150): p. 151-6.
3. Driever, W. and C. Nusslein-Volhard, *The bicoid protein determines position in the Drosophila embryo in a concentration-dependent manner.* Cell, 1988. **54**(1): p. 95-104.
4. Nusslein-Volhard, C., H.G. Frohnhofer, and R. Lehmann, *Determination of anteroposterior polarity in Drosophila.* Science, 1987. **238**(4834): p. 1675-81.
5. Waddington, C.H. and International Union of Biological Sciences., *Towards a theoretical biology. An IUBS symposium*. 1968, Chicago: Aldine Pub. Co. v.
6. Wolpert, L., *Positional information and the spatial pattern of cellular differentiation.* J Theor Biol, 1969. **25**(1): p. 1-47.
7. Green, J.B. and J. Sharpe, *Positional information and reaction-diffusion: two big ideas in developmental biology combine.* Development, 2015. **142**(7): p. 1203-11.
8. Heemskerk, I., et al., *Rapid changes in morphogen concentration control self-organized patterning in human embryonic stem cells.* Elife, 2019. **8**.
9. Gregor, T., et al., *Probing the limits to positional information.* Cell, 2007. **130**(1): p. 153-64.
10. Krotov, D., et al., *Morphogenesis at criticality.* Proc Natl Acad Sci U S A, 2014. **111**(10): p. 3683-8.
11. Chan, C.J., C.P. Heisenberg, and T. Hiiragi, *Coordination of Morphogenesis and Cell-Fate Specification in Development.* Curr Biol, 2017. **27**(18): p. R1024-R1035.
12. Gross, P., K.V. Kumar, and S.W. Grill, *How Active Mechanics and Regulatory Biochemistry Combine to Form Patterns in Development.* Annual Review of Biophysics, 2017. **46**(1): p. 337-356.
13. Hannezo, E. and C.P. Heisenberg, *Mechanochemical Feedback Loops in Development and Disease.* Cell, 2019. **178**(1): p. 12-25.
14. Engler, A.J., et al., *Matrix elasticity directs stem cell lineage specification.* Cell, 2006. **126**(4): p. 677-89.
15. Buxboim, A. and D.E. Discher, *Stem cells feel the difference.* Nat Methods, 2010. **7**(9): p. 695-7.
16. Fu, J., et al., *Mechanical regulation of cell function with geometrically modulated elastomeric substrates.* Nat Methods, 2010. **7**(9): p. 733-6.
17. Xue, X., et al., *Mechanics-guided embryonic patterning of neuroectoderm tissue from human pluripotent stem cells.* Nat Mater, 2018. **17**(7): p. 633-641.
18. Xia, P., et al., *Lateral Inhibition in Cell Specification Mediated by Mechanical Signals Modulating TAZ Activity.* Cell, 2019. **176**(6): p. 1379-1392 e14.
19. Desprat, N., et al., *Tissue deformation modulates twist expression to determine anterior midgut differentiation in Drosophila embryos.* Dev Cell, 2008. **15**(3): p. 470-7.

20. Brunet, T., et al., *Evolutionary conservation of early mesoderm specification by mechanotransduction in Bilateria.* Nat Commun, 2013. **4**: p. 2821.
21. Huckfeldt, R.M., et al., *Transient neurites of retinal horizontal cells exhibit columnar tiling via homotypic interactions.* Nat Neurosci, 2009. **12**(1): p. 35-43.
22. Grueber, W.B., et al., *Dendrites of distinct classes of Drosophila sensory neurons show different capacities for homotypic repulsion.* Curr Biol, 2003. **13**(8): p. 618-26.
23. Cohen, R., et al., *Shear forces drive precise patterning of hair cells in the mammalian inner ear.* bioRxiv, 2019: p. 707422.
24. Aliee, M., et al., *Physical mechanisms shaping the Drosophila dorsoventral compartment boundary.* Curr Biol, 2012. **22**(11): p. 967-76.
25. Cochet-Escartin, O., et al., *Physical Mechanisms Driving Cell Sorting in Hydra.* Biophys J, 2017. **113**(12): p. 2827-2841.
26. Cohen, D.J., *Sorting Things Out: Cell Sorting during Hydra Regeneration.* Biophys J, 2017. **113**(12): p. 2577-2578.
27. Cerchiari, A.E., et al., *A strategy for tissue self-organization that is robust to cellular heterogeneity and plasticity.* Proc Natl Acad Sci U S A, 2015. **112**(7): p. 2287-92.
28. Yevick, H.G., et al., *Structural Redundancy in Supracellular Actomyosin Networks Enables Robust Tissue Folding.* Dev Cell, 2019. **50**(5): p. 586-598 e3.
29. Hashimoto, H., et al., *Sequential contraction and exchange of apical junctions drives zippering and neural tube closure in a simple chordate.* Dev Cell, 2015. **32**(2): p. 241-55.
30. Turing, A.M., *The chemical basis of morphogenesis. 1953.* Bull Math Biol, 1990. **52**(1-2): p. 153-97; discussion 119-52.
31. Ghysen, A., et al., *Cell interactions and gene interactions in peripheral neurogenesis.* Genes Dev, 1993. **7**(5): p. 723-33.
32. Kim, S., et al., *Hexagonal Patterning of the Insect Compound Eye: Facet Area Variation, Defects, and Disorder.* Biophys J, 2016. **111**(12): p. 2735-2746.
33. Lubensky, D.K., et al., *A dynamical model of ommatidial crystal formation.* Proc Natl Acad Sci U S A, 2011. **108**(27): p. 11145-50.
34. McKenzie, E., A. Krupin, and M.W. Kelley, *Cellular growth and rearrangement during the development of the mammalian organ of Corti.* Dev Dyn, 2004. **229**(4): p. 802-12.
35. Owen, M.R. and J.A. Sherratt, *Mathematical modelling of juxtacrine cell signalling.* Math Biosci, 1998. **153**(2): p. 125-50.
36. Pennington, M.W. and D.K. Lubensky, *Switch and template pattern formation in a discrete reaction-diffusion system inspired by the Drosophila eye.* Eur Phys J E Soft Matter, 2010. **33**(2): p. 129-48.
37. Simpson, P., *Notch signalling in development: on equivalence groups and asymmetric developmental potential.* Curr Opin Genet Dev, 1997. **7**(4): p. 537-42.
38. Tomlinson, A. and D.F. Ready, *Neuronal differentiation in Drosophila ommatidium.* Dev Biol, 1987. **120**(2): p. 366-76.
39. EngstrÖM, K., *Cone Types and Cone Arrangements in Teleost Retinae1.* Acta Zoologica, 1963. **44**(1-2): p. 179-243.
40. Larison, K.D. and R. Bremiller, *Early onset of phenotype and cell patterning in the embryonic zebrafish retina.* Development, 1990. **109**(3): p. 567-76.
41. Raymond, P.A. and L.K. Barthel, *A moving wave patterns the cone photoreceptor mosaic array in the zebrafish retina.* Int J Dev Biol, 2004. **48**(8-9): p. 935-45.

42. Collin, S.P. and J. Shand, *Retinal Sampling and the Visual Field in Fishes*, in *Sensory Processing in Aquatic Environments*, S.P. Collin and N.J. Marshall, Editors. 2003, Springer New York: New York, NY. p. 139-169.
43. Viets, K., K. Eldred, and R.J. Johnston, Jr., *Mechanisms of Photoreceptor Patterning in Vertebrates and Invertebrates.* Trends Genet, 2016. **32**(10): p. 638-659.
44. Chinen, A., et al., *Gene duplication and spectral diversification of cone visual pigments of zebrafish.* Genetics, 2003. **163**(2): p. 663-75.
45. Nawrocki, L., et al., *Larval and adult visual pigments of the zebrafish, Brachydanio rerio.* Vision Res, 1985. **25**(11): p. 1569-76.
46. Ochocinska, M.J. and P.F. Hitchcock, *NeuroD regulates proliferation of photoreceptor progenitors in the retina of the zebrafish.* Mech Dev, 2009. **126**(3-4): p. 128-41.
47. Raymond, P.A., et al., *Molecular characterization of retinal stem cells and their niches in adult zebrafish.* BMC Dev Biol, 2006. **6**: p. 36.
48. Raymond, P.A. and S.S. Easter, Jr., *Postembryonic growth of the optic tectum in goldfish. I. Location of germinal cells and numbers of neurons produced.* J Neurosci, 1983. **3**(5): p. 1077-91.
49. Stenkamp, D.L. and D.A. Cameron, *Cellular pattern formation in the retina: retinal regeneration as a model system.* Mol Vis, 2002. **8**: p. 280-93.
50. Allison, W.T., et al., *Ontogeny of cone photoreceptor mosaics in zebrafish.* J Comp Neurol, 2010. **518**(20): p. 4182-95.
51. Salbreux, G., et al., *Coupling mechanical deformations and planar cell polarity to create regular patterns in the zebrafish retina.* PLoS Comput Biol, 2012. **8**(8): p. e1002618.
52. Nishiwaki, Y., et al., *Three-Dimensional Reconstitution of Cone Arrangement on the Spherical Surface of the Retina in the Medaka Eyes.* Zoological Science, 1997. **14**(5): p. 795-801.
53. Bowick, M., et al., *Crystalline order on a sphere and the generalized Thomson problem.* Phys Rev Lett, 2002. **89**(18): p. 185502.
54. Bowick, M.J., D.R. Nelson, and A. Travesset, *Interacting topological defects on frozen topographies.* Physical Review B, 2000. **62**(13): p. 8738-8751.
55. Flegg, G., *From geometry to topology*. 1st Dover ed. 2001, Mineola, N.Y.: Dover Publications. vi, 186 p.
56. Wales, D.J., H. McKay, and E.L. Altschuler, *Defect motifs for spherical topologies.* Physical Review B, 2009. **79**(22): p. 224115.
57. Corson, F., et al., *Self-organized Notch dynamics generate stereotyped sensory organ patterns in Drosophila.* Science, 2017. **356**(6337).
58. Duclos, G., et al., *Topological defects in confined populations of spindle-shaped cells.* Nature Physics, 2017. **13**(1): p. 58-62.
59. Kawaguchi, K., R. Kageyama, and M. Sano, *Topological defects control collective dynamics in neural progenitor cell cultures.* Nature, 2017. **545**(7654): p. 327-331.
60. Saw, T.B., et al., *Topological defects in epithelia govern cell death and extrusion.* Nature, 2017. **544**(7649): p. 212-216.
61. Nabarro, F.R.N., *Theory of crystal dislocations*. International series of monographs on physics. 1967, Oxford,: Clarendon P. xviii, 821 p.
62. Weertman, J. and J.R. Weertman, *Elementary dislocation theory*. Macmillan series in materials science. 1964, New York,: Macmillan. ix, 213 p.

63. Azadi, A. and G.M. Grason, *Emergent structure of multidislocation ground States in curved crystals.* Phys Rev Lett, 2014. **112**(22): p. 225502.
64. Azadi, A. and G.M. Grason, *Neutral versus charged defect patterns in curved crystals.* Phys Rev E, 2016. **94**(1-1): p. 013003.
65. Einert, T., et al., *Grain boundary scars on spherical crystals.* Langmuir, 2005. **21**(26): p. 12076-9.
66. Irvine, W.T., et al., *Dislocation reactions, grain boundaries, and irreversibility in two-dimensional lattices using topological tweezers.* Proc Natl Acad Sci U S A, 2013. **110**(39): p. 15544-8.
67. Irvine, W.T., V. Vitelli, and P.M. Chaikin, *Pleats in crystals on curved surfaces.* Nature, 2010. **468**(7326): p. 947-51.
68. Lipowsky, P., et al., *Direct visualization of dislocation dynamics in grain-boundary scars.* Nat Mater, 2005. **4**(5): p. 407-11.
69. Garcia, N.A., et al., *Defect formation and coarsening in hexagonal 2D curved crystals.* Soft Matter, 2015. **11**(5): p. 898-907.
70. Nagashima, M., et al., *Anisotropic Muller glial scaffolding supports a multiplex lattice mosaic of photoreceptors in zebrafish retina.* Neural Dev, 2017. **12**(1): p. 20.
71. Zou, J., X. Wang, and X. Wei, *Crb apical polarity proteins maintain zebrafish retinal cone mosaics via intercellular binding of their extracellular domains.* Dev Cell, 2012. **22**(6): p. 1261-74.
72. Suzuki, S.C., et al., *Cone photoreceptor types in zebrafish are generated by symmetric terminal divisions of dedicated precursors.* Proc Natl Acad Sci U S A, 2013. **110**(37): p. 15109-14.
73. Godinho, L., et al., *Targeting of amacrine cell neurites to appropriate synaptic laminae in the developing zebrafish retina.* Development, 2005. **132**(22): p. 5069-79.
74. Reese, B.E. and L. Galli-Resta, *The role of tangential dispersion in retinal mosaic formation.* Prog Retin Eye Res, 2002. **21**(2): p. 153-68.
75. Reese, B.E., et al., *Clonal expansion and cell dispersion in the developing mouse retina.* Eur J Neurosci, 1999. **11**(8): p. 2965-78.
76. Bausch, A.R., et al., *Grain boundary scars and spherical crystallography.* Science, 2003. **299**(5613): p. 1716-8.
77. Travesset, A., *Ground state of a large number of particles on a frozen topography.* Phys Rev E Stat Nonlin Soft Matter Phys, 2005. **72**(3 Pt 2): p. 036110.
78. Kohler, C., R. Backofen, and A. Voigt, *Stress Induced Branching of Growing Crystals on Curved Surfaces.* Phys Rev Lett, 2016. **116**(13): p. 135502.
79. Meng, G., et al., *Elastic instability of a crystal growing on a curved surface.* Science, 2014. **343**(6171): p. 634-7.
80. Stoop, N. and J. Dunkel, *Defect formation dynamics in curved elastic surface crystals.* Soft Matter, 2018. **14**(12): p. 2329-2338.
81. Chaikin, P.M. and T.C. Lubensky, *Principles of condensed matter physics*. 1995, Cambridge ; New York, NY, USA: Cambridge University Press. xx, 699 p.
82. Carpio, A., et al., *Dislocations in graphene.* New Journal of Physics, 2008. **10**(5): p. 053021.
83. Castro Neto, A.H., et al., *The electronic properties of graphene.* Reviews of Modern Physics, 2009. **81**(1): p. 109-162.

84. Dierker, S.B., R. Pindak, and R.B. Meyer, *Consequences of bond-orientational order on the macroscopic orientation patterns of thin tilted hexatic liquid-crystal films.* Phys Rev Lett, 1986. **56**(17): p. 1819-1822.
85. Nelson, D.R., *Defects and geometry in condensed matter physics*. 2002, Cambridge ; New York: Cambridge University Press. xiii, 377 p.
86. Raymond, P.A., et al., *Patterning the cone mosaic array in zebrafish retina requires specification of ultraviolet-sensitive cones.* PLoS One, 2014. **9**(1): p. e85325.
87. Elder, K.R. and M. Grant, *Modeling elastic and plastic deformations in nonequilibrium processing using phase field crystals.* Physical Review E, 2004. **70**(5): p. 051605.
88. Emmerich, H., et al., *Phase-field-crystal models for condensed matter dynamics on atomic length and diffusive time scales: an overview.* Advances in Physics, 2012. **61**(6): p. 665-743.
89. Elder, K.R., et al., *Modeling elasticity in crystal growth.* Phys Rev Lett, 2002. **88**(24): p. 245701.
90. Kundin, J. and M.A. Choudhary, *Application of the anisotropic phase-field crystal model to investigate the lattice systems of different anisotropic parameters and orientations.* Modelling and Simulation in Materials Science and Engineering, 2017. **25**(5): p. 055004.
91. Kundin, J., M.A. Choudhary, and H. Emmerich, *Bridging the phase-field and phase-field crystal approaches for anisotropic material systems.* The European Physical Journal Special Topics, 2014. **223**(3): p. 363-372.
92. Mkhonta, S.K., K.R. Elder, and Z.F. Huang, *Exploring the complex world of two-dimensional ordering with three modes.* Phys Rev Lett, 2013. **111**(3): p. 035501.
93. Prieler, R., et al., *An anisotropic phase-field crystal model for heterogeneous nucleation of ellipsoidal colloids.* Journal of Physics: Condensed Matter, 2009. **21**(46): p. 464110.
94. van Teeffelen, S., et al., *Derivation of the phase-field-crystal model for colloidal solidification.* Phys Rev E Stat Nonlin Soft Matter Phys, 2009. **79**(5 Pt 1): p. 051404.
95. Elder, K.R., et al., *Phase-field crystal modeling and classical density functional theory of freezing.* Physical Review B, 2007. **75**(6): p. 064107.
96. Collier, J.R., et al., *Pattern formation by lateral inhibition with feedback: a mathematical model of delta-notch intercellular signalling.* J Theor Biol, 1996. **183**(4): p. 429-46.
97. Formosa-Jordan, P., et al., *Regulation of neuronal differentiation at the neurogenic wavefront.* Development, 2012. **139**(13): p. 2321-9.
98. Sprinzak, D., et al., *Mutual inactivation of Notch receptors and ligands facilitates developmental patterning.* PLoS Comput Biol, 2011. **7**(6): p. e1002069.
99. Djamgoz, M.B.A., S.N. Archer, and S. Vallerga, *Neurobiology and clinical aspects of the outer retina*. 1st ed. 1995, London ; New York: Chapman & Hall. xi, 501 p.
100. Noel, N.C.L. and W.T. Allison, *Connectivity of cone photoreceptor telodendria in the zebrafish retina.* J Comp Neurol, 2018. **526**(4): p. 609-625.
101. Westerfield, M., *The zebrafish book : a guide for the laboratory use of zebrafish (Brachydanio rerio)*. 1993, Eugene, OR: M. Westerfield.
102. Takechi, M., T. Hamaoka, and S. Kawamura, *Fluorescence visualization of ultraviolet-sensitive cone photoreceptor development in living zebrafish.* FEBS Lett, 2003. **553**(1-2): p. 90-4.
103. Takechi, M., S. Seno, and S. Kawamura, *Identification of cis-acting elements repressing blue opsin expression in zebrafish UV cones and pineal cells.* J Biol Chem, 2008. **283**(46): p. 31625-32.

104. Barthel, L.K. and P.A. Raymond, *Improved method for obtaining 3-microns cryosections for immunocytochemistry.* J Histochem Cytochem, 1990. **38**(9): p. 1383-8.
105. Bernardos, R.L., et al., *Notch-Delta signaling is required for spatial patterning and Muller glia differentiation in the zebrafish retina.* Dev Biol, 2005. **278**(2): p. 381-95.
106. Vihtelic, T.S., C.J. Doro, and D.R. Hyde, *Cloning and characterization of six zebrafish photoreceptor opsin cDNAs and immunolocalization of their corresponding proteins.* Vis Neurosci, 1999. **16**(3): p. 571-85.
107. Kwan, K.M., et al., *The Tol2kit: a multisite gateway-based construction kit for Tol2 transposon transgenesis constructs.* Dev Dyn, 2007. **236**(11): p. 3088-99.
108. Kawakami, K., et al., *A transposon-mediated gene trap approach identifies developmentally regulated genes in zebrafish.* Dev Cell, 2004. **7**(1): p. 133-44.
109. Jao, L.E., S.R. Wente, and W. Chen, *Efficient multiplex biallelic zebrafish genome editing using a CRISPR nuclease system.* Proc Natl Acad Sci U S A, 2013. **110**(34): p. 13904-9.
110. McKinney, S.A., et al., *A bright and photostable photoconvertible fluorescent protein.* Nat Methods, 2009. **6**(2): p. 131-3.
111. Spencer, M.A., Z. Jabeen, and D.K. Lubensky, *Vertex stability and topological transitions in vertex models of foams and epithelia.* Eur Phys J E Soft Matter, 2017. **40**(1): p. 2.
112. Spencer, M.A., et al. *Multicellular actomyosin cables in epithelia under external anisotropic stress*. arXiv e-prints, 2018. arXiv:1809.04569.
113. Backofen, R., A. Rätz, and A. Voigt, *Nucleation and growth by a phase field crystal (PFC) model.* Philosophical Magazine Letters, 2007. **87**(11): p. 813-820.
114. Ascher, U.M., S.J. Ruuth, and B.T.R. Wetton, *Implicit-Explicit Methods for Time-Dependent Partial Differential Equations.* SIAM Journal on Numerical Analysis, 1995. **32**(3): p. 797-823.
115. LeVeque, R.J., *Finite difference methods for ordinary and partial differential equations : steady-state and time-dependent problems*. 2007, Philadelphia, PA: Society for Industrial and Applied Mathematics. xv, 341 p.
116. Davis, J.R. and N. Tapon, *Hippo signalling during development.* Development, 2019. **146**(18).
117. Bosveld, F., et al., *Mechanical control of morphogenesis by Fat/Dachsous/Four-jointed planar cell polarity pathway.* Science, 2012. **336**(6082): p. 724-7.
118. Bosveld, F., et al., *Epithelial tricellular junctions act as interphase cell shape sensors to orient mitosis.* Nature, 2016. **530**(7591): p. 495-8.
119. Curran, S., et al., *Myosin II Controls Junction Fluctuations to Guide Epithelial Tissue Ordering.* Dev Cell, 2017. **43**(4): p. 480-492 e6.
120. Founounou, N., N. Loyer, and R. Le Borgne, *Septins regulate the contractility of the actomyosin ring to enable adherens junction remodeling during cytokinesis of epithelial cells.* Dev Cell, 2013. **24**(3): p. 242-55.
121. Levayer, R., C. Dupont, and E. Moreno, *Tissue Crowding Induces Caspase-Dependent Competition for Space.* Curr Biol, 2016. **26**(5): p. 670-7.
122. Pinheiro, D., et al., *Transmission of cytokinesis forces via E-cadherin dilution and actomyosin flows.* Nature, 2017. **545**(7652): p. 103-107.
123. Guirao, B., et al., *Unified quantitative characterization of epithelial tissue development.* Elife, 2015. **4**.

124. Han, M.K.L. and J. de Rooij, *Converging and Unique Mechanisms of Mechanotransduction at Adhesion Sites.* Trends Cell Biol, 2016. **26**(8): p. 612-623.
125. Huveneers, S., et al., *Vinculin associates with endothelial VE-cadherin junctions to control force-dependent remodeling.* J Cell Biol, 2012. **196**(5): p. 641-52.
126. Millan, J., et al., *Adherens junctions connect stress fibres between adjacent endothelial cells.* BMC Biol, 2010. **8**: p. 11.
127. Vasioukhin, V., et al., *Directed actin polymerization is the driving force for epithelial cell-cell adhesion.* Cell, 2000. **100**(2): p. 209-19.
128. Dawes-Hoang, R.E., et al., *folded gastrulation, cell shape change and the control of myosin localization.* Development, 2005. **132**(18): p. 4165-78.
129. Alt, S., P. Ganguly, and G. Salbreux, *Vertex models: from cell mechanics to tissue morphogenesis.* Philos Trans R Soc Lond B Biol Sci, 2017. **372**(1720).
130. Heer, N.C. and A.C. Martin, *Tension, contraction and tissue morphogenesis.* Development, 2017. **144**(23): p. 4249-4260.
131. Lecuit, T. and A.S. Yap, *E-cadherin junctions as active mechanical integrators in tissue dynamics.* Nat Cell Biol, 2015. **17**(5): p. 533-9.
132. Elosegui-Artola, A., et al., *Force Triggers YAP Nuclear Entry by Regulating Transport across Nuclear Pores.* Cell, 2017. **171**(6): p. 1397-1410 e14.
133. Abe, Y., et al., *LATS2-Ajuba complex regulates gamma-tubulin recruitment to centrosomes and spindle organization during mitosis.* FEBS Lett, 2006. **580**(3): p. 782-8.
134. Das Thakur, M., et al., *Ajuba LIM proteins are negative regulators of the Hippo signaling pathway.* Curr Biol, 2010. **20**(7): p. 657-62.
135. Alegot, H., et al., *Recruitment of Jub by alpha-catenin promotes Yki activity and Drosophila wing growth.* J Cell Sci, 2019. **132**(5).
136. Ibar, C., et al., *Tension-dependent regulation of mammalian Hippo signaling through LIMD1.* J Cell Sci, 2018. **131**(5).
137. Rauskolb, C., et al., *Cytoskeletal tension inhibits Hippo signaling through an Ajuba-Warts complex.* Cell, 2014. **158**(1): p. 143-156.
138. Sarpal, R., et al., *Role of alpha-Catenin and its mechanosensing properties in regulating Hippo/YAP-dependent tissue growth.* PLoS Genet, 2019. **15**(11): p. e1008454.
139. Taslimi, A., et al., *An optimized optogenetic clustering tool for probing protein interaction and function.* Nat Commun, 2014. **5**: p. 4925.
140. Matakatsu, H. and S.S. Blair, *Separating planar cell polarity and Hippo pathway activities of the protocadherins Fat and Dachsous.* Development, 2012. **139**(8): p. 1498-508.
141. Blanchoin, L., et al., *Actin dynamics, architecture, and mechanics in cell motility.* Physiol Rev, 2014. **94**(1): p. 235-63.
142. Kassianidou, E., et al., *Extracellular Matrix Geometry and Initial Adhesive Position Determine Stress Fiber Network Organization during Cell Spreading.* Cell Rep, 2019. **27**(6): p. 1897-1909 e4.
143. Higashi, T. and A.L. Miller, *Tricellular junctions: how to build junctions at the TRICkiest points of epithelial cells.* Mol Biol Cell, 2017. **28**(15): p. 2023-2034.
144. Gibson, M.C., et al., *The emergence of geometric order in proliferating metazoan epithelia.* Nature, 2006. **442**(7106): p. 1038-41.
145. Gibson, W.T., et al., *Control of the mitotic cleavage plane by local epithelial topology.* Cell, 2011. **144**(3): p. 427-38.

146. McMahon, T.A. and J.T. Bonner, *On size and life*. 1983, New York: Scientific American Library : Distributed by W.H. Freeman. xiii, 255 p., 1 leaf of plates.
147. Spence, A.J., *Scaling in biology.* Curr Biol, 2009. **19**(2): p. R57-61.
148. Capek, D. and P. Muller, *Positional information and tissue scaling during development and regeneration.* Development, 2019. **146**(24).
149. Shilo, B.Z. and N. Barkai, *Buffering Global Variability of Morphogen Gradients.* Dev Cell, 2017. **40**(5): p. 429-438.
150. Irvine, K.D. and B.I. Shraiman, *Mechanical control of growth: ideas, facts and challenges.* Development, 2017. **144**(23): p. 4238-4248.
151. Totaro, A., T. Panciera, and S. Piccolo, *YAP/TAZ upstream signals and downstream responses.* Nat Cell Biol, 2018. **20**(8): p. 888-899.
152. Pratt, S.J., et al., *The LIM protein Ajuba influences p130Cas localization and Rac1 activity during cell migration.* J Cell Biol, 2005. **168**(5): p. 813-24.
153. Aragona, M., et al., *A mechanical checkpoint controls multicellular growth through YAP/TAZ regulation by actin-processing factors.* Cell, 2013. **154**(5): p. 1047-1059.
154. Meng, Z., et al., *RAP2 mediates mechanoresponses of the Hippo pathway.* Nature, 2018. **560**(7720): p. 655-660.
155. Wada, K., et al., *Hippo pathway regulation by cell morphology and stress fibers.* Development, 2011. **138**(18): p. 3907-14.
156. Uroz, M., et al., *Regulation of cell cycle progression by cell-cell and cell-matrix forces.* Nat Cell Biol, 2018. **20**(6): p. 646-654.
157. Brand, A.H. and N. Perrimon, *Targeted gene expression as a means of altering cell fates and generating dominant phenotypes.* Development, 1993. **118**(2): p. 401-15.
158. Lee, T. and L. Luo, *Mosaic analysis with a repressible cell marker for studies of gene function in neuronal morphogenesis.* Neuron, 1999. **22**(3): p. 451-61.
159. Xu, T. and G.M. Rubin, *Analysis of genetic mosaics in developing and adult Drosophila tissues.* Development, 1993. **117**(4): p. 1223-37.
160. Gratz, S.J., et al., *Highly specific and efficient CRISPR/Cas9-catalyzed homology-directed repair in Drosophila.* Genetics, 2014. **196**(4): p. 961-71.
161. Port, F., et al., *Optimized CRISPR/Cas tools for efficient germline and somatic genome engineering in Drosophila.* Proc Natl Acad Sci U S A, 2014. **111**(29): p. E2967-76.
162. Huang, J., et al., *Efficient ends-out gene targeting in Drosophila.* Genetics, 2008. **180**(1): p. 703-7.
163. Sabino, D., N.H. Brown, and R. Basto, *Drosophila Ajuba is not an Aurora-A activator but is required to maintain Aurora-A at the centrosome.* J Cell Sci, 2011. **124**(Pt 7): p. 1156-66.
164. Bardet, P.L., et al., *PTEN controls junction lengthening and stability during cell rearrangement in epithelial tissue.* Dev Cell, 2013. **25**(5): p. 534-46.
165. Herbert, A.D., A.M. Carr, and E. Hoffmann, *FindFoci: a focus detection algorithm with automated parameter training that closely matches human assignments, reduces human inconsistencies and increases speed of analysis.* PLoS One, 2014. **9**(12): p. e114749.
166. Blanchard, G.B., et al., *Tissue tectonics: morphogenetic strain rates, cell shape change and intercalation.* Nat Methods, 2009. **6**(6): p. 458-64.
167. Lin, X., et al., *Z-disc-associated, alternatively spliced, PDZ motif-containing protein (ZASP) mutations in the actin-binding domain cause disruption of skeletal muscle actin filaments in myofibrillar myopathy.* J Biol Chem, 2014. **289**(19): p. 13615-26.

168. Tamura, N., et al., *The PDZ-LIM protein CLP36 is required for actin stress fiber formation and focal adhesion assembly in BeWo cells.* Biochem Biophys Res Commun, 2007. **364**(3): p. 589-94.
169. Smith, M.A., et al., *LIM domains target actin regulators paxillin and zyxin to sites of stress fiber strain.* PLoS One, 2013. **8**(8): p. e69378.
170. Carley, W.W., A. Bretscher, and W.W. Webb, *F-actin aggregates in transformed cells contain alpha-actinin and fimbrin but apparently lack tropomyosin.* Eur J Cell Biol, 1986. **39**(2): p. 313-20.
171. Maninova, M. and T. Vomastek, *Dorsal stress fibers, transverse actin arcs, and perinuclear actin fibers form an interconnected network that induces nuclear movement in polarizing fibroblasts.* FEBS J, 2016. **283**(20): p. 3676-3693.
172. Yamashiro-Matsumura, S. and F. Matsumura, *Intracellular localization of the 55-kD actin-bundling protein in cultured cells: spatial relationships with actin, alpha-actinin, tropomyosin, and fimbrin.* J Cell Biol, 1986. **103**(2): p. 631-40.
173. Machnicka, B., et al., *The role of spectrin in cell adhesion and cell-cell contact.* Exp Biol Med (Maywood), 2019. **244**(15): p. 1303-1312.
174. Ehrlicher, A.J., et al., *Mechanical strain in actin networks regulates FilGAP and integrin binding to filamin A.* Nature, 2011. **478**(7368): p. 260-3.
175. Chen, H.M., et al., *Overexpression of integrin-beta1 in leiomyoma promotes cell spreading and proliferation.* J Clin Endocrinol Metab, 2013. **98**(5): p. E837-46.
176. Albiges-Rizo, C., P. Frachet, and M.R. Block, *Down regulation of talin alters cell adhesion and the processing of the alpha 5 beta 1 integrin.* J Cell Sci, 1995. **108 (Pt 10)**: p. 3317-29.
177. Furman, C., et al., *Ena/VASP is required for endothelial barrier function in vivo.* J Cell Biol, 2007. **179**(4): p. 761-75.
178. Gateva, G., et al., *Palladin promotes assembly of non-contractile dorsal stress fibers through VASP recruitment.* J Cell Sci, 2014. **127**(Pt 9): p. 1887-98.
179. Rosowski, K.A., et al., *Vinculin and the mechanical response of adherent fibroblasts to matrix deformation.* Sci Rep, 2018. **8**(1): p. 17967.
180. Suzuki, C., et al., *ANLN plays a critical role in human lung carcinogenesis through the activation of RHOA and by involvement in the phosphoinositide 3-kinase/AKT pathway.* Cancer Res, 2005. **65**(24): p. 11314-25.
181. Hotulainen, P. and P. Lappalainen, *Stress fibers are generated by two distinct actin assembly mechanisms in motile cells.* J Cell Biol, 2006. **173**(3): p. 383-94.
182. Sharma, P., et al., *Role of dystrophin in airway smooth muscle phenotype, contraction and lung function.* PLoS One, 2014. **9**(7): p. e102737.
183. Elkhatib, N., et al., *Fascin plays a role in stress fiber organization and focal adhesion disassembly.* Curr Biol, 2014. **24**(13): p. 1492-9.
184. Kamioka, H., et al., *Terminal differentiation of osteoblasts to osteocytes is accompanied by dramatic changes in the distribution of actin-binding proteins.* J Bone Miner Res, 2004. **19**(3): p. 471-8.
185. Sandbo, N., et al., *Control of myofibroblast differentiation by microtubule dynamics through a regulated localization of mDia2.* J Biol Chem, 2013. **288**(22): p. 15466-73.
186. Honda, H., et al., *Cardiovascular anomaly, impaired actin bundling and resistance to Src-induced transformation in mice lacking p130Cas.* Nat Genet, 1998. **19**(4): p. 361-5.

187. Dolat, L., et al., *Septins promote stress fiber-mediated maturation of focal adhesions and renal epithelial motility.* J Cell Biol, 2014. **207**(2): p. 225-35.
188. Sudo, K., et al., *SEPT9 sequence alternations causing hereditary neuralgic amyotrophy are associated with altered interactions with SEPT4/SEPT11 and resistance to Rho/Rhotekin-signaling.* Hum Mutat, 2007. **28**(10): p. 1005-13.
189. Cho, A., et al., *An Atypical Tropomyosin in Drosophila with Intermediate Filament-like Properties.* Cell Rep, 2016. **16**(4): p. 928-938.
190. Tojkander, S., et al., *A molecular pathway for myosin II recruitment to stress fibers.* Curr Biol, 2011. **21**(7): p. 539-50.
191. Morrison, C.M. and G. Halder, *Characterization of a dorsal-eye Gal4 Line in Drosophila.* Genesis, 2010. **48**(1): p. 3-7.
192. Mummery-Widmer, J.L., et al., *Genome-wide analysis of Notch signalling in Drosophila by transgenic RNAi.* Nature, 2009. **458**(7241): p. 987-92.
193. Herszterg, S., et al., *Interplay between the dividing cell and its neighbors regulates adherens junction formation during cytokinesis in epithelial tissue.* Dev Cell, 2013. **24**(3): p. 256-70.
194. Kanca, O., et al., *Raeppli: a whole-tissue labeling tool for live imaging of Drosophila development.* Development, 2014. **141**(2): p. 472-80.
195. Grosshans, J. and E. Wieschaus, *A genetic link between morphogenesis and cell division during formation of the ventral furrow in Drosophila.* Cell, 2000. **101**(5): p. 523-31.
196. Zanet, J., et al., *Fascin is required for blood cell migration during Drosophila embryogenesis.* Development, 2009. **136**(15): p. 2557-65.
197. Klapholz, B., et al., *Alternative mechanisms for talin to mediate integrin function.* Curr Biol, 2015. **25**(7): p. 847-57.
198. Morin, X., et al., *A protein trap strategy to detect GFP-tagged proteins expressed from their endogenous loci in Drosophila.* Proc Natl Acad Sci U S A, 2001. **98**(26): p. 15050-5.
199. Vrabioiu, A.M. and G. Struhl, *Fat/Dachsous Signaling Promotes Drosophila Wing Growth by Regulating the Conformational State of the NDR Kinase Warts.* Dev Cell, 2015. **35**(6): p. 737-49.
200. Zhang, L., et al., *The TEAD/TEF family of transcription factor Scalloped mediates Hippo signaling in organ size control.* Dev Cell, 2008. **14**(3): p. 377-87.
201. Britton, G., et al., *A novel self-organizing embryonic stem cell system reveals signaling logic underlying the patterning of human ectoderm.* Development, 2019. **146**(20).
202. Martyn, I., et al., *Self-organization of a human organizer by combined Wnt and Nodal signalling.* Nature, 2018. **558**(7708): p. 132-135.
203. Spemann, H. and H. Mangold, *Induction of embryonic primordia by implantation of organizers from a different species. 1923.* Int J Dev Biol, 2001. **45**(1): p. 13-38.
204. Wilson, P.A., et al., *Concentration-dependent patterning of the Xenopus ectoderm by BMP4 and its signal transducer Smad1.* Development, 1997. **124**(16): p. 3177-84.
205. Bois, J.S., F. Julicher, and S.W. Grill, *Pattern formation in active fluids.* Phys Rev Lett, 2011. **106**(2): p. 028103.
206. Recho, P., A. Hallou, and E. Hannezo, *Theory of mechanochemical patterning in biphasic biological tissues.* Proc Natl Acad Sci U S A, 2019. **116**(12): p. 5344-5349.
207. Murray, J.D. and G.F. Oster, *Cell traction models for generating pattern and form in morphogenesis.* J Math Biol, 1984. **19**(3): p. 265-79.

208. Murray, J.D. and G.F. Oster, *Generation of biological pattern and form.* IMA J Math Appl Med Biol, 1984. **1**(1): p. 51-75.
209. Odell, G.M., et al., *The mechanical basis of morphogenesis. I. Epithelial folding and invagination.* Dev Biol, 1981. **85**(2): p. 446-62.
210. Maruthamuthu, V., et al., *Cell-ECM traction force modulates endogenous tension at cell-cell contacts.* Proc Natl Acad Sci U S A, 2011. **108**(12): p. 4708-13.
211. Mertz, A.F., et al., *Cadherin-based intercellular adhesions organize epithelial cell-matrix traction forces.* Proc Natl Acad Sci U S A, 2013. **110**(3): p. 842-7.
212. Banerjee, S. and M.C. Marchetti, *Substrate rigidity deforms and polarizes active gels.* EPL (Europhysics Letters), 2011. **96**(2): p. 28003.
213. Banerjee, S. and M.C. Marchetti, *Contractile stresses in cohesive cell layers on finite-thickness substrates.* Phys Rev Lett, 2012. **109**(10): p. 108101.
214. Edwards, C.M. and U.S. Schwarz, *Force localization in contracting cell layers.* Phys Rev Lett, 2011. **107**(12): p. 128101.
215. Oakes, P.W., et al., *Geometry regulates traction stresses in adherent cells.* Biophys J, 2014. **107**(4): p. 825-33.
216. Schaumann, E.N., et al., *Force localization modes in dynamic epithelial colonies.* Mol Biol Cell, 2018. **29**(23): p. 2835-2847.
217. Corson, F. and E.D. Siggia, *Geometry, epistasis, and developmental patterning.* Proc Natl Acad Sci U S A, 2012. **109**(15): p. 5568-75.
218. Cross, M. and H. Greenside, *Pattern formation and dynamics in nonequilibrium systems*. 2009, Cambridge, UK ; New York: Cambridge University Press. xvi, 535 p.
219. Narva, E., et al., *A Strong Contractile Actin Fence and Large Adhesions Direct Human Pluripotent Colony Morphology and Adhesion.* Stem Cell Reports, 2017. **9**(1): p. 67-76.
220. Rosowski, K.A., et al., *Edges of human embryonic stem cell colonies display distinct mechanical properties and differentiation potential.* Sci Rep, 2015. **5**: p. 14218.
221. Chhabra, S., et al., *Dissecting the dynamics of signaling events in the BMP, WNT, and NODAL cascade during self-organized fate patterning in human gastruloids.* PLoS Biol, 2019. **17**(10): p. e3000498.
222. Etoc, F., et al., *A Balance between Secreted Inhibitors and Edge Sensing Controls Gastruloid Self-Organization.* Dev Cell, 2016. **39**(3): p. 302-315.
223. Haremaki, T., et al., *Self-organizing neuruloids model developmental aspects of Huntington's disease in the ectodermal compartment.* Nat Biotechnol, 2019. **37**(10): p. 1198-1208.
224. Martyn, I., A.H. Brivanlou, and E.D. Siggia, *A wave of WNT signaling balanced by secreted inhibitors controls primitive streak formation in micropattern colonies of human embryonic stem cells.* Development, 2019. **146**(6).
225. Tewary, M., et al., *A stepwise model of reaction-diffusion and positional information governs self-organized human peri-gastrulation-like patterning.* Development, 2017. **144**(23): p. 4298-4312.
226. Chambers, S.M., et al., *Highly efficient neural conversion of human ES and iPS cells by dual inhibition of SMAD signaling.* Nat Biotechnol, 2009. **27**(3): p. 275-80.
227. Mica, Y., et al., *Modeling neural crest induction, melanocyte specification, and disease-related pigmentation defects in hESCs and patient-specific iPSCs.* Cell Rep, 2013. **3**(4): p. 1140-52.

228. Tchieu, J., et al., *A Modular Platform for Differentiation of Human PSCs into All Major Ectodermal Lineages.* Cell Stem Cell, 2017. **21**(3): p. 399-410 e7.
229. Saez, A., et al., *Is the mechanical activity of epithelial cells controlled by deformations or forces?* Biophys J, 2005. **89**(6): p. L52-4.
230. Sun, Y., et al., *Hippo/YAP-mediated rigidity-dependent motor neuron differentiation of human pluripotent stem cells.* Nat Mater, 2014. **13**(6): p. 599-604.
231. Das, T., et al., *A molecular mechanotransduction pathway regulates collective migration of epithelial cells.* Nat Cell Biol, 2015. **17**(3): p. 276-87.
232. Mertz, A.F., et al., *Scaling of traction forces with the size of cohesive cell colonies.* Phys Rev Lett, 2012. **108**(19): p. 198101.
233. Trepat, X., et al., *Physical forces during collective cell migration.* Nature Physics, 2009. **5**(6): p. 426-430.
234. Amack, J.D. and M.L. Manning, *Knowing the boundaries: extending the differential adhesion hypothesis in embryonic cell sorting.* Science, 2012. **338**(6104): p. 212-5.
235. Manning, M.L., et al., *Coaction of intercellular adhesion and cortical tension specifies tissue surface tension.* Proc Natl Acad Sci U S A, 2010. **107**(28): p. 12517-22.
236. Muratov, C.B. and V.V. Osipov, *General theory of instabilities for patterns with sharp interfaces in reaction-diffusion systems.* Physical Review E, 1996. **53**(4): p. 3101-3116.
237. Muratov, C.B. and S.Y. Shvartsman, *An asymptotic study of the inductive pattern formation mechanism in Drosophila egg development.* Physica D: Nonlinear Phenomena, 2003. **186**(1): p. 93-108.
238. van Saarloos, W., *Three basic issues concerning interface dynamics in nonequilibrium pattern formation.* arXiv e-prints, 1998: p. patt-sol/9801002.
239. Dokukin, M.E., N.V. Guz, and I. Sokolov, *Quantitative study of the elastic modulus of loosely attached cells in AFM indentation experiments.* Biophys J, 2013. **104**(10): p. 2123-31.
240. Lam, R.H., et al., *Live-cell subcellular measurement of cell stiffness using a microengineered stretchable micropost array membrane.* Integr Biol (Camb), 2012. **4**(10): p. 1289-98.
241. Tambe, D.T., et al., *Collective cell guidance by cooperative intercellular forces.* Nat Mater, 2011. **10**(6): p. 469-75.
242. Vishwakarma, M., et al., *Mechanical interactions among followers determine the emergence of leaders in migrating epithelial cell collectives.* Nature Communications, 2018. **9**(1): p. 3469.
243. Muncie, J.M., et al., *Mechanics regulate human embryonic stem cell self-organization to specify mesoderm.* bioRxiv, 2020: p. 2020.02.10.943076.
244. Nikolopoulou, E., et al., *Neural tube closure: cellular, molecular and biomechanical mechanisms.* Development, 2017. **144**(4): p. 552-566.
245. Przybyla, L., J.N. Lakins, and V.M. Weaver, *Tissue Mechanics Orchestrate Wnt-Dependent Human Embryonic Stem Cell Differentiation.* Cell Stem Cell, 2016. **19**(4): p. 462-475.
246. Gilbert, S.F., *Developmental biology*. 7th ed. 2003, Sunderland, Mass.: Sinauer Associates. xvii, 838 p.
247. Farhadifar, R., et al., *The influence of cell mechanics, cell-cell interactions, and proliferation on epithelial packing.* Curr Biol, 2007. **17**(24): p. 2095-104.

248. Fletcher, A.G., et al., *Vertex models of epithelial morphogenesis.* Biophys J, 2014. **106**(11): p. 2291-304.
249. Nagai, T. and H. Honda, *A dynamic cell model for the formation of epithelial tissues.* Philosophical Magazine B, 2001. **81**(7): p. 699-719.
250. Aigouy, B., et al., *Cell flow reorients the axis of planar polarity in the wing epithelium of Drosophila.* Cell, 2010. **142**(5): p. 773-86.
251. Rauzi, M., et al., *Nature and anisotropy of cortical forces orienting Drosophila tissue morphogenesis.* Nat Cell Biol, 2008. **10**(12): p. 1401-10.
252. Bi, D., et al., *Energy barriers and cell migration in densely packed tissues.* Soft Matter, 2014. **10**(12): p. 1885-90.
253. Bi, D., et al., *A density-independent rigidity transition in biological tissues.* Nature Physics, 2015. **11**(12): p. 1074-1079.
254. Bi, D., et al., *Motility-driven glass and jamming transitions in biological tissues.* Phys Rev X, 2016. **6**(2).
255. Cantat, I., *Foams : structure and dynamics*. First English edition. ed. 2013, Oxford ; New York, NY, United States of America: Oxford University Press. xii, 265, 8 pages of color plates.
256. Weaire, D.L. and S. Hutzler, *The physics of foams*. 1999, Oxford ; New York: Clarendon Press. xiii, 246 p.
257. Spencer, M.A., et al., *Multicellular actomyosin cables in epithelia under external anisotropic stress.* arXiv e-prints, 2018: p. arXiv:1809.04569.
258. Allen, M.P., *Understanding regression analysis*. 1997, New York: Plenum Press. ix, 216 p.
259. Kanji, G.K., *100 statistical tests*. New edition. ed. 1999, London ; Thousand Oaks, CA: Sage Publications. 215 p.
260. Collinet, C., et al., *Local and tissue-scale forces drive oriented junction growth during tissue extension.* Nat Cell Biol, 2015. **17**(10): p. 1247-58.
261. Ikawa, K. and K. Sugimura, *AIP1 and cofilin ensure a resistance to tissue tension and promote directional cell rearrangement.* Nat Commun, 2018. **9**(1): p. 3295.
262. Pinheiro, D. and Y. Bellaiche, *Mechanical Force-Driven Adherens Junction Remodeling and Epithelial Dynamics.* Dev Cell, 2018. **47**(1): p. 3-19.
263. Reyes, C.C., et al., *Anillin regulates cell-cell junction integrity by organizing junctional accumulation of Rho-GTP and actomyosin.* Curr Biol, 2014. **24**(11): p. 1263-70.
264. Bade, N.D., et al., *Curvature and Rho activation differentially control the alignment of cells and stress fibers.* Sci Adv, 2017. **3**(9): p. e1700150.
265. Burridge, K. and E.S. Wittchen, *The tension mounts: stress fibers as force-generating mechanotransducers.* J Cell Biol, 2013. **200**(1): p. 9-19.
266. Ishizaki, T., et al., *Coordination of microtubules and the actin cytoskeleton by the Rho effector mDia1.* Nat Cell Biol, 2001. **3**(1): p. 8-14.
267. Kassianidou, E., et al., *Geometry and network connectivity govern the mechanics of stress fibers.* Proc Natl Acad Sci U S A, 2017. **114**(10): p. 2622-2627.
268. Kaunas, R., et al., *Cooperative effects of Rho and mechanical stretch on stress fiber organization.* Proc Natl Acad Sci U S A, 2005. **102**(44): p. 15895-900.
269. Oakes, P.W., et al., *Optogenetic control of RhoA reveals zyxin-mediated elasticity of stress fibres.* Nat Commun, 2017. **8**: p. 15817.

270. Wang, J.H., P. Goldschmidt-Clermont, and F.C. Yin, *Contractility affects stress fiber remodeling and reorientation of endothelial cells subjected to cyclic mechanical stretching.* Ann Biomed Eng, 2000. **28**(10): p. 1165-71.
271. Nestor-Bergmann, A., et al., *Mechanical characterization of disordered and anisotropic cellular monolayers.* Phys Rev E, 2018. **97**(5-1): p. 052409.
272. Charras, G. and A.S. Yap, *Tensile Forces and Mechanotransduction at Cell-Cell Junctions.* Curr Biol, 2018. **28**(8): p. R445-R457.
273. Choi, W., et al., *Remodeling the zonula adherens in response to tension and the role of afadin in this response.* J Cell Biol, 2016. **213**(2): p. 243-60.
274. Kale, G.R., et al., *Distinct contributions of tensile and shear stress on E-cadherin levels during morphogenesis.* Nat Commun, 2018. **9**(1): p. 5021.
275. Noll, N., et al., *Active Tension Network model suggests an exotic mechanical state realized in epithelial tissues.* Nat Phys, 2017. **13**(12): p. 1221-1226.
276. Teixeira, P.I., F. Graner, and M.A. Fortes, *Mixing and sorting of bidisperse two-dimensional bubbles.* Eur Phys J E Soft Matter, 2002. **9**(2): p. 161-9.
277. Brochard-Wyart, F. and P.-G. de Gennes, *Unbinding of adhesive vesicles.* Comptes Rendus Physique, 2003. **4**(2): p. 281-287.
278. Finegan, T.M., et al., *The tricellular vertex-specific adhesion molecule Sidekick facilitates polarised cell intercalation during Drosophila axis extension.* PLoS Biol, 2019. **17**(12): p. e3000522.
279. Letizia, A., et al., *Sidekick Is a Key Component of Tricellular Adherens Junctions that Acts to Resolve Cell Rearrangements.* Dev Cell, 2019. **50**(3): p. 313-326 e5.
280. Uechi, H. and E. Kuranaga, *The Tricellular Junction Protein Sidekick Regulates Vertex Dynamics to Promote Bicellular Junction Extension.* Dev Cell, 2019. **50**(3): p. 327-338 e5.
281. Banerjee, S. and M. Cristina Marchetti, *Controlling cell–matrix traction forces by extracellular geometry.* New Journal of Physics, 2013. **15**(3): p. 035015.
282. Raftery, A.E., *Bayesian Model Selection in Social Research.* Sociological Methodology, 1995. **25**: p. 111-163.
283. Wagenmakers, E.J., *A practical solution to the pervasive problems of p values.* Psychon Bull Rev, 2007. **14**(5): p. 779-804.
284. Wasserman, L., *Bayesian Model Selection and Model Averaging.* Journal of Mathematical Psychology, 2000. **44**(1): p. 92-107.
285. Ghibaudo, M., et al., *Traction forces and rigidity sensing regulate cell functions.* Soft Matter, 2008. **4**(9): p. 1836-1843.